The role of the sheath in magnetized plasma turbulence and flows

THÈSE N^{O} 5985 (2013)

PRÉSENTÉE LE 6 DÉCEMBRE 2013

À LA FACULTÉ DES SCIENCES DE BASE

CRPP - THÉORIE

PROGRAMME DOCTORAL EN PHYSIQUE

ÉCOLE POLYTECHNIQUE FÉDÉRALE DE LAUSANNE

POUR L'OBTENTION DU GRADE DE DOCTEUR ÈS SCIENCES

PAR

Joaquim LOIZU

acceptée sur proposition du jury:

Prof. H. M. Rønnow, président du jury
Prof. P. Ricci, directeur de thèse
Prof. A. Fasoli, rapporteur
Prof. I. Hutchinson, rapporteur
Prof. H. R. Wilson, rapporteur

ÉCOLE POLYTECHNIQUE
FÉDÉRALE DE LAUSANNE

Suisse
2013

Abstract

Controlled nuclear fusion could provide our society with a clean, safe, and virtually inexhaustible source of electric power production. The tokamak has proven to be capable of producing large amounts of fusion reactions by confining magnetically the fusion fuel at sufficiently high density and temperature, thus in the plasma state. Because of turbulence, however, high temperature plasma reaches the outermost region of the tokamak, the Scrape-Off Layer (SOL), which features open magnetic field lines that channel particles and heat into a dedicated region of the vacuum vessel. The plasma dynamics in the SOL is crucial in determining the performance of tokamak devices, and constitutes one of the greatest uncertainties in the success of the fusion program. In the last few years, the development of numerical codes based on reduced fluid models has provided a tool to study turbulence in open field line configurations. In particular, the GBS (Global Braginskii Solver) code has been developed at CRPP and is used to perform global, three-dimensional, full-n, flux-driven simulations of plasma turbulence in open field lines.

Reaching predictive capabilities is an outstanding challenge that involves a proper treatment of the plasma-wall interactions at the end of the field lines, to well describe the particle and energy losses. This involves the study of plasma sheaths, namely the layers forming at the interface between plasmas and solid surfaces, where the drift and quasineutrality approximations break down. This is an investigation of general interest, as sheaths are present in all laboratory plasmas.

This thesis presents progress in the understanding of plasma sheaths and their coupling with the turbulence in the main plasma. A kinetic code is developed to study the magnetized plasma-wall transition region and derive a complete set of analytical boundary conditions that supply the sheath physics to fluid codes. These boundary conditions are implemented in the GBS code and simulations of SOL turbulence are carried out to investigate the importance of the sheath in determining the equilibrium electric fields, intrinsic toroidal rotation, and SOL width, in different limited configurations. For each study carried out in this thesis, simple analytical models are developed to interpret the simulation results and reveal the fundamental mechanisms underlying the system dynamics. The electrostatic potential appears to be determined by a combined effect of sheath physics and electron adiabaticity. Intrinsic flows are driven by the sheath, while turbulence provides the mechanism for radial momentum transport. The position of the limiter can modify the turbulence properties in the SOL, thus playing an important role in setting the SOL width.

Keywords:
plasma physics, controlled fusion, scrape-off layer, plasma turbulence, plasma sheaths, boundary conditions, kinetic simulations, fluid simulations, intrinsic rotation, limiter configuration.

Résumé

La fusion nucléaire controllée pourrait devenir une source de production de puissance électrique propre, sûre, et virtuellement illimitée. Le tokamak a démontré être capable de produire des quantités énormes de réactions de fusion en confinant magnétiquement le combustible à fusion à des températures et densités suffisamment élevées. Dans ces conditions, le combustible est dans l'état de plasma.
De façon similaire aux fluides, les plasmas sont souvent turbulents. La turbulence dans le plasma d'un tokamak induit un transport de chaleur et de particules, du coeur vers la couche extérieure, appellée *scrape-off layer* (SOL). La SOL est caractérisée par des lignes de champ magnétique ouvertes qui acheminent les particules vers une région de la paroi conçue pour supporter des grandes quantités de chaleur, toutefois limitées. La dynamique du plasma dans la SOL est déterminante pour ce qui concerne la performance des tokamaks et ceci représente un des défis majeurs pour le succès du programme de fusion.
Au cours des dernières années, des codes numériques basés sur des modèles fluides réduits ont été développés pour étudier la turbulence dans la SOL. En particulier, le code GBS (Global Braginskii Solver) a été développé au CRPP pour tourner des simulations tridimensionnelles de la turbulence du plasma dans des configurations magnétiques ouvertes. Cependant, pouvoir prédire le comportement du plasma dans la SOL est un but qui nécessite, entre autres, un traitement rigoureux des intéractions plasma-paroi pour ainsi bien décrire les pertes d'énergie et de particules. Ceci requiert l'étude des gaines, c'est-à-dire les couches qui se forment à l'interface entre les plasmas et les surfaces solides, où les hypothèses de quasineutralité et de dérive sont brisées. L'étude des gaines est d'intérêt géneral car elles sont présentes dans tous les plasmas de laboratoire.
Cette thèse présente des progrès dans la compréhension des gaines dans les plasmas, ainsi que leur couplage avec le plasma turbulent. Un code cinétique est développé dans le but d'étudier la transition plasma-paroi magnetisée et de dériver un ensemble complet de conditions au bord analytiques, capables de fournir la physique des gaines aux codes fluides. Ces conditions au bord sont implémentées dans le code GBS, puis des simulations de la turbulence dans la SOL sont tournées pour examiner l'effet de la gaine sur les champs électriques d'équilibre, la rotation intrinsèque du plasma, ainsi que la largeur de la SOL, dans des configurations limitées différentes. Pour chaque étude poursuivi dans cette thèse, des modèles analytiques simples sont développés afin d'interpréter les résultats des simulations et de découvrir les mécanismes fondamentaux à la base de la dynamique du système. Il s'avère que le potentiel électrique dans le plasma est déterminé par la combinaison de la physique de la gaine et de la condition d'adiabaticité des électrons. Des flux intrinsèques sont générés par la gaine dans la direction parallèle au champ magnétique, puis sont transportés radialement

par la turbulence. La position du limiteur peut modifier les propriétés de la turbulence dans la SOL et donc représente un élément important dans la détermination de la largeur de la SOL.

Mots-clefs:
physique des plasmas, fusion controlée, scrape-off layer, turbulence, gaines, conditions au bord, simulations cinétiques, simulations fluides, rotation intrinsèque, position du limiteur.

Contents

Chapter 1

Introduction

Matter in the Universe can exist in different states. While the most common states of matter found on planet Earth are solid, liquid, and gas, practically all the visible contents of the cosmos are in the state of plasma, the so-called fourth state of matter [1]: stars, nebulae, the solar wind and even the matter surrounding black holes (Figure 1). A plasma is a quasineutral gas of charged particles exhibiting collective behavior [2]. It is obtained when a gas exceeds a temperature, typically of the order of 10 000 °K. Above such temperatures, a gas becomes partially or completely ionized. A plasma remains nevertheless electrically neutral up to very small scales. This is ensured by the strong electric forces generated in the presence of local charge imbalance.

Plasmas almost never arise naturally on Earth. Some spectacular exceptions are the aurora borealis or lightning. The upper part of the atmosphere, the ionosphere, is also maintained in the state of plasma by solar radiation. These are all low density and low temperature plasmas, at most reaching a few eV (1 eV $\approx$ 11 000 °K). In space, however, plasmas can reach much higher densities and temperatures. For example, the center of the Sun is at a temperature of about 1 keV. At such high temperatures, particles in the plasma are very energetic. In particular, two positive nuclei can get extremely close to each other despite being repelled by the electric force. At very short distances, nuclear attractive forces enter into play, thus allowing the two nuclei to fuse together and form a heavier element. This reaction is called thermonuclear fusion. It is the process through which all elements in the Universe (except hydrogen) are created, by successive fusion of heavier and heavier elements.

The mass of the products of a fusion reaction is different than the mass of the initial colliding nuclei. In fact, when the fusion product is lighter than iron, a lack of mass is observed at the end of the fusion reaction. This shortage of mass has indeed been converted into energy according to Einstein's relation $E = mc^2$. If such fusion reactions occur in a plasma at a sufficient rate, this release of energy (in the form of photons or kinetic energy of the products) can sustain the conditions for nuclear fusion without any external supply of energy. The threshold condition above which

Figure 1: The Sun undergoing an enormous plasma ejection, much larger than the size of planet Earth (top left). Columns of cool interstellar hydrogen gas and dust in M16, the Eagle Nebula, where the tallest pillar is about a light-year long from base to tip (top middle). The spiral galaxy NGC 1365, where a huge black hole lies at its center and forms an accretion disk of matter around it that funnels gas and dust (top right). Aurora borealis as seen from space by a satellite (bottom left) and from the ground (bottom middle). Lightning over a city during a thunderstorm (bottom right).

a plasma undergoes self-sustained fusion reactions is refered to as *ignition*. Stars are considered to be born when they reach ignition. Yet their fuel is finite and as fusion reactions take place, their elements become heavier, until it becomes too difficult to sustain the plasma in burning conditions and the star approaches its death [3].

Humans artificially create plasmas in their everyday life: neon tubes and plasma screens are everyday examples. Plasmas are also widely used in industry, for instance to build solar panels [4] or aerospace propulsion systems [5, 6]. Since the beginning of the 1950's, the idea of inducing thermonuclear fusion in a controlled manner has driven an enormous research effort in the field of plasma physics [7]. In fact, controlled fusion could provide our society with a clean, safe, and virtually inexhaustible source of electric power production [8]. However, achieving fusion relevant conditions, e.g. ignition, requires a plasma to be confined at very high densities and temperatures for a sufficiently long time [9]. One way of confining a plasma is to use magnetic fields, as charged particles tend to move more easily along than across magnetic field lines. In the last sixty years, different magnetic confinement concepts have been explored: the magnetic mirror, the pinch, the stellerator, and the tokamak, among others [7]. The most advanced concept nowadays is the tokamak, a doughnut-shaped magnetic confinement device which has proven to be

capable of reaching very high densities ($\sim 10^{20}$ m^{-3}) and temperatures ($\sim$ 10 keV) for a sufficiently long time ($\sim 1s$) to produce large amounts of fusion reactions. In 1991, the world's largest tokamak, the Joint European Torus (JET), achieved the first controlled release of fusion power in history (Figure 2). In 1993, the Tokamak Fusion Test Reactor (TFTR) at Princeton Plasma Physics Laboratory was the first in the world to use 50-50 mixtures of deuterium-tritium, yielding an unprecedented 10.7 MW of fusion power. In 1997, JET reached a fusion gain of $Q \approx 65\%$ [10], where Q is the ratio of the energy produced by fusion reactions to the energy externally injected into the plasma. All these achievements have led fusion science to an exciting period where the breakeven point may be reached: fusion power output at least as large as the total power required to run the reactor. It should be noted, however, that achieving $Q > 1$ does not imply that the tokamak is producing more net power than it consumes. Accounting for the efficiency of all the energy production process in a fusion reactor, producing net energy may require approximately $Q = 10$. This is the target of the fusion experiment ITER [11], currently under construction in Cadarache, France. The precise goal of ITER is to "demonstrate the scientific and technological feasability of fusion power for peaceful purposes". However, some challenges that involve deepening our physics understanding of tokamak plasmas are still present in the adventure of making controlled fusion an energy source for mankind.

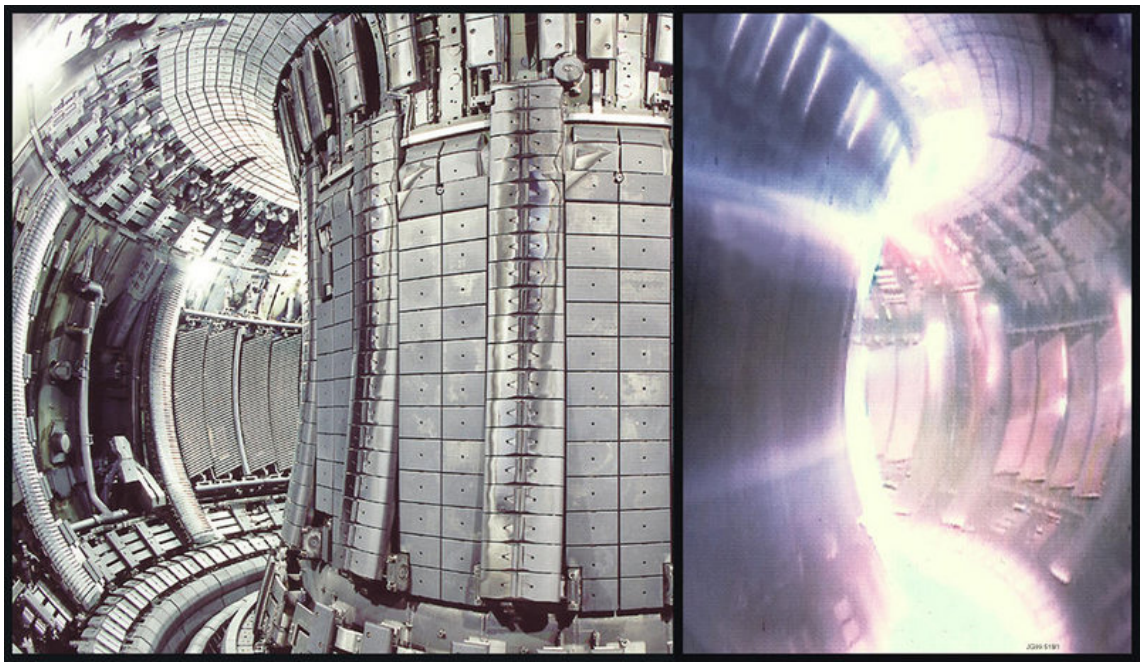

Figure 2: Interior of the vacuum vessel of the Joint European Torus (JET), the world's largest tokamak. On the right we see a picture taken during a plasma discharge, where visible light only comes from the regions where the plasma is relatively cold, namely at the very edge of the plasma volume.

In a tokamak, the plasma is confined in a toroidal chamber by using an externally applied toroidal magnetic field (Figure 3). As the presence of magnetic field curvature and gradients makes a purely toroidal magnetic configuration unstable, a poloidal magnetic field is also introduced [12]. Producing a poloidal magnetic field that is toroidally symmetric is not trivial. In a tokamak, a current is induced inside the plasma which in turn generates the desired poloidal magnetic field. Induction of plasma current is possible since plasmas are very good conductors, with a conductivity that increases with plasma temperature [13]. Therefore the desired current can be achieved by means of external coils which induce an electromotive force via time-varying coil currents. The resulting magnetic configuration is such that a magnetic field line winds around the torus lying on a given toroidal surface called *flux surface* (Figure 3). Therefore the magnetic topology consists of nested closed flux surfaces. Finally, additional coils are used for the vertical stability and shaping of the plasma volume.

Plasma heating in a tokamak is a consequence of resistive dissipation of the induced plasma current (Joule effect). However, as the plasma temperature increases its resistivity decreases and therefore the Joule heating (also called Ohmic heating) becomes less and less efficient. Reaching the very high temperatures required for fusion is only possible via injection of high power microwaves or neutral particle beams, among other methods. The plasma confinement in a tokamak is nevertheless not perfect: transport of particles and heat takes place across the flux surfaces. Although this is in part due to the finite collisionality between plasma particles, which eventually leads to cross-field diffusion, the level of cross-field transport observed in tokamaks exceeds by many orders of magnitude the expected collisional transport level [14]. It is now well established that the mechanism leading to the observed levels of cross-field transport is plasma turbulence [15].

Because of plasma turbulence, high temperature plasma reaches the outermost flux surfaces of a tokamak, which eventually intersect parts of the vacuum vessel. This leads to undesired heat loads caused by the motion of particles along and across the field lines. In order to control the unavoidable outflow of plasma from the tokamak core, a physical object called *limiter* can be inserted into the peripheral region of the plasma [16] (Figure 4). This sets in a controlled manner, the separation between the confined plasma and the region where the magnetic field lines are open and intersect the vessel walls, defining the Last Closed Flux Surface (LCFS). The region of open field lines lying outside the LCFS is called the Scrape-Off Layer (SOL). Another strategy to control the power output of the device is to use external magnets to modify the magnetic field lines in the outermost region of the plasma. It is then possible to channel particles and heat into a dedicated region of the wall, the so-called divertor, which is capable of handling larger heat loads than the rest of the vessel, while keeping the plasma-facing components away from the confined region. Moreover, the divertor configuration is well suited for the pumping of both

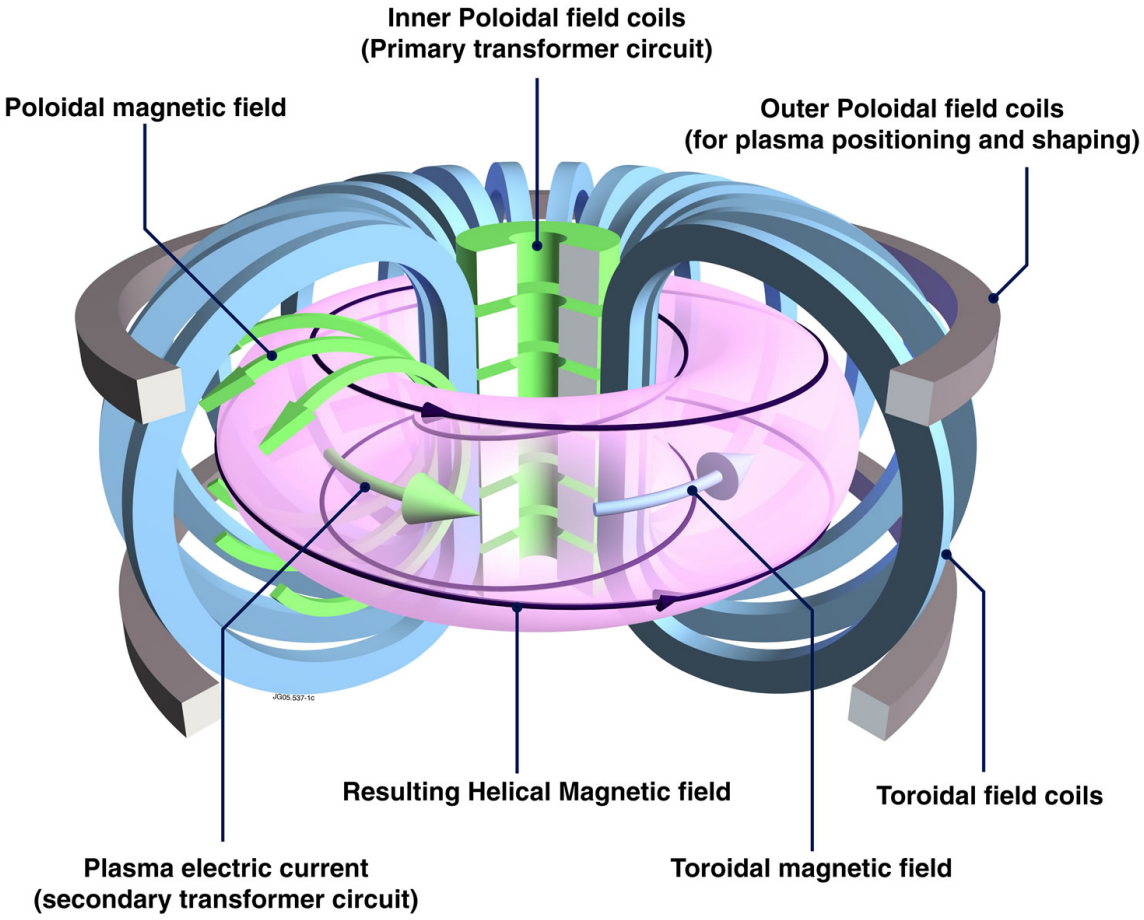

Figure 3: Tokamak basic principles. In blue: the toroidal field coils produce the main toroidal magnetic field. In green: the poloidal field coils induce a current in the plasma, generating the poloidal magnetic field. In black: the resulting helical magnetic field ensures good plasma confinement. In pink: a magnetic flux surface. In grey: additional coils are used for the vertical stability and shaping of the plasma volume.

the impurities released by particle sputtering and the helium "ash" produced by fusion reactions.

The plasma dynamics in the SOL, which is present in both limited and diverted configurations, is crucial in determining the performance of tokamak devices, and constitutes one of the greatest uncertainties in the success of the fusion program [17]. As a matter of fact, the SOL determines the boundary conditions for the core plasma, controls the plasma refueling, heat losses, and impurity dynamics, largely governing the fusion power output of the entire device [18]. Therefore understanding, controlling and predicting the behavior of the plasma in the SOL is of crucial importance for the success of ITER and future magnetic fusion reactors.

The dynamics of the plasma in the SOL of tokamaks is characterized by the interplay between plasma coming from the core, cross-field turbulent transport and parallel

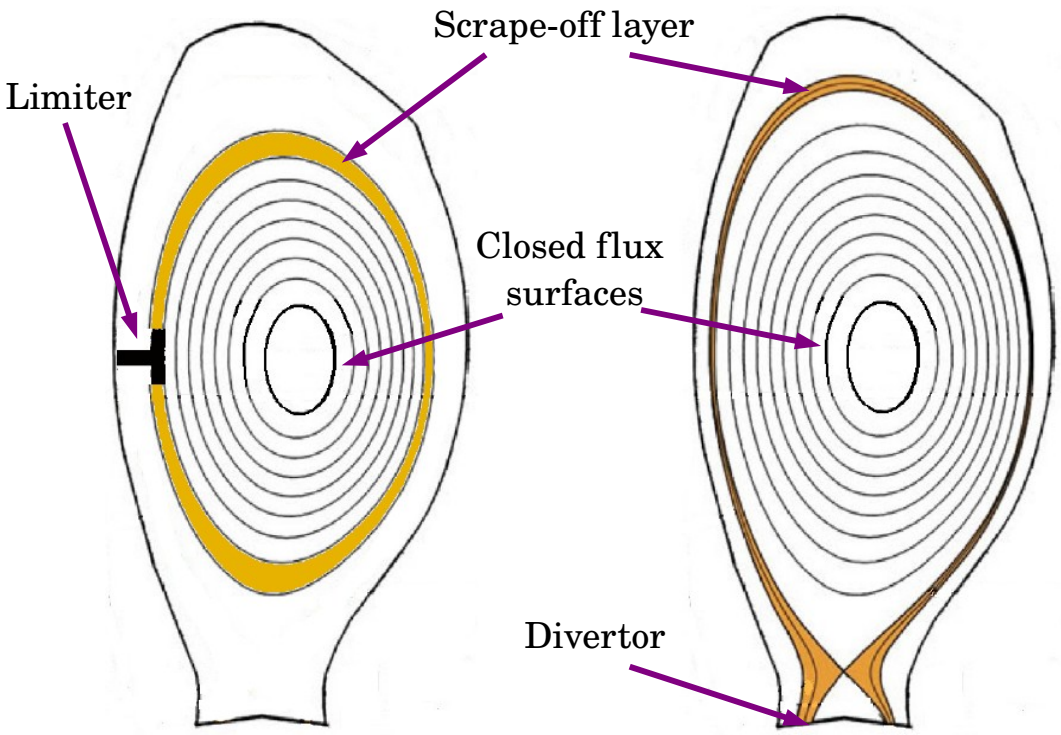

Figure 4: Poloidal cross-sections showing the magnetic flux surfaces of a tokamak in both limited (left) and diverted (right) configurations. Shown in orange is the SOL region, where magnetic field lines are open and intersect the limiter or divertor.

losses at the end of the field lines [16]. Therefore the understanding of plasma turbulence and plasma-wall interactions is essential for a complete description of the SOL dynamics.
More generally, turbulence in open field line configurations is an outstanding problem. Many basic plasma physics experiments feature plasma turbulence in an open field line configuration. These experiments include linear devices such as the Large Plasma Device [19] (LAPD) at the University of California, or the HelCat device [20] at the University of New Mexico. Also, simple magnetized toroidal devices such as the Toroidal Plasma Experiment [21] (TORPEX) at the Center for Research in Plasma Physics, Switzerland, or the Helimak device [22] at the University of Texas, Austin, are endowed with the main ingredients of SOL turbulence, namely plasma gradients, magnetic curvature and parallel losses.

A common feature of open field line plasma turbulence is a relatively low plasma temperature which makes the plasma rather collisional. This is due the fact that the plasma is not confined but instead particles are continuously lost along the field lines. The relatively large collision rate allows local thermodynamic equilibrium to

be reached relatively quickly, and a few moments of the particle distribution functions (i.e., the density, momentum, temperature) can be reasonably used to model the plasma dynamics. This justifies the use of fluid models to describe plasma turbulence in open field lines, or even in the outermost region of the confined plasma in tokamaks, which remains reasonably cold for kinetic effects to play an important role. A closed set of two-fluid equations describing plasma turbulence under such conditions was summarized by Braginskii in 1965 [23]. Later, a number of reduced models more suited for computational treatment were deduced [24], in some cases taking into account ion gyro-motion effects or kinetic effects neglected in the original Braginskii equations [25, 26, 27]. A number of codes have been recently developed based on the reduced models [28, 29, 30, 31, 32, 33, 34]. Numerical simulations using these codes have been carried out over the last years, shedding light on the origin and nature of plasma turbulence in open magnetic field line configurations. In particular, the Global Braginskii Solver code, GBS, has been developed at CRPP and is used to perform global, three-dimensional simulations of plasma turbulence in open field lines [34]. Reaching predictive capabilities remains, however, an outstanding challenge that involves a proper treatment of the plasma-wall interactions at the end of the field lines.

The understanding of the plasma-wall transition involves the study of plasma sheaths, namely the non-neutral layers forming at the interface between plasmas and solid surfaces [16]. Sheaths are present in the edge of magnetically confined fusion plasmas, at the interface between spacecrafts and space plasmas, in the fabrication of semiconductor devices, and wherever a plasma interacts with a solid surface. In particular, their understanding is at the heart of electrostatic probe theory [35, 36]. Plasma sheaths represent one of the oldest problems in plasma physics [37], and yet, an enormous research effort is still ongoing [38, 39]. Generally speaking, sheaths determine the particle and energy losses in all laboratory plasmas, hence their knowledge is essential to describe the dynamics of the main plasma and to predict the particle and energy fluxes at the solid surface. This is of particular importance for ITER and future fusion reactors [17].

In the last few years, the development of numerical codes based on reduced fluid models has provided a tool to study turbulence in open field line configurations. Unclear remains, however, how these codes can properly describe the physics of the plasma-wall transition, and more importantly what is the effect of sheath physics on the turbulence and flows that are developed far from the walls.

In this thesis, we present progress in the understanding of plasma sheaths and their coupling with the main turbulent plasma. We develop a simple numerical tool to study the magnetized plasma-wall transition region and derive a complete set of analytical boundary conditions that supply the sheath physics to fluid codes. These boundary conditions are implemented in a three-dimensional fluid code and simula-

tions of SOL turbulence are carried out to investigate the importance of the sheath in determining the equilibrium electric fields, intrinsic toroidal rotation and scrape-off layer width in a limited configuration. For each study carried out in this thesis, we develop simple analytical models to interpret the simulations and reveal the fundamental mechanisms underlying the complexity of the system.

Chapter 2 starts with an introduction to plasma sheaths, followed by a description of the numerical tool developed to study the magnetized plasma-wall transition. First, simulations of non-magnetized sheaths are presented where the standard Bohm criterion for the ion outflow is retrieved. We show that under certain conditions plasma sheaths can display arbitrarily small ion flows, and an analytical formula generalizing the standard Bohm criterion is presented. We further investigate the effect of biasing on the plasma-wall transition and find that a plasma bound between an ion and an electron sheath displays abrupt transitions in the plasma potential. An analytical model supports the observed simulations results. Second, simulations of magnetized plasma sheaths are presented where the standard Bohm-Chodura condition for the ion outflow is retrieved. The structure of the magnetized sheath is analyzed in detail and its dependence on some relevant physical parameters is discussed. An analytical model is derived in order to obtain a complete set of boundary conditions for plasma fluid models at the magnetic presheath entrance, which are then verified in some limits via kinetic simulations.

In Chapter 3, the Braginskii equations and their drift-reduced form are described. We then present the GBS code, which is based on the drift-reduced Braginskii equations. The boundary conditions derived in Chapter 2 are implemented in GBS, and as an example we present results from simulations of SOL turbulence in a limited configuration. We show that smooth profiles form at the interface between the plasma and the limiter. Finally, examples of turbulence simulations of TORPEX plasmas are presented.

In Chapter 4, we investigate analytically the structure of the equilibrium electrostatic potential that is expected in an open field line turbulent plasma. A simple model based on the generalized Ohm's law reveals the relative importance of the sheath in setting the value of the plasma potential far from the walls. Simulations of SOL turbulence in a sheath-limited regime confirm the analytical predictions. The implications for different tokamak regimes are discussed.

In Chapter 5, we show that intrinsic toroidal plasma rotation is present in SOL simulations, as a consequence of poloidally asymmetric parallel flows. We investigate analytically the origin and nature of these flows and derive an equation describing the generation and transport of parallel momentum in the SOL of tokamaks. We present an approximate analytical solution which reveals the contribution of the sheath in driving intrinsic rotation in the SOL, as well as the role of turbulence in

transporting momentum radially. We show that the two-dimensional analytical profiles for the parallel Mach number in a poloidal cross-section are in good agreement with the GBS results. Finally, the analytical solution is shown to explain the experimental trends that are observed for the magnitude and direction of the parallel Mach number in the SOL of tokamaks.

Chapter 6 explores the effect of the limiter position on the SOL equilibrium profiles. In particular, we show that the width of the SOL varies significantly with the limiter position and has a clear poloidal dependence which is explained qualitatively. The limiter position also modifies substantially the equilibrium electrostatic potential and the intrinsic rotation profiles. We show that the analytical models developed in Chapters 4 and 5 are able to capture these dependences.

Finally, Chapter 7 summarizes the achievements of this thesis and offers an outlook on possible future developments.

Chapter 2

The plasma-wall transition

2.1 Introduction

The simplest way to understand the plasma-wall transition is to imagine a collisionless, non-magnetized, fully ionized plasma with singly charged ions and in contact with a perfectly conducting, infinite, planar wall that is grounded and absorbs all charged particles reaching the surface. In practice, more complicated processes may be present, such as ion-neutral collisions, recycling, secondary electron emission or sputtering. Also the wall may be an insulator in which case it may get charged by the plasma particles. However, let us consider the simplest situation first.

For $T_e \sim T_i$, the typical speed of an electron, $v_{the} = \sqrt{T_e/m_e}$, is much larger than the typical speed of an ion, $v_{thi} = \sqrt{T_i/m_i}$. Therefore electrons reach the wall at a much higher rate than the ions. This would lead to a continuous increase of the charge imbalance in the plasma, with $n_i > n_e$, thus breaking the quasi-neutrality condition $n_e \simeq n_i$. However, the plasma generates an electric field $\mathbf{E} = -\nabla\phi$ according to Poisson's equation,

$$\nabla^2\phi = -\frac{e(n_i - n_e)}{\epsilon_0} \quad . \tag{2.1.1}$$

Since $\nabla^2\phi < 0$, a drop in the electrostatic potential is established when approaching the wall (Figure 2.1.1). This means that the electric field $\mathbf{E}$ points towards the surface, thus preventing most of the electrons from leaving the plasma and accelerating the ions. A quasi-steady state is then established, such that the particle outflow from the system is ambipolar. Quasi-neutrality is therefore maintained far from the wall, while a thin, non-neutral layer with $n_i > n_e$ forms at the plasma-wall interface and ensures the existence of this electric field. This layer is called the Debye sheath and has a width of the order of a few Debye lengts $\lambda_D = \sqrt{\epsilon_0 T_e/e^2 n_e}$, similarly to the Debye shielding that occurs when a charge perturbation is introduced in a plasma. As we show later, the potential barrier in the sheath is a few times the electron temperature, thus repelling most of the incoming electrons. For example,

a plasma with $T_e = 2$ eV and $n_e = 10^{16}$ m^{-3} has a Debye length $\lambda_D \approx 0.1$ mm and therefore the sheath electric field is $E \approx 10$ kV/m.

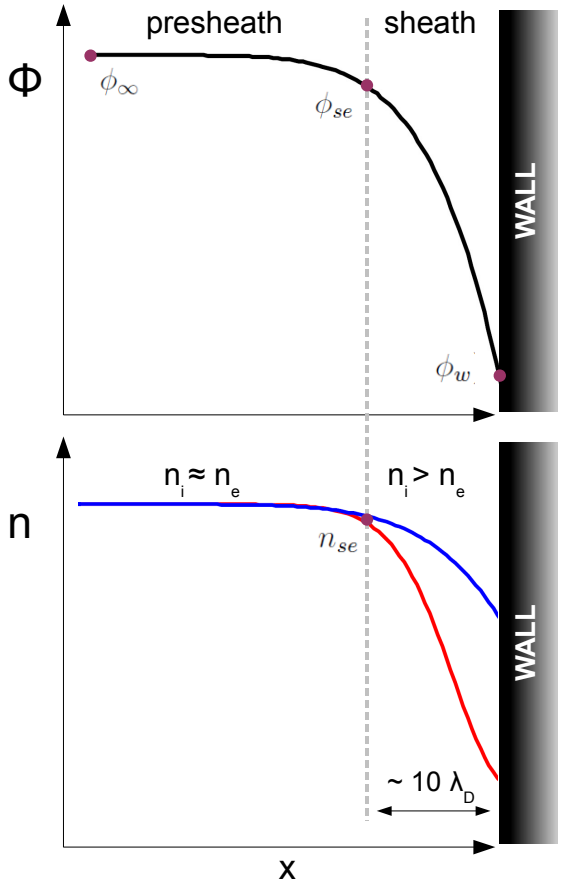

Figure 2.1.1: Schematic representation of the plasma-wall transition. Top: electrostatic potential in the plasma. Bottom: Ion (blue) and electron (red) densities. The vertical dashed line indicates the entrance of the Debye sheath, where quasi-neutrality is broken.

The exact location of the sheath entrance cannot be defined by the breaking of quasi-neutrality, $n_i \not\approx n_e$, as this would be somewhat arbitrary. The commonly accepted theory to describe the sheath edge location is given by the Bohm criterion, stating that ions need to be accelerated up to the plasma sound speed, $c_s = \sqrt{T_e/m_i}$, in order for a sheath to exist [40]. One can derive Bohm's criterion assuming that electrons have a constant temperature T_e and follow the Boltzmann relation

$$n_e = n_{se} \exp\left[e(\phi - \phi_{se})/T_e\right] \tag{2.1.2}$$

where n_{se} and ϕ_{se} denote the electron density and the plasma potential at the sheath edge. Ions are assumed to be monoenergetic ($T_i = 0$) and collisionless, with a velocity $V_\infty = 0$ far from the sheath. The conservation of the ion flux, $\Gamma_i = n_i V_i$,

and energy, $m_i V_i^2/2 = e(\phi_\infty - \phi)$, where ϕ_∞ is the potential far from the sheath, leads to estimating the ion density as

$$n_i = n_{se}\sqrt{\frac{\Delta\phi_{ps}}{(\phi_\infty - \phi)}} \quad . \tag{2.1.3}$$

Here $\Delta\phi_{ps} = \phi_\infty - \phi_{se}$ is the presheath potential drop (Figure 2.1.1). The Bohm criterion is obtained by linearizing Eqs. (2.1.2) and (2.1.3) around $\phi = \phi_{se}$ and inserting them in the one-dimensional Poisson equation,

$$\frac{\partial^2\phi}{\partial x^2} \approx e^2 n_{se}\left[\frac{1}{T_e} - \frac{1}{2e\Delta\phi_{ps}}\right](\phi - \phi_{se}) \quad . \tag{2.1.4}$$

A physically acceptable, non oscillatory solution for ϕ exists only if $\partial_x^2\phi \leq 0$. This gives a condition on the presheath potential drop, $e\Delta\phi_{ps} \geq T_e/2$, which implies $V_{i,se} \geq c_s$, namely that ions are at least sonic when entering the sheath. On the other hand, by treating separately the presheath region, one can show that $V_i \leq c_s$ before entering the sheath [16], thus implying that the sheath edge location is defined by the point where $V_i = c_s$.

The ions are pre-accelerated by the presheath electric field and enter the sheath at the sound speed. Thus the electrons must, on average, enter the sheath with the same velocity in order to ensure an ambipolar flow $\Gamma = n_{se}c_s$. A kinetic description of the electrons is necessary in order to predict their average velocity. Let us assume that their distribution function far from the wall is a Maxwellian with zero mean velocity and a temperature T_e. An electron that arrives at the sheath edge with a velocity v reaches the wall only if it overcomes the sheath potential barrier, i.e. if $v > v_{cut} = \sqrt{2e(\phi_{se} - \phi_w)/m_e}$. If $v < v_{cut}$, the electron is reflected in the sheath region back into the main plasma, and thus returns to the sheath entrance with a velocity $-v$. Hence the electron distribution function at the sheath edge is a Maxwellian of temperature T_e but truncated at v_{cut} on one side. The average electron velocity at the sheath edge, obtained from this distribution function, is approximately [35]

$$V_{e,se} = c_s \exp\left[\Lambda - e(\phi_{se} - \phi_w)/T_e\right] \tag{2.1.5}$$

where $\Lambda = \log\sqrt{m_i/2\pi m_e} \approx 3$ for hydrogen. Therefore the ambipolarity of the particle flow, $V_{e,se} = V_{i,se} = c_s$, imposes the magnitude of the potential drop in the sheath, namely $e(\phi_{se} - \phi_w) = \Lambda T_e$. One therefore expects currents to the wall if the potential at the sheath edge deviates from this value.

Sheaths have been studied since the pioneering work of Langmuir in 1929 [37], followed by an enormous research effort [38, 16, 35], which persists still (see, e.g.,

Refs. [41, 42, 43, 44, 45, 46]). Only recently their detailed experimental investigation has become possible [47, 48, 49]. Many different questions are usually addressed in studies of plasma sheaths. Some examples are: how is the Bohm criterion modified by finite ion temperature, magnetic field, secondary electron emission, recycling, ion-neutral collisions, or surface geometry? What is the ion distribution function at the sheath edge and at the wall? What is the effect of multiple ion species? Are there instabilities in the sheath? What is the effect of electrical biasing? How should we interpret the I-V curve of an electrostatic probe immersed in a plasma?

The final purpose of this chapter is to answer the following question: what are the boundary conditions that should be imposed in a drift-reduced fluid code in order to properly describe the magnetized plasma-wall transition? This problem is crucial for the modeling of plasma turbulence in open field lines. We approach it by steps of increasing complexity, starting from the study of unmagnetized ion sheaths, for which the standard Bohm criterion is generalized to non-ambipolar conditions. Then, we look at the effect of wall biasing on the plasma potential, shedding some light on the properties of ion and electron sheaths with finite ion temperature. Leveraging the analysis technique developed for the case of unmagnetized sheaths, we then turn to the study of magnetized plasma sheaths and the derivation of boundary conditions to be applied to plasma turbulence codes. In each of these steps, we perform kinetic simulations and analytical modeling of the plasma-wall transition region.

In the following section, the numerical tool used to carry out simulations of the plasma-wall transition is presented.

2.2 The ODISEE code

In this section, we describe the One-DImensional Sheath Edge Explorer (ODISEE) code, which was developed within the framework of this thesis. ODISEE is a fully kinetic, electrostatic particle-in-cell (PIC) code akin to previous simulations [50, 51]. It was originally developed to simulate a one-dimensional, source-driven, unmagnetized plasma bound between two perfectly conducting walls [52]. It was then used to study the effect of strong biasing on the plasma potential [53]. Different additional options have been added in the last years, for example the possibility of insulating walls or electrically biased grids, which have been used to tackle the problem of biasing in basic plasma physics experiments such as the HelCat device [20, 54]. The code is also capable of simulating a magnetized plasma with a constant magnetic field oblique to the walls and in the presence of an external electric field [55].

ODISEE solves the Vlasov-Poisson system in one dimension in real space and three dimensions in velocity space. Physical boundaries representing planar walls set the extension of the system in real space (Figure 2.2.1). A quasi-steady state results

from the balance between a plasma source and the losses at the sheaths. The code is written in Fortran 90 and parallelized using the Message Passing Interface (MPI). In the following, we briefly describe the model and numerical methods used in the code.

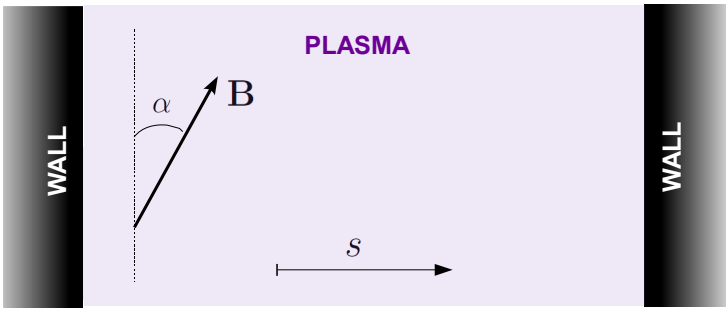

Figure 2.2.1: Sketch of a one-dimensional plasma bound between two walls and in the presence of a constant magnetic field oblique to the walls at an angle α. The coordinate s is normal to the wall surfaces.

2.2.1 Vlasov-Poisson model

In the electrostatic, collisionless limit, the dynamics of a plasma can be described by the Vlasov-Poisson system,

$$\begin{aligned} &\frac{\partial f_\alpha}{\partial t} + \mathbf{v}\cdot\frac{\partial f_\alpha}{\partial \mathbf{x}} + \frac{q_\alpha}{m_\alpha}(\mathbf{E}+\mathbf{v}\times\mathbf{B})\cdot\frac{\partial f_\alpha}{\partial \mathbf{v}} = 0 \\ &\nabla^2\phi = -\frac{1}{\epsilon_0}\sum_\alpha q_\alpha \int f_\alpha(\mathbf{x},\mathbf{v})d^3v \end{aligned} \tag{2.2.1}$$

with $\alpha = \{i, e\}$ denoting the particle species of charge q_α and mass m_α. This system (2.2.1) describes the time evolution of the distribution functions for ions and electrons, $f_\alpha(\mathbf{x}, \mathbf{v}, t)$, as well as the space-time evolution of the electrostatic potential, $\phi(\mathbf{x}, t)$, with $\mathbf{E} = -\nabla\phi$. In the following, we consider the magnetic field $\mathbf{B}$ to be constant and externally imposed. One way of solving this system numerically is by means of the so-called particle-in-cell (PIC) method, a powerful technique based on the Lagrangian description of the plasma.

2.2.2 Particle-in-cell method

The fundamental assumption of the PIC method is that the distribution function of each species can be described by a superposition of N finite elements called superparticles or computational particles [56], which are localized in velocity space

and have some spatial shape. The particle distribution function for a given species is written as

$$f(\mathbf{x},\mathbf{v},t) = \sum_{p=1}^{N} f_p(\mathbf{x},\mathbf{v},t) = \sum_{p=1}^{N} w_p S(\mathbf{x}-\mathbf{x}_p(t))\delta(\mathbf{v}-\mathbf{v}_p(t)) \tag{2.2.2}$$

where S is the so-called shape function, δ is the Dirac delta function, and w_p is the weight of each superparticle p. The shape function is defined to be symmetric and with a unitary integral. Typically, S is chosen to be either a Dirac's delta or a b-spline, the lowest order being a flat-top function [57]. The weight w_p is the number of physical particles present in the element of phase space represented by the computational particle p. Thus the integral of $f(\mathbf{x},\mathbf{v},t)$ over all phase space,

$$\int\int f(\mathbf{x},\mathbf{v},t)\ \mathbf{dxdv} = \sum_{p=1}^{N} w_p \tag{2.2.3}$$

corresponds to the total number of physical particles of a given species in the system. Finally, each superparticle is characterized by two time-dependent parameters, the superparticle position $\mathbf{x}_p(t)$ and velocity $\mathbf{v}_p(t)$.

We now assume that the time evolution of each superparticle is still described by a Vlasov equation,

$$\frac{\partial f_p}{\partial t} + \mathbf{v}\cdot\frac{\partial f_p}{\partial \mathbf{x}} + \frac{q}{m}(\mathbf{E}+\mathbf{v}\times\mathbf{B})\cdot\frac{\partial f_p}{\partial \mathbf{v}} = 0 \quad . \tag{2.2.4}$$

where the electric field used in the Vlasov equation (2.2.4) is due to all elements, namely the same entering the complete Vlasov equation. Taking different moments of Eq. (2.2.4), one can show that the following equations must be satisfied by each superparticle:

$$\begin{aligned}
\frac{dw_p}{dt} &= 0 \\
\frac{d\mathbf{x}_p}{dt} &= \mathbf{v}_p(t) \\
\frac{d\mathbf{v}_p}{dt} &= \mathbf{a}_p(\mathbf{x}_p,\mathbf{v}_p,t) = \frac{q_\alpha}{m_\alpha}(\mathbf{E}_p+\mathbf{v}_p\times\mathbf{B}) \quad ,
\end{aligned} \tag{2.2.5}$$

where

$$\mathbf{E}_p = \int S(\mathbf{x}-\mathbf{x}_p(t))\mathbf{E}(\mathbf{x})\ \mathbf{dx} \tag{2.2.6}$$

is the average electric field acting on a computational particle. The system (2.2.5) represents the complete set of evolution equations for the parameters defining the functional dependence of the distribution f_p in Eq. (2.2.2). In particular, the first of these equations describes the conservation of the number of physical particles per computational particle.

A crucial advantage of the PIC method is that its evolution equations resemble the Newton equation followed by the regular physical particles, with the difference that the field is computed as the average over the particle spatial extension, as seen in the definition of $\mathbf{E_p}$.

The electric field $\mathbf{E}(\mathbf{x})$ is itself given by the Poisson equation, which is solved in a certain grid with M cells of width Δs and centered at $\mathbf{x}_c$, where $c = 1,...,M$. Then the electric field is defined in each grid cell as $\mathbf{E}_c$. An interpolation of the electric field from the grid onto the particles is therefore required. Let us call $T(\mathbf{x}-\mathbf{x}_c)$ the flat-top function centered at $\mathbf{x}_c$ and equal to one within the cell span. Then

$$\mathbf{E}(\mathbf{x}) = \sum_{c=1}^{M} T(\mathbf{x}-\mathbf{x}_c)\mathbf{E}_c \quad . \tag{2.2.7}$$

The information can then be carried between the particles and the grid through the so-called interpolation function, which is defined as the convolution of S and T, namely

$$I(\mathbf{x}_c - \mathbf{x}_p) = \int S(\mathbf{x}-\mathbf{x}_p)T(\mathbf{x}-\mathbf{x}_c)\ \mathbf{dx} \quad . \tag{2.2.8}$$

The interpolation function allows a direct computation of both the superparticle electric field $\mathbf{E}_p$ (required to evolve the superparticles) and the cell charge density ρ_c (required to solve the Poisson equation) without the need for integration. In fact, we can write

$$\mathbf{E}_p = \sum_{c=1}^{M} I(\mathbf{x}_c - \mathbf{x}_p)\mathbf{E}_c \tag{2.2.9}$$

and

$$\rho_c = \frac{1}{V}\sum_{\alpha} q_\alpha \sum_{p_\alpha=1}^{N_\alpha} w_{p\alpha} I(\mathbf{x}_c - \mathbf{x}_{p\alpha}) \ , \tag{2.2.10}$$

where V is the volume of a grid cell ($V = \Delta s$ in one dimension). Within this framework, one can pass the information of the particles onto the grid and viceversa. These two processes will be referred to as *Particle to Grid Interpolation* (PGI) and

Grid to Particle Interpolation (GPI).

The Vlasov-Poisson system (2.2.1) can thus be solved numerically by initializing the system with a certain distribution of superparticles and repeating the following cycle:

(1) Apply PGI to get ρ_c,
(2) Solve the Poisson equation to get ϕ_c and then E_c,
(3) Apply GPI to get E_p and then a_p,
(4) Move particles according to a_p
(5) The cycle restarts.

In ODISEE, the shape function is chosen to be a Dirac's delta, $S(\mathbf{x}-\mathbf{x_p}) = \delta(\mathbf{x}-\mathbf{x_p})$. This minimizes the number of arithmetic operations in steps (1) and (3), as well as for the parallelization. Also, particle removal at the walls and inter-particle collisions are easier to implement. The caveat is the strong numerical noise which requires a large number of computational particles. We now describe the method used in ODISEE to solve the Poisson equation (step 2) and the equations of motion of the superparticles (step 4).

2.2.3 Poisson solver

In a one dimensional, non-periodic system, it is possible to solve the Poisson equation by using finite differences in a uniform spatial grid with M cells of width Δs and centered at $s = s_c$, with $c = 2,...,M-1$. The Laplacian of the electrostatic potential can be written by using a standard second order, central difference scheme, namely

$$\nabla^2\phi(s_c) \approx \frac{\phi_{c+1} - 2\phi_c + \phi_{c-1}}{\Delta s^2} = \sigma_c \tag{2.2.11}$$

where $\sigma_c = -\rho_c/\epsilon_0$ is the source term and ϕ_1 and ϕ_M are imposed at the boundaries (Dirichlet boundary conditions) or related to ϕ_2 and ϕ_{M-1} (Neumann boundary conditions).

The system (2.2.11) is a set of $M-2$ coupled linear equations which can be written as a matrix equation $Ax = b$. Let us first consider the case of Dirichlet boundary conditions. Then we have

$$x = (\phi_2, ..., \phi_{M-1}) \quad ,$$
$$b = (\sigma_2\Delta s^2 - \phi_1, \sigma_3\Delta s^2, ..., \sigma_{M-2}\Delta s^2, \sigma_{M-1}\Delta s^2 - \phi_M) \quad ,$$

and

$$A = \begin{pmatrix} -2 & 1 & 0 & 0 & 0 & 0 & \dots \\ 1 & -2 & 1 & 0 & 0 & 0 & \dots \\ 0 & 1 & -2 & 1 & 0 & 0 & \dots \\ 0 & 0 & 1 & -2 & 1 & 0 & \dots \\ & & & \ddots & \ddots & \ddots & \end{pmatrix} \quad . \tag{2.2.12}$$

As A is tridiagonal, the solution $x = A^{-1}b$ can be computed with an algorithm for which the number of operations scales like $O(M)$ [58]. This algorithm is implemented in ODISEE to solve the matrix system at each time step.

In the case of Neumann boundary conditions, the gradient of ϕ is imposed at the boundaries. This can be expressed as

$$\begin{aligned} \phi_2 - \phi_1 &= \phi_1' \Delta s \quad , \\ \phi_M - \phi_{M-1} &= \phi_M' \Delta s \quad , \end{aligned}$$

thus leading to a different expression for the matrix A and the vector b. These are:

$$b = (\sigma_2 \Delta s^2 + \phi_1' \Delta s, \sigma_3 \Delta s^2, ..., \sigma_{M-2} \Delta s^2, \sigma_{M-1} \Delta s^2 - \phi_M' \Delta s) \tag{2.2.13}$$

and

$$A = \begin{pmatrix} -1 & 1 & 0 & 0 & 0 & 0 & \dots & 0 \\ 1 & -2 & 1 & 0 & 0 & 0 & \dots & 0 \\ 0 & 1 & -2 & 1 & 0 & 0 & \dots & 0 \\ & & \ddots & \ddots & \ddots & & & \vdots \\ & & & \ddots & \ddots & \ddots & & \\ & & & & \ddots & \ddots & \ddots & \\ & & & & & 1 & -2 & 1 \\ & & & & & & 1 & -1 \end{pmatrix} \quad . \tag{2.2.14}$$

The tridiagonal matrix can again be inverted by using the same algorithm. As discussed later, both Dirichlet and Neumann boundary conditions are used in ODISEE, depending on whether the wall is a conductor or an insulator.

Finally, we note that the grid spacing needs to resolve the electron Debye length to avoid the so-called finite grid instability [57], i.e. $\Delta s < \xi \lambda_D$, where ξ is a constant of order 1 whose exact value depends on the choice of the interpolation function.

2.2.4 Particle motion

A simple algorithm to integrate the equations of motion for charged particles in the presence of both electric and magnetic fields is the *Boris algorithm* [57], which is an explicit integrator based on a leapfrog scheme. The time step to advance the particle velocities $\mathbf{v}_p$ from $t - \Delta t/2$ to $t + \Delta t/2$ and the particle positions $\mathbf{x}_p$ from t to $t + \Delta t$ is composed, in the non-relativistic limit, as follows:

(1) the particle is accelerated by the electric field force, from $t - \Delta t/2$ to t,
(2) the particle velocity $\mathbf{v}$ undergoes a rotation due to the magnetic field force,
(3) the particle is accelerated by the electric field force from t to $t + \Delta t/2$,
(4) the particle position $\mathbf{x}$ is updated according to the new velocity.

Explicitly, it reads:

$$
\begin{aligned}
&(1) \quad \mathbf{v}_- = \mathbf{v}_{t-\Delta t/2} + \tfrac{q\Delta t}{2m}\mathbf{E} \quad , \\
&(2) \quad \mathbf{v}_+ = \mathbf{v}_- + \mathbf{v}' \times \mathbf{s} \quad \text{where} \quad \mathbf{v}' = \mathbf{v}_- + \mathbf{v}_- \times \mathbf{t} \quad , \\
&(3) \quad \mathbf{v}_{t+\Delta t/2} = \mathbf{v}_+ + \tfrac{q\Delta t}{2m}\mathbf{E} \quad , \\
&(4) \quad \mathbf{x}_{t+\Delta t} = \mathbf{x}_t + \mathbf{v}_{t+\Delta t/2}\Delta t \quad .
\end{aligned}
$$

Two vectors have been defined for the rotation of the velocity,

$$
\begin{aligned}
\mathbf{s} &= \frac{2\mathbf{t}}{1+\mathbf{t}^2} \quad , \\
\mathbf{t} &= \frac{q\Delta t}{2m}\mathbf{B} \quad .
\end{aligned}
\tag{2.2.15}
$$

Accurate particle trajectories require $\omega_{ce}\Delta t < 1$, where $\omega_{ce} = eB/m_e$ is the electron gyrofrequency, although stability within the Vlasov-Poisson model requires resolving Langmuir wave propagation, $\omega_{pe}\Delta t < 2$, which is typically more constraining. Here $\omega_{pe} = \sqrt{e^2 n_e/\epsilon_0 m_e}$ is the electron plasma frequency.

In the one-dimensional problem (Figure 2.2.1), particle positions only need to be advanced in the s direction. However, each component of the particle velocities must be evolved since these are coupled through the Lorentz force.

2.2.5 Particle collisions

A method to implement binary Coulomb collisions in a particle code was developed by Takizuka and Abe in 1977 based on the Monte Carlo method, and it is described in great detail in [59]. The model is shown to be equivalent to a collision term of the Landau form,

$$
\left.\frac{\partial f_\alpha}{\partial t}\right|_{\text{coll}} = -\sum_\beta \frac{\partial}{\partial v_j}\frac{e_\alpha^2 e_\beta^2 \lambda}{8\pi\epsilon_0^2 m_\alpha}\int \mathbf{dv}' \left[\frac{\delta_{jk}}{u} - \frac{u_j u_k}{u^3}\right]\left[\frac{f_\alpha}{m_\beta}\frac{\partial f_\beta(\mathbf{v}')}{\partial v_k'} - \frac{f_\beta(\mathbf{v}')}{m_\alpha}\frac{\partial f_\alpha}{\partial v_k}\right]
$$

(2.2.16)

which enters on the right hand side of the the kinetic equation, Eq. (2.2.1). Here λ is the Coulomb logarithm [12], $u = ||\mathbf{v} - \mathbf{v}'||$ is the relative velocity between the two colliding particles of species α and β, and the Einstein convention is used for the summation over the velocity components.

The main idea of the algorithm proposed by Takizuka and Abe is that at each time step (i) particles are grouped according to the cell they belong to, (ii) pairs of particles suffering binary collisions are determined randomly within a cell, and (iii) the effect of the collision for each pair of colliding particles is deduced by computing the scattering angle ϑ of their relative velocity. More precisely, the variable $\delta \equiv \tan(\vartheta/2)$ is chosen randomly with a Gaussian distribution of zero mean and a variance given by

$$\langle \delta^2 \rangle = \frac{e_\alpha^2 e_\beta^2 n_L \lambda}{8\pi\epsilon_0^2 m_{\alpha\beta}^2 u^3} \Delta t \tag{2.2.17}$$

where $m_{\alpha\beta} = m_\alpha m_\beta/(m_\alpha + m_\beta)$ is the reduced mass and n_L is the lower density between n_α and n_β. For more details about the algorithm, see Ref. [59].

This algorithm is implemented in ODISEE to model both electron-electron and ion-ion collisions. In our simulations of the plasma-wall transition, we choose a value of collisionality which ensures a thermalized distribution function far from the walls, while the sheath remains essentially collisionless, $\lambda_D \ll \lambda_{mfp}$, where λ_{mfp} is the mean free path for the Coulomb collisions.

2.2.6 Particle sources and sinks

Particles eventually reach one of the two walls. If a wall is a perfect conductor then the particle is absorbed and thus removed from the system. If instead the wall is an insulator, the particle sticks to the wall and contributes to its charge. In this case, the contribution to the surface charge is taken into account before the particle is removed from the system. As a matter of fact, the only practical difference between the two types of walls comes when solving Poisson's equation. In the case of a conducting wall, the electrostatic potential is imposed at the boundary by the wall potential ϕ_w, which is an input parameter. If instead the wall is an insulator, the accumulated charge on its surface imposes the boundary electric field, $E_w = \sigma_w/\epsilon_0$, where σ_w is the wall surface charge density and the electric field E_w is normal to the wall, namely along the s direction. Thus the boundary conditions for the electrostatic potential are either Dirichlet or Neumann depending on whether the wall is respectively a conductor or an insulator.

Particles arriving at the boundaries are lost, thus a source of particles is needed in order for the plasma to be in a quasi-steady state. In ODISEE, ions and electrons are injected in the simulated domain with a chosen distribution in real space $S_\alpha(\mathbf{x})$, and a Maxwellian distribution function in velocity space. This adds a term on the right hand side of the the kinetic equation, Eq. (2.2.1),

$$\left.\frac{\partial f_\alpha}{\partial t}\right|_{\text{source}} = S_\alpha(\mathbf{x}) \left(\frac{m_\alpha}{2\pi T_{\alpha 0}}\right)^{\frac{3}{2}} \exp\left(-\frac{m_\alpha \mathbf{v}^2}{2T_{\alpha 0}}\right) \tag{2.2.18}$$

where $T_{\alpha 0}$ is the input temperature and S_α is the number of physical particles injected per unit time and length.

2.2.7 Normalization

Quantities in the ODISEE are normalized with the natural units of the system by using as a reference the input electron temperature T_{e0} and the magnetic field strenght $||\mathbf{B}|| = B_0$. Namely $s \to s/\rho_{s0}$ and $t \to \omega_{ci} t$, where $\rho_{s0} = c_{s0}/\omega_{ci}$ is the ion sound larmor radius, $c_{s0} = \sqrt{T_{e0}/m_i}$ is the plasma sound speed and $\omega_{ci} = eB_0/m_i$ is the ion gyrofrequency. Velocities are therefore normalized to the sound speed, $v \to v/c_{s0}$. Finally, the electrostatic potential is normalized as $\phi \to e\phi/T_{e0}$. Using these units, the normalized equations of motion for the computational particles only depend on two parameters, namely the magnetic field angle α and the ion to electron mass ratio $\mu = m_i/m_e$.

On the other hand, the Poisson equation in these same units,

$$\frac{\partial^2 \tilde{\phi}}{\partial \tilde{s}^2} = -\gamma_0(\tilde{n}_{li} - \tilde{n}_{le}) \ , \tag{2.2.19}$$

introduces a new parameter $\gamma_0 = (\rho_{s0}/\lambda_{D0})^2$, which is the ratio of the two fundamental scales present in the system. Here $\lambda_{D0} = \sqrt{\epsilon_0 T_{e0}/(e^2 n_{l0}^3)}$ is the reference Debye length computed from the reference electron temperature T_{e0} and a reference linear density n_{l0}. The parameter γ_0 plays an important role in simulations of the magnetized plasma-wall transition, since it measures the scale separation between the Debye sheath and the magnetic presheath.

2.2.8 Parallelization

The ODISEE code is parallelized by using the Message Passing Interface (MPI). The parallelization method used in ODISEE is the so-called *domain decomposition method*, which consists of splitting the spatial domain into smaller subdomains and solving the equations of the system by coordinating the solution between adjacent subdomains. More precisely, the spatial domain is decomposed in N_{proc} subdomains,

each one associated with a separate processor. At each time step, each processor advances the particles that are present in the corresponding subdomain. Then, the processor communicates with its neighbours the positions and velocities of the particles outflowing and inflowing in the subdomain. The solution of Poisson's equation is computed in each processor by gathering the information of the charge density in the full domain.

Typically, the code runs on 64 or 128 processors and a standard simulation takes about a day to reach a steady-state. Figure 2.2.2 shows the results of a performance analysis carried out in the Rosa Cray XE6 supercomputer at the Swiss National Supercomputing Center [60]. A simulation was carried out with a system size $L = 10\rho_{s0}$, a number of grid points $M = 7071$, and a number of computational particles of the order of 10^6. The speed up of the simulation scales almost ideally with the number of processors up to about $N_{proc} = 128$. For $N_{proc} > 128$, communication between processors starts to dominate over computation, and the speed up factor saturates.

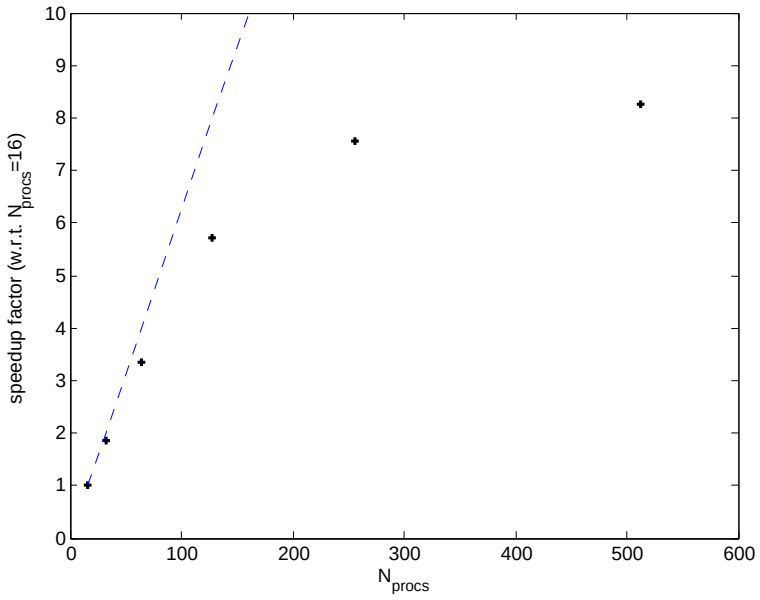

Figure 2.2.2: Speed up factor for the wall-clock time of a simulation for different numbers of processors ($N_{procs} = 16$, 32, 64, 128, 256, 512), with respect to the case $N_{proc} = 16$. The dashed line indicates the ideal situation where the speed up factor is proportional to N_{proc}.

2.2.9 Diagnostics

Usually PIC codes do not save all the particle positions and velocities at each time step because this would yield unreasonably large amounts of data. Instead, specific diagnostics are implemented in order to extract the most important information

about the particles and the fields.

In ODISEE, zero-dimensional diagnostics keep track of the number of ions $N_i(t)$ and electrons $N_e(t)$ in the system, and of the accumulated net charge $Q_w(t)$ at the wall surfaces. One-dimensional diagnostics compute the profiles of the electrostatic potential $\phi(s,t)$, the ion and electron densities, $n_i(s,t)$ and $n_e(s,t)$, or the ion and electron mean velocities in all directions, $\mathbf{V}_i(s,t)$ and $\mathbf{V}_e(s,t)$. Higher order moments of the particle distribution functions are also computed, in particular the pressure tensor $\mathbf{\Pi}_\alpha(s,t)$, defined for a given species as

$$\Pi_{jk}(s,t) = \int f(s,\mathbf{v},t)(v_j - V_j)(v_k - V_k)\ \mathbf{dv}\ . \tag{2.2.20}$$

We note that the ion and electron temperatures in each direction can be extracted from the diagonal terms of the pressure tensor, i.e. $T_j = \Pi_{jj}$, as a measure of the average disordered kinetic energy. The highest order moment computed in ODISEE is the microscopic heat flux $\mathbf{q}_\alpha(s,t)$, defined for a given species as

$$q_j = \int f(s,\mathbf{v},t)(v_j - V_j)(\mathbf{v} - \mathbf{V})^2\ \mathbf{dv}\ . \tag{2.2.21}$$

Finally, it is possible to reconstruct the ion and electron velocity distribution functions $f_\alpha(s_0,\mathbf{v},t)$ at a given position s_0. The diagnostic essentially saves the velocities of all particles present in the grid cell containing s_0.

2.3 Unmagnetized plasma sheaths

In this section, we present the results of our investigations of the plasma-wall transition in the case of zero magnetic field. First, an example of a simulation showing the formation of a sheath and the acceleration of ions to the sound speed is shown. Then, the possibility of subsonic ion sheaths is explored by considering the presence of electrical currents in the plasma. An analytical theory is developed to predict the ion velocity at the entrance of the non-neutral sheath, and numerical simulations are performed to verify the predictions. Finally, the effect of wall biasing on the plasma potential is explored both analytically and numerically, shedding some light on the properties of both ion and electron sheaths. We remark that the results presented in this section are also valid in the case of a magnetic field perpendicular to the walls.

We start by considering the simplest case of an unmagnetized plasma with cold ions, namely $B_0 = 0$ and $\tau = T_{i0}/T_{e0} \ll 1$. The system size is $L \simeq 140\lambda_{D0}$ and the mass ratio is $\mu = 100$. Electrons undergo Coulomb collisions with a mean free path λ_{mfp} such that $\lambda_{D0} \ll \lambda_{mfp} \lesssim L$. The walls are conductors with a potential $\phi_w = 0$. The initial condition is simply empty space and a uniform, neutral plasma source,

$S_i = S_e = S_0$, continuously injects particles in the system. Figure 2.3.1 shows the time evolution of the number of ions $N_i(t)$ and electrons $N_e(t)$ in the system. Since there is no magnetic field, the characteristic permanence time of a particle in the system is L/c_{s0}. After a few characteristic times, which corresponds to about 5×10^5 time steps, the number of particles in the system reaches a steady value of the order of 10^7 particles. The relative charge imbalance in the system, $(N_i - N_e)/N_i$ is also shown in Fig. 2.3.1. It reaches a positive steady value of about 0.1%. This finite value accounts for the non-neutral sheaths forming at both walls.

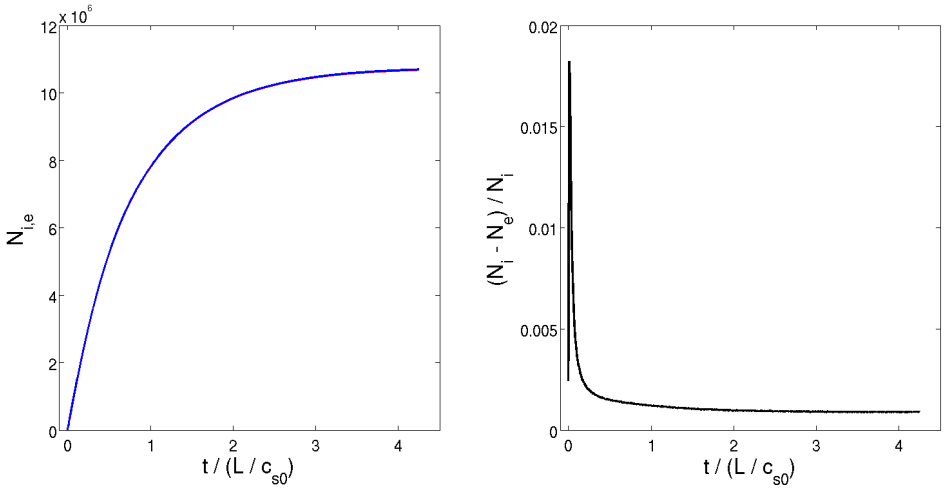

Figure 2.3.1: Left: number of computational particles in the system as a function of time, for ions (blue) and electrons (red). Right: relative charge imbalance in the system as a function of time.

Figure 2.3.2 shows the time-averaged spatial profiles of the ion and electron densities, the electrostatic potential, the electron temperature in the s direction, the ion and electron mean velocities in the s direction, and the ion and electron mean fluxes in the s direction. These are computed in the quasi-steady state reached by the system. As expected, the profiles are completely symmetric with respect to the center of the system $s = L/2$. Also, an electrostatic potential barrier for the electrons is formed and quasi-neutrality is satisfied almost up to the wall, where a thin, non-neutral sheath with $n_i > n_e$ is observed. As they approach the walls, both ions and electrons are (on average) accelerated. Since the plasma source is neutral, the ion and electron fluxes in the s direction are equal, $\Gamma_{i,s}(s) = \Gamma_{e,s}(s)$, and their divergence is a constant given by the source, $\partial_s \Gamma_s = S_0$, as expected from the steady state continuity equation.

We note that the electron temperature along the s direction, $T_{e,s}$, is smaller than the input electron temperature T_{e0} (Figure 2.3.2). This is because the electrons leaving the system are those with large enough energy to overcome the potential barrier, and therefore the plasma cools down as it loses the high energy particles

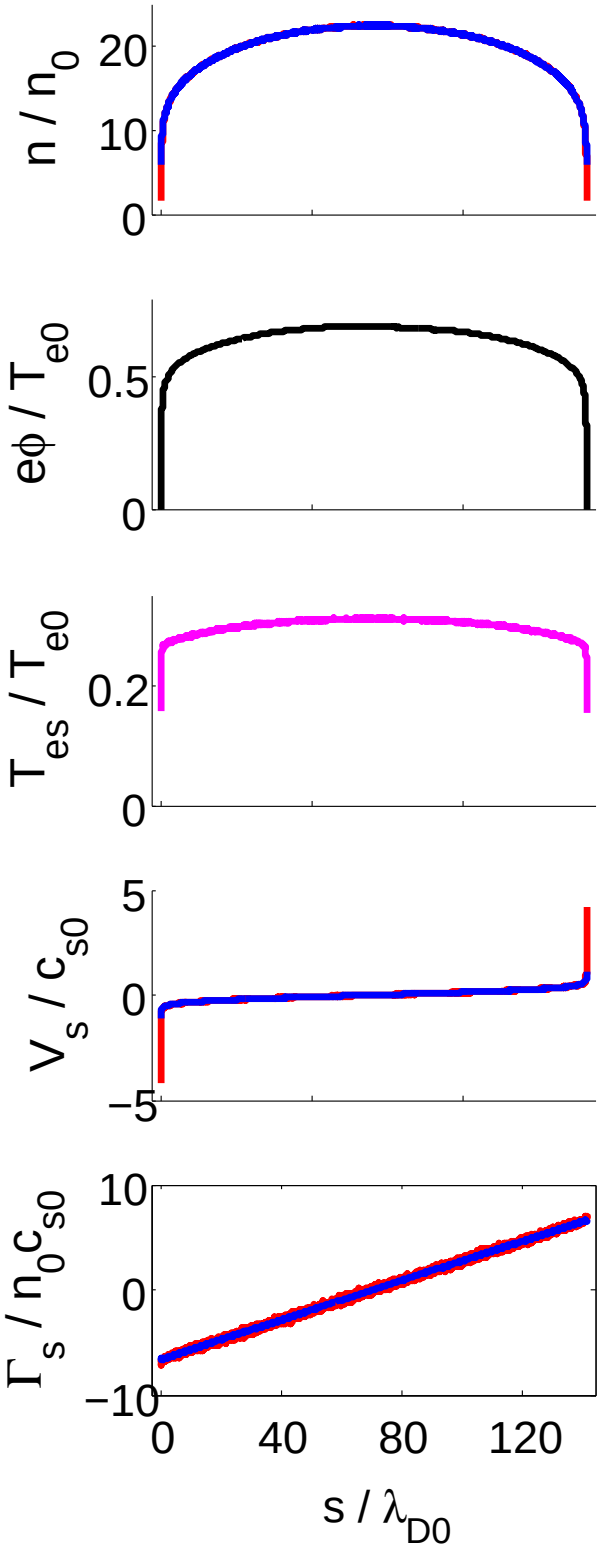

Figure 2.3.2: Time-averaged profiles of ion (blue) and electron (red) densities, electrostatic potential (black), electron temperature (magenta), ion (blue) and electron (red) mean velocities, and ion (blue) and electron (red) mean fluxes.

injected by the source. We can nevertheless conclude that the electron temperature is reasonably constant in the system, except inside the sheaths where it drops substantially. We remark that, as the electron velocity distribution function is not in thermal equilibrium inside the sheaths, temperature here is meant as the measure of the average disordered kinetic energy of the particles.

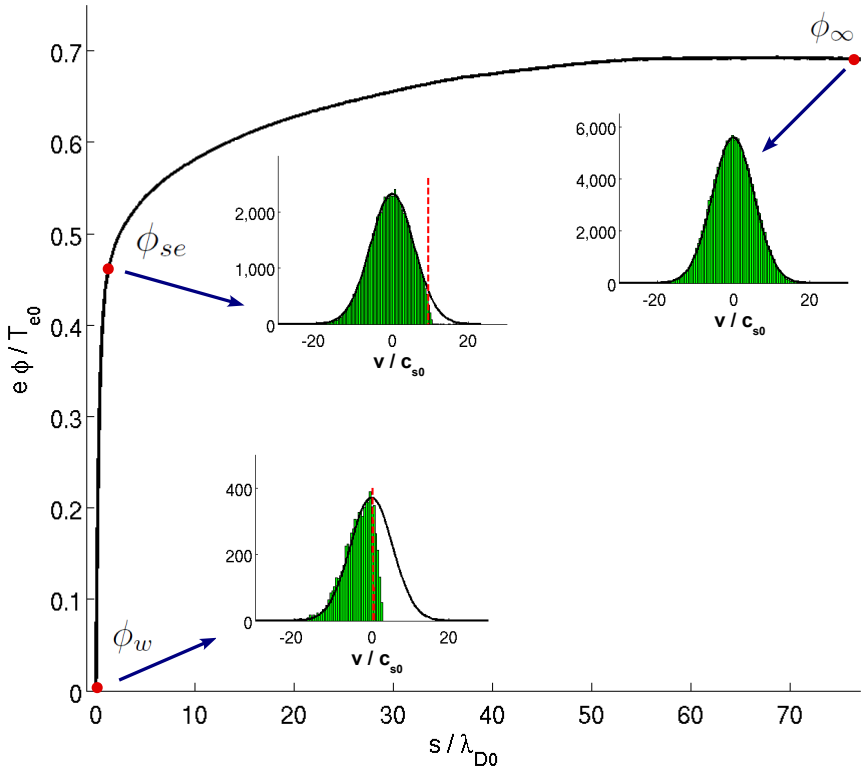

Figure 2.3.3: Time-averaged profile of the electrostatic potential as the left wall is approached. The electron velocity distribution function $f_e(s, v)$ is shown (green) at three different locations, namely in the bulk plasma ($\phi = \phi_\infty$), at the sheath entrance ($\phi = \phi_{se}$) and at the wall ($\phi = \phi_w$). The vertical dashed-red line indicates the value of v_{cut} and the black curve is a Maxwellian with temperature $T_{e\infty}$.

Figure 2.3.3 shows the time-averaged electron distribution function at different locations as the left wall is approached. The distribution function in the bulk can be well described by a Maxwellian with temperature equal to the bulk plasma temperature $T_{e\infty} = T_{e,s}(s = L/2)$. As the wall is approached, the distribution function is depleted on one side and can be described by a Maxwellian with temperature $T_{e\infty}$ truncated at a cut-off velocity given by $v_{cut}(s) = \sqrt{2e\phi(s)/m_e}$. At the wall, $v_{cut} = 0$ and the distribution function is a half-Maxwellian.

In order to interpret the physics at the plasma sheath we renormalize the plasma properties using $T_{e\infty}$ as a reference temperature. In particular, the reference sound

speed is $c_s = \sqrt{T_{e\infty}/m_i}$. Similarly, we shall express the sheath width in units of $\lambda_D = \sqrt{\epsilon_0 T_{e\infty}/e^2 n_\infty}$, where n_∞ is the bulk plasma density. In fact, the plasma density is larger than the reference density n_0, thus the actual Debye length is smaller than the reference Debye length λ_{D0}. Figure 2.3.4 shows the normalized profiles of ion and electron densities, electrostatic potential and ion velocity in the vicinity of the left wall. The location where ions reach the sound speed, $V_{i,s} = c_s$, is consistent with the breaking of quasi-neutrality. Therefore the Bohm criterion well describes the entrance of the sheath, whose thickness is of the order of $10\lambda_D$. Also, the electrostatic potential at the sheath edge is $e\phi \approx 1.4 T_{e\infty}$, which is in perfect agreement with the ambipolar condition $e\phi \approx \Lambda T_e$. In fact, $\Lambda = \log\left(\sqrt{\mu/(2\pi)}\right) \approx 1.4$ for a mass ratio $\mu = 100$.

2.3.1 Existence of subsonic plasma sheaths

The possibility of the existence of sheaths with subsonic ions at the edge was widely addressed in the literature, by exploring if the presheath processes (collisions, ionization) or the geometry could influence the transition to the non-neutral region [61,62,63]. It was concluded that the Bohm criterion, $V_i = c_s$, is a ubiquitous property of ion sheaths in the limit $T_i \ll T_e$ and $\lambda_D \ll L_{ps}$, where L_{ps} is the scale length of the presheath [38].

In this section we analytically derive the location of the sheath edge where quasi-neutrality is broken, by using an appropriate kinetic description of the plasma. We show that an ion sheath can exist with arbitrarily small ion velocity and that this may be relevant in many situations. The standard Bohm criterion, $V_i = \sqrt{T_{e\infty}/m_i}$, is recovered in the case of large enough ion current through the wall ($\Gamma_i \gg \Gamma_e$) and it is found to be a reasonable approximation in floating potential conditions ($\Gamma_i = \Gamma_e$). However, in the case of predominant electron current through the wall ($\Gamma_e > \Gamma_i$), the standard Bohm criterion is not able to describe the sheath edge transition. We assume a one-dimensional plasma with a very small ion to electron temperature ratio, $T_i \ll T_e$, weakly collisional electrons with a mean free path larger than the sheath scale, $\lambda_{mfp} \gg \lambda_D$, and a totally absorbing wall. The results are supported by numerical simulations performed with the ODISEE code.

We start by writing the first two moments of Vlasov equation for ions and the first moment for electrons, i.e. continuity and momentum equations, which in steady state conditions are:

$$\begin{aligned} n_i \frac{\partial V_i}{\partial s} + V_i \frac{\partial n_i}{\partial s} &= S_{pi} \\ n_e \frac{\partial V_e}{\partial s} + V_e \frac{\partial n_e}{\partial s} &= S_{pe} \\ m_i n_i V_i \frac{\partial V_i}{\partial s} &= -e n_i \frac{\partial \phi}{\partial s} + S_{mi} \end{aligned} \tag{2.3.1}$$

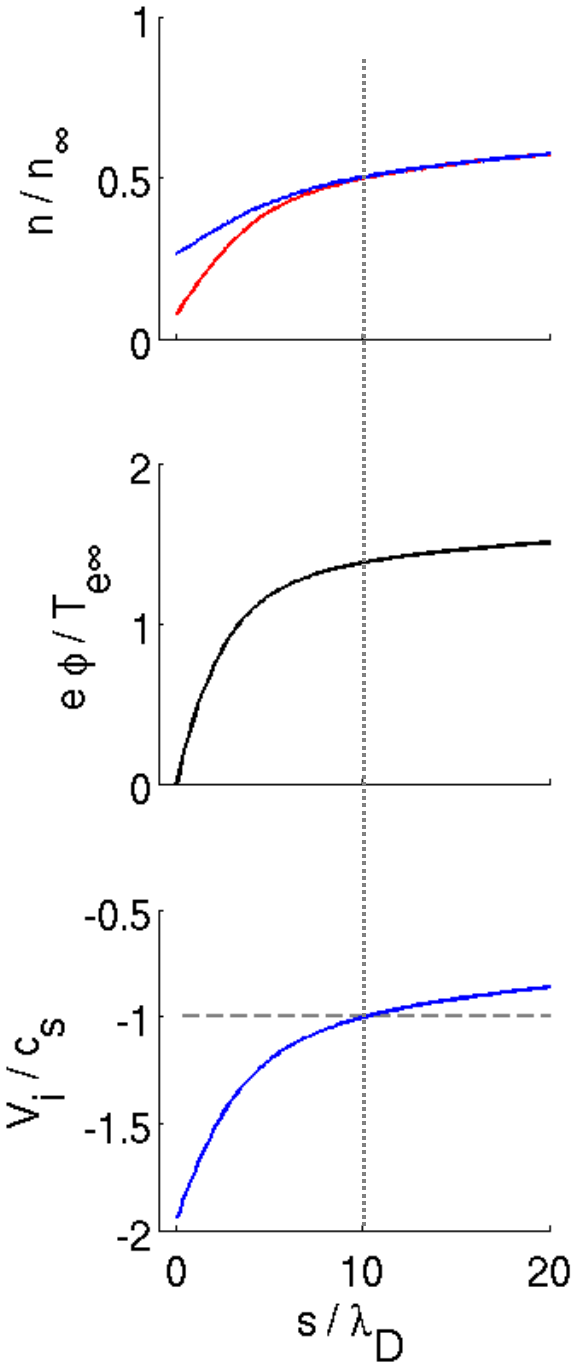

Figure 2.3.4: Profiles of n_i (blue), n_e (red), ϕ, and V_{is} in the vicinity of the left wall. The vertical dashed line indicates the position where $V_{i,s} = c_s$.

The particle and momentum sources, S_p and S_m, result from integrating the terms in Vlasov equation related to the injection of particles, ionization processes or collisions. The ion pressure is neglected since $T_i \ll T_e$. In the following, the potential is defined so that at the wall $\phi_w = 0$, implying that $\phi(s)$ represents the potential drop up to the wall. We now express V_e by using our knowledge of the electron

distribution function. In fact, in the case of a monotonic ion sheath, the electron velocity distribution function approaching a wall can be described by a truncated Maxwellian [35, 64], as confirmed experimentally [65, 66] and by our simulations. The cutoff velocity is due to the fact that all the electrons having an energy above the potential barrier flow out from the system and no electrons can be reflected with $v > \sqrt{2e\phi(s)/m_e} = v_{cut}(s)$. By defining the quantity $\eta(s) = e\phi(s)/T_{e\infty}$, we have

$$f_e(v,\eta) = \begin{cases} \frac{1}{I(\eta)\sqrt{2\pi v_{the}^2}} \exp\left(-\frac{v^2}{2v_{the}^2}\right) & \text{if } v < v_{cut}(\eta) \\ 0 & \text{otherwise} \end{cases} \tag{2.3.2}$$

where $v_{the} = \sqrt{T_{e\infty}/m_e}$, $v_{cut}(\eta) = \sqrt{2\eta}v_{the}$ is the cutoff velocity, and

$$I(\eta) = \left[1 + \mathrm{erf}(\sqrt{\eta})\right]/2 \tag{2.3.3}$$

is the normalization factor. We can now compute the electron fluid velocity $V_e = \langle v \rangle$, having defined $\langle a \rangle = \int f_e(v)a(v)dv$. V_e increases as the Maxwellian is progressively truncated when approaching the wall,

$$V_e = \frac{c_s}{I(\eta)} e^{\Lambda - \eta} \quad . \tag{2.3.4}$$

Equation (2.3.4) is the common expression used as a sheath boundary condition except for the correction given by $I(\eta)$. We also note that the term $\partial_s V_e$ in system (2.3.1) can be evaluated as $\partial_s V_e = \partial_\phi V_e \partial_s \phi$, where

$$\partial_\phi V_e = -\frac{eV_e}{T_{e\infty}} \left[1 + \frac{e^{-\eta}}{2\sqrt{\pi\eta} I(\eta)}\right] \quad . \tag{2.3.5}$$

Thus far the system (2.3.1) together with Eq. (2.3.4) is very general and should be satisfied within both the sheath and the presheath regions, as long as the collisionality is small enough for the closure to be valid. In the presheath, quasi-neutrality is preserved and the condition $n_e = n_i = n$ has to be fulfilled up to the sheath entrance. By imposing it, we are left with three unknowns (n, V_i, ϕ) and their respective gradients, and our system of equations can be reduced to a matrix system $\mathbf{M}\vec{X} = \vec{S}$, where

$$\vec{X} = \begin{pmatrix} \partial_s n \\ \partial_s V_i \\ \partial_s \phi \end{pmatrix}, \qquad \vec{S} = \begin{pmatrix} S_{pi} \\ S_{pe} \\ S_{mi} \end{pmatrix}, \tag{2.3.6}$$

and the matrix $\mathbf{M}$ depends only on local quantities,

$$\mathbf{M} = \begin{pmatrix} V_i & n & 0 \\ V_e & 0 & n\partial_\phi V_e \\ 0 & m_i n V_i & en \end{pmatrix}. \tag{2.3.7}$$

This reduced system is valid in the presheath up to the sheath edge. In the presheath region, gradients are typically small and are due to the presence of the plasma source. At the sheath edge, gradients become much steeper, i.e. $|M_{jk}X_k| \gg |S_j|$ for all j,k such that $M_{jk} \neq 0$. In other words, at the sheath edge the source terms are much smaller than any other term in the fluid equations, and the fluid system (2.3.1) reduces to $\mathbf{M}\overrightarrow{X} \simeq 0$. Now, the presence of non-zero gradients imposes $\det(\mathbf{M}) = 0$, which defines the position of the sheath edge. We note that $\det(\mathbf{M}) = 0$ is also a valid definition of the sheath edge in the particular case of a source-free system. In fact, in this case $\mathbf{M}\overrightarrow{X} = 0$ is satisfied everywhere in the presheath and the macroscopic quantities display flat profiles [50], therefore $\overrightarrow{X} = 0$. At the sheath edge, gradients become non zero, still requiring $\det(\mathbf{M}) = 0$. Hence in all cases $\det(\mathbf{M}) = 0$ at the sheath entrance, which gives

$$V_{i,se} = c_{sb}\sqrt{\frac{1}{1+\kappa}} \tag{2.3.8}$$

where

$$\kappa = \frac{e^{-\eta_{se}}}{2\sqrt{\pi\eta_{se}}I(\eta_{se})} \ . \tag{2.3.9}$$

Figure 2.3.5 shows the dependence of $V_{i,se}$ and $V_{e,se}$ on the sheath edge potential η_{se}. The condition of ambipolar flow $\Gamma_i = \Gamma_e$ can be found by solving $V_{i,se} = V_{e,se}$, expressed by Eqs. (2.3.4) and (2.3.8). This defines the floating potential, which is found to be at $\eta_{se} \approx \Lambda$ for the hydrogen mass ratio ($\mu = 1836$, $\Lambda \simeq 2.8$) or higher. In correspondence of the floating potential, we have $V_{i,se} \approx c_{sb}$.
In the limit of $\eta_{se} \to \infty$, or equivalently $\Gamma_i \gg \Gamma_e$, one has that $\kappa \to 0$, thus reducing Eq. (2.3.8) to the standard Bohm criterion. However, for $\eta_{se} \to 0$, or equivalently $\Gamma_e \gg \Gamma_i$, the function $\kappa \to \infty$ and the ion velocity $V_{i,se} \to 0$. From this we conclude that the standard Bohm criterion is not valid for non-ambipolar conditions, since it is violated when $\eta_{se} < \Lambda$ (or $\Gamma_e > \Gamma_i$).

In order to confirm the validity of the presented results, we perform numerical simulations with the ODISEE code. The system size is much larger than the sheath scale ($L \simeq 10^3\lambda_D$). A source of ions and electrons uniformly distributed between two absorbing walls maintains the plasma in steady state. Ions have a temperature much smaller than the electrons ($T_i/T_e \simeq 10^{-2}$), electrons undergo Coulomb collisions with each other with a mean free path much larger than the sheath scale ($\lambda_{mfp} \simeq 300\lambda_D$), and Poisson's equation is solved by imposing a fixed potential at the two boundaries, $\phi_w = 0$. The mass ratio is $\mu = 400$ (essentially the same results are obtained in tests performed with $\mu = 800$). Sheath currents can be driven by injecting an unbalanced amount of ions and electrons throughout the domain, in such a way that the sheath potential is varied and sheath edge quantities are studied as a function of η_{se}.

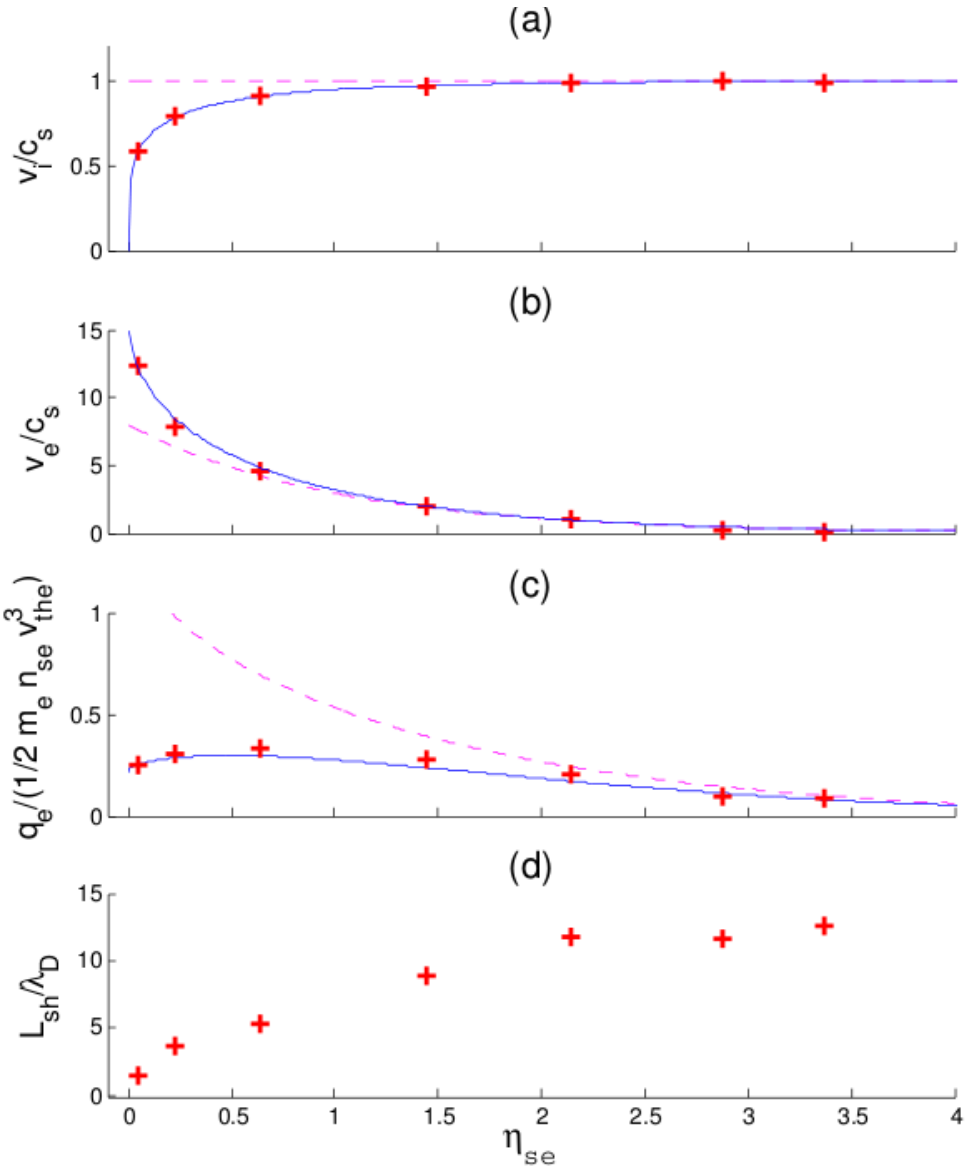

Figure 2.3.5: Sheath edge quantities as a function of the normalized sheath edge potential η_{se}. (a-c) Analytical expressions (solid blue lines) for V_i, V_e, and q_e [Eqs. (2.3.4), (2.3.8), and (2.3.10)], are compared with the simulations results (red crosses). The sheath edge position is found according to Eq. (2.3.8). The expressions deduced from textbook formulas are also shown (dashed magenta lines), i.e. $V_i = c_s$, $V_e = c_s \exp(\Lambda - \eta)$, and $q_e = Q_e - \delta$, where $Q_e = \gamma \Gamma_e T_{e\infty}$ is the macroscopic heat flux [16], $\gamma = \eta_{se} + \Delta\phi_{ps}/T_{e\infty}$, and $\delta = (m_e n_{se}/2)\left[\langle v\rangle^3 + 3\langle v\rangle\langle(v - \langle v\rangle)^2\rangle\right]$ is evaluated according to Eq. (2.3.2). (d) The sheath length L_{sh} is obtained from the simulations and normalized to the local Debye length $\lambda_D = \sqrt{\epsilon_0 T_{e\infty}/(e^2 n_{se})}$. The only expression that depends on the mass ratio is V_e/c_s, plotted here for $\mu = 400$.

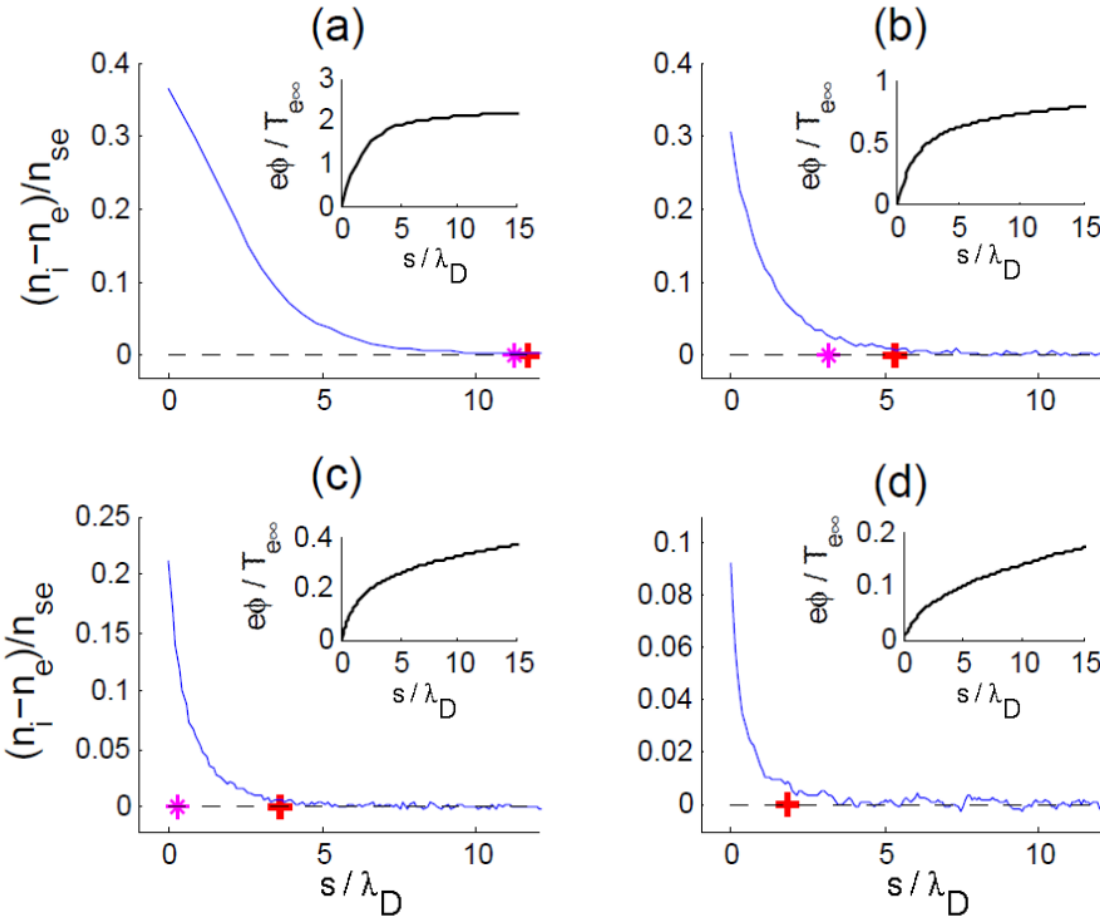

Figure 2.3.6: Steady-state charge imbalance in the vicinity of the wall (inset: potential profiles). Results from the simulations are shown for four different cases, with increasing electron current: (a) $\eta_{se} \approx 2.1$ (floating potential for $\mu = 400$), (b) $\eta_{se} \approx 0.63$, (c) $\eta_{se} \approx 0.22$, (d) $\eta_{se} \approx 0.05$. The location of the sheath edge according to Bohm criterion (magenta stars) and according to Eq. (2.3.8) (red crosses) are displayed. In (d) the ion velocity never reaches c_s so according to the standard Bohm criterion there is no sheath.

Simulations confirm that the sheath edge position is well described by Eq. (2.3.8). Figure 2.3.6 shows, in fact, that the position of the sheath entrance defined by (2.3.8) is always coherent with the breaking of quasi-neutrality, while the standard Bohm criterion fails to describe the transition for small values of η_{se}. In particular, for $\eta_{se} \lesssim 0.25$, we observe that $V_i < c_s$ everywhere, even at the wall, and yet a significant charge imbalance with a smooth potential drop is observed, pointing out the existence of a sheath. The numerical results for V_i, V_e, and the microscopic heat flux, $q_e = n_e m_e \langle (v - V_e)^3 \rangle / 2$, at the sheath edge are shown in Fig. 2.3.5 for different values of η_{se}, and compared with the analytical predictions provided by Eqs. (2.3.4), (2.3.8), and

$$q_e = \frac{n_{se} m_e v_{the}^3}{\sqrt{2\pi} I(\eta)} \left[e^{-\eta} \left(\eta - \frac{1}{2} \right) + \frac{3}{2} \sqrt{\frac{\eta}{\pi}} \frac{e^{-2\eta}}{I(\eta)} + \frac{e^{-3\eta}}{2\pi I^2(\eta)} \right] . \tag{2.3.10}$$

The results for V_e and q_e are in addition compared with the corresponding analytical expressions deduced from textbook formulas [16], showing disagreement for $\eta_{se} < \Lambda$. The sheath length, L_{sh}, is also shown in Fig. 2.3.5 as a function of η_{se}. The sheath is expanded in the region where $\Gamma_i > \Gamma_e$, consistent with the Child-Langmuir model [35], whereas it is compressed when $\Gamma_e > \Gamma_i$, with $L_{sh} \to 0$ when $\eta_{se} \to 0$.

How can a smooth sheath exist with subsonic ion velocity at the sheath edge and yet $\partial_s^2 \phi < 0$, which is impossible according to Eq. (2.1.4)? The fact is that Eq. (2.1.4) assumes that n_e decreases according to the Boltzmann factor, which accounts for the fraction of the electron population that is reflected before reaching the wall. However, the absorbing boundary reduces even more the electron density since it gives rise to a truncated distribution function. The more general formula is [35]

$$n_e = n_{se} \exp \left[\frac{e(\phi - \phi_{se})}{T_b} \right] \frac{I(\eta)}{I(\eta_{se})} \tag{2.3.11}$$

which reduces to the Boltzmann relation in the limit of large η_{se}. For small values of η_{se}, this correction is important and the linearized Poisson equation with the expression for n_e given by Eq. (2.3.11) is

$$\frac{\partial^2 \phi}{\partial s^2} \approx e^2 n_{se} \left[\frac{1}{T_b} (1 + \kappa) - \frac{1}{2e\Delta\phi_{ps}} \right] (\phi - \phi_{se}) \ . \tag{2.3.12}$$

If we impose $\partial_s^2 \phi \leq 0$ we find $V_{i,se} \geq c_{sb} \sqrt{1/(1+\kappa)}$, an inequality that is compatible with Eq. (2.3.8), showing that it is therefore possible to find smooth sheath solutions with arbitrarily small ion velocity at the sheath entrance. Since the function $\kappa \to \infty$ as $\eta_{se} \to 0$, the scaling analysis of Eq. (2.3.12) shows that $L_{sh} \to 0$ in this limit, as confirmed by Fig. 2.3.5.

We would like to remark that while the ion flow at the sheath entrance can be arbitrarily small, as shown in Eq. (2.3.8), the generalized form of the Bohm criterion

remains valid [38], in the sense that ions always enter the sheath at the local speed of sound. As a matter of fact, the local value of the plasma sound speed at the entrance of the sheath, computed by solving the dispersion relation of ion acoustic waves, is exactly given by Eq. (2.3.8). A derivation of this is given in Appendix A.

An experimental verification of these predictions could be carried out by measuring the ion velocity in the vicinity of an ion sheath that has been biased so that the plasma potential is only slightly above the wall potential. Such sheaths have been recently produced and characterized, showing monotonic potential profiles [67].
The deviations from textbook formulas that we derived in this section are relevant in a number of physical situations. As an example, we cite the Edge Localized Modes in tokamak fusion devices, where large plasma currents to the divertor plates can be observed [68, 69]. In the case of a transient event where $\Gamma_e \gg \Gamma_i$, corresponding to small values of η_{se}, according to Eq. (2.3.8) the ion flow is strongly reduced with respect to the standard Bohm prediction. This is important because ions determine the plasma momentum flux, even in the case of predominant electron current. We also mention the plasma thrusters used for spacecraft propulsion, where large electron currents are locally observed in the conducting walls [70]. As a last example, we allude to the subsonic origin of the solar wind plasma, which has been recently explained through a *gravito-electrostatic sheath* created at the surface boundary of the Sun. This boundary acts as a negatively biased wall and thus also draws electron current [71]. In general, our results are important for setting the boundary conditions at the sheath edge in plasma fluid models.

We conclude that in floating conditions where $\eta_{se} \approx \Lambda$, or in the case of predominant ion current ($\Gamma_i > \Gamma_e$), the usual Bohm criterion together with the commonly used expression for the electron velocity are a reasonable approximation. However, when the plasma sheath potential is small ($\Gamma_e > \Gamma_i$), the standard Bohm condition is not consistent anymore with the breaking of quasi-neutrality. The electron kinetic effects have a strong impact on the ion velocity and the sheath edge definition needs to be refined according to Eq. (2.3.8). This new definition of the sheath edge is coherent with the breaking of neutrality and other sheath edge quantities, and is valid for all $\eta_{se} > 0$. It also applies if there is a magnetic field perpendicular to the wall. Its validity breaks down if the electron mean free path becomes very small, $\lambda_{mfp} \sim \lambda_D$, if the source terms become large enough to strongly affect the properties of the sheath, and for $\eta_{se} < 0$, since in this case Eq. (2.3.2) is not valid anymore. Finally, Eq. (2.3.8) can also be derived by considering the general dispersion relation of ion-acoustic waves in the limit $\omega/k = 0$ [39] with the distribution function given by Eq. (2.3.2).

In this respect, however, we notice that the method described here provides a new rigorous way of deriving the sheath edge location, leading to the sheath criterion directly in its equality form, thus avoiding the problem of matching the presheath

and sheath regions. Moreover, as such technique makes possible to determine how gradients are related to each other at the sheath edge, it provides a rigorous tool to determine the boundary conditions in the more complicated case of magnetized sheaths.

2.3.2 Potential of a plasma bound between two biased walls

Before turning to the study of the magnetized plasma sheath, let us take a detour, and look at the potential of a plasma bound between two walls. This will allow us to get more acquainted with the physics of the sheath, applying the technique we have developed in Sec. 2.3.1, and shed light into a crucial problem in plasma physics.

The existence of the sheath ensures that quasi-neutrality is maintained in the plasma bulk by a strong electric field, typically leading to no net current to the walls. A more complicated situation is present when a region of the wall in contact with the plasma is electrically biased with respect to the rest of the wall. Time-independent biasing is used in plasma experiments for different purposes, namely for the measure of the ion and electron temperatures with electrostatic probes [35, 72], in plasma thrusters for space propulsion [6], to study the effect of shear flow on turbulence [73, 74, 75, 20], for the study of dust particles [76], and for the control of turbulence in magnetic fusion devices [77, 78, 79]. A bias may induce local perturbations of the plasma potential. Electric fields are then produced and can give rise to plasma currents which may close at the sheath. A commonly-shared feature in biasing experiments is that the plasma potential sets its value in between two surface potentials (see, e.g., Ref. [72]). While in some relatively simple cases the underlying physical mechanism has been understood [67], the exact general relation between the currents measured at the sheaths, the applied bias and the resulting potential in the plasma bulk is not well established, and remains to date a challenging general problem of plasma physics [80].

In this section we address this problem in a relatively simple framework, focusing on a one-dimensional, steady-state, plasma bound between two perfectly absorbing walls that are biased with respect to each other. In particular, we derive an analytical expression relating the bulk plasma potential with the wall currents, showing that the plasma potential undergoes an abrupt transition when currents cross a critical value. This result is confirmed by numerical simulations performed with the ODISEE code. Finally, we suggest an experimental setup that could provide a measure of this transition and we show an example of experimental results obtained in the TORPEX device.

The electrostatic potential established in the plasma bulk depends on the interplay between sheaths driving different currents to the walls. Typically, sheaths are positive space-charge layers forming a potential barrier, $\eta_{se} = e(\phi_{se} - \phi_w)/T_e > 0$, that

prevents most of electrons from flowing out. An enormous research effort on these sheaths, called *ion sheaths*, has been carried out in the past decades (see Ref. [38] for a review), and it is the case that we have considered in Sec. 2.3.1. Standard sheath theory shows that the sheath current I is such that $I_{sat}^{el} < I < I_{sat}^{ion}$ for $\eta_{se} > 0$, where $I_{sat}^{ion} = en_{se}c_s > 0$ is the ion saturation current and $I_{sat}^{el} = -en_{se}\sqrt{2/\pi}v_{the} < 0$ is the electron saturation current. When a strong positive bias is locally applied with a probe or at the wall confining the plasma, the formation of negative space-charge sheaths or *electron sheaths* is observed [72,67,79]. In the case of the electron sheath, a potential barrier $\eta_{se} < 0$ accelerates electrons and prevents most of ions from arriving at the wall (Figure 2.3.7). As a matter of fact, biasing experiments often show that the plasma is bound between an ion and an electron sheath. This is the plasma scenario that we consider in this section, which starts with the analysis of the ion and electron sheaths, shedding new light on their properties. These results are then used to describe the interplay between the two sheaths and their effect on the bulk plasma potential.

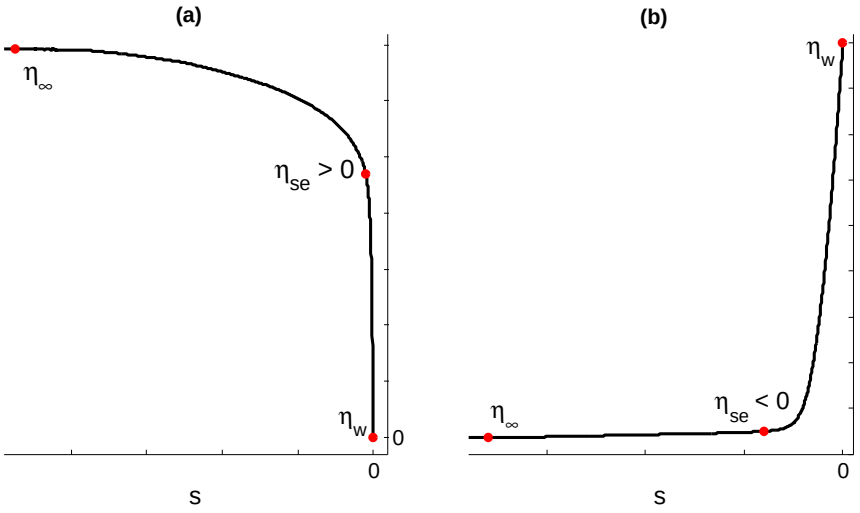

Figure 2.3.7: Example of potential drop η as a function of the distance to the wall for an ion sheath (left) and an electron sheath (right). Indicated are the electrostatic potential far from the wall (η_∞), at the sheath edge (η_{se}), and at the wall ($\eta_w = 0$). Plots are obtained from ODISEE simulations.

2.3.2.1 Ion and electron sheaths

The goal of the present section is to find the ion and electron velocities at the sheath entrance in the case of perfectly absorbing walls. We consider separately the ion and the electron sheaths, i.e. $\eta_{se} > 0$ and $\eta_{se} < 0$, respectively.

Let us first consider a plasma in contact with an absorbing wall in the case of an ion sheath where $\eta_{se} > 0$ (Fig. 2.3.7a). In this situation, the ion and electron velocities at the sheath edge were derived in Sec. 2.3.1. We now extend the results to the case of finite ion temperature. As we have seen in Sec. 2.3.1, in the presence of a monotonic ion sheath, the electron fluid velocity in the direction normal to the wall is given by

$$V_e = \frac{v_{the}}{\sqrt{2\pi} I(\eta)} e^{-\eta} = \frac{c_s}{I(\eta)} e^{\Lambda - \eta} \ . \tag{2.3.13}$$

Here $\eta(s) = e(\phi(s) - \phi_w)/T_{e\infty}$ is the normalized potential relative to the wall such that $\eta(0) = 0$ (here we allow $\phi_w \neq 0$). Notice that the spatial dependence of V_e is contained in the potential η. We consider the steady state continuity equations for ions and electrons and the momentum equation for ions, Eq. (2.3.1), which for $T_i \neq 0$ becomes

$$\begin{aligned} n_i \frac{\partial V_i}{\partial s} + V_i \frac{\partial n_i}{\partial s} &= S_{pi} \\ n_e \frac{\partial V_e}{\partial s} + V_e \frac{\partial n_e}{\partial s} &= S_{pe} \\ m_i n_i V_i \frac{\partial V_i}{\partial s} &= -e n_i \frac{\partial \phi}{\partial s} - \frac{\partial (n_i T_i)}{\partial s} + S_{mi} \ . \end{aligned} \tag{2.3.14}$$

As in Sec. 2.3.1, system (2.3.14) can be reduced to a matrix equation. The term related to the ion pressure, $\partial_s(nT_i)$, can be simplified by assuming that the ion fluid expands (accelerates) adiabatically, namely without heat exchange (this is only valid in the vicinity of the sheath, where flows are strong). This leads to $d(n_i^{1-\gamma} T_i)/dt = 0$ and thus $\partial_s(n_i T_i) = \gamma T_i \partial_s n_i$, where the coefficient γ is given by the kinetic theory of gases as $\gamma = (\nu + 2)/\nu$, ν being the number of degrees of freedom of the particles (for one-dimensional flow $\gamma = 3$). Finally, we note that in the presheath and up to the sheath entrance, quasi-neutrality is preserved and the condition $n_e = n_i = n$ has to be fulfilled. Therefore, our system of equations can be reduced to a matrix equation $\mathbf{M}\overrightarrow{X} = \overrightarrow{S}$, where

$$\overrightarrow{X} = \begin{pmatrix} \partial_s n \\ \partial_s V_i \\ \partial_s \phi \end{pmatrix}, \qquad \overrightarrow{S} = \begin{pmatrix} S_{pi} \\ S_{pe} \\ S_{mi} \end{pmatrix}, \tag{2.3.15}$$

and

$$\mathbf{M} = \begin{pmatrix} V_i & n & 0 \\ V_e & 0 & n\partial_\phi V_e \\ \gamma T_i & m_i n V_i & en \end{pmatrix}. \tag{2.3.16}$$

As shown in Sec. 2.3.1, the location of the sheath entrance is given by the condition $\det(\mathbf{M}) = 0$, which gives

$$V_{i,se} = c_s \sqrt{\frac{1}{1+\kappa(\eta_{se})} + f_i} \ , \tag{2.3.17}$$

where the function κ, defined in Eq. (2.3.9), represents the kinetic effect of the depleted Maxwellian electron distribution function [52]. This effect becomes important when $\eta_{se} \to 0$, while it vanishes for $\eta_{se} \to \infty$. Also, we define

$$f_\alpha = \gamma \frac{T_{\alpha,se}}{T_{e\infty}} \ , \tag{2.3.18}$$

which represents the effect of a finite-temperature fluid of species α expanding adiabatically. We note that f_i is related to the presheath density drop. In the case of adiabatic flow, in fact, $T_{i,se}/T_{i\infty} = \tilde{n}_{se}^{\gamma-1}$, where $\tilde{n}_{se} = n_{se}/n_\infty$ is the sheath edge density normalized to the bulk plasma density n_∞. Therefore, $f_i = \gamma\tau\tilde{n}_{se}^{\gamma-1}$ where $\tau = T_{i\infty}/T_{e\infty}$. As a consequence, $f_i \to 0$ for $\tau \to 0$, and thus Eq. (2.3.17) reduces to the Bohm criterion, $V_i = c_s$, in the limits $\eta_{se} \to \infty$ and $\tau = 0$. Another well-known result is retrieved by considering the limit $\eta_{se} \to \infty$ for arbitrary τ, which gives $V_{i,se} = \sqrt{(T_{e\infty} + \gamma T_{i,se})/m_i}$ [16].

Equations (2.3.13) and (2.3.17) provide the ion and electron velocities at the entrance of ion sheaths. In particular, one can obtain the so-called floating potential, η_f, for which the flow is ambipolar, by solving $V_{i,se} = V_{e,se}$. For $\tau = 0$, this gives $\eta_f \simeq \Lambda$, consistently with the results found previously.

Let us now consider the case of an electron sheath, namely $\eta_{se} < 0$ (Fig. 2.3.7b). In this case, electrons are accelerated through the sheath electric field and are all absorbed, while ions are repelled unless they are sufficiently energetic to overcome the sheath potential barrier, a situation that is reversed with respect to ion sheaths. Thus the ion fluid velocity in the direction normal to the wall can be expressed as

$$V_i = \frac{v_{thi}}{\sqrt{2\pi} I(|\eta|/\tau)} e^{-|\eta|/\tau} = \frac{c_s\sqrt{\tau}}{\sqrt{2\pi} I(|\eta|/\tau)} e^{-|\eta|/\tau} \ , \tag{2.3.19}$$

where $v_{thi} = \sqrt{T_{i\infty}/m_i}$ and $|\eta(x)|/\tau = e(\phi_w - \phi(x))/T_{i\infty}$. In steady state, the continuity equations for electrons and ions, and the momentum equation for electrons are

$$
\begin{aligned}
&n_e\frac{\partial V_e}{\partial s} + V_e\frac{\partial n_e}{\partial s} = S_{pe} \\
&n_i\frac{\partial V_i}{\partial s} + V_i\frac{\partial n_i}{\partial s} = S_{pi} \\
&m_e n_e V_e\frac{\partial V_e}{\partial s} = e n_e\frac{\partial \phi}{\partial s} - \frac{\partial (n_e T_e)}{\partial s} + S_{me} \ .
\end{aligned} \tag{2.3.20}
$$

The term $\partial_s V_i$ in System (2.3.20) can be evaluated as $\partial_s V_i = \partial_\phi V_i \partial_s \phi$, and $\partial_\phi V_i$ can be obtained from Eq. (2.3.19). The quasi-neutrality in the presheath and the adiabaticity of the electron flow lead to a matrix equation $\mathbf{M}\overrightarrow{X} = \overrightarrow{S}$, where

$$
\overrightarrow{X} = \begin{pmatrix} \partial_s n \\ \partial_s V_e \\ \partial_s \phi \end{pmatrix}, \qquad \overrightarrow{S} = \begin{pmatrix} S_{pe} \\ S_{pi} \\ S_{me} \end{pmatrix}, \tag{2.3.21}
$$

$$
\mathbf{M} = \begin{pmatrix} V_e & n & 0 \\ V_i & 0 & n\partial_\phi V_i \\ \gamma T_e & m_e n V_e & -en \end{pmatrix}. \tag{2.3.22}
$$

As for the ion sheath, the condition $\det(\mathbf{M}) = 0$ sets the sheath entrance, namely

$$
V_{e,se} = v_{the}\sqrt{\frac{\tau}{1+\kappa(|\eta_{se}/\tau|)} + f_e} \ . \tag{2.3.23}
$$

We notice that the electron velocity at the sheath entrance is of the order of the thermal velocity, v_{the}, since all electrons are absorbed. In fact, in the limit $\tau \to 0$, Eq. (2.3.23) gives $V_e = \sqrt{\gamma T_{e,se}/m_e} \sim v_{the}$. The quantity f_e can also be related to the presheath density drop by using the assumption of adiabatic flow, i.e. $T_{e,se}/T_{e\infty} = \tilde{n}_{se}^{\gamma-1}$, which leads to $f_e = \gamma \tilde{n}_{se}^{\gamma-1}$.

Equations (2.3.19) and (2.3.23) provide the ion and electron velocities at the entrance of electron sheaths. As a final remark, we mention that in the limit $\eta_{se} \to 0$ both electron and ion sheaths disappear and the electron and ion velocities at the wall are given by Eqs. (2.3.13) and (2.3.19), respectively.

2.3.2.2 Plasma between two biased walls

Let us now consider the situation of a one-dimensional, steady-state plasma bound in between two perfectly absorbing walls. Let us call ϕ_w^l and ϕ_w^r the potentials of the left and right walls, and denote with $\delta = e(\phi_w^r - \phi_w^l)/T_{e\infty} > 0$ the bias applied between the walls. From now on we use the left wall as the reference for the normalized plasma potential, namely $\eta(s) = e[\phi(s) - \phi_w^l]/T_{e\infty}$. In order to maintain a

steady-state, a source replenishes the plasma that is continuously lost at both ends due to the sheath condition. In particular, the plasma source may be non-neutral and currents may be established at the sheaths in order to ensure quasi-neutrality in the plasma bulk. This situation is very common in biasing experiments, where plasma currents feed the biased region by acting as non-neutral sources. These currents are eventually closed at the sheaths [79].

Two situations may be observed depending on the electric charge introduced by the source, see Fig. 2.3.8. If the plasma source is such that $S_i \geq S_e$, the plasma potential stays always above the highest wall potential ϕ_w^r, and ion sheaths are present on both sides. On the left side, the sheath edge potential is above the floating potential, leading therefore to an ion current, $|\Gamma_i| > |\Gamma_e|$, where $\Gamma_\alpha = n_{\alpha,se} V_{\alpha,se}$. On the right side, the sheath edge potential is such that the current established maintains the quasi-neutrality. If the source is negatively charged, $S_i < S_e$, the potential of the plasma bulk approaches ϕ_w^r in order for the sheath to evacuate the excess of electrons (see Fig. 2.3.8). If the negative source is strong enough, the plasma potential sets its value below ϕ_w^r. In this regime, an ion sheath is established on one wall, while an electron sheath is present on the other wall. This situation is found in many experiments where a positive bias is applied (see, e.g., Refs. [72,67,79]). In the following, we focus on this particularly interesting regime. We derive an expression relating the bulk plasma potential, the bias and the wall currents, by using the results of Sec. 2.3.2.1.

We consider the steady-state charge balance of a one-dimensional plasma bound between two biased walls, in the presence of a non-neutral plasma source. We define J_{ie} as the ratio between the ion and electron sources,

$$J_{ie} = \frac{\int_0^L S_i dx}{\int_0^L S_e dx} \tag{2.3.24}$$

where L is the size of the system. From the steady-state continuity equation for ions and electrons, it follows that J_{ie} is also equal to the ratio between the total ion outflux and the total electron outflux,

$$J_{ie} = \frac{\Gamma_{iw}^r - \Gamma_{iw}^l}{\Gamma_{ew}^r - \Gamma_{ew}^l} = \frac{|\Gamma_{iw}^r| + |\Gamma_{iw}^l|}{|\Gamma_{ew}^r| + |\Gamma_{ew}^l|} , \tag{2.3.25}$$

where $\Gamma_{\alpha w}^l = n_{\alpha w}^l V_{\alpha w}^l$ and $\Gamma_{\alpha w}^r = n_{\alpha w}^r V_{\alpha w}^r$ are the particle fluxes at the left and right walls. These are all outflowing, i.e. $\Gamma_{\alpha w}^l < 0$ and $\Gamma_{\alpha w}^r > 0$.
We assume that inside the sheaths the effect of S_i and S_e can be neglected. This can be quantified as $S_\alpha \ll n_{se}\omega_{pi}$, where $\omega_{pi} = \sqrt{e^2 n_{se}/\epsilon_0 m_i}$ is the ion plasma frequency. This condition is derived by imposing $S_\alpha \ll V_\alpha \partial_s n$ and taking $V_\alpha \sim c_s$ and $\partial_s \sim 1/\lambda_D$. As a consequence, the particle fluxes are conserved inside the sheaths

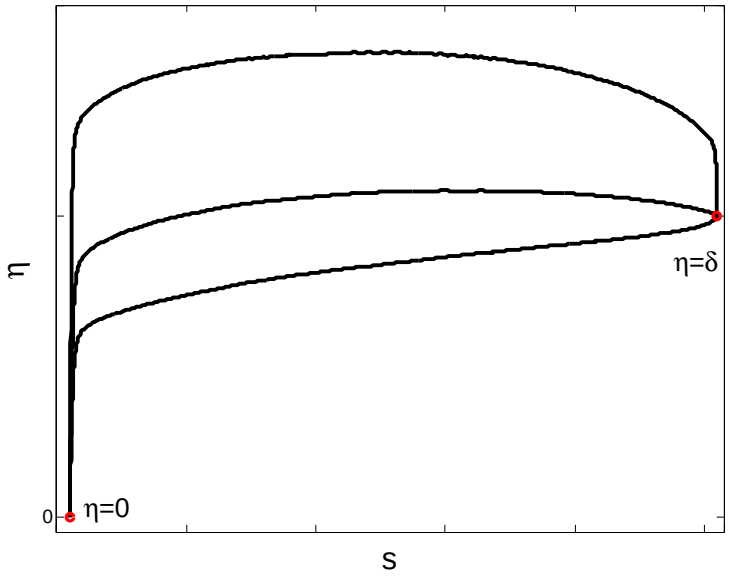

Figure 2.3.8: Examples of plasma potential profiles $\eta(s)$ for a bias $\delta = e(\phi_w^r - \phi_w^l)/T_{e\infty}$ applied between the two walls. The top curve is for the case of a neutral plasma source. The middle curve is for a moderately charged negative source ($S_i \lesssim S_e$), while the bottom curve is for a strongly charged negative source ($S_i \ll S_e$). Plots are obtained from ODISEE simulations in the case of $\tau = 1$.

and thus we can write $\Gamma_{\alpha w}^l = \Gamma_{\alpha se}^l$ and similarly for the right wall. The fluxes in Eq. (2.3.25) are therefore given by the fluxes at each sheath edge, and one can make use of the ion and electron velocities at the sheath entrance derived in the previous section, i.e. Eqs. (2.3.17) and (2.3.19) for the ions, and Eqs. (2.3.13) and (2.3.23) for the electrons, to derive a relation between J_{ie} and the potential in the plasma bulk.

For this purpose, we assume L to be much larger than the sheath length, $L \gg \lambda_D$. This allows us to consider the main plasma as infinitely far from both walls, defining the bulk plasma potential as $\eta_\infty = \eta(L/2)$ and its density as $n_\infty = n(L/2)$. We further assume that the normalized bias is large, namely $\delta = e(\phi_w^r - \phi_w^l)/T_{e\infty} \gg 1$, such that the presheath potential drop can be neglected with respect to the sheath potential drop. It follows that the sheath potential barrier at the left wall is $\eta_\infty > 0$ (ion sheath) and that at the right wall is $\eta_\infty - \delta < 0$ (electron sheath). We recall that this situation corresponds to the bottom curve of Fig. 2.3.8. Using Eqs. (2.3.13), (2.3.17), (2.3.19), (2.3.23), and $\Gamma_{\alpha w}^{l,r} = \Gamma_{\alpha se}^{l,r}$, we can write Eq. (2.3.25) as

$$J_{ie} = \frac{1}{\sqrt{\mu}} \frac{\tilde{n}_l \sqrt{\frac{1}{1+\kappa(\eta_\infty)} + \gamma\tau\tilde{n}_l^{\gamma-1}} + \tilde{n}_r \frac{\sqrt{\tau} e^{-(\delta-\eta_\infty)/\tau}}{\sqrt{2\pi} I((\delta-\eta_\infty)/\tau)}}{\tilde{n}_l \frac{e^{-\eta_\infty}}{\sqrt{2\pi} I(\eta_\infty)} + \tilde{n}_r \sqrt{\frac{\tau}{1+\kappa((\delta-\eta_\infty)/\tau)} + \gamma\tilde{n}_r^{\gamma-1}}} \,. \tag{2.3.26}$$

Here $\tilde{n}_l = n^l_{se}/n_\infty$ and $\tilde{n}_r = n^r_{se}/n_\infty$ are the sheath edge densities at the left and right sides normalized to the bulk density, and the identity $c_s/v_{the} = 1/\sqrt{\mu}$ has been used. Equation (2.3.26) directly relates J_{ie} to η_∞, and it is valid for $0 < \eta_\infty < \delta$, which corresponds to the regime of an ion sheath on one wall and an electron sheath on the other wall. Six parameters modulate the function $J_{ie}(\eta_\infty)$, namely μ, τ, δ, γ, $\tilde{n}_l$ and $\tilde{n}_r$. Figure 2.3.9 shows the bulk plasma potential as a function of J_{ie} as given by Eq. (2.3.26), for different values of τ and $\tilde{n}_l/\tilde{n}_r$.

It is interesting to note that in all cases there is an abrupt transition of the plasma potential occurring around a critical value of the current ratio J_{ie}. This can be explained as follows. When the bulk plasma potential is $\eta_\infty \simeq \delta$, the current at the left wall is due to ions entering the sheath at approximately the sound speed, while the current at the right wall is fundamentally due to electrons entering at approximately the thermal speed, thus giving $J_{ie} \simeq 1/\sqrt{\mu}$. As a matter of fact, the right sheath draws electrons at about the thermal speed regardless of the value of η_∞, if $\eta_\infty < \delta$, since no potential barrier prevents them from being absorbed. On the other hand, the left sheath draws ions at about the sound speed and electrons at a speed that depends on the potential barrier, since $V_e \sim c_s \exp(\Lambda - \eta_\infty)$, see Eq. (2.3.13). This exponential dependence explains why η_∞ must approach the floating potential $\eta_f \simeq \Lambda$ in order for the left sheath to start drawing a significant amount of electron current, therefore changing the value of J_{ie}. Thus, for $\eta_f \lesssim \eta_\infty < \delta$ the left and right sheaths respectively draw almost the same ion and electron currents as in the case $\eta_\infty \simeq \delta$, thus explaining the sharpness of the transition observed in Fig. 2.3.9.

The transition in η_∞ occurs at a certain current ratio $J_{ie} = J_t$, which we identify as the current ratio at which $\eta_\infty = \delta/2$. A general expression for J_t can be derived from Eq. (2.3.26) by taking simultaneously the limits $\eta_\infty \gg 1$ and $\delta - \eta_\infty \gg 1$, and it is given by

$$J_t = \frac{1}{\sqrt{\mu}} \frac{\tilde{n}_l}{\tilde{n}_r} \sqrt{\frac{1 + \gamma\tau\tilde{n}_l^{\gamma-1}}{\tau + \gamma\tilde{n}_r^{\gamma-1}}} \tag{2.3.27}$$

A weak dependence of J_t on τ is found, as displayed in Fig. 2.3.9. Thus $\sqrt{\mu}J_t$ mainly depends on the ratio of sheath edge densities. Figure 2.3.9 shows the dependence of J_t on $\tilde{n}_l/\tilde{n}_r$. We can make a rough estimate of the expected density ratio $\tilde{n}_l/\tilde{n}_r$. In the collisionless, isothermal limit, and neglecting sources and inertia, the density drop in the presheath is given by the Boltzmann factor. Also, in order to accelerate ions to sound speed (left presheath) and electrons to thermal speed (right presheath), both presheath potential drops are expected to be approximately equal to $T_{e\infty}/2$. As a consequence we expect $\tilde{n}_l/\tilde{n}_r \simeq 1$ for $\tau \sim 1$, implying that $J_t \simeq 1/\sqrt{\mu}$.

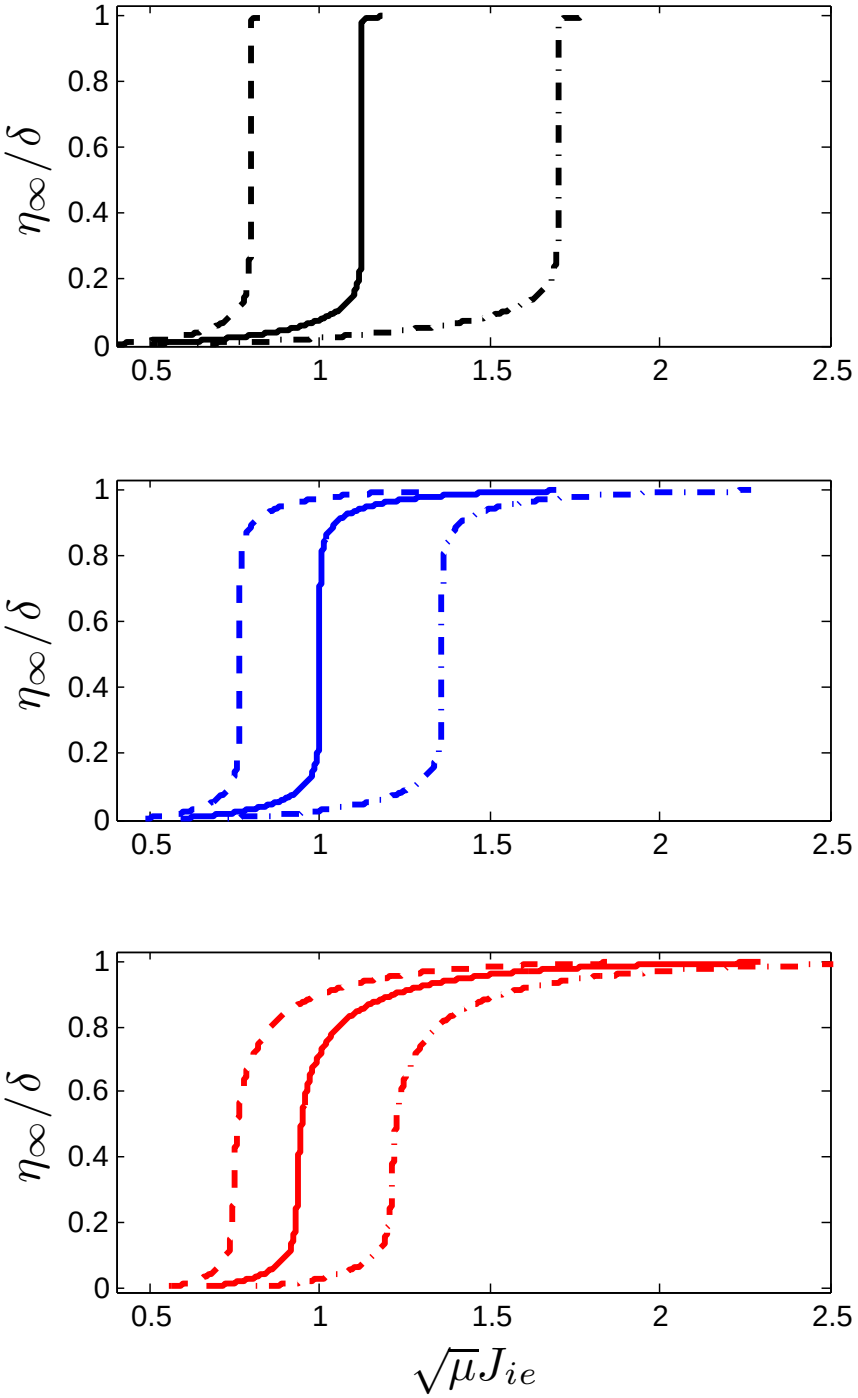

Figure 2.3.9: Normalized main plasma potential η_∞ as a function of the charge source ratio J_{ie} as given by Eq. (2.3.26) with $\delta = 20$, $\gamma = 3$, and for different temperature ratios: $\tau = 0.1$ (top, black), $\tau = 1$ (middle, blue), and $\tau = 3$ (bottom, red). Different density ratios are considered: $\tilde{n}_l/\tilde{n}_r = 0.66$ (left, dashed), $\tilde{n}_l/\tilde{n}_r = 1$ (middle, solid) and $\tilde{n}_l/\tilde{n}_r = 1.25$ (right, dashed-dot).

On the other hand, the sharpness of the transition is strongly dependent on the temperature ratio τ. In fact, as one can see in Fig. 2.3.9, the smaller the value of τ, the steeper is the approach of η_∞ to δ when $J_{ie} > J_t$. To quantify this, we consider the limit of Eq. (2.3.26) when $\eta_\infty \to \delta$, which is

$$\lim_{\eta_\infty \to \delta} J_{ie} = J_t \sqrt{\frac{\tau + \gamma \tilde{n}_r^{\gamma-1}}{\gamma \tilde{n}_r^{\gamma-1}}} + \sqrt{\frac{2\tau}{\mu\pi\gamma\tilde{n}_r^{\gamma-1}}} \tag{2.3.28}$$

Equation (2.3.28) gives J_t for $\tau = 0$, therefore a very sharp transition, and is a monotonically increasing function of τ. This explains why the potential transition is more abrupt for small values of τ.

We finally remark that the function $J_{ie}(\eta_\infty)$ does not strongly depend on the value of γ, which is expected to lie in between $\gamma = 5/3$ (three-dimensional flow) and $\gamma = 3$ (one-dimensional flow). Therefore the value of the transition current mainly depends on μ and $\tilde{n}_l/\tilde{n}_r$ and the sharpness of the potential transition mainly depends on τ.

2.3.2.3 Numerical simulations

In order to confirm the validity of the analytical results presented in the previous section, we perform numerical simulations with the ODISEE code. We simulate a one-dimensional plasma bound between two absorbing walls at $s = 0$ and $s = L$, where L is much larger than the sheath scale, $L \gg \lambda_D$. A source of ions and electrons maintains the plasma in steady-state. Sources are located in the central region $[L/3, 2L/3]$ in order to avoid an influence on the sheath dynamics, and are taken to be spatially uniform in this interval. In velocity space, ions and electrons are injected according to a Maxwellian distribution with zero average velocity and temperatures T_{i0} and T_{e0} respectively. Notice that, as commonly observed in PIC simulations [16], the steady state bulk plasma temperatures, $T_{i\infty}$ and $T_{e\infty}$, are not necessarily equal to the corresponding source temperatures, therefore we cannot choose *a priori* the value of $\tau = T_{i\infty}/T_{e\infty}$. As electrons and ions undergo Coulomb self-collisions with a mean free path λ_{mfp} smaller than the system size but much larger than the sheath scale, i.e. $L > \lambda_{mfp} \gg \lambda_D$, particles present a thermalized distribution function far from the walls, while the sheath remains essentially collisionless. Finally, Poisson's equation is solved by imposing the potential at the two boundaries, $\phi(0) = \phi_w^l$ and $\phi(L) = \phi_w^r$, such that $e(\phi_w^r - \phi_w^l)/T_{e0} \gg 1$. The mass ratio is set to $\mu = 100$. Sheath currents can be driven by varying the relative intensity of the ion and electron sources, therefore varying J_{ie}.

Figure 2.3.10 shows time-averaged profiles of the plasma potential from simulations performed with bias $e(\phi_w^r - \phi_w^l)/T_{e0} = 20$ and $\tau_0 = T_{i0}/T_{e0} = 1$. A number of simulations are performed for different values of J_{ie} around the estimated transition current ratio, namely $J_t \approx 1/\sqrt{\mu}$ as $\tilde{n}_l \simeq \tilde{n}_r$. Clearly an abrupt transition in

the plasma potential is observed when the charge source ratio J_{ie} is slightly varied around $J_{ie} = 1/\sqrt{\mu}$, and variations of less than 5% around this value are enough to bring the potential of the plasma bulk from one wall potential to the other wall potential.

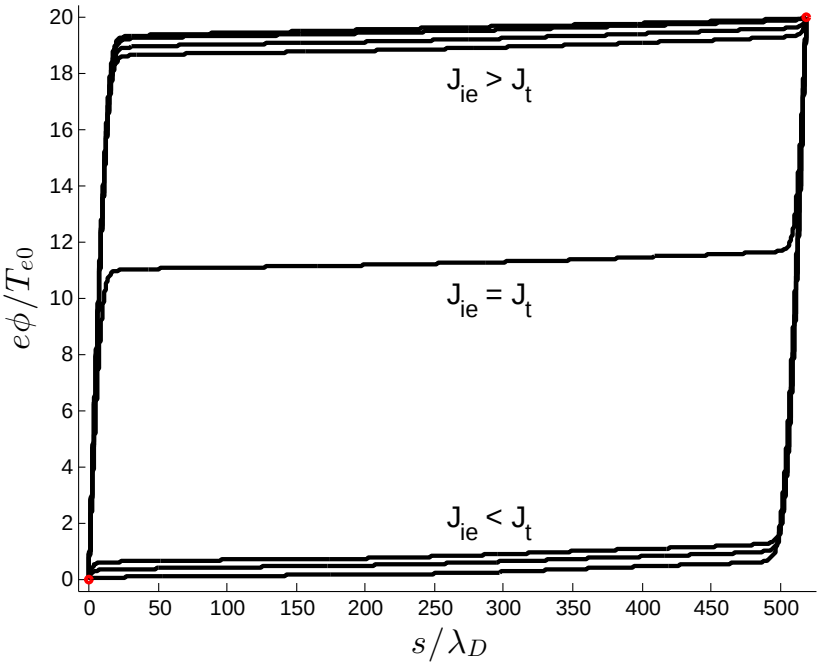

Figure 2.3.10: Time averaged profiles of the plasma potential for $e(\phi_w^r - \phi_w^l)/T_{e0} = 20$, $\tau_0 = 1$, and for different values of J_{ie}. Top curves are for $\sqrt{\mu}J_{ie} = 1.05, 1.1, 1.3, 1.5$. Middle curve is for $\sqrt{\mu}J_{ie} = 1$. Bottom curves are for $\sqrt{\mu}J_{ie} = 0.95, 0.9, 0.7$.

In Fig. 2.3.11, we show the bulk plasma potential as a function of J_{ie} for different values of τ_s. The presence of a sharp transition closely recalls the analytical results of Fig. 2.3.9. We remark that the comparison with the curves in Fig. 2.3.9 can only be qualitative, since a curve with constant τ_0 does not exactly correspond to a curve with constant τ.

In order to accurately verify the general analytical expression in Eq. (2.3.26), we proceed as follows. A set of simulations is performed where τ_0 and J_{ie} are varied. Each pair of parameters (τ_0, J_{ie}) produces a certain steady state, from which $\phi(L/2)$, $\tilde{n}_l$, $\tilde{n}_r$, $T_{i\infty}$ and $T_{e\infty}$ are extracted. One can then obtain the following parameters: $\tau = T_{i\infty}/T_{e\infty}$, $\eta_\infty = e(\phi(L/2) - \phi_w^l)/T_{e\infty}$, and $\delta = e(\phi_w^l - \phi_w^r)/T_{e\infty}$. Finally, the theoretical prediction for J_{ie} is computed using Eq. (2.3.26) and compared with the corresponding simulation parameter. This exercise is carried out for different values of τ_0 and J_{ie}. Figure 2.3.12 shows the results of this comparison, which confirms the validity of Eq. (2.3.26).

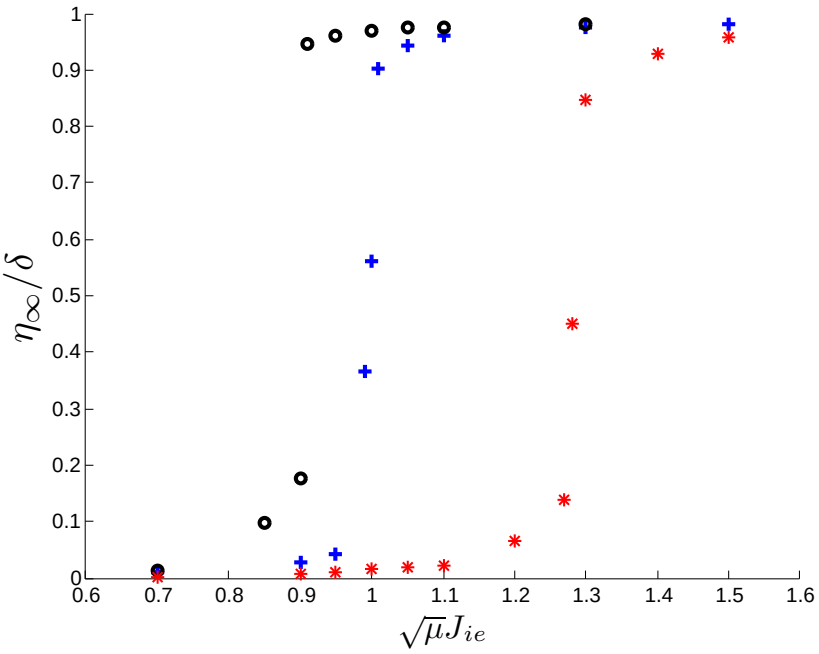

Figure 2.3.11: Steady-state bulk potential as a function of J_{ie}, for $\tau_0 = 0.5$ (black circles), $\tau_0 = 1$ (blue crosses), and $\tau_0 = 3$ (red stars). For all simulations $e(\phi_w^r - \phi_w^l)/T_{e0} = 20$.

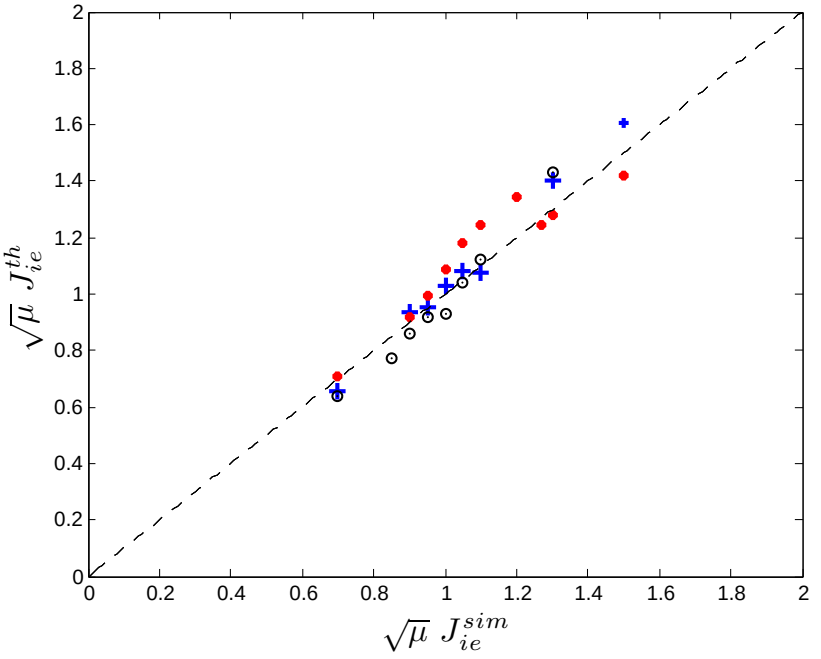

Figure 2.3.12: Comparison between the current ratio J_{ie}^{th} predicted by Eq. (2.3.26) with $\gamma = 3$ and the corresponding current ratio J_{ie}^{sim} used as an input parameter in the simulation. Labels are as in Fig. 2.3.11. Dashed line indicates $J_{ie}^{th} = J_{ie}^{sim}$.

We now discuss the dependence of the transition current ratio J_t on the sheath edge

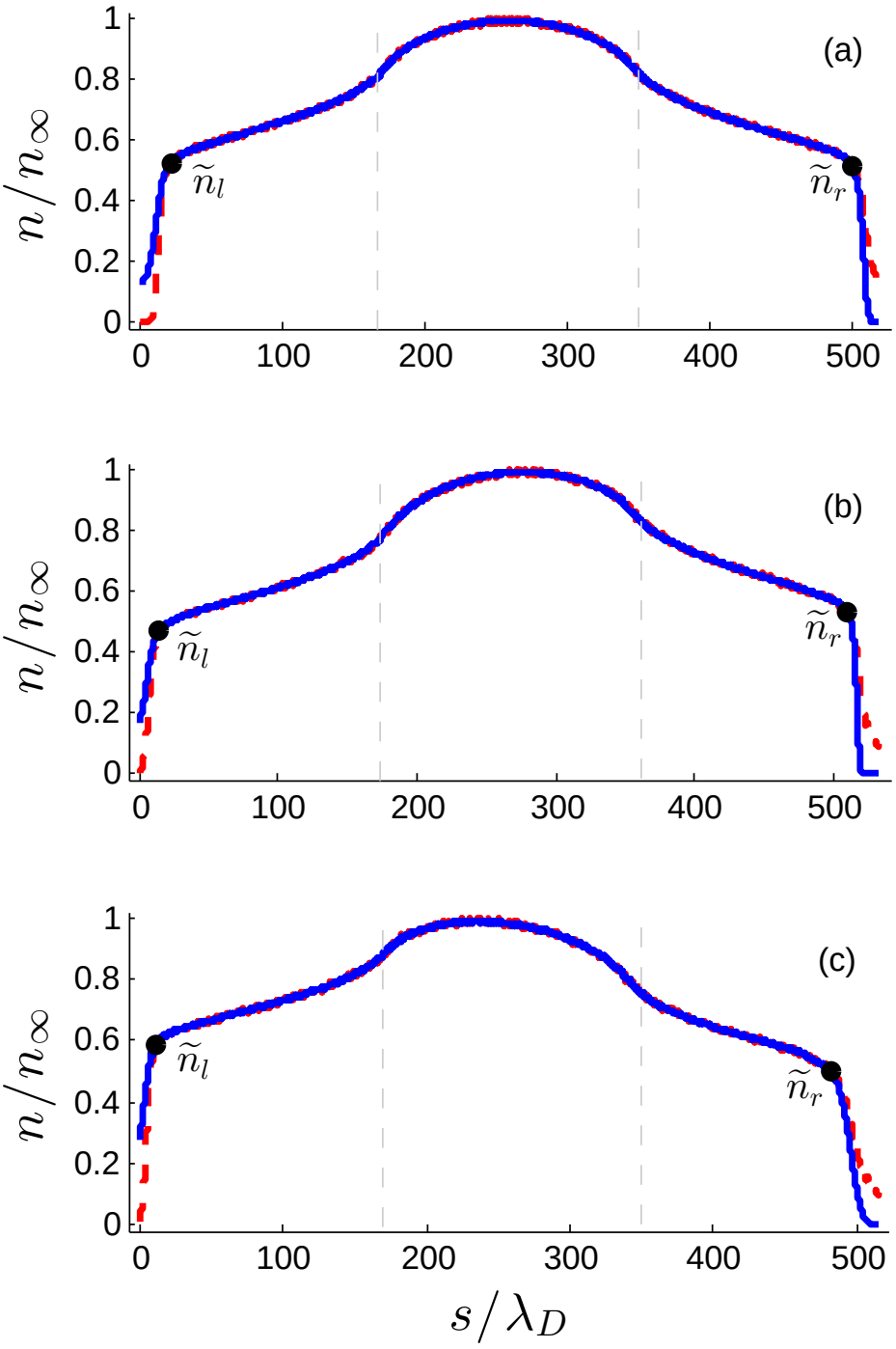

Figure 2.3.13: Time averaged profiles of the ion density (solid, blue) and the electron density (dashed, red) for $e(\phi_w^r - \phi_w^l)/T_{e0} = 20$ and $J_{ie} \simeq J_t$. (a) $\tau_0 = 1$, (b) $\tau_0 = 0.5$, (c) $\tau_0 = 3$. Indicated are the normalized sheath edge densities. The source is located between the two vertical dashed lines.

densities $\tilde{n}_l$ and $\tilde{n}_r$. According to Eq. (2.3.27), the value of J_t mainly depends on the mass ratio μ and the density ratio $\tilde{n}_l/\tilde{n}_r$. In simulations with $\tau_0 = 1 \simeq \tau$, the sheath edge densities are about the same on both sides, as shown in Fig. 2.3.13a. This explains why, in the case displayed in Fig. 2.3.11, the potential transition occurs at $J_{ie} \simeq 1/\sqrt{\mu}$. In simulations with $\tau_0 = 0.5$, however, the sheath edge densities are not the same on both sides, $\tilde{n}_l \lesssim \tilde{n}_r$ (see Fig. 2.3.13b). Therefore, the potential transition occurs at smaller values of J_{ie}, as expected from Eq. (2.3.27). An opposite trend is observed in simulations performed with $\tau_0 = 3$, namely $\tilde{n}_l \gtrsim \tilde{n}_r$ (see Fig. 2.3.13c). As one can observe in Fig. 2.3.13, the density ratios $\tilde{n}_l/\tilde{n}_r$ are always approximately equal to 1. In particular, $\tilde{n}_l/\tilde{n}_r \simeq 0.9$ for $\tau_0 = 0.5$, and $\tilde{n}_l/\tilde{n}_r \simeq 1.2$ for $\tau_0 = 3$. In Fig. 2.3.13 one can also note that the left sheath is positively charged with $n_i > n_e$ (ion sheath) and the right sheath is negatively charged with $n_e > n_i$ (electron sheath). We finally remark that, in the limit of $\tau = 0$, simulations show an unstable behavior of the bulk plasma potential, which oscillates between $\eta_\infty \simeq 0$ and $\eta_\infty \simeq \delta$. These oscillations may be due to kinetic instabilities such as the two-beam instability [81].

2.3.2.4 Experimental implications

When a bias is locally applied with a probe or at the wall confining a plasma, and if the bias is strongly positive with respect to the potential of the vessel wall, the resulting plasma potential has a value that is usually between the two surface potentials. More precisely, the bulk potential η_∞ is found to be close to either of the two wall potentials for most values of J_{ie} and shows an abrupt transition between these two potentials around a value $J_t \sim 1/\sqrt{\mu}$. While this transition current ratio J_t mainly depends on μ and $\tilde{n}_l/\tilde{n}_r$, the shape of the curve $\eta_\infty(J_{ie})$ is strongly modulated by τ. Therefore, a setup that would allow the experimental determination of the curve $\eta_\infty(J_{ie})$ could in principle provide a measure of the ion to electron temperature ratio in the plasma and constrain the values of μ. A scheme of such experimental setup is shown in Fig. 2.3.14. Two electrodes are immersed in a plasma and biased with respect to each other with a constant value $V_1 - V_2 \gg T_e/e$. The second electrode is then biased with respect to the vessel with a value $\Delta V = V_2 - V_{vessel}$ that can be varied. If the surface of the electrodes is small compared to that of the vessel, the variations of ΔV are not expected to modify significantly the plasma potential [79]. Thus the value of the bulk plasma potential ϕ_∞ with respect to the electrode potential V_1 can be varied, therefore varying η_∞. The corresponding current ratio J_{ie} can be measured by operating the electrodes as Langmuir probes (measuring the total current) and as Grid Energy Analyzers (collecting exclusively the ion current).

This experimental scheme was further developed, designed and constructed by the TORPEX group at CRPP, in the framework of a Master thesis [82]. Figure 2.3.15 shows an example of measurements carried out in TORPEX plasmas, showing the presence of the predicted transition. While the position of the transition is at around

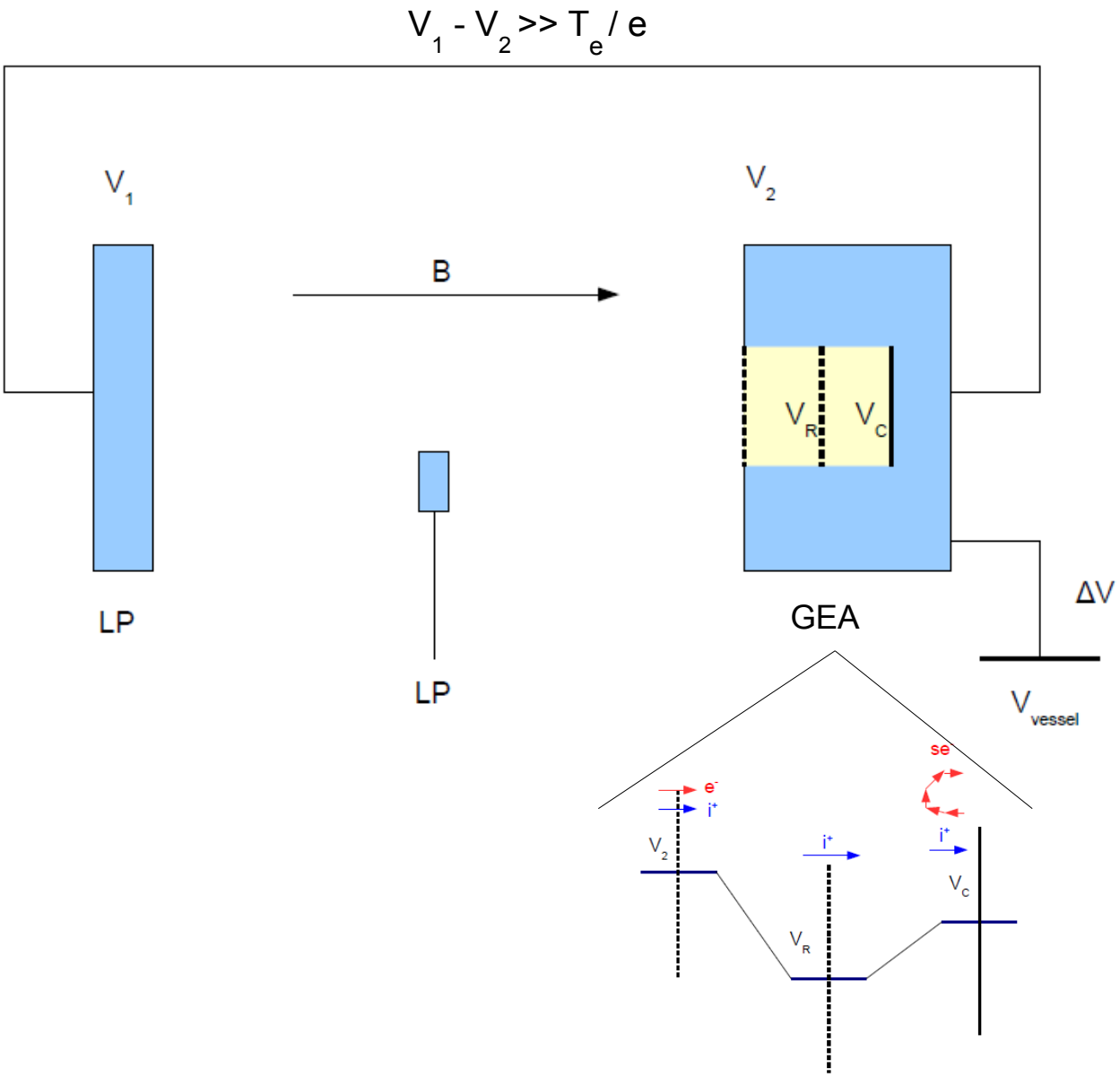

Figure 2.3.14: An idea for an experimental setup that could provide a measure of the normalized plasma potential η_∞ as a function of the current ratio J_{ie}. Two electrodes are immersed in a plasma and biased with respect to each other with a constant value $V_1 - V_2 \gg T_e/e$. The second electrode is then biased with respect to the vessel with a value $\Delta V = V_2 - V_{vessel}$ that can be varied. Variations of $\Delta V = V_2 - V_{vessel}$ allow varying the value of η_∞. The electrodes can be operated as Langmuir probes (LP) or Grid Energy Analyzers (GEA) to measure the corresponding current ratio J_{ie}. The GEA consists of at least two biased grids at V_2 and V_R and a collector at V_C, repelling the electron current from the plasma and reducing the effect of secondary electron emission at the collector. A small LP is inserted half way between the two electrodes and measures the plasma potential and electron temperature, thus providing the value of η_∞.

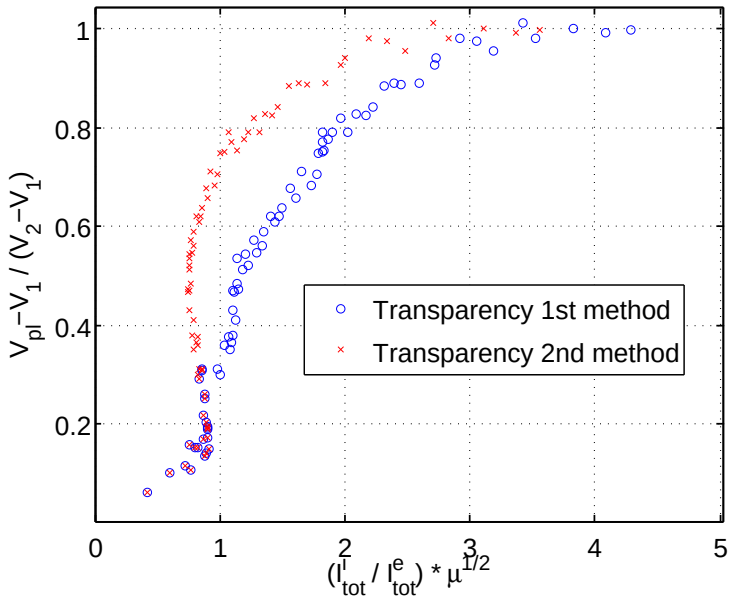

Figure 2.3.15: Experimental results obtained in the TORPEX device showing the predicted transition for the plasma potential as a function of the current ratio drawn at the biased walls. Two different methods were used to estimate the transparency of the Grid Energy Analyzer. The first method (blue circles) was based on a calibration curve deduced from a reference measurement, while the second one (red crosses) assumed a transparency independent of the GEA voltage. Figure from [82].

the expected value of $\sqrt{\mu}J_{ie} \sim 1$, the sharpness of the transition (which should provide an estimate of τ) is hard to interpret and requires further study. First, the GEA transparency is voltage-dependent and therefore difficult to calibrate. High dimensional PIC simulations are probably necessary to investigate those effects. Second, the presheath density drops $\tilde{n}_l$ and $\tilde{n}_r$ are not known and may depend on the value of J_{ie}. The measurement of these is possible, however the experimental device needs to be modified. We can nevertheless conclude that the predicted behaviour of the plasma potential is qualitatively well reproduced experimentally and that our study opens the way to the development of a device capable of measuring T_i in edge plasma conditions.

2.4 Magnetized plasma sheaths

Leveraging the analysis technique that we have developed for the case of unmagnetized sheaths, we now turn to the study of magnetized plasma sheaths and the derivation of boundary conditions to be applied to plasma turbulence codes.

When the magnetic field is oblique with respect to an absorbing wall, the plasma-wall

transition consists of three subregions (see, e.g., Ref. [38] for a review): the collisional presheath (CP), the magnetic presheath (MP), also called Chodura sheath, and the Debye sheath (DS), which is in contact with the wall. In each of these regions a potential drop proportional to the electron temperature is observed, $\Delta\phi \propto T_e$, but on very different spatial scales. The CP width typically scales with the ion mean free path, λ_{mfp}. The scale length of the MP is the ion sound larmor radius, ρ_s. The DS width has a scale length of the order of the Debye length, λ_D. In the CP plasma is quasineutral, ions are magnetized and accelerated towards the wall, reaching the plasma sound speed c_s at the MP entrance along the magnetic field direction. The MP is also quasineutral but the electric field is strong enough to demagnetize the ions, which are deflected and reach the DS entrance flowing at c_s in the direction normal to the wall. Inside the DS quasineutrality is violated.

Plasma turbulence fluid codes (see Refs. [28, 83, 29, 31, 32, 33, 34] for some examples) are based on the quasineutrality approximation, which breaks down at the DS entrance. They are also typically based on the *ion drift approximation* (IDA), which breaks down in the MP. Therefore the magnetic presheath cannot be described by a fluid model based on the IDA. More precisely, in plasma fluid turbulence codes the analysis of the dynamics is usually split into the direction parallel and perpendicular to the magnetic field, i.e. by decomposing $\mathbf{v}_i = v_{||i}\mathbf{b} + \mathbf{v}_{\perp i}$, where $\mathbf{b} = \mathbf{B}/B$. The drift ordering usually adopted, $d/dt \ll \omega_{ci}$, where $d/dt = \partial_t + \mathbf{v}_i \cdot \nabla$, implies that the inertia term is small compared to the electric and magnetic forces in the ion momentum equation, which in the cold ion limit is

$$m_i n \frac{d}{dt}\mathbf{v}_i = en\mathbf{E} + en\mathbf{v}_i \times \mathbf{B} \ . \tag{2.4.1}$$

One can therefore write the perpendicular velocity as $\mathbf{v}_{\perp i} = \mathbf{v}_E + \mathbf{v}_{pol}$, where $\mathbf{v}_E = \mathbf{E}\times\mathbf{B}/B^2$ is the leading order term, and $\mathbf{v}_{pol} = (\mathbf{b}/\omega_{ci}) \times d\mathbf{v}_{\perp i}/dt$ is the polarization drift velocity which contains all terms of order one and higher in $(1/\omega_{ci})d/dt$. Within the IDA, only the first order terms are retained, leading to

$$\mathbf{v}_{\perp i} = \mathbf{v}_E + \frac{\mathbf{b}}{\omega_{ci}} \times \frac{d^0}{dt}\mathbf{v}_E \tag{2.4.2}$$

where $d_t^0 = \partial_t + (v_{||i}\mathbf{b} + \mathbf{v}_E)\cdot\nabla$. In the MP, the deflection of the sonic ion flow from the direction parallel to the magnetic field to the direction of the electric field, which is normal to the wall, requires that ions are demagnetized and therefore violates the IDA. In fact, in the MP the ion inertia term is comparable to the other terms in Eq. (2.4.1), $m_i n(\mathbf{v}_i \cdot \nabla)\mathbf{v}_{\perp i} \sim en\mathbf{v}_{\perp i} \times \mathbf{B}$, which provides a scaling for the size of the MP, λ_m, since $m_i c_s^2/\lambda_m \sim ec_s B$, and hence $\lambda_m \sim c_s/\omega_{ci} = \rho_s$. Thus, in the MP where the electric field varies on a scale length of the order of the ion sound Larmor radius, the ion motion cannot be described within the ion drift approximation. As a consequence, plasma turbulence fluid codes based on the IDA require boundary

conditions at the MP entrance in order to account correctly for the plasma-wall transition.

The magnetic presheath has been studied since the pioneering work of Chodura [84], followed by an extensive research effort that has brought to light many important aspects of this physical system, such as the effect of collisions [85, 86, 87], magnetic field angle [84, 87, 88, 89], $\mathbf{E} \times \mathbf{B}$ and diamagnetic drifts [90, 91, 92, 93, 94, 95], and finite ion temperature [84, 96]. Most of these studies provide a boundary condition for the parallel ion velocity at the MP entrance, whereas the boundary conditions for the other fluid quantities remain unclear.

The goal of the present section is to provide a complete set of boundary conditions to be used at the MP entrance in IDA-based fluid codes. We target a set of boundary conditions which can faithfully supply the sheath physics to the fluid codes and which, at the same time, remain simple enough to be easily implemented. We work under the assumption of a weakly collisional, steady-state plasma sheath with cold ions and in contact with a totally absorbing wall, and we assume that gradients in the directions parallel to the wall are on a scale much larger than ρ_s. In this framework we determine rigorously the MP entrance condition and the boundary conditions for the plasma density and temperature, the electrostatic potential, the ion and electron parallel velocities, and the vorticity. The correctness of these boundary conditions is verified via kinetic simulations of the magnetized plasma-wall transition carried out with the ODISEE code.

2.4.1 The magnetic presheath entrance condition

We consider a weakly collisional, steady-state plasma in contact with an absorbing wall, with $T_i \ll T_e$ and for which $\lambda_D \ll \rho_s \ll \lambda_{mfp}$. We assume a constant magnetic field oblique to the wall at an angle α. For a suitable analytical description we use a field aligned coordinate system, (x, y, z), where z is along $\mathbf{B}$, x is perpendicular to $\mathbf{B}$ and parallel to the wall, and y is perpendicular to both x and z, directed towards the wall (see Fig. 2.4.1). In such geometry the magnetic field is $\mathbf{B} = (0, 0, B_0)$. We also define the coordinate normal to the wall surface, $s = y \cos\alpha + z \sin\alpha$.

We consider the presence of plasma gradients in the x direction with an ordering $\epsilon = \rho_s/L_n \sim \rho_s/L_\phi \sim \rho_s/L_{T_e} \ll 1$, where L_n, L_ϕ, and L_{T_e} are the density, potential, and temperature scale lengths in the x direction. Since the MP electric field has a characteristic scale length of the order of ρ_s, it is much stronger than the electric field present in the bulk plasma, and gradients eventually dominate along the s direction. We remark that plasma gradients in the direction perpendicular to both s and x do not affect the results derived herein, therefore we do not consider them for the sake of simplicity.

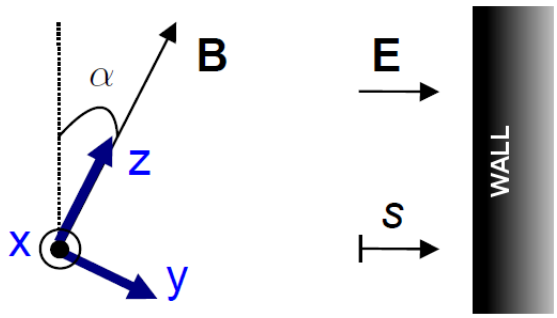

Figure 2.4.1: Schematic representation of the sheath geometry. The magnetic field **B** is oblique to the wall at an angle α. The wall is indicated on the right together with the sheath electric field **E**, which is along the normal direction s.

In order to simplify the notation, in the present section space and time are expressed in the natural units of the system, using a reference electron temperature T_{e0}, as in Sec. 2.2.7. Namely the electron temperature and the electrostatic potential are normalized as $T_e \to T_e/T_{e0}$ and $\phi \to e\phi/T_{e0}$, while space and time are normalized as $x \to x/\rho_{s0}$ and $t \to \omega_{ci}t$, where $\rho_{s0} = c_{s0}/\omega_{ci}$, $c_{s0} = \sqrt{T_{e0}/m_i}$, and $\omega_{ci} = eB_0/m_i$. Velocities are therefore normalized to the sound speed, $v \to v/c_{s0}$. Finally, the density is normalized to a reference density, $n \to n/n_0$. In the following, all quantities will be expressed in normalized units.

In order to describe the steady-state dynamics of the CP, similarly to what was done in the case of unmagnetized sheaths, we now write a system of equations including the ion continuity equation and the ion and electron parallel momentum equations. We then derive the condition defining the MP entrance by following an approach similar to that described in Sec. 2.3 in the case of unmagnetized sheaths. The steady state continuity equation for ions is

$$\nabla \cdot (n\mathbf{v}_i) = S_{pi} \ , \tag{2.4.3}$$

where S_{pi} is the ion particle source. Using the relation $v_{si} = v_{||i} \sin\alpha + v_{yi} \cos\alpha$, it can be written as

$$v_{si}\frac{\partial n}{\partial s} + n\sin\alpha\frac{\partial v_{||i}}{\partial s} + n\cos\alpha\frac{\partial v_{yi}}{\partial s} + n\frac{\partial v_{xi}}{\partial x} + v_{xi}\frac{\partial n}{\partial x} = S_{pi} \ . \tag{2.4.4}$$

Equation (2.4.4) can be simplified by noting that the ion drift approximation, Eq. (2.4.2), can be used in the CP to express the perpendicular velocities. At the zeroth order in $(1/\omega_{ci})d/dt$, namely neglecting the ion polarization drift, Eq. (2.4.2) gives $v_{xi} = -\cos\alpha\partial_s\phi$ and $v_{yi} = \partial_x\phi$. As a matter of fact, these expressions describe well the perpendicular ion velocities in the CP, as shown later in the kinetic simulation results (Section 2.4.3). Therefore the third and fourth terms in Eq. (2.4.4) cancel each other since we have $n\cos\alpha\partial_s v_{yi} = n\cos\alpha\partial_s\partial_x\phi = -n\partial_x v_{xi}$, and for the fifth

term we have $v_{xi}\partial_x n = -\partial_x n \cos\alpha \partial_s \phi \sim O(\epsilon)$. The continuity equation, Eq. (2.4.4), can then be rewritten in a simpler form, that is

$$v_{si}\frac{\partial n}{\partial s} + n\sin\alpha\frac{\partial v_{||i}}{\partial s} - \cos\alpha\frac{\partial n}{\partial x}\frac{\partial \phi}{\partial s} = S_{pi} \tag{2.4.5}$$

which is valid in the CP up to the MP entrance, where the polarization drift becomes important and the IDA breaks down.

We now consider the parallel component of the ion momentum equation, Eq. (2.4.1), which in steady-state is

$$n\left(v_{si}\frac{\partial}{\partial s} + v_{xi}\frac{\partial}{\partial x}\right)v_{||i} = -n\sin\alpha\frac{\partial \phi}{\partial s} + S_{||mi}\ , \tag{2.4.6}$$

where we have introduced a source of momentum, $S_{||mi}$, eventually present in the system and due to either injection of particles, ionization or collisions. Using again the relation $v_{xi} = -\cos\alpha\partial_s\phi$, Eq. (2.4.6) can be written as

$$nv_{si}\frac{\partial v_{||i}}{\partial s} + n\left(\sin\alpha - \cos\alpha\frac{\partial v_{||i}}{\partial x}\right)\frac{\partial \phi}{\partial s} = S_{||mi}\ . \tag{2.4.7}$$

Finally, we consider the steady-state momentum equation for electrons, that is

$$n(\mathbf{v}_e\cdot\nabla)\mathbf{v}_e = -\mu(n\mathbf{E} + n\mathbf{v_e}\times\mathbf{b} + \nabla p_e) + \mathbf{S}_{me}\ , \tag{2.4.8}$$

where $\mu = m_i/m_e$ and $p_e = nT_e$. Equation (2.4.8) can be simplified since $\mu \gg 1$, and therefore the electron inertia term can be neglected almost all the way up to the wall (electron inertia may become important only if the electric field varies on a scale length that is comparable to the electron gyroradius ρ_e). Moreover, it is reasonable to assume isothermal electrons in the CP, namely $\partial_s T_e = 0$; this considerably simplifies the calculation and the expressions of the boundary conditions. A complete calculation relaxing the hypothesis $\partial_s T_e = 0$ is presented in Appendix B, which shows that the temperature gradient is in fact small at the MP entrance. Hence, we have $\partial_s p_e = T_e\partial_s n$, and the parallel component of Eq. (2.4.8) is

$$\mu\sin\alpha T_e\frac{\partial n}{\partial s} - \mu\sin\alpha n\frac{\partial \phi}{\partial s} = S_{||me}\ . \tag{2.4.9}$$

The ion continuity equation, Eq. (2.4.5), and the parallel ion and electron momentum equations, Eqs. (2.4.7) and (2.4.9), form a system of equations,

$$
\begin{aligned}
&v_{si}\frac{\partial n}{\partial s} + n\sin\alpha\frac{\partial v_{||i}}{\partial s} - \cos\alpha\frac{\partial n}{\partial x}\frac{\partial \phi}{\partial s} = S_{pi} \\
&nv_{si}\frac{\partial v_{||i}}{\partial s} + n\left(\sin\alpha - \cos\alpha\frac{\partial v_{||i}}{\partial x}\right)\frac{\partial \phi}{\partial s} = S_{||mi} \\
&\mu\sin\alpha T_e\frac{\partial n}{\partial s} - \mu\sin\alpha n\frac{\partial \phi}{\partial s} = S_{||me}
\end{aligned}
\tag{2.4.10}
$$

containing three unknowns $(n, v_{||i}, \phi)$ and their respective gradients. The system of equations (2.4.10) can also be written as a matrix system $\mathbf{M}\overrightarrow{X} = \overrightarrow{S}$, where

$$
\overrightarrow{X} = \begin{pmatrix} \partial_s n \\ \partial_s v_{||i} \\ \partial_s \phi \end{pmatrix}, \qquad \overrightarrow{S} = \begin{pmatrix} S_{pi} \\ S_{||mi} \\ S_{||me} \end{pmatrix}, \tag{2.4.11}
$$

and

$$
\mathbf{M} = \begin{pmatrix} v_{si} & n\sin\alpha & -\partial_x n\cos\alpha \\ 0 & nv_{si} & n(\sin\alpha - \partial_x v_{||i}\cos\alpha) \\ \mu\sin\alpha T_e & 0 & -\mu n\sin\alpha \end{pmatrix}. \tag{2.4.12}
$$

The system of equations (2.4.10) is valid in the CP up to the MP entrance, where the IDA breaks down. In the CP, gradients are small and due to the presence of the sources. At the MP entrance, gradients become large, $\partial_s \sim 1$, and the source terms are much smaller than any other term in the fluid equations, i.e. $|M_{ij}X_j| \gg |S_i|$ for all i, j such that $M_{ij} \neq 0$. In other words, nonzero gradients can be sustained without sources at the MP entrance, which leads to $\mathbf{M}\overrightarrow{X} \simeq 0$ at this location. Now, the presence of nonzero gradients imposes $\det(\mathbf{M}) = 0$, which defines the position of the MP entrance. This condition can be written as

$$
v_{si} = c_s\sin\alpha\left(\frac{\rho_s}{2\tan\alpha}\frac{\partial_x n}{n} \pm \sqrt{1 + \left(\frac{\rho_s}{2\tan\alpha}\frac{\partial_x n}{n}\right)^2 - \frac{\partial_x v_{||i}}{\tan\alpha}}\right). \tag{2.4.13}
$$

Notice that there are two solutions corresponding to the two opposite ends of the field line; we keep the positive solution for which the coordinate s increases moving towards the wall, as in Fig. 2.4.1. Recalling that $v_{si} = v_{||i}\sin\alpha + v_{yi}\cos\alpha$ and that $v_{yi} = \partial_x\phi \sim O(\epsilon)$, we can deduce that $\partial_x v_{||i}\sin\alpha = \partial_x v_{si} + O(\epsilon^2)$. Therefore from Eq. (2.4.13) we have that $\partial_x v_{||i} = \partial_x c_s + O(\epsilon^2)$, with $\partial_x c_s = \partial_x T_e/(2\sqrt{T_e})$. We can thus write Eq. (2.4.13) as

$$
v_{si} = c_s\sin\alpha\left(\theta_n + \sqrt{1 + \theta_n^2 - \theta_{T_e}}\right) \tag{2.4.14}
$$

where

$$\theta_n = \frac{\rho_s}{2\tan\alpha}\frac{\partial_x n}{n} \quad , \tag{2.4.15}$$

$$\theta_{T_e} = \frac{\rho_s}{2\tan\alpha}\frac{\partial_x T_e}{T_e} \quad . \tag{2.4.16}$$

Retaining only first order terms in $\theta_n \sim \theta_{T_e} \sim \epsilon/\tan\alpha$, we obtain

$$v_{si} = c_s \sin\alpha\,(1 + \theta_n - \theta_{T_e}/2) \quad . \tag{2.4.17}$$

2.4.2 Boundary conditions at the magnetic presheath entrance

We now derive the boundary conditions for fluid turbulence codes at the MP entrance for the parallel ion and electron velocities, the plasma density, the electron temperature, the electrostatic potential, and the vorticity.

2.4.2.1 Parallel ion velocity

Recalling that $v_{si} = v_{yi}\cos\alpha + v_{||i}\sin\alpha$ and $v_{yi} = \partial_x\phi$, the parallel ion velocity at the MP entrance can be obtained by using Eq. (2.4.17). This leads to

$$\begin{aligned} v_{||i} &= c_s\left(1 + \theta_n - \frac{1}{2}\theta_{T_e}\right) - \frac{1}{\tan\alpha}\frac{\partial\phi}{\partial x} \\ &= c_s\left(1 + \theta_n - \frac{1}{2}\theta_{T_e} - \frac{2\phi}{T_e}\theta_\phi\right) \end{aligned} \tag{2.4.18}$$

where

$$\theta_\phi = \frac{\rho_s}{2\tan\alpha}\frac{\partial_x\phi}{\phi} \quad . \tag{2.4.19}$$

In the limit $\theta_n = \theta_{T_e} = \theta_\phi = 0$, Eq. (2.4.18) retrieves the so-called Bohm-Chodura criterion $v_{||i} = c_s$ [16]. In the presence of plasma gradients in the x direction, the main correction in Eq. (2.4.18) is typically due to the potential gradient. In fact, assuming $\theta_n \sim \theta_{T_e} \sim \theta_\phi$ and $\phi \approx 3T_e$, the correction related with the potential gradient is six times larger than the density gradient correction, and twelve times larger than the temperature gradient one. We note that the correction given by the $\mathbf{E}\times\mathbf{B}$ drift, namely the last term in Eq. (2.4.18), is valid at any order in ϵ. As a matter of fact, $v_{||i}$ may become negative at the MP entrance when θ_ϕ becomes large, as shown later in the kinetic simulations presented in Sec. 2.4.3. Finally, we note that in Ref. [94] the case $\theta_\phi \neq 0$ was studied, neglecting the fourth term on the left hand side of Eq. (2.4.4). This leads to a different expression for $v_{||i}$ than in Eq. (2.4.18).

2.4.2.2 Density and potential

The density and potential gradients at the MP entrance can be obtained by observing that, being $\det(\mathbf{M}) = 0$, the system $\mathbf{M}\overrightarrow{X} = 0$ allows us to relate among themselves the components of $\overrightarrow{X}$, namely the gradients of n, $v_{||i}$ and ϕ in the s direction. In particular, we choose to express $\partial_s\phi$ and $\partial_s n$ as a function of $\partial_s v_{||i}$. The second and third equations of the system $\mathbf{M}\overrightarrow{X} = 0$ provide

$$\frac{\partial\phi}{\partial s} = -\frac{v_{si}}{\sin\alpha - \cos\alpha\partial_x v_{||i}}\frac{\partial v_{||i}}{\partial s} \ , \tag{2.4.20}$$

$$\frac{\partial n}{\partial s} = \frac{n}{T_e}\frac{\partial\phi}{\partial s} \ . \tag{2.4.21}$$

Using Eq. (2.4.17) to express v_{si} and again retaining only first order terms in θ_n and θ_{T_e}, we obtain

$$\frac{\partial\phi}{\partial s} = -\left(1 + \theta_n + \theta_{T_e}/2\right) c_s \frac{\partial v_{||i}}{\partial s} \ , \tag{2.4.22}$$

$$\frac{\partial n}{\partial s} = -\left(1 + \theta_n + \theta_{T_e}/2\right) \frac{n}{c_s}\frac{\partial v_{||i}}{\partial s} \ . \tag{2.4.23}$$

2.4.2.3 Temperature

The MP entrance condition was derived assuming no temperature gradient in the s direction. For consistency,

$$\frac{\partial T_e}{\partial s} = 0 \tag{2.4.24}$$

can be used as a boundary condition for the electron temperature. A more detailed calculation that takes into account temperature variations is presented in Appendix B and shows that the temperature gradient at the MP entrance is indeed small.

2.4.2.4 Vorticity

The vorticity represents the curl of the $\mathbf{E}\times\mathbf{B}$ drift in the parallel direction, being defined as $\omega = \left[\nabla\times(\mathbf{E}\times\mathbf{b})\right]\cdot\mathbf{b} = \nabla_\perp^2\phi$, and it measures the frequency of the plasma rotation in the plane perpendicular to the magnetic field. In the system under consideration, we can write $\nabla_\perp^2\phi = \partial_x^2\phi + \partial_y^2\phi = \partial_y^2\phi + O(\epsilon^2)$, and the term of order ϵ^2 can be neglected. Moreover, we have $\partial_y^2\phi = \cos^2\alpha\,\partial_s^2\phi$, and $\partial_s^2\phi$ at the MP entrance can be estimated by computing the derivative of Eq. (2.4.20) along the s direction and then using again Eq. (2.4.17) to express v_{si}. This leads to

$$\omega = -\cos^2\alpha\left[\left(1+\theta_{T_e}\right)\left(\frac{\partial v_{||i}}{\partial s}\right)^2 + c_s\left(1+\theta_n+\frac{1}{2}\theta_{T_e}\right)\frac{\partial^2 v_{||i}}{\partial s^2}\right] . \tag{2.4.25}$$

2.4.2.5 Parallel electron velocity

While in the MP electrons are always magnetized since $\rho_e \ll \rho_s$, in the DS the electron dynamics depends on the relative magnitude between λ_D and ρ_e. We focus on the $\rho_e \ll \lambda_D$ regime, where electrons remain magnetized all the way up to the wall, and the value of $v_{||e}$ at the MP entrance essentially depends on $\eta_m = (\phi_{MPE} - \phi_W)/T_e$, the normalized potential drop from the MP entrance to the wall. A detailed kinetic treatment of the electron trajectories, taking into account the presence of gradients in the x direction, leads to the following result [90]:

$$v_{||e} = c_s \exp(\Lambda - \eta_m) - \frac{1}{\tan\alpha}\frac{\partial\phi}{\partial x} + \frac{1}{n\tan\alpha}\frac{\partial p_e}{\partial x} \tag{2.4.26}$$

where $\Lambda = \log\sqrt{\mu/2\pi}$, and $\partial_x p_e/n$ is the diamagnetic drift velocity. Using the definition of θ_n, θ_{T_e} and θ_ϕ, Eqs. (2.4.15), (2.4.16), and (2.4.19), we can write Eq. (2.4.26) as

$$v_{||e} = c_s\big[\exp(\Lambda - \eta_m) - \frac{2\phi}{T_e}\theta_\phi + 2(\theta_n + \theta_{T_e})\big] \tag{2.4.27}$$

which shows that both potential and diamagnetic corrections are comparable. We remark that if $\rho_e \gtrsim \lambda_D$, electron trajectories may become rather complex in the Debye sheath [97,98], and it is not possible to find a simple expression for $v_{||e}$ as in Eq. (2.4.26).

Equation (2.4.27) together with Eqs. (2.4.18), (2.4.22), (2.4.23), (2.4.24) and (2.4.25), constitute the boundary conditions to be implemented in plasma fluid turbulence codes at the MP entrance.

2.4.3 Particle simulations of the magnetic presheath

In order to confirm the validity of the analytical results presented in Secs. 2.4.1 and 2.4.2, we perform numerical simulations with the ODISEE code. In this case we consider two absorbing walls at $s = 0$ and $s = L$, with $L \simeq 20\rho_s \simeq 10^3\lambda_D$, a source of ions and electrons uniformly distributed in space, $T_i/T_e \simeq 10^{-2}$, electron-electron Coulomb collisions, $\phi_w = 0$ at the two boundaries, and a magnetic field constant and tilted with respect to the wall at an angle α, as shown in Fig. 2.4.1. Parameters are chosen such that the scaling

$$\rho_e \lesssim \lambda_D \ll \rho_s \ll \lambda_{mfp} < L \tag{2.4.28}$$

is ensured. In particular, to guarantee $\rho_s/\rho_e = \sqrt{\mu} \gg 1$, the realistic mass ratio $\mu = 1836$ is used in the simulations. We first show that the main features of the CP, MP, and DS are retrieved by the simulations, and then we verify the boundary

conditions presented in Sec. 2.4.2.

In order to describe the main features of the plasma-wall transition, we start by considering floating conditions, namely no net current to the walls, and no gradients in the x direction, i.e. $\theta_n = \theta_{T_e} = \theta_\phi = 0$. This is achieved by setting equal ion and electron particle sources, $S_{pi} = S_{pe}$. Figures 2.4.2a and 2.4.2b show the time-averaged profiles of the plasma potential and the ion velocity v_{si}, in proximity of the $s = L$ wall (exactly the same consideration can be made for the $s = 0$ wall). In the CP (black region in Fig. 2.4.2a), ions are accelerated and, according to the analytical derivation of Sec. 2.4.1, the entrance of the MP is defined by the point where $v_{si} = c_s \sin\alpha$, corresponding to the point where the IDA is expected to break down. This is confirmed by Figs. 2.4.2c and 2.4.2d, where one observes that in the MP the ion perpendicular dynamics can no longer be described by the IDA, Eq. (2.4.2). In Fig. 2.4.2a one can see that the thickness of the MP (green region in Fig. 2.4.2a) is of the order of ρ_s. In this region, ions are accelerated from $v_{si} = c_s \sin\alpha$ to $v_{si} = c_s$, as evident from Fig. 2.4.2b. The entrance of the DS corresponds to the point where ions reach the sound speed along the s direction, $v_{si} = c_s$, and inside the DS (red region in Fig. 2.4.2a) quasineutrality is violated, as visible in Fig. 2.4.2e.

The results shown in Fig. 2.4.2 are all relative to the $\alpha = 30°$ case; the effect of the angle α on the plasma potential in the different regions of the plasma-wall transition is now discussed. Since in the MP ions are accelerated from $v_{si} = c_s \sin\alpha$ to $v_{si} = c_s$, the potential drop from the MP entrance to the DS entrance, $\Delta\phi_{MP}$, depends on α. We can estimate $\Delta\phi_{MP}$ by observing that the ion flux is approximately constant throughout the sheath. Therefore the ratio between the ion velocities at the DS entrance and at the MP entrance is inversely proportional to the ratio between the densities at the same locations. Assuming that the ratio of densities is given by the Boltzmann factor, we deduce $e\Delta\phi_{MP}/T_e = -\log(\sin\alpha)$, as confirmed by Fig. 2.4.3. On the other hand, $\Delta\phi_{DS}$, the potential drop in the DS, has the opposite trend (see Fig. 2.4.3), in such a way that the total drop from the MP entrance to the wall is always equal to the floating potential, $\eta_m = \Lambda$. Finally, $\Delta\phi_{CP}$, the potential drop in the CP, depends on the specific presheath process present in the plasma, such as collisions or sources. Since those are independent of α in our simulations, $\Delta\phi_{CP}$ does not depend on α, as shown in Fig. 2.4.3, being $e\Delta\phi_{CP}/T_e \approx 0.7$, as predicted in Ref. [16].

Turning now to the validity of the boundary conditions derived in Sec. 2.4.2, we note that a constant electric field E_x can be included in the one-dimensional model considered by ODISEE, whereas plasma scenarios with $\theta_n \neq 0$ and $\theta_{T_e} \neq 0$ cannot be simulated. We thus limit ourselves to the analysis of the finite E_x effect, which corresponds to a finite θ_ϕ in the boundary conditions. Figure 2.4.4 shows that the ion parallel velocity at the MP entrance is, within a good approximation, independent of α when $E_x = 0$, while it follows rather well Eq. (2.4.18) when $E_x \neq 0$. We

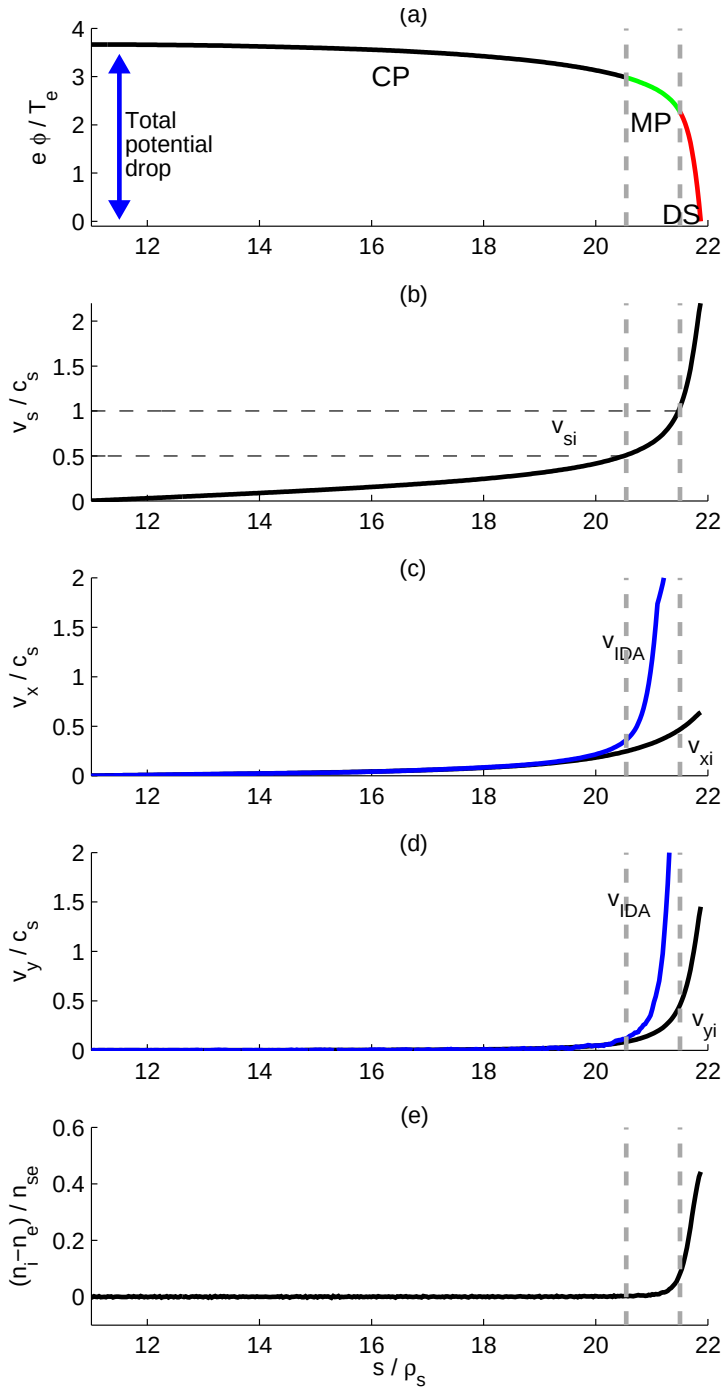

Figure 2.4.2: Time-averaged profiles in proximity of the $s = L$ wall, obtained from ODISEE simulations, with $\alpha = 30°$: (a) electrostatic potential, (b) ion velocity in the s direction, (c) ion velocity in the x direction (bottom, black) and the corresponding velocity as given by the IDA (top, blue), in this case $v_{xi} = -\cos\alpha\partial_s\phi$ according to Eq. (2.4.2), (d) ion velocity in the y direction (bottom, black) and the corresponding velocity as given by the IDA (top, blue), in this case $v_{yi} = -v_{||i}\sin\alpha\cos\alpha\partial_s^2\phi$ according to Eq. (2.4.2), (e) normalized charge imbalance. Vertical dashed lines indicate the location of the MP entrance and the DS entrance. Horizontal dashed lines indicate Mach numbers $M = 1$ and $M = \sin\alpha = 0.5$.

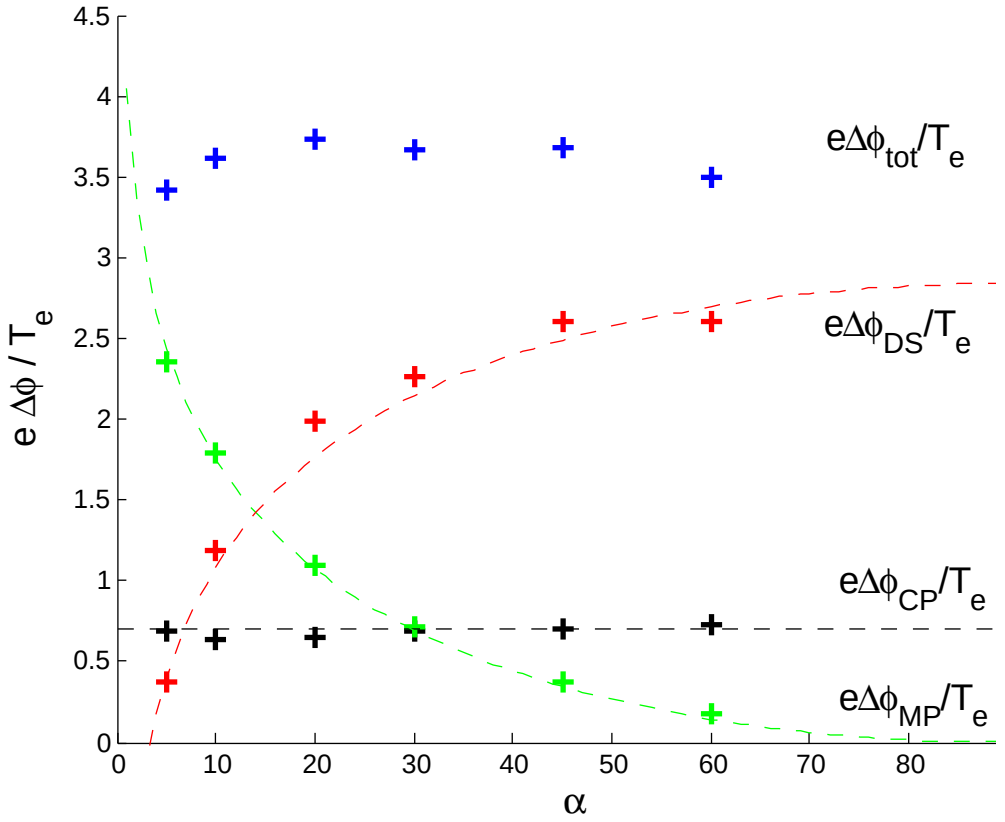

Figure 2.4.3: Potential drop in the CP (black crosses), MP (green crosses), DS (red crosses), for different values of α. Results are obtained from PIC simulations carried out with the ODISEE code. The total potential drop is also indicated (blue crosses). The horizontal black dashed line indicates the value $e\Delta\phi/T_e = 0.7$, while the green dashed line represents the function $e\Delta\phi/T_e = -\log(\sin\alpha)$ and the red dashed line is $e\Delta\phi/T_e = \Lambda + \log(\sin\alpha)$.

note that the small discrepancy observed in the $E_x = 0$ case with respect to Eq. (2.4.18), $v_{||i} = c_s$, is due to the contribution of the polarization drift (see Fig. 2.4.2d) which is not taken into account in the derivation of the boundary conditions. For the case $E_x \neq 0$, it is interesting to notice that, for sufficiently large $\mathbf{E} \times \mathbf{B}$ correction, one has $v_{||i} < 0$, thus indicating that particles are flowing, in the parallel direction, from the wall into the main plasma. As a matter of fact, the flow in the direction normal to the wall is given by the MP entrance condition, $v_{si} = c_s \sin\alpha$, which is independent of E_x. Since $v_{si} = v_{||i} \sin\alpha + v_{yi} \cos\alpha$, particles that are convected in the y direction at the $\mathbf{E} \times \mathbf{B}$ velocity must travel backwards, into the main plasma, along the magnetic field in order to ensure that $v_{si} = c_s \sin\alpha$, from which $v_{||i} < 0$.

The electron parallel velocity at the MP entrance is also shown in Fig. 2.4.4 as a function of α, showing good agreement with Eq. (2.4.27) in both the $E_x = 0$ and the $E_x \neq 0$ cases. In order to verify the dependence of the boundary condi-

tion for the parallel electron velocity on the potential barrier η_m, which in the limit $\theta_n = \theta_{T_e} = \theta_\phi = 0$ is $v_{||e} = c_s \exp(\Lambda - \eta_m)$, we explore the steady-state of the system in non-ambipolar conditions. A non-neutral particle source is considered, $S_{pi} \neq S_{pe}$, inducing a net current to the walls and therefore modifying the value of the potential at the MP entrance. Figure 2.4.5 shows the value of $v_{||e}$ at the MP entrance, as a function of the potential at this same position. The results are compared with the analytical prediction, showing a fairly good agreement. Moreover Fig. 2.4.5 shows that $v_{||i}$ at the MP entrance is independent of η_m.

Finally, we verify the expressions for the gradients of potential and density at the MP entrance, Eqs. (2.4.22) and (2.4.23), and for the vorticity, Eq. (2.4.25), by comparing those with the numerical values from the simulations. This is shown in Fig. 2.4.6. The agreement is very good for the potential gradient and for the vorticity, and reasonable for the density gradient. The difference between simulation results and the analytical expressions is mainly due to the effect of $S_{pi} \neq 0$ and $S_{pe} \neq 0$ in the MP.

2.4.4 Conclusion

We have provided a complete set of analytical boundary conditions at the MP entrance for plasma fluid turbulence codes based on the IDA. These are summarized below for convenience, for both sides of the field line:

$$v_{||i} = c_s \left(\pm 1 + \theta_n \mp \frac{1}{2}\theta_{T_e} - \frac{2\phi}{T_e}\theta_\phi \right) \tag{2.4.29}$$

$$v_{||e} = c_s \left(\pm \exp(\Lambda - \eta_m) - \frac{2\phi}{T_e}\theta_\phi + 2(\theta_n + \theta_{T_e}) \right) \tag{2.4.30}$$

$$\frac{\partial \phi}{\partial s} = -\left(\pm 1 + \theta_n \pm \frac{1}{2}\theta_{T_e} \right) c_s \frac{\partial v_{||i}}{\partial s} \tag{2.4.31}$$

$$\frac{\partial n}{\partial s} = -\left(\pm 1 + \theta_n \pm \frac{1}{2}\theta_{T_e} \right) \frac{n}{c_s} \frac{\partial v_{||i}}{\partial s} \tag{2.4.32}$$

$$\frac{\partial T_e}{\partial s} = 0 \tag{2.4.33}$$

$$\omega = -\cos^2\alpha \left[(1 + \theta_{T_e}) \left(\frac{\partial v_{||i}}{\partial s} \right)^2 + c_s \left(1 + \theta_n + \frac{1}{2}\theta_{T_e} \right) \frac{\partial^2 v_{||i}}{\partial s^2} \right] \tag{2.4.34}$$

where the upper signs apply if the magnetic field is directed towards the wall, and the lower signs apply in the opposite case. We now make a few comments on the newly derived boundary conditions.

For the parallel ion and electron velocities, Eqs. (2.4.29) and (2.4.30), the corrections due to $\mathbf{E} \times \mathbf{B}$ and diamagnetic drifts might have a significant impact. In fact,

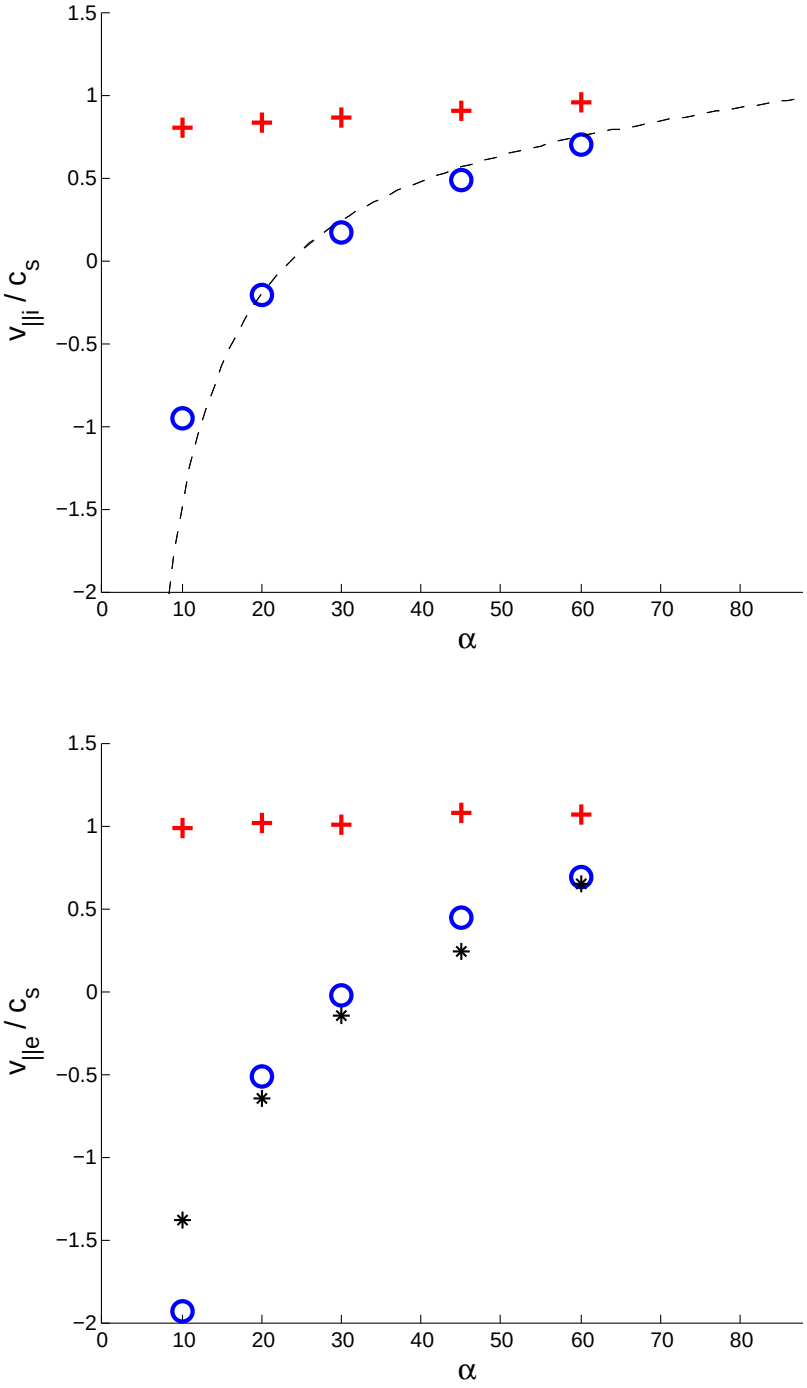

Figure 2.4.4: Ion (top) and electron (bottom) parallel velocities at the MP entrance as a function of α, for $E_x = 0$ (red crosses) and $E_x/B = -0.2c_s$ (blue circles). Results are obtained from PIC simulations performed with ODISEE. Dashed line on the top panel is the function $f(\alpha) = 1 - 0.2/\tan\alpha$, which denotes the expected value from the proposed set of boundary conditions. Black stars on the bottom panel denote $g(\alpha) = \exp(\Lambda - \eta_m) - 0.2/\tan\alpha$, the expected value, being η_m the potential barrier at the MP entrance observed in the simulations for each value of α.

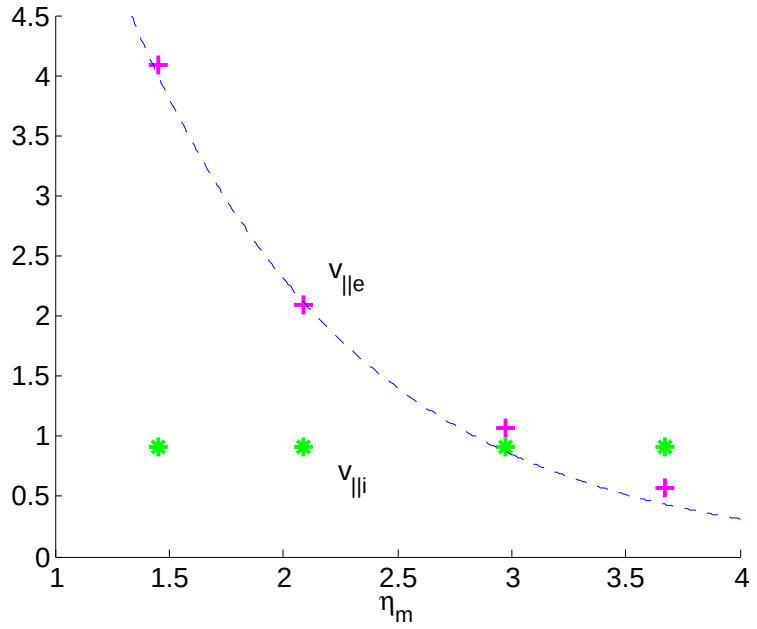

Figure 2.4.5: Ion (green stars) and electron (magenta crosses) parallel velocities at the MP entrance as a function of η_m, for $\alpha = 45°$. Results are obtained from PIC simulations carried out with the ODISEE code. The dashed curve represents the function $\exp(\Lambda - \eta_m)$.

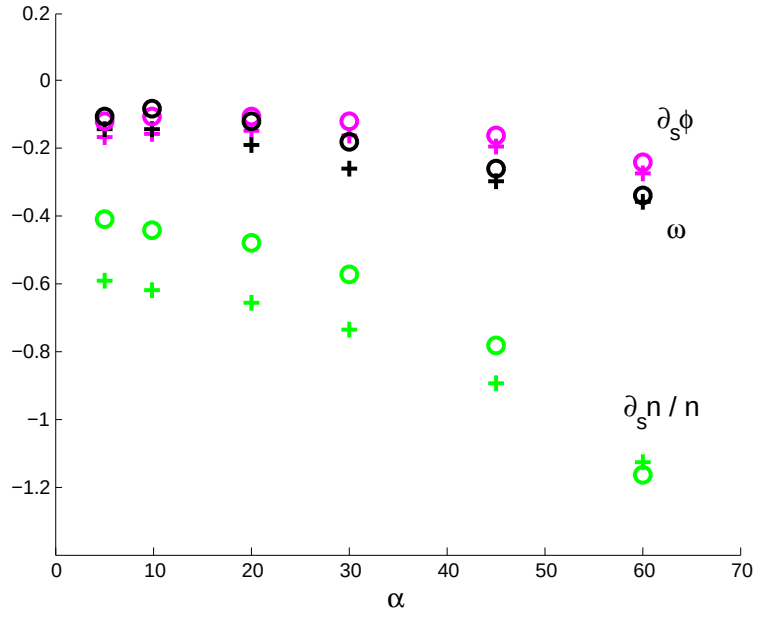

Figure 2.4.6: Comparison between ODISEE simulations results (crosses) and the boundary conditions (circles), expressed in Eqs. (2.4.22), (2.4.23), and (2.4.25), for the potential gradient $\partial_s\phi$ (magenta), the density gradient $\partial_s n/n$ (green), and the vorticity ω (black), at the MP entrance.

in the presence of strong radial gradients, the parallel velocities may display an inflowing character, as already discussed in Sec. 2.4.2 and observed in Fig. 2.4.4. To our knowledge, while this effect has already been suggested in the literature [16], these corrections to the parallel velocities have never been implemented in plasma turbulence codes. The potential gradient in Eq. (2.4.31), $\partial_s \phi$, is proportional to $\partial_s v_{\|i}$. Since ions are accelerated towards the wall, we typically have $\partial_s v_{\|i} > 0$, and therefore $\partial_s \phi < 0$, which is consistent with the potential drop expected in the vicinity of the wall. Similarly for the density gradient, Eq. (2.4.32): we expect $\partial_s n < 0$, consistent with the conservation of ion particle flux. The vorticity, Eq. (2.4.34), is also expected to be negative, $\omega < 0$, setting the direction of rotation of the $\mathbf{E} \times \mathbf{B}$ flow at the edge. This is consistent with the fact that the sheath electric field, which induces an $\mathbf{E} \times \mathbf{B}$ flow parallel to the wall, increases when approaching the MP entrance.

We remark that in the limit of $\alpha \to \pi/2$, namely when the magnetic field is perpendicular to the wall, the MP disappears and the plasma-wall transition region is reduced to the presence of the DS. In this limit, $\theta_n, \theta_T, \theta_\phi \to 0$, and the boundary conditions for $v_{\|i}$ and $v_{\|e}$ reduce to the Bohm boundary conditions at the DS entrance.

With the set of boundary conditions at the MP entrance presented here, it becomes possible to describe the plasma dynamics in an open magnetic field line geometry with a model based on the IDA, still taking into account properly the sheath physics.

2.5 Summary and outlook

In this chapter, we have investigated a certain number of basic aspects of the plasma-wall transition region. First, we have described the ODISEE code, a numerical tool that has been developed to gain insights on the physics of the plasma-wall transition and to guide the derivation of analytical models describing this region. Second, we have presented simulations of unmagnetized plasma sheaths, showing both numerically and analytically that the ion flow at the sheath entrance becomes arbitrarily small in the presence of electron currents. Also the effect of wall biasing on the plasma potential has been investigated in a simple framework. An analytical model predicts an abrupt transition of the plasma potential when the ratio of ion to electron wall currents exceeds a certain treshold. This transition is observed both in simulations and experimentally. Finally, we have presented a study of magnetized plasma sheaths. Leveraging our experience on the unmagnetized sheath, we have developed a simple mathematical framework from which one can derive a complete set of boundary conditions at the entrance of the magnetic presheath, where the ion drift approximation breaks down. Simulations of the magnetized plasma-wall transition support the analytical results.

These boundary conditions can be used in drift-reduced fluid models for the simulation of plasma turbulence in open field lines. The implementation of these boundary conditions on the GBS code is the subject of Chapter 3.

Chapter 3

Simulations of open field line plasma turbulence

3.1 Introduction

A common feature of open field line plasmas is a relatively low temperature which makes the plasma rather collisional. This is due the fact that the plasma is not confined but instead particles are continuously lost along the field lines. The relatively large collision rate allows local thermodynamic equilibrium to be attained relatively quickly. Therefore a few moments of the particle distribution functions can be reasonably used to model the plasma dynamics. This justifies the use of fluid models to describe open field line plasma turbulence.

The lowest three moments of the particle distribution functions $f_\alpha(\mathbf{x}, \mathbf{v}, t)$, where $\alpha = \{i, e\}$, can be identified with the particle density, the mean velocity and the temperature,

$$n_\alpha(\mathbf{x}, t) = \int f_\alpha(\mathbf{x}, \mathbf{v}, t) \mathbf{dv} \ , \tag{3.1.1}$$

$$\mathbf{V}_\alpha(\mathbf{x}, t) = \frac{1}{n_\alpha} \int \mathbf{v} f_\alpha(\mathbf{x}, \mathbf{v}, t) \mathbf{dv} \ , \tag{3.1.2}$$

$$T_\alpha(\mathbf{x}, t) = \frac{1}{n_\alpha} \int \frac{m_{i,j}}{3} \left(\mathbf{v} - \mathbf{V}_\alpha\right)^2 f_\alpha(\mathbf{x}, \mathbf{v}, t) \mathbf{dv} \ . \tag{3.1.3}$$

The spatio-temporal evolution of these quantities is described by a set of fluid equations derived by taking successive moments of the Boltzmann equation,

$$\frac{\partial f_\alpha}{\partial t} + \mathbf{v} \cdot \frac{\partial f_\alpha}{\partial \mathbf{x}} + \frac{\mathbf{F}_\alpha}{m_\alpha} \cdot \frac{\partial f_\alpha}{\partial \mathbf{v}} = \left(\frac{\partial f_\alpha}{\partial t}\right)_{coll} \ , \tag{3.1.4}$$

where $\mathbf{F}_\alpha = q_\alpha(\mathbf{E} + \mathbf{v} \times \mathbf{B})$ is the Lorentz force given by the large scale electric and magnetic fields, and the term on the right hand side accounts for the scattering due to binary Coulomb collisions. The fluid equations obtained from moments of Eq. 3.1.4 are coupled and the time evolution of each moment depends on one higher order moment, leading to an infinite hierarchy of moments. This is generally refered to as the closure problem.

A closed set of two-fluid equations describing plasma turbulence in strongly collisional, strongly magnetized plasmas was summarized by Braginskii in 1965 [23]. Later, a number of reduced models more suited for computational treatment were deduced [24], in some cases taking into account ion gyro-motion effects or kinetic effects neglected in the original Braginskii equations [25, 26, 27]. A number of codes have been recently developed based on this reduced model [28, 29, 30, 31, 32, 33, 34]. Numerical simulations using these codes have been carried out over the last years, shedding light on the origin and nature of plasma turbulence in open magnetic field line configurations. In particular, the GBS code has been developed at CRPP and is used to perform global, three-dimensional simulations of plasma turbulence in open field line configurations [34]. Reaching predictive capabilities remains, however, an outstanding challenge that involves a proper treatment of the plasma-wall interactions at the end of the field lines.

In this chapter, we first present the Braginskii equations and then we derive their drift-reduced limit. We then present the GBS code, which is based on the drift-reduced Braginskii equations. The implementation in GBS of the boundary conditions derived in Chapter 2 is described and, as an example, we present results from simulations of tokamak SOL turbulence in a limited configuration. We discuss the equilibrium profiles and the parallel currents present at the interface between the plasma and the limiter, and we briefly describe the main features of plasma turbulence. Finally, we show two examples of turbulence simulations in a simple magnetized toroidal geometry: the first aiming to describe TORPEX plasmas, the second focused on the simulation of three-dimensional seeded blobs.

3.2 Braginskii equations

It is a general result of statistical mechanics that the particles of any gas in thermal equilibrium are characterized by a Maxwellian velocity distribution,

$$f_0(\mathbf{v}) = n \left(\frac{m}{2\pi T}\right)^{3/2} \exp\left(-\frac{m(\mathbf{v}-\mathbf{V})^2}{2T}\right) . \tag{3.2.1}$$

Moreover, if the distribution function evolves only by virtue of collisions, then no matter what the initial conditions are the distribution function will approach a

Maxwellian in a time of the order of the collision time.

In a strongly collisional plasma, the characteristic time τ for energy exchange under collisions between like particles is smaller than the characteristic time T for the variation of the macroscopic quantities,

$$\tau_\alpha \ll T \quad . \tag{3.2.2}$$

Here τ_i and τ_e are respectively the ion and electron collision times, defined as

$$\tau_i = \frac{3\sqrt{m_i}T_i^{3/2}}{4\sqrt{2\pi}\lambda Z^4 e^4 n_i} \quad , \qquad \tau_e = \frac{3\sqrt{m_e}T_e^{3/2}}{4\sqrt{2\pi}\lambda Z^2 e^4 n_i} \quad , \tag{3.2.3}$$

and represent the characteristic times for isotropization and thermalization within a given species population. Also, in a collisional plasma, the macroscopic quantities do not change significantly over distances comparable to that traversed by the particles between collisions. For a strongly magnetized plasma, $\omega_{c\alpha}\tau_\alpha \gg 1$, this condition is

$$L_{||} \gg \lambda^\alpha_{mfp} \ , \qquad L_\perp \gg \rho_\alpha \ , \tag{3.2.4}$$

where $L_{||}$ and $L_\perp$ are the typical plasma scale lengths parallel and perpendicular to the magnetic field, $\lambda^\alpha_{mfp} = v_{thi,e}\tau_\alpha$ is the mean free path for momentum exchange and $\rho_\alpha = v_{th\alpha}/\omega_{c\alpha}$ is the Larmor radius. In fact, the motion of particles across the magnetic field is bound by the Larmor radius, which is smaller than the mean free path by a factor $\omega_{c\alpha}\tau_\alpha \gg 1$. Therefore in a strongly collisional, strongly magnetized plasma satisfying (3.2.2) and (3.2.4), the local distribution of each species is always very close to a Maxwellian.

As the solution of the Boltzmann equation for a given species approximates a Maxwellian in a strongly collisional plasma, we can write

$$f(\mathbf{x}, \mathbf{v}, t) = f_0(\mathbf{x}, \mathbf{v}, t) + f_1(\mathbf{x}, \mathbf{v}, t) \tag{3.2.5}$$

where

$$f_0(\mathbf{x}, \mathbf{v}, t) = n(\mathbf{x}, t)\left(\frac{m}{2\pi T(\mathbf{x}, t)}\right)^{3/2} \exp\left(-\frac{m(\mathbf{v} - \mathbf{V}(\mathbf{x}, t))^2}{2T(\mathbf{x}, t)}\right) \tag{3.2.6}$$

and $|f_1|/f_0 \ll 1$ is treated as a small perturbation on the zeroth-order distribution function f_0. The idea behind the Braginskii closure is to plug the expression (3.2.5) into the Boltzmann equation (3.1.4), and then find an expression for f_1 as a function

of the Maxwellian parameters n, $\mathbf{V}$ and T, and their spatio-temporal derivatives. Then the temporal derivatives can be expressed in terms of the spatial derivatives by using the not-yet-closed fluid equations, e.g. $\partial_t n = -\nabla \cdot (n\mathbf{V})$. Finally, the gradients of f_1 are neglected and the Coulomb collision operator is linearized in f_1. This procedure leads to a linear integro-differential equation for the function f_1 in velocity space (see, e.g., Ref. [99]). Solving this equation provides an expression for $f_1(\mathbf{v})$ that is linear in the factors that disturb the Maxwellian distribution function, e.g. ∇T, $\partial V_j/\partial x_k$, etc. The fluid equations can then be closed by substituting f_1 in the expression for the higher order fluid moments, namely the heat flux, the momentum flux, etc. The resulting closed set of fluid equations was summarized by Braginskii in 1965 and is given by

$$\frac{\partial n_\alpha}{\partial t} + \boldsymbol{\nabla} \cdot (n_\alpha \mathbf{V}_\alpha) = 0 \tag{3.2.7}$$

$$m_\alpha n_\alpha \frac{d_\alpha \mathbf{V}_\alpha}{dt} = -\boldsymbol{\nabla} p_\alpha - \boldsymbol{\nabla} \cdot \underline{\underline{\pi_\alpha}} + e_\alpha n_\alpha \left(\mathbf{E} + \mathbf{V}_\alpha \times \mathbf{B}\right) + \mathbf{R_\alpha} \tag{3.2.8}$$

$$\frac{3}{2} n_\alpha \frac{d_\alpha T_\alpha}{dt} = -p_\alpha \boldsymbol{\nabla} \cdot \mathbf{V}_\alpha - \boldsymbol{\nabla} \cdot \mathbf{q}_\alpha + Q_\alpha^{visc} + Q_\alpha \tag{3.2.9}$$

where $p_\alpha = n_\alpha T_\alpha$ is the scalar pressure and $\underline{\underline{\pi_\alpha}}$ is the stress tensor. The complete pressure tensor for a given species is then $\Pi_{jk} = p\delta_{jk} + \pi_{jk}$. Also, $\frac{d_\alpha}{dt} = \frac{\partial}{\partial t} + \mathbf{V}_\alpha \cdot \boldsymbol{\nabla}$ is the Lagrangian derivative, and $e_i = +Ze$ and $e_e = -e$ are the electric charges. The density equation is a standard continuity equation without sources. The equation for $\mathbf{V}_\alpha$ is a Newton equation and results into a balance between inertia, the pressure gradient force, the stress tensor force, the electromagnetic Lorentz force and the collisional friction force $\mathbf{R}$, such that $\mathbf{R} = \mathbf{R}_e = -\mathbf{R}_i$. The equation for T_α is a heat equation and includes the heat flux divergence $\boldsymbol{\nabla} \cdot \mathbf{q}_\alpha$, the viscous heat losses Q_α^{visc} and the collisional heat exchange Q_α. The Braginskii equations are closed and thus provide analytical expressions for the terms related to disturbances from thermal equilibrium, namely $\mathbf{R}$, $\underline{\underline{\pi_e}}$, $\underline{\underline{\pi_i}}$, $\mathbf{q}_e$, $\mathbf{q}_i$, Q_e^{visc}, Q_i^{visc}, Q_e, and Q_i. We now give their expressions and discuss their meaning. A qualitative description of the origin of each term is presented in great detail in [23].

The friction force term is $\mathbf{R} = \mathbf{R}_u + \mathbf{R}_T$, with

$$\mathbf{R}_u = -\frac{m_e n_e}{\tau_e}(0.51\mathbf{u}_\parallel + \mathbf{u}_\perp) \equiv e n_e \left(\frac{\mathbf{j}_\parallel}{\sigma_\parallel} + \frac{\mathbf{j}_\perp}{\sigma_\perp}\right) \quad , \tag{3.2.10}$$

$$\mathbf{R}_T = -0.71 n_e \nabla_\parallel T_e \mathbf{b} - \frac{3}{2}\frac{n_e}{\omega_{ce}\tau_e}\mathbf{b} \times \boldsymbol{\nabla} T_e \quad , \tag{3.2.11}$$

where $\sigma_\parallel = 1.96\sigma_\perp$ and $\sigma_\perp = e^2 n_e \tau_e / m_e$ are the parallel and perpendicular conductivities, $\mathbf{b} = \mathbf{B}/B$ is the unitary magnetic field vector, and $\mathbf{j}_\parallel = e n_e (V_{\parallel i} - V_{\parallel e})\mathbf{b}$ and $\mathbf{j}_\perp = e n_e (\mathbf{V}_{\perp i} - \mathbf{V}_{\perp e})$ are the parallel and perpendicular current densities. $\mathbf{R}_u$ is

the friction force due to the existence of a relative velocity $\mathbf{u} = \mathbf{V}_e - \mathbf{V}_i$ and $\mathbf{R}_T$ is the friction force due to an electron temperature gradient. The first term in $\mathbf{R}_T$ arises as a consequence of electrons losing momentum on ions through collisions, even though it does not contain τ_e explicitly. The second term in $\mathbf{R}_T$ is due to finite electron Larmor motion.

The electron heat flux is defined in a similar way, $\mathbf{q}_e = \mathbf{q}_{eu} + \mathbf{q}_{eT}$, with

$$\mathbf{q}_{eu} = 0.71 n_e T_e \mathbf{u}_\parallel + \frac{3}{2}\frac{n_e T_e}{\omega_{ce}\tau_e}\mathbf{b}\times\mathbf{u} \quad , \tag{3.2.12}$$

$$\mathbf{q}_{eT} = -\chi_{\parallel e}\nabla_\parallel T_e \mathbf{b} - \chi_{\perp e}\boldsymbol{\nabla}_\perp T_e - \frac{5}{2}\frac{n_e T_e}{eB}\mathbf{b}\times\boldsymbol{\nabla} T_e \quad , \tag{3.2.13}$$

where $\chi_{\parallel e} = 3.16 n_e T_e \tau_e / m_e$ and $\chi_{\perp e} = 4.66 n_e T_e / m_e \omega_e^2 \tau_e$ are the parallel and perpendicular electron heat diffusivities. The meaning of each of these terms is nontrivial but they all arise from electron-electron or electron-ion collisions. In particular, the first term in $\mathbf{q}_{eu}$ can be related to the Onsager symmetry with respect to $\mathbf{R}_T$ [23].

For the ion species, $\mathbf{q}_{iu}$ can be neglected since the characteristic time for ions losing momentum on electrons is very large, therefore $\mathbf{q}_i = \mathbf{q}_{iT}$, with

$$\mathbf{q}_{iT} = -\chi_{\parallel i}\nabla_\parallel T_i \mathbf{b} - \chi_{\perp i}\boldsymbol{\nabla}_\perp T_i + \frac{5}{2}\frac{n_i T_i}{Z_i eB}\mathbf{b}\times\boldsymbol{\nabla} T_i \quad . \tag{3.2.14}$$

For a strongly magnetized plasma, the components of the stress tensor π_{jk} for a given species have the following form (with the z axis parallel to the magnetic field):

$$\pi_{zz} = -\eta_0 W_{zz} \tag{3.2.15}$$

$$\pi_{xx} = -\eta_0 \frac{1}{2}(W_{xx} + W_{yy}) - \eta_1 \frac{1}{2}(W_{xx} - W_{yy}) - \eta_3 W_{xy} \tag{3.2.16}$$

$$\pi_{yy} = -\eta_0 \frac{1}{2}(W_{xx} + W_{yy}) - \eta_1 \frac{1}{2}(W_{yy} - W_{xx}) + \eta_3 W_{xy} \tag{3.2.17}$$

$$\pi_{xy} = \pi_{yx} = -\eta_1 W_{xy} + \eta_3 \frac{1}{2}(W_{xx} - W_{yy}) \tag{3.2.18}$$

$$\pi_{xz} = \pi_{zx} = -\eta_2 W_{xz} - \eta_4 W_{yz} \tag{3.2.19}$$

$$\pi_{yz} = \pi_{zy} = -\eta_2 W_{yz} + \eta_4 W_{xz} \tag{3.2.20}$$

where W_{jk} is the so-called rate-of-strain tensor and is given by

$$W_{jk} = \frac{\partial V_j}{\partial x_k} + \frac{\partial V_k}{\partial x_j} - \frac{2}{3}\delta_{jk}\boldsymbol{\nabla}\cdot\mathbf{V} \tag{3.2.21}$$

and the viscosity coefficients η are different for ions and electrons. For electrons,

$$\eta_{0e} = 0.73 n_e T_e \tau_e \ , \tag{3.2.22}$$

$$\eta_{1e} = 0.51 \frac{n_e T_e}{\omega_{ce}^2 \tau_e} \ , \quad \eta_{2e} = 4\eta_{1e} \ , \tag{3.2.23}$$

$$\eta_{3e} = -\frac{1}{2} \frac{n_e T_e}{\omega_{ce}} \ , \quad \eta_{4e} = 2\eta_{3e} \ , \tag{3.2.24}$$

while for ions,

$$\eta_{0i} = 0.96 n_i T_i \tau_i \ , \tag{3.2.25}$$

$$\eta_{1i} = \frac{3}{10} \frac{n_i T_i}{\omega_{ci}^2 \tau_i} \ , \quad \eta_{2i} = 4\eta_{1i} \ , \tag{3.2.26}$$

$$\eta_{3i} = \frac{1}{2} \frac{n_i T_i}{\omega_{ci}} \ , \quad \eta_{4i} = 2\eta_{3i} \ . \tag{3.2.27}$$

The heat Q_i, acquired by ions through collisions with electrons, is given by

$$Q_i = 3 \frac{m_e}{m_i} \frac{n_e}{\tau_e} (T_e - T_i) \ , \tag{3.2.28}$$

and it is responsible for the equilibration of the ion and electron temperatures. The heat Q_e lost by the electrons through collisions with the ions is

$$Q_e = -\mathbf{R} \cdot \mathbf{u} - Q_i = \frac{j_\parallel^2}{\sigma_\parallel} + \frac{j_\perp^2}{\sigma_\perp} + \frac{1}{e n_e} \mathbf{j} \cdot \mathbf{R}_T - 3 \frac{m_e}{m_i} \frac{n_e}{\tau_e} (T_e - T_i) \tag{3.2.29}$$

where the heat loss due to the work of the friction force $\mathbf{R}$ is the dominant term.

The viscous heat losses Q^{vis} for a given species is given by

$$Q^{vis} \equiv -\underline{\underline{\pi}} : \underline{\underline{\boldsymbol{\nabla} \mathbf{V}}} = -\pi_{jk} \frac{\partial V_j}{\partial x_k} = -\frac{1}{2} \pi_{jk} W_{jk} \tag{3.2.30}$$

where $\underline{\underline{A}} : \underline{\underline{B}}$ is the Frobenius inner product between two tensors.

Equations (3.2.7)-(3.2.9), together with the expressions for $\mathbf{R}$, $\underline{\underline{\pi_e}}$, $\underline{\underline{\pi_i}}$, $\mathbf{q}_e$, $\mathbf{q}_i$, Q_e^{visc}, Q_i^{visc}, Q_e, and Q_i, represent a closed set of two-fluid equations called the Braginskii equations. They describe the dynamics of a strongly collisional, strongly magnetized plasma and are derived entirely from first principles.

3.3 Drift-reduced Braginskii equations

The Braginskii equations, Eqs. (3.2.7)-(3.2.9), describe the plasma dynamics at time scales ranging from the electron Larmor scale, $\omega_{ce}^{-1} \sim 10^{-11}$ s, to the confinement time scale of order 1 s, with the turbulent fluctuations occurring at intermediate time scales. It is therefore of crucial importance for a suitable computational treatment to eliminate the fast time scales from the equations. In this section, we describe the drift-reduced Braginskii equations derived by Zeiler in 1997 [24]. We consider the electrostatic, cold ion limit, which yields the reduced model equations used in the framework of this thesis to perform tokamak SOL turbulence simulations.

We start by simplifying the terms in the Braginskii equations that are related to disturbances from thermal equilibrium, namely the friction force $\mathbf{R}$, the stress tensors $\underline{\underline{\pi_\alpha}}$, the heat fluxes $\mathbf{q}_\alpha$, and the collisional heating terms Q_α and Q_α^{visc}. First, since $T_i = 0$ in the cold ion limit, the ion temperature is not evolved and the ion pressure terms in the momentum equation vanish, i.e. $p_i = 0$ and $\underline{\underline{\pi_i}} = 0$. Second, we can assume $\omega_{ce}\tau_e \gg 1$ and neglect terms of order $(\omega_{ce}\tau_e)^{-1}$. The friction force then becomes

$$\mathbf{R} = \left(en_e\nu_\parallel j_\parallel - 0.71 n_e \nabla_\parallel T_e\right)\mathbf{b} \quad , \tag{3.3.1}$$

where $\nu_\parallel = 1/\sigma_\parallel$ is the parallel plasma resistivity. The resulting friction force has only a parallel component, since the perpendicular component is smaller than the Lorentz force by a factor $\omega_{ce}\tau_e$. Similarly, the electron heat flux becomes

$$\mathbf{q}_e = -\left(0.71 T_e j_\parallel/e + \chi_{\parallel e}\nabla_\parallel T_e\right)\mathbf{b} - \frac{5}{2}\frac{n_e T_e}{eB}\mathbf{b}\times\boldsymbol{\nabla} T_e \quad . \tag{3.3.2}$$

The viscosities η_1 and η_2 vanish in the limit of a strongly magnetized plasma, and the electron stress tensor $\underline{\underline{\pi_e}}$ can be written as

$$\underline{\underline{\pi_e}} = \underline{\underline{\pi_e}}^{visc} + \underline{\underline{\pi_e}}^{FLR} \quad , \tag{3.3.3}$$

where the viscous part contains the terms proportional to η_0 and the finite Larmor radius part contains the terms proportional to η_3. Finally, the heat acquired by the electrons through collisional processes, $Q_e^{visc} + Q_e$, is dominantly given by the term arising from the thermal force [24],

$$Q_e^{visc} + Q_e \simeq \frac{1}{en_e}\mathbf{j}\cdot\mathbf{R}_T = -0.71 j_\parallel \nabla_\parallel T_e/e \quad . \tag{3.3.4}$$

3.3.1 Drift-reduced approximation

We now proceed in removing the fastest time scales from the fluid equations by splitting the perpendicular dynamics into the fast gyro motion and the cross-field drifts. Since the gyro motion averages to zero only the drifts will persist in the final equations.

The idea of the drift-reduction is to solve the electron and ion momentum equations, Eq. (3.2.8), in the limit

$$\frac{d}{dt} \ll \omega_{ci} \quad , \tag{3.3.5}$$

which is based on the assumption that $\rho_s/L_\perp \ll 1$ and on the estimate

$$\frac{\partial}{\partial t} \sim \mathbf{V}\cdot\boldsymbol{\nabla} \sim \frac{V_E}{L_\perp} \sim \left(\frac{\rho_s}{L_\perp}\right)^2 \omega_{ci} \ll \omega_{ci} \ . \tag{3.3.6}$$

Here V_E is the equilibrium $\mathbf{E}\times\mathbf{B}$ drift with $E \sim \phi/L_\perp \sim T_e/(eL_\perp)$, and ρ_s is the ion sound larmor radius. An estimate of the convective term as given by the fluctuations of the $\mathbf{E}\times\mathbf{B}$ drift, $\tilde{V}_E$, is also compatible with Eq. (3.3.5) if one assumes $(k_\perp\rho_s)^2 \ll 1$, namely

$$\frac{\partial}{\partial t} \sim \mathbf{V}\cdot\boldsymbol{\nabla} \sim k_\perp \tilde{V}_E \sim (k_\perp\rho_s)^2\,\omega_{ci} \ll \omega_{ci} \ , \tag{3.3.7}$$

where $k_\perp$ is the perpendicular wavenumber of the fluctuations and we have assumed that $\tilde{\phi} \sim \phi$. Therefore in the ion momentum equation, Eq. (3.2.8), the ratio of the inertia term to the Lorentz force term is of the order of $\omega_{ci}^{-1}(d/dt) \ll 1$, and similarly for the electrons since $\omega_{ci} \ll \omega_{ce}$. This implies that we do not need to time evolve the momentum equations to evaluate the ion and electron perpendicular velocities. In fact, by crossing Eq. (3.2.8) with $\mathbf{B}/(en_\alpha B^2)$, we can express $\mathbf{V}_{\perp i}$ and $\mathbf{V}_{\perp e}$ as

$$\mathbf{V}_{\perp i} = \mathbf{V}_E + \mathbf{V}_{pol,i} \quad , \tag{3.3.8}$$

$$\mathbf{V}_{\perp e} = \mathbf{V}_E + \mathbf{V}_{de} + \mathbf{V}_{pol,e} + \mathbf{V}_{visc} + \mathbf{V}_{FLR} \quad , \tag{3.3.9}$$

where

$$\mathbf{V}_E = \frac{\mathbf{E}\times\mathbf{B}}{B^2} \quad , \tag{3.3.10}$$

$$\mathbf{V}_{de} = \frac{\boldsymbol{\nabla} p_e \times \mathbf{B}}{e n_e B^2} \quad , \tag{3.3.11}$$

$$\mathbf{V}_{pol,i} = \frac{\mathbf{b}}{\omega_{ci}} \times \frac{d}{dt}\mathbf{V}_{\perp i} \quad , \tag{3.3.12}$$

$$\mathbf{V}_{pol,e} = \frac{d}{dt}\mathbf{V}_{\perp e} \times \frac{\mathbf{b}}{\omega_{ce}} \quad , \tag{3.3.13}$$

$$\mathbf{V}_{visc} = \boldsymbol{\nabla}\cdot \underline{\underline{\pi_e}}^{visc} \times \frac{\mathbf{b}}{e n_e B} \quad , \tag{3.3.14}$$

$$\mathbf{V}_{FLR} = \boldsymbol{\nabla}\cdot \underline{\underline{\pi_e}}^{FLR} \times \frac{\mathbf{b}}{e n_e B} \quad . \tag{3.3.15}$$

The velocities given by Eqs. (3.3.12) and (3.3.13) are the so-called polarization drifts (or inertia drifts) and account for the effect of finite inertia. Within the drift-reduced assumption, Eq. (3.3.5), the polarization drifts are small compared to the $\mathbf{E}\times\mathbf{B}$ drift. Keeping only terms of order one in $\omega_{ci}^{-1}(d/dt)$, we can write

$$\mathbf{V}_{pol,i} = \frac{\mathbf{b}}{\omega_{ci}} \times \frac{d_{i0}}{dt}\mathbf{V}_E + O\left(\left[\omega_{ci}^{-1}(d/dt)\right]^2\right) \simeq \frac{\mathbf{b}}{\omega_{ci}} \times \frac{d_{i0}}{dt}\mathbf{V}_E \tag{3.3.16}$$

where

$$\frac{d_{i0}}{dt} = \frac{\partial}{\partial t} + \left(\mathbf{V}_E + V_{\|i}\mathbf{b}\right)\cdot\boldsymbol{\nabla} \tag{3.3.17}$$

is the Lagrangian derivative at the zeroth order in $\omega_{ci}^{-1}(d/dt)$. While the electron diamagnetic drift is comparable to the the $\mathbf{E}\times\mathbf{B}$ drift, $\mathbf{V}_{de}\sim\mathbf{V}_E$, we can neglect the electron polarization drift since $\mathbf{V}_{pol,e}/\mathbf{V}_{pol,i}\sim m_e/m_i$. The electron drifts that are due to the stress tensor force are also negligible. In fact, the dominant term in the divergence of $\underline{\underline{\pi_e}}^{FLR}$ is

$$\boldsymbol{\nabla}\cdot\underline{\underline{\pi_e}}^{FLR} \simeq -m_e n_e \left(\mathbf{V}_{de}\cdot\nabla\right)\mathbf{V}_e \ , \tag{3.3.18}$$

where the definition of the gyroviscosity $\eta_{3e} = -p_e/(2\omega_{ce})$ has been used. It is then easy to show that $\mathbf{V}_{FLR}/\mathbf{V}_{pol,i}\sim m_e/m_i$ by substituting Eq. (3.3.18) into Eq. (3.3.15). Similarly, using the dominant term in the divergence of $\underline{\underline{\pi_e}}^{visc}$, together with the definition of the viscosity $\eta_{0e} = 0.73 p_e\tau_e$, one can show from Eq. (3.3.14) that $\mathbf{V}_{visc}/\mathbf{V}_{pol,i}\sim\sqrt{m_e/m_i}(\lambda_{mfp}/L_{\|})(k_\perp\rho_s)^{-2}$, which is negligible for sufficiently large collisionality.

The drift-reduction procedure thus leads to

$$\mathbf{V}_{\perp i} = \mathbf{V}_E + \mathbf{V}_{pol,i} \quad , \tag{3.3.19}$$

$$\mathbf{V}_{\perp e} = \mathbf{V}_E + \mathbf{V}_{de} \quad , \tag{3.3.20}$$

where $\mathbf{V}_E$, $\mathbf{V}_{de}$ and $\mathbf{V}_{pol,i}$ are given by Eqs. (3.3.10), (3.3.11) and (3.3.16).

3.3.2 Quasi-neutrality

The Braginskii equations are further simplified by assuming quasi-neutrality. In fact, using Poisson's equation we see that the charge imbalance scales as

$$\frac{n_e - Z_i n_i}{n_e} = \frac{\epsilon_0 \nabla^2 \phi}{e n_e} \sim \left(\frac{\lambda_D}{L}\right)^2 \ll 1 \tag{3.3.21}$$

where $\lambda_D = \sqrt{\epsilon_0 T_e / e^2 n_e}$ is the Debye length, L is the typical scale length for the variation of the potential, and we have assumed $e\phi \sim T_e$. We can therefore assume

$$Z_i n_i \simeq n_e \equiv n \ . \tag{3.3.22}$$

3.3.3 Continuity and vorticity equations

Under both the drift-reduced and the quasi-neutrality approximations, the electron and ion continuity equations, Eq. (3.2.7), become

$$\frac{\partial n}{\partial t} + \boldsymbol{\nabla} \cdot \left[n(\mathbf{V}_E + \mathbf{V}_{de} + V_{\|e}\mathbf{b}) \right] = 0 \quad , \tag{3.3.23}$$

$$\frac{\partial n}{\partial t} + \boldsymbol{\nabla} \cdot \left[n(\mathbf{V}_E + \mathbf{V}_{pol,i} + V_{\|i}\mathbf{b}) \right] = 0 \quad . \tag{3.3.24}$$

As Eqs. (3.3.23) and (3.3.24) must yield the same time evolution of the plasma density n, by substracting the two equations we deduce the so-called vorticity equation,

$$\boldsymbol{\nabla} \cdot (en\mathbf{V}_{pol,i}) + \nabla_\| j_\| - \boldsymbol{\nabla} \cdot (en\mathbf{V}_{de}) = 0 \tag{3.3.25}$$

which is equivalent to a current continuity equation $\nabla \cdot \mathbf{j} = 0$. In fact, Eq. (3.3.25) is a balance between the divergence of the polarization current, the parallel current, and the electron diamagnetic current. We notice that $\nabla \cdot (j_\| \mathbf{b}) = \nabla_\| j_\|$ has been assumed, which corresponds to assuming $\nabla \cdot \mathbf{b} = 0$ or $\nabla_\| B = 0$. In a tokamak, this corresponds to neglecting finite aspect ratio effects. We now rewrite Eq. (3.3.25) by using the definition of the ion polarization drift, Eq. (3.3.16). This gives

$$\boldsymbol{\nabla} \cdot \left(\frac{en}{B\omega_{ci}} \frac{d_{i0}}{dt} \boldsymbol{\nabla}_\perp \phi \right) = \nabla_\| j_\| - \boldsymbol{\nabla} \cdot (en\mathbf{V}_{de}) \quad , \tag{3.3.26}$$

which describes the time evolution of the vorticity, $\omega = \boldsymbol{\nabla}_\perp^2 \phi$, a measure of the frequency of rotation of the plasma eddies in the plane perpendicular to the magnetic field. For the expression of the polarization current in Eq. (3.3.26), we have neglected variations of the magnetic field.

The electron continuity equation, Eq. (3.3.24), and the vorticity equation, Eq. (3.3.26), are part of the set of drift-reduced Braginskii equations.

3.3.4 Motion along the magnetic field

The parallel component of the electron momentum equation, Eqs. (3.2.8), is

$$m_e n \frac{d_e V_{\parallel e}}{dt} = -\nabla_\parallel p_e - \left(\boldsymbol{\nabla}\cdot\underline{\underline{\pi_e}}\right)_\parallel + en\nabla_\parallel\phi + R_\parallel \tag{3.3.27}$$

where

$$\left(\boldsymbol{\nabla}\cdot\underline{\underline{\pi_e}}^{visc}\right)_\parallel = \frac{2}{3}\nabla_\parallel G_e \ , \tag{3.3.28}$$

$$\left(\boldsymbol{\nabla}\cdot\underline{\underline{\pi_e}}^{FLR}\right)_\parallel = -m_e n\left(\mathbf{V}_{de}\cdot\nabla\right)\mathbf{V}_{\parallel e} \ , \tag{3.3.29}$$

and

$$G_e = -3\eta_{0e}\left(\nabla_\parallel V_{\parallel e} - \boldsymbol{\kappa}\cdot\mathbf{V}_e - \frac{1}{3}\nabla\cdot\mathbf{V}_e\right) \ . \tag{3.3.30}$$

Here $\boldsymbol{\kappa} = (\mathbf{b}\cdot\nabla)\mathbf{b}$ is the field line curvature. The FLR term, Eq. (3.3.29), leads to the so-called diamagnetic cancellation, namely the cancellation of the diamagnetic convection term in the Lagrangian derivative. Using the expression for the parallel component of the friction force $\mathbf{R}$,

$$R_\parallel = en_e\nu_\parallel j_\parallel - 0.71 n_e\nabla_\parallel T_e \ \ , \tag{3.3.31}$$

we can write Eq. (3.3.27) as

$$m_e n\frac{d_{e0}V_{\parallel e}}{dt} = -\nabla_\parallel p_e + en\nabla_\parallel\phi - 0.71 n_e\nabla_\parallel T_e + en_e\nu_\parallel j_\parallel - \frac{2}{3}\nabla_\parallel G_e \ . \tag{3.3.32}$$

where

$$\frac{d_{e0}}{dt} = \frac{\partial}{\partial t} + \left(\mathbf{V}_E + V_{\parallel e}\mathbf{b}\right)\cdot\boldsymbol{\nabla} \tag{3.3.33}$$

is the Lagrangian derivative without the diamagnetic drift. Eq. (3.3.32) is a generalized Ohm's law and belongs to the set of drift-reduced Braginskii equations.

The parallel component of the ion momentum equation, Eq. (3.2.8), is given by

$$m_i n\frac{d_i V_{\parallel i}}{dt} = -en\nabla_\parallel\phi - R_\parallel \ . \tag{3.3.34}$$

Adding up the ion and electron parallel momentum equations, Eq. (3.3.34) and (3.3.32), leads to

$$m_i n\frac{d_{i0}V_{\parallel i}}{dt} = -\nabla_\parallel p_e \ . \tag{3.3.35}$$

Here we have neglected the electron inertia, the electron viscosity and the ion polarization drift. Eq. (3.3.35) describes the time evolution of the parallel ion velocity and is part of the set of drift-reduced Braginskii equations.

3.3.5 Electron temperature equation

The time evolution of the electron temperature, Eq. (3.2.9), is

$$\frac{3}{2}n\frac{d_e T_e}{dt} = -p_e \boldsymbol{\nabla}\cdot\mathbf{V}_e - \boldsymbol{\nabla}\cdot\mathbf{q}_e + Q_e^{visc} + Q_e \ . \tag{3.3.36}$$

Using the simplified expressions for the electron heat flux, Eq. (3.3.2), and for the viscous and frictional electron heating, Eq. (3.3.4), we can write

$$\frac{3}{2}n\frac{d_e T_e}{dt} = -p_e \boldsymbol{\nabla}\cdot\mathbf{V}_e + 0.71\frac{T_e}{e}\nabla_\parallel j_\parallel + \chi_{\parallel e}\nabla_\parallel^2 T_e + \boldsymbol{\nabla}\cdot(\frac{5}{2}\frac{nT_e}{eB}\mathbf{b}\times\boldsymbol{\nabla}T_e) \tag{3.3.37}$$

where we have assumed $\chi_{\parallel e}$ to be constant.

3.3.6 Summary

The drift-reduced Braginskii equations are summarized below for convenience:

$$\frac{\partial n}{\partial t} = -\boldsymbol{\nabla}\cdot\left[n(\mathbf{V}_E + \mathbf{V}_{de} + V_{\parallel e}\mathbf{b})\right] \ , \tag{3.3.38}$$

$$\boldsymbol{\nabla}\cdot\left(\frac{en}{B\omega_{ci}}\frac{d_{i0}}{dt}\boldsymbol{\nabla}_\perp\phi\right) = \nabla_\parallel j_\parallel - \boldsymbol{\nabla}\cdot(en\mathbf{V}_{de}) \ , \tag{3.3.39}$$

$$m_e n\frac{d_{e0}V_{\parallel e}}{dt} = -\nabla_\parallel p_e + en\nabla_\parallel\phi - 0.71 n_e\nabla_\parallel T_e + en_e\nu_\parallel j_\parallel - \frac{2}{3}\nabla_\parallel G_e \ , \tag{3.3.40}$$

$$m_i n\frac{d_{i0}V_{\parallel i}}{dt} = -\nabla_\parallel p_e \ , \tag{3.3.41}$$

$$\frac{3}{2}n_e\frac{d_e T_e}{dt} = -p_e\boldsymbol{\nabla}\cdot\mathbf{V}_e + 0.71\frac{T_e}{e}\nabla_\parallel j_\parallel + \chi_{\parallel e}\nabla_\parallel^2 T_e + \boldsymbol{\nabla}\cdot(\frac{5}{2}\frac{nT_e}{eB}\mathbf{b}\times\boldsymbol{\nabla}T_e) \tag{3.3.42}$$

which form a self-consistent set of two-fluid equations, evolving the plasma density n, the electrostatic potential ϕ, the parallel electron velocity $V_{\parallel e}$, the parallel ion velocity $V_{\parallel i}$, and the electron temperature T_e.

3.4 The GBS code

In this section, we present the GBS code, which is based on the drift-reduced Braginskii equations, Eqs. (3.3.38)-(3.3.42). After a brief summary of the past developments and achievements of the GBS code, we describe the model equations and summarize their numerical implementation. In particular, we desribe the implementation of the magnetic presheath boundary conditions derived in Chapter 2.

3.4.1 Introduction

In the last few years, the Global Braginskii Solver code, GBS, has been developed with the goal of simulating plasma turbulence in the tokamak SOL by evolving the full profiles of the various quantities with no separation between "perturbations" and "equilibrium". These simulations can explore the self-consistent evolution and structure of the plasma profiles in the presence of (i) plasma density and heat input from the core of the fusion machine, (ii) cross-field transport produced by plasma instabilities (interchange instability or drift waves, for example), and (iii) parallel losses at the sheaths where the magnetic field lines terminate on the walls.

In order to progressively approach the complexity of tokamak edge simulations, the GBS code was initially developed and used to simulate turbulent dynamics in basic plasma physics devices of increasing complexity [100, 101, 102, 103, 104, 105, 106, 107, 75, 108]. Containing some of the main elements of SOL plasma dynamics, some of these devices offer a simple and well-diagnosed testbed to study the basic physics of plasma edge turbulence and the associated transport of heat and particles in a simplified setting. In particular, the initial GBS simulations were focused on linear devices, such as LAPD [19], and on the simple magnetized toroidal configuration (SMT), such as the TORPEX device [21], in which a vertical magnetic field B_v, superimposed on a toroidal field B_ϕ, creates helicoidal field lines with both ends terminating on the torus vessel.

The first version of the code was able to follow the two-dimensional plasma dynamics in the plane perpendicular to the magnetic field [100, 102, 103, 104, 107, 108], and was developed from ESEL [28], a code that implements the algorithm described in Ref. [109]. The two-dimensional code was used for the simulation of ideal interchange SMT turbulence, based on the fact that in this regime $k_\parallel = 0$. GBS was then extended to the third dimension, in order to describe the dynamics in the direction parallel to the magnetic field. Starting from flux-tube simulations [103], GBS reached the capability of performing global simulations of SMT and linear devices [105, 106, 107, 75], and was eventually updated to perform global simulations of the tokamak SOL [110]. We would like to remark that a fluid description of the SOL dynamics with a model based on the Braginskii equations may be limited to low-temperature regimes such as the L-mode. In fact, high-temperature events such as the Edge Localized Modes (ELMs) observed in H-mode plasmas [111], may require more sophisticated fluid closures [112].

Following the study on sheath physics presented in Chapter 2, we have implemented in GBS the complete set of boundary conditions supplying the sheath physics at the end of the field lines [55]. This has allowed a detailed study of the turbulent regimes present in the SOL [113, 114, 115] and a comparison with experimental results from a number of tokamaks [116]. Also, the effects of the sheath on the plasma turbulence

and flows have been investigated [117, 118]. In particular, the role of the limiter position in determining the SOL poloidal asymmetries has been elucidated [119]. Finally, a dedicated study of blob dynamics has been possible via three-dimensional simulations of seeded blobs in a simple magnetized configuration [120].

Within the GBS development, a validation project of the GBS data has been carried out [102, 107]. In general, validation of edge turbulence codes is challenging because of the difficult diagnostic access in tokamak plasmas and the complexity of the interpretation of the experimental measurements. Being applied to a well-diagnosed basic plasma physics experiment such as TORPEX, we have been able to compare the GBS results to experimental data in great detail. We have also established a rigorous framework to compare quantitatively simulations and experiments and unravel the missing mechanisms in the physical model.

3.4.2 Model equations

In the electrostatic limit, the GBS code evolves the drift-reduced Braginskii equations, Eqs. (3.3.38)-(3.3.42), where the vorticity equation is further simplified by using the Boussinesq approximation [121],

$$\boldsymbol{\nabla}\cdot\left(\frac{en}{B\omega_{ci}}\frac{d_{i0}}{dt}\boldsymbol{\nabla}_\perp\phi\right)\simeq\frac{en}{B\omega_{ci}}\frac{d_{i0}}{dt}\boldsymbol{\nabla}_\perp^2\phi \quad , \tag{3.4.1}$$

which is a common approximation in the fluid community that considerably simplifies the vorticity equation. Also, GBS is a flux-driven code, i.e. the equilibrium gradients are not imposed but result from the balance between density and temperature sources, S_n and S_T, included in the density and temperature equations, and the parallel and perpendicular transport of particles and heat. This allows to follow the self-consistent evolution of both the plasma profiles and their fluctuations.

In order to better capture the structure of the equations and the meaning of each term, we define the Poisson bracket $\{f,g\}$ and the curvature operator $C(f)$,

$$\{f,g\}\equiv\mathbf{b}\cdot(\boldsymbol{\nabla}f\times\boldsymbol{\nabla}g) \quad , \tag{3.4.2}$$

$$C(f)\equiv\frac{B}{2}\left(\boldsymbol{\nabla}\times\frac{\mathbf{b}}{B}\right)\cdot\boldsymbol{\nabla}f \quad . \tag{3.4.3}$$

With these definitions, the GBS model equations are:

$$\frac{\partial n}{\partial t} = -\frac{1}{B}\{\phi, n\} - \nabla_\parallel \left(nV_{\parallel e}\right) + \frac{2}{eB}\left[C(p_e) - enC(\phi)\right] + S_n \ , \tag{3.4.4}$$

$$\frac{en}{B\omega_{ci}}\frac{\partial \omega}{\partial t} = -\frac{en}{B\omega_{ci}}\{\phi, \omega\} - \frac{en}{B\omega_{ci}}V_{\parallel i}\nabla_\parallel \omega + \nabla_\parallel j_\parallel + \frac{2e}{B}C(p_e) \ , \tag{3.4.5}$$

$$\begin{aligned} m_e n\frac{\partial V_{\parallel e}}{\partial t} =& -m_e n\frac{1}{B}\{\phi, V_{\parallel e}\} - m_e n V_{\parallel e}\nabla_\parallel V_{\parallel e} - \nabla_\parallel p_e \\ &+ en\nabla_\parallel \phi - 0.71 n_e \nabla_\parallel T_e + en_e\nu_\parallel j_\parallel - \frac{4}{3}\eta_{0e}\nabla_\parallel^2 V_{\parallel e} \\ &- \frac{2\eta_{0e}}{3eB}\nabla_\parallel \left(5C(T_e) + 5\frac{T_e}{n}C(n) + eC(\phi)\right) \ , \end{aligned} \tag{3.4.6}$$

$$m_i n\frac{\partial V_{\parallel i}}{\partial t} = -m_i n\frac{1}{B}\{\phi, V_{\parallel i}\} - m_i n V_{\parallel i}\nabla_\parallel V_{\parallel i} - \nabla_\parallel p_e \ , \tag{3.4.7}$$

$$\begin{aligned} \frac{\partial T_e}{\partial t} =& -\frac{1}{B}\{\phi, T_e\} - V_{\parallel e}\nabla_\parallel T_e - \frac{2}{3}T_e\nabla_\parallel V_{\parallel e} \\ &+ 0.71\frac{2}{3}\frac{T_e}{en}\nabla_\parallel j_\parallel + \frac{2}{3n}\chi_{\parallel e}\nabla_\parallel^2 T_e \\ &+ \frac{4}{3}\frac{1}{eB}\left[\frac{7}{2}T_e C(T_e) + \frac{T_e^2}{n}C(n) - eT_e C(\phi)\right] + S_T \ , \end{aligned} \tag{3.4.8}$$

which are coupled to the Poisson equation $\boldsymbol{\nabla}_\perp^2\phi = \omega$. We remark that the Poisson brackets are all of the form $\{\phi, f\}$ and represent the convection of the quantity f with the $\mathbf{E}\times\mathbf{B}$ drift. The terms containing the curvature operator $C(f)$ arise from the divergence of the $\mathbf{E}\times\mathbf{B}$ and diamagnetic drifts, which is non-vanishing for finite magnetic field curvature.

Finally, GBS works with normalized quantities defined through a reference temperature T_{e0}, a reference density n_0, and a magnetic field B_0. In particular, the electron temperature and the electrostatic potential are normalized such that $T_e \to T_e/T_{e0}$ and $\phi \to e\phi/T_{e0}$, and analogously for the density, $n \to n/n_0$. The perpendicular coordinates are normalized with respect to $\rho_{s0} = c_{s0}/\Omega_{ci0}$, where $c_{s0} = \sqrt{T_{e0}/m_i}$ and $\Omega_{ci0} = eB_0/m_i$. In the parallel direction, the macroscopic length R is used (for SMT and tokamak simulations it corresponds to the major radius). Finally, time is normalized such that $t \to t/(R/c_{s0})$. The normalized system of equations evolved by GBS can be found in Ref. [34].

3.4.3 Geometry

The curvature operator, $C(f)$, the perpendicular Laplacian operator, $\nabla_\perp^2$, the parallel gradient, $\nabla_\parallel$, and the Poisson bracket, $\{f, g\}$, that appear in the model equations, have to be specified for each particular geometry; this is made easy by the GBS modular coding. We now provide the expressions for the operators in two

different geometries: the SMT geometry (Figure 3.4.1) and the tokamak SOL geometry (Figure 3.4.2). In both geometries, we consider a coordinate system where we denote the perpendicular coordinates with x and y, being x the radial coordinate, and y the coordinate perpendicular to both x and the magnetic field. We define z as the parallel coordinate and we use z_φ for the periodic toroidal direction, such that $0 < z_\varphi < 2\pi R$. We also remark that in both geometries the coordinate system is such that (y, x, z) is right-handed. Also, the magnetic field is dominantly along the toroidal direction, thus the magnetic field lines intersect the vessel walls at very shallow angles.

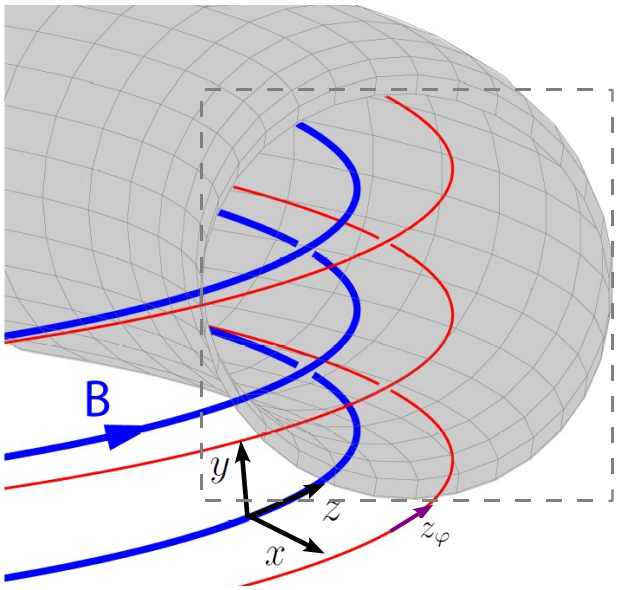

Figure 3.4.1: Sketch of the SMT geometry. The magnetic field has a dominant toroidal component and a small vertical component. The resulting helical field lines start at the bottom of the vessel and wind around the torus N times before intersecting the top of the vessel (here $N = 3$). The dashed square indicates the actual simulation boundary, which is toroidal symmetric.

In the SMT, the expressions for the operators are

$$C = \frac{1}{R}\frac{\partial}{\partial y} , \tag{3.4.9}$$

$$\{f, g\} = \frac{\partial f}{\partial y}\frac{\partial g}{\partial x} - \frac{\partial g}{\partial y}\frac{\partial f}{\partial x} , \tag{3.4.10}$$

$$\nabla_\perp^2 = \frac{\partial^2}{\partial x^2} + \frac{\partial^2}{\partial y^2} , \tag{3.4.11}$$

$$\nabla_\parallel = \frac{\partial}{\partial z} = \frac{\partial}{\partial z_\varphi} + \frac{L_v}{2\pi N R}\frac{\partial}{\partial y} , \tag{3.4.12}$$

where N is the number of field line turns in the SMT, R its major radius, and L_v is the height of the device. The quantity $\alpha = L_v/(2\pi N R)$ is the pitch angle of the magnetic field lines with respect to the toroidal direction. Since $\alpha \ll 1$, the y

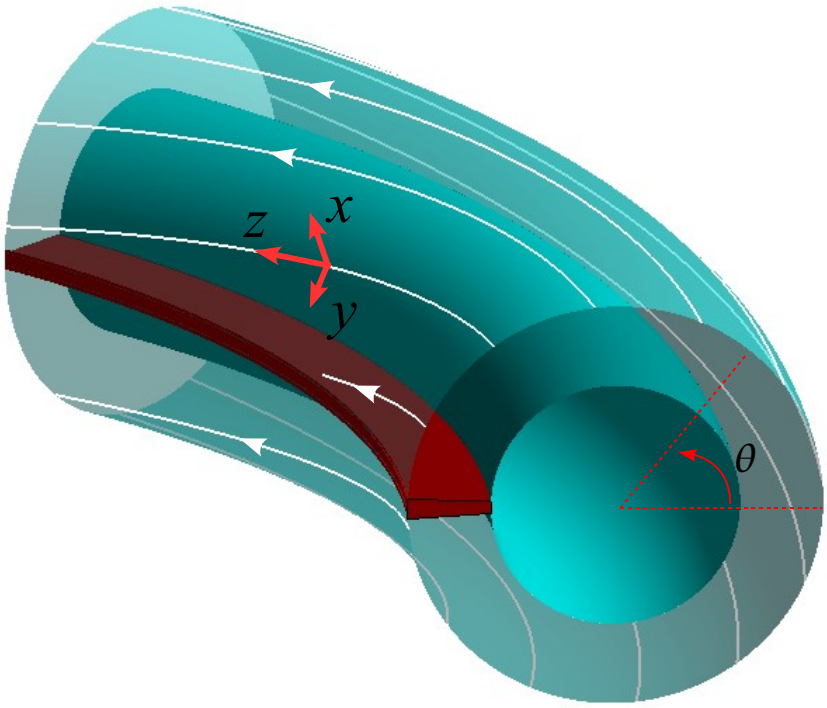

Figure 3.4.2: Sketch of the SOL geometry. The magnetic field has a dominant toroidal component and a small poloidal component. The resulting helical field lines start at the bottom side of the limiter and wind around the torus q times before intersecting the top of the limiter. Here $q = 1$ and $\theta_l = \pi$.

direction almost coincides with the vertical direction (Figure 3.4.1).

On the other hand, for tokamak SOL electrostatic turbulence, herein we consider configurations with circular magnetic flux surfaces, no magnetic shear, and a large aspect ratio (we remark that work is being done to remove these approximations [115]). A toroidal limiter at a given poloidal location θ_l defines the boundaries of the system along the poloidal direction (Figure 3.4.2). In this case we have

$$C = \frac{1}{R}\left(\sin\theta\frac{\partial}{\partial x} + \cos\theta\frac{\partial}{\partial y}\right) , \tag{3.4.13}$$

$$\{f, g\} = \frac{\partial f}{\partial y}\frac{\partial g}{\partial x} - \frac{\partial g}{\partial y}\frac{\partial f}{\partial x} , \tag{3.4.14}$$

$$\nabla_\perp^2 = \frac{\partial^2}{\partial x^2} + \frac{\partial^2}{\partial y^2} , \tag{3.4.15}$$

$$\nabla_\parallel = \frac{\partial}{\partial z} = \frac{\partial}{\partial z_\varphi} + \frac{a}{Rq}\frac{\partial}{\partial y} \tag{3.4.16}$$

where q is the safety factor, R is the tokamak major radius, a is the tokamak minor radius, and $\theta = \theta_l + y/a$ is the poloidal angle defined so that $\theta = 0$ at the low-field-side midplane and $y = 0$ and $y = 2\pi a$ at the two sides of the limiter. In this case, the pitch angle is $\alpha = \epsilon_a/q$ where $\epsilon_a = a/R$ is the tokamak inverse aspect ratio.

Since $\alpha \ll 1$, the (x, y) plane almost coincides with the poloidal plane (x, θ).

3.4.4 Boundary conditions

The GBS model equations, Eqs. (3.4.4)-(3.4.8), are solved in a domain that covers the full toroidal angle but is bound in the x and y directions. Therefore the set of fluid equations must be completed with a set of boundary conditions in the radial direction and at the end of the field lines. The latter are given by the magnetic presheath entrance condition [55] and have been derived in Chapter 2. We summarize them here for convenience,

$$V_{||i} = c_s \left[\pm 1 + \theta_n \mp \frac{1}{2}\theta_{T_e} - 2\frac{e\phi}{T_e}\theta_\phi \right] \tag{3.4.17}$$

$$V_{||e} = c_s \left[\pm \exp\left(\Lambda - e\phi/T_e\right) - 2\frac{e\phi}{T_e}\theta_\phi + 2(\theta_n + \theta_{T_e}) \right] \tag{3.4.18}$$

$$\frac{\partial \phi}{\partial y} = -\frac{m_i c_s}{e}\left[\pm 1 + \theta_n \pm \frac{1}{2}\theta_{T_e} \right] \frac{\partial V_{||i}}{\partial y} \tag{3.4.19}$$

$$\frac{\partial n}{\partial y} = -\frac{n}{c_s}\left[\pm 1 + \theta_n \pm \frac{1}{2}\theta_{T_e} \right] \frac{\partial V_{||i}}{\partial y} \tag{3.4.20}$$

$$\frac{\partial T_e}{\partial y} = e\kappa_T \frac{\partial \phi}{\partial y} \tag{3.4.21}$$

$$\nabla_\perp^2 \phi = -\frac{m_i}{e}\left[(1 + \theta_{T_e}) \left(\frac{\partial V_{||i}}{\partial y} \right)^2 + c_s \left(\pm 1 + \theta_n \pm \theta_{T_e}/2 \right) \frac{\partial^2 V_{||i}}{\partial y^2} \right] \tag{3.4.22}$$

where the upper signs apply if the magnetic field is directed towards the wall, the lower signs apply in the opposite case, and in the GBS geometry

$$\theta_f = -\frac{\rho_s}{2\tan\alpha}\frac{\partial_x f}{f} \ . \tag{3.4.23}$$

We remark that the electrostatic potential ϕ in Eq. (3.4.18) is measured with respect to the wall potential, which is assumed to be zero. Also, the temperature gradient is very small since $\kappa_T \approx 0.1$ (see Appendix B). The numerical implementation of these boundary conditions is given in Sec. 3.4.6.

In the radial direction, ad-hoc boundary conditions are implemented. In the SMT geometry, the radial boundaries correspond to the radially inner and outer parts of the toroidal vessel where the magnetic field is parallel to the wall surfaces. In this case, the plasma-wall transition is singular as particles can only reach the wall through collisions, drifts, or orbit losses [16]. However, the radial boundaries are not expected to affect much the plasma dynamics since most of the plasma is lost along the field lines at the top and bottom of the device. In the tokamak SOL geometry, on the inner side, the radial boundaries correspond to an artificial core-edge separation. The tokamak vessel wall corresponds to the outer side. Since most

of the plasma is lost at the limiter plates before it can reach the outer vessel wall through cross-field turbulent transport, the same argument presented for the SMT applies to the tokamak SOL, and therefore the boundary conditions at this wall do not affect turbulence much. At the core-edge separation, however, plasma comes from the core and thus one must be more careful when treating this boundary. In GBS the density and heat sources are radially localized to mimic the outflow from the core (see Fig. 3.4.3), and thus when analyzing the simulation results only the region lying radially outwards from the source is considered. The peak of the source thus acts as the effective separatrix, defining the SOL region, and the region lying radially inwards is akin to a buffer region.

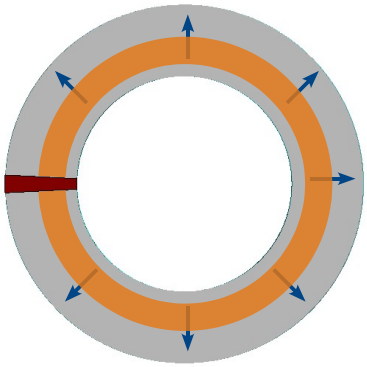

Figure 3.4.3: Sketch of the SOL source in a poloidal cross-section. The source (orange annulus) is toroidally and poloidally symmetric and is radially localized to mimic the outflow of plasma from the core. The region of interest to study SOL turbulence is that lying radially outwards from the source.

3.4.5 Initial conditions

When a new GBS simulation is started, each quantity A is initialized according to $A(t_0) = A_0 + \tilde{A}(x, y, z)$, where A_0 is a constant value, and $\tilde{A}(x, y, z)$ is a random field whose amplitude can be chosen. Sources inject plasma particles and heat, increasing the plasma gradients and triggering a number of instabilities. After a transient phase, a quasistationary state is reached in which the plasma, generated by the source and transported by turbulence, is eventually removed from the system by losses at the vessel walls. Our analysis is typically focused on this quasi-stationary phase.

3.4.6 Numerics

In GBS, a cartesian grid is used to discretize the domain in the radial, poloidal (or vertical in the SMT geometry), and toroidal directions, (x, θ, z_φ). We note that since $\alpha \ll 1$, the grid coordinate θ almost coincides with the model coordinate y, and we thus use the same labels. The domain is discretized with N_x, N_y, N_{z_φ} intervals, and

we define the grid point $x_i = (i-1/2)\Delta x$, for $i = 0, .., N_x + 1$, the width of intervals being $\Delta x = L_x/N_x$, and the points corresponding to $i = 0$ and $i = N_x + 1$ therefore representing the ghost cells. Analogous expressions are valid in the y and z_φ directions, with $\Delta y = L_y/N_y$ and $\Delta z_\varphi = 2\pi R/N_{z_\varphi}$. Regarding the toroidal direction, the grid is defined for the n, T_e, ϕ, and ω variables as $z_{\varphi k} = k\Delta z_\varphi$ while, for numerical reasons, it is shifted by half a cell for $V_{\parallel i}$ and $V_{\parallel e}$, i.e. $z_{\varphi k} = (k-1/2)\Delta z_\varphi$. Each physical quantity $A(x, y, z_\varphi)$ is written as $A_{ijk} \equiv A(x_i, y_j, z_{\varphi k})$.

The derivatives in the x, y directions are performed with a standard centered finite-difference scheme, e.g.

$$\left.\frac{\partial A}{\partial x}\right|_{i,j,k} \simeq \frac{A_{i+1,j,k} - A_{i-1,j,k}}{2\Delta x} \tag{3.4.24}$$

except for the Poisson bracket terms, which are discretized according to the Arakawa scheme [122]. The parallel gradient has to be approached with particular care. The discretization of the operator in Eqs. (3.4.12) and (3.4.16) has to take advantage of the fact that turbulence is mostly aligned with the field lines in order to reduce the computational cost of the simulations. For the SOL, we choose the number of grid points, N_y and N_{z_φ}, in such a way that $\Delta j = N_y/(qN_{z_\varphi})$ is an integer (an analogous expression is valid for the SMT). This means that for a field line the shift Δj of grid points along the y direction, in correspondence of a z_φ shift of one grid point, is an integer. The resolution along z_φ can then remain low and we can approximate the parallel derivative as

$$(\mathbf{b}\cdot\boldsymbol{\nabla})A|_{i,j,k} \simeq \frac{1}{2\Delta z_\varphi}\left(A_{i,j+\Delta j,k+1} - A_{i,j-\Delta j,k-1}\right) \ . \tag{3.4.25}$$

In doing this, care must be taken in considering that the parallel velocities are evaluated in correspondence of a different z_φ grid with respect to the density, temperature and potential.

The Laplacian operator in the Poisson equation is discretized using a standard second-order finite difference scheme. Depending on the geometry, the obtained matrix can be solved by direct matrix inversion or can be reduced to the solution of a set of tridiagonal systems, by applying the Fast Fourier Transform (FFT) algorithm in one direction. In order to time advance the fluid equations we use a standard fourth order Runge-Kutta scheme. For numerical stability reasons, small diffusive terms are introduced for all quantities. Finally, we note that the equations implemented in GBS are rewritten in terms of $\Theta_n = \log n$ and $t_e = \log T_e$, to ensure the positivity of n and T_e.

GBS is parallelized with a domain decomposition technique using MPI. The physical domain in the x direction is equally divided into N_{P_x} parts and the physical domain

in the z direction is equally divided into N_{P_z} parts; the total number of processes is therefore $N_P = N_{P_x} N_{P_z}$. In each process, in the x and z directions, one ghost cell must be added to both sides of the domain. For a more detailed description of the parallelization method and of the convergence properties of GBS, see Ref. [34].

We now describe the numerical implementation of the magnetic presheath boundary conditions, Eqs. (3.4.17)-(3.4.21). We start by considering the case where no radial corrections are applied to the boundary conditions, namely when the limit $\theta_f \to 0$ is taken. In this case, Eqs. (3.4.17)-(3.4.21) in normalized units reduce to

$$V_{||i} = \pm\sqrt{T_e} \tag{3.4.26}$$

$$V_{||e} = \pm\sqrt{T_e}\exp\left(\Lambda - \phi/T_e\right) \tag{3.4.27}$$

$$\frac{\partial\phi}{\partial y} = \mp\sqrt{T_e}\frac{\partial V_{||i}}{\partial y} \tag{3.4.28}$$

$$\frac{\partial\Theta_n}{\partial y} = \mp\frac{1}{\sqrt{T_e}}\frac{\partial V_{||i}}{\partial y} \tag{3.4.29}$$

$$\frac{\partial t_e}{\partial y} = \frac{\kappa_T}{T_e}\frac{\partial\phi}{\partial y} \tag{3.4.30}$$

$$\omega = -\Big[\left(\frac{\partial V_{||i}}{\partial y}\right)^2 \pm \sqrt{T_e}\frac{\partial^2 V_{||i}}{\partial y^2}\Big] \tag{3.4.31}$$

The expressions for $V_{\|i}$, $V_{\|e}$ and ω, are in the form of Dirichlet boundary conditions. We apply those at $j = 0$ and $j = N_j + 1$. As the $V_{\|i}$ and $V_{\|e}$ grid is shifted by half a cell with respect to the n, T_e, and ϕ grid, the boundary conditions are applied by interpolating the two nearest grid points in the toroidal direction. For example, for the ion parallel velocity at $y = 0$ we write

$$V_{\|i}\big|_{i,0,k} = -\frac{1}{2}\left(\sqrt{T_e|_{i,0,k}} + \sqrt{T_e|_{i,0,k+1}}\right) \ . \tag{3.4.32}$$

The expressions for n, ϕ and T_e, are in the form of Neumann boundary conditions. These are rewritten as Dirichlet boundary conditions by using a standard first-order finite difference between the last two grid points in the y direction. For example, for the electrostatic potential at $y = 0$, we write

$$\phi|_{i,0,k} = \phi|_{i,1,k} - \frac{1}{2}\sqrt{T_e|_{i,0,k}}\left(V_{\|i}\big|_{i,1,k} - V_{\|i}\big|_{i,0,k} + V_{\|i}\big|_{i,1,k+1} - V_{\|i}\big|_{i,0,k+1}\right) \tag{3.4.33}$$

where we still interpolate the two nearest grid points in the toroidal direction. We note that this implies that the Neumann boundary conditions are not exactly applied at the last grid point ($j = 0$ and $j = N_j + 1$) but half a cell away ($j = 1/2$ and

$j = N_j + 1/2$).

We now focus on the implementation of the θ_f terms as given by Eq.(3.4.23). Since $\theta_f \sim \partial_x f/f \sim 1/L_\perp$, these terms require the calculation of the equilibrium radial scale lengths of density, L_n, temperature, L_{T_e}, and potential, L_ϕ, at the plasma-wall interface. For this purpose, a spatial smoothing of each quantity is first carried out by suppressing oscillations having radial scale lengths shorter than $10\rho_{s0}$. More precisely, we evolve an artificial diffusion equation,

$$\frac{\partial f}{\partial t} = D\frac{\partial^2 f}{\partial x^2} \quad , \tag{3.4.34}$$

for a given amount of artificial time steps, with $f = n,\ T_e,\ \phi$ and using as initial conditions the profiles of $n,\ T_e,\ \phi$ resulting from the GBS simulation. In Fourier space, this corresponds to a damping of the high k_x modes $\hat{f}(k_x, t)$,

$$\frac{\partial \hat{f}}{\partial t} = -Dk_x^2 \hat{f} \quad , \tag{3.4.35}$$

and from this expression one finds that the number of iterations required to suppress oscillations with $k_x > k_{cut}$ is given by $N_{it} \approx 1/(k_{cut}\Delta x)^2$. Then, a standard second-order finite difference scheme is applied to the smoothed profile of f in order to extract the radial scale length and compute θ_f. Finally, for numerical reasons the value of θ_f is time-averaged over a time window of the order of 1 R/c_{s0}, which is the typical time scale of the turbulence. Tests were performed to verify that the results do not depend much on the value of the time window over which θ_f is averaged. We remark that values of order $\theta_f \sim 0.1$ are typically obtained. This implies that the ion parallel velocity, Eq. (3.4.17), may deviate substantially from the sound speed as $2(e\phi/T_e)\theta_\phi \sim 0.5$.

3.5 Turbulence simulations in SOL conditions

In this section, we present an example of global, three-dimensional, full-n, flux-driven simulations of plasma turbulence in open field lines carried out with the GBS code. We focus here on tokamak SOL simulations with circular magnetic flux surfaces, no magnetic shear, and a toroidal limiter located on the equatorial plane, at the high-field side.

We use the following model parameters: major radius $R = 500\rho_{s0}$, aspect ratio $a/R \approx 0.25$, radial extension $L_x = x_{max} - x_{min} = 100\rho_{s0}$, safety factor $q = 4$, mass ratio $m_i/m_e = 200$, sheath coefficient $\Lambda = 3$, parallel resistivity $\nu_\parallel = 0.1\nu_0$, where $\nu_0 = m_i c_{s0}/(e^2 nR)$ is the reference resistivity, and viscosity $\eta_{0e} = \eta_{00}$, where $\eta_{00} = n_0 T_{e0}(R/c_{s0})(m_e/m_i)$ is the reference viscosity. The angle between the magnetic field and the limiter is such that $\tan\alpha = a/qR \approx 0.0625$, corresponding to

$\alpha \approx 3.6°$. The particle and heat outflow from the core is modeled by density and temperature Gaussian sources that are radially-localized at $x = x_s = x_{min} + 30\rho_{s0}$ and have a width of $5\rho_{s0}$. We apply the MP boundary conditions at the limiter plates, i.e. at $y = 0$ and $y = 2\pi a = 800\rho_{s0}$, and we note that Neumann boundary conditions are imposed at x_{min} and x_{max} for all fields, except for ϕ, which is set to $\phi = \Lambda T_e$.

Figure 3.5.1 shows snapshots of the different fields in a poloidal cross-section of the torus. Here we note, from a qualitative point of view, that smooth profiles form at the limiters, suggesting that the set of boundary conditions for the plasma-wall transition is compatible with the GBS model equations. In fact, this is confirmed by Figure 3.5.2, which shows time-averaged poloidal profiles of n, ϕ and T_e, at different radial locations. We note that in the previous version of the code, Bohm boundary conditions were applied to the parallel velocities, while *ad hoc* boundary conditions were applied to the other fields. This was leading to the formation of non-physical boundary layers at the plasma-wall interface, thus hampering the interpretation of the simulation results.

The different turbulent regimes present in the SOL of limited tokamaks have been studied in detail with the GBS code, both linearly [123] and nonlinearly [114, 113]. Typically, turbulence is field aligned with $k_\parallel \ll k_\perp$, as shown in Fig. 3.5.3. For example, in the simulation results shown in this section, we have $k_y\rho_s \simeq 0.2$ and $k_\parallel \simeq 1/qR$, which gives $k_\parallel/k_y \sim 10^{-3}$. According to Ref. [114], the turbulent transport in this particular simulation is the result of two competing instabilities: the resistive ballooning mode and the resistive drift-wave.

Finally, we notice that according to the magnetic presheath boundary conditions, the plasma potential ϕ can fluctuate at the limiter and thus allows for finite parallel currents, as typically observed at the edge of basic plasma physics experiments [108] and at the limiters or divertors of tokamaks [124]. Figure 3.5.4 shows a snapshot of the parallel currents that form at both sides of the limiter.

3.6 Turbulence simulations in SMT conditions

In this section, we present two examples of turbulence simulations carried out with the GBS code in the SMT configuration: the first aiming to describe turbulence in the SMT configuration, the second focused on the simulation of three-dimensional seeded blobs.

In the SMT configuraion, see Fig. 3.4.1, a small vertical magnetic field B_v, superimposed on a toroidal field B_ϕ, creates helicoidal field lines that wind around N times in the toroidal direction, with both ends terminating on the torus vessel. Thanks to

the curvature of the open field lines, and the radial gradient of B, the SMT features the main elements of the SOL but in a simplified setting that facilitates experimental measurements and theoretical understanding. Our simulations aim at describing typical parameters of the TORPEX experiment.

For the first example, we use the following model parameters: major radius $R = 500\rho_{s0}$, minor radius $a = 100\rho_{s0}$ (which implies a radial and vertical extension of the poloidal cross-section $L_x = L_y = 200\rho_{s0}$), number of field line turns $N = 4$, mass ratio $m_i/m_e = 200$, sheath coefficient $\Lambda = 3$, parallel resistivity $\nu_\parallel = 0.1\nu_0$ and viscosity $\eta_{0e} = \eta_{00}$. The angle between the magnetic field and the limiter is such that $\tan\alpha = L_y/(2\pi RN) \approx 0.016$, corresponding to $\alpha \approx 1°$. The plasma production in TORPEX results from an Electron Cyclotron (EC) and an Upper Hybrid (UH) resonance, the latter being more efficient [21]. Therefore in order to mimic the plasma production in TORPEX, the density and temperature sources are chosen to have a Gaussian radial profile, centered at $x_{EC} = 35\rho_{s0}$ and $x_{UH} = 90\rho_{s0}$, uniform in the vertical direction and with different relative amplitudes, $S_{UH} = 1.5S_{EC}$. The MP boundary conditions, here in the limit of $\theta_\phi = \theta_n = \theta_T = 0$, are applied at the bottom and top of the domain, i.e. at $y = 0$ and $y = L_y$, and we note that Neumann boundary conditions are imposed in the radial direction for all fields, except for ϕ, which is set to $\phi = \Lambda T_e$.

Figure 3.6.1 shows snapshots of density and potential in a cross-section of the torus. According to the turbulence phase space of SMT plasmas, which is described in detail in Ref. [105], the turbulent transport in this particular simulation is the result of an ideal interchange instability with $k_\parallel = 0$ and $k_y = 2\pi N/L_y$. As in the case of the SOL, smooth profiles are observed in proximity of the vessel walls, confirming the consistency of the boundary conditions with the plasma dynamics described by the drift-reduced Braginskii equations.

In the framework of a Master thesis [120], a dedicated study of blob dynamics [125] was carried out via three-dimensional simulations. In particular, seeded blobs in a SMT configuration have been considered, by initializing GBS simulations with a localized gaussian distribution of density and temperature, elongated in the direction of the magnetic field [120]. Figure 3.6.2 shows an example of a seeded blob simulation with the number of field line turns $N = 2$. One can observe, in a poloidal cross-section of the torus, the propagation and deformation of the blob density, the associated parallel currents, as well as the evolution of the dipolar potential structure responsible of the $\mathbf{E} \times \mathbf{B}$ velocity driving the blob motion.

3.7 Summary and outlook

In this chapter, we have first presented the Braginskii equations, which describe the dynamics of a strongly collisional, strongly magnetized plasma. We have then derived the drift-reduced Braginskii equations, which are suitable for the description of low frequency turbulence in open field lines. Third, we have presented the GBS code, which is based on the drift-reduced Braginskii equations. We have described the implementation of the model equations and that of the boundary conditions derived in Chapter 2. Finally, we have shown examples of GBS simulations in both SOL and SMT conditions. Results indicate compatibility of the boundary conditions with three-dimensional global fluid turbulence simulations.

Simulations of plasma turbulence with a proper treatment of the plasma-wall transition, now possible with the GBS code [55], have allowed a detailed study of the turbulent regimes present in the SOL [113, 114, 115] and a comparison with experimental results from a number of tokamaks [116]. Simulation of turbulence in the SMT configuration has been made possible, as well as a dedicated study of blob dynamics, which has been carried out via three-dimensional simulations of seeded blobs [120].

In the next chapters, we investigate the different effects the sheath has on the turbulence and flows, with simple analytical models and through GBS simulations.

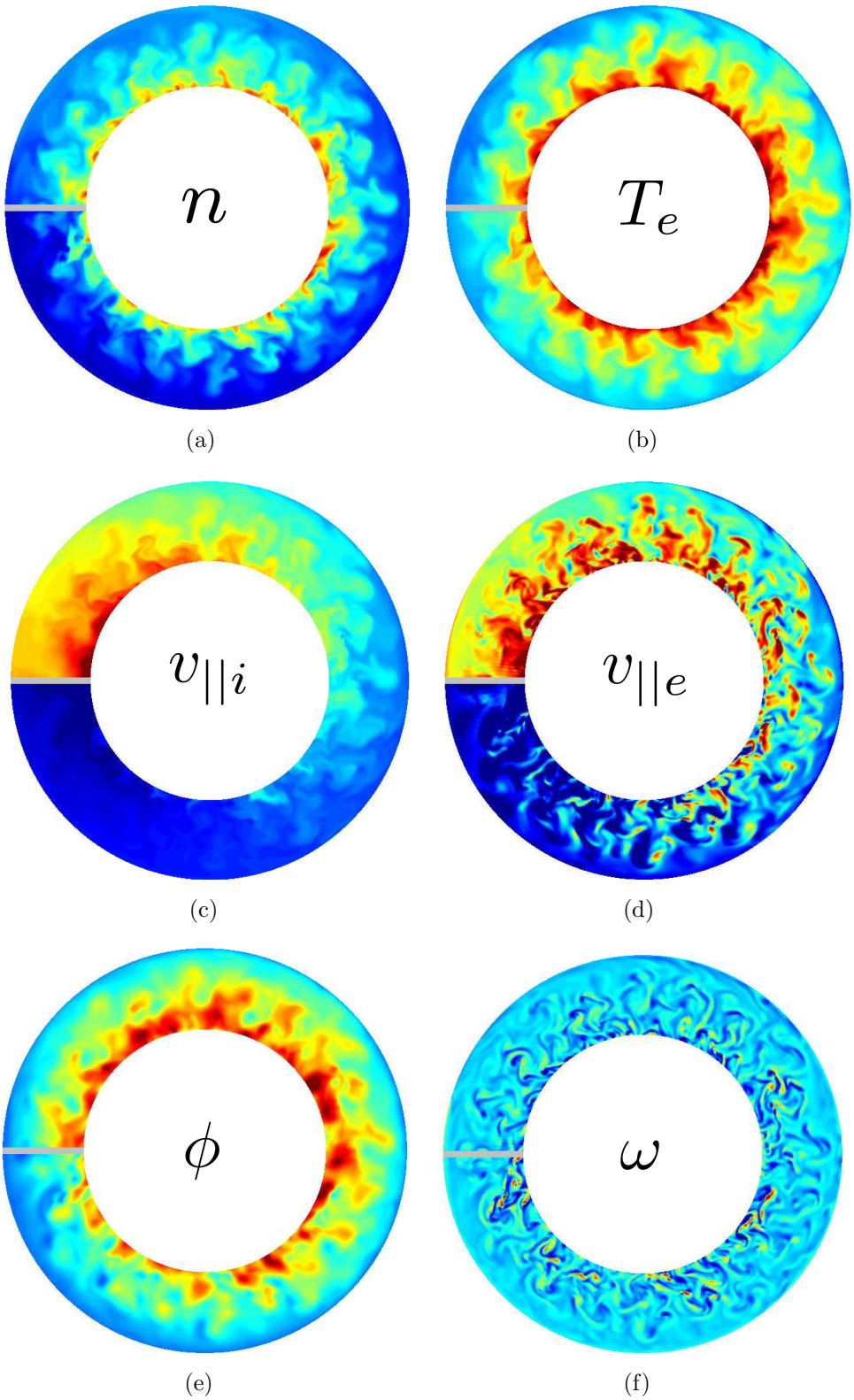

Figure 3.5.1: Snapshots in a poloidal cross-section of (a) density, (b) electron temperature, (c) ion parallel velocity, (d) electron parallel velocity, (e) electrostatic potential, and (f) vorticity. Results are obtained from GBS simulations of a limited tokamak SOL. Boundary conditions at the MP entrance are implemented at the limiter plate, located at $\theta_l = \pi$. The snaphot covers the radial extension (x_s, x_{max}).

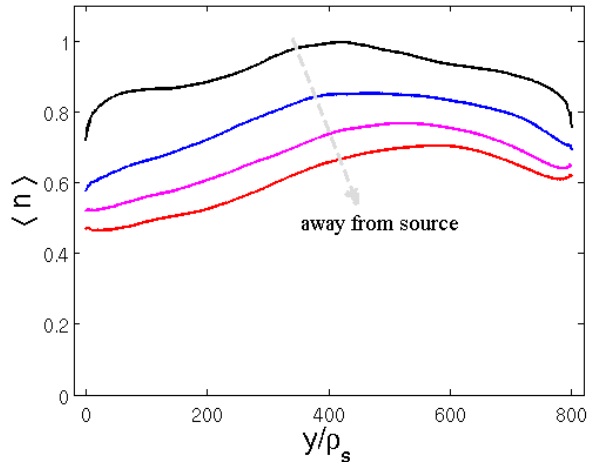

(a)

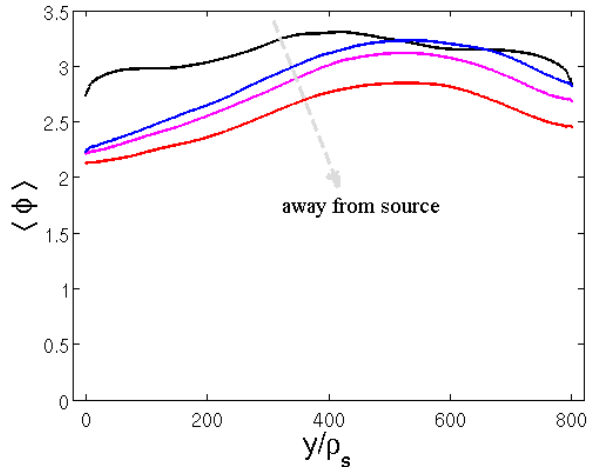

(b)

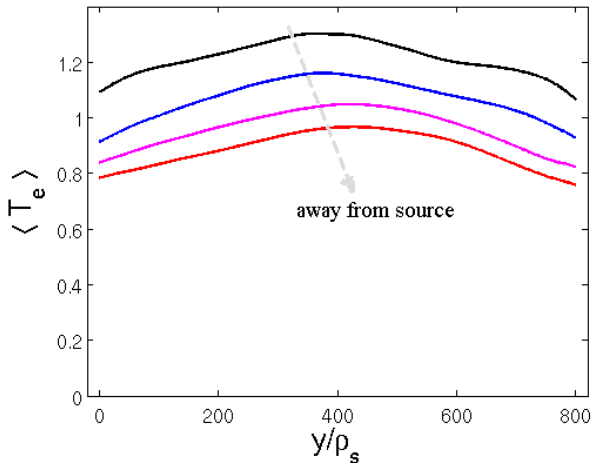

(c)

Figure 3.5.2: Time-averaged poloidal profiles of (a) density, (b) electrostatic potential, and (c) electron temperature. Different colors indicate different radial positions, from the source location $x = x_s$ (black) to $x = x_s + 50\rho_{s0}$ (red).

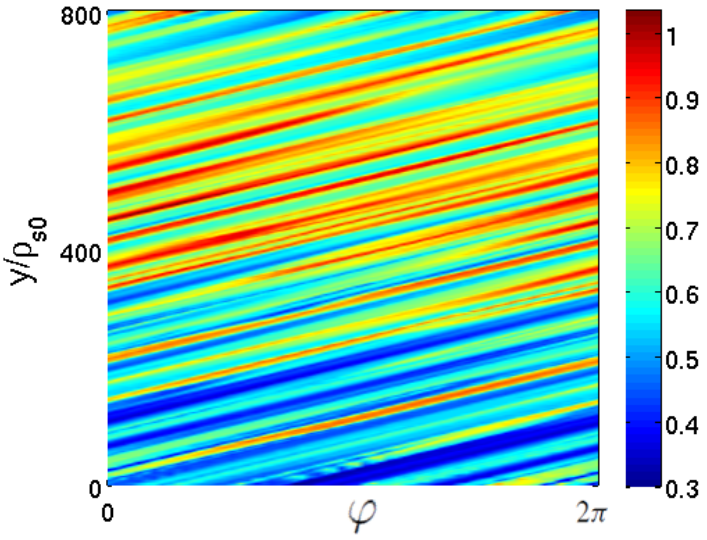

Figure 3.5.3: Snapshot of the density n in a plane covering the full toroidal and poloidal angles, at a given radial position $x = x_s + 20\rho_{s0}$. Turbulence is cleary aligned with the magnetic field, which has $q = 4$. Results are obtained from the GBS simulations.

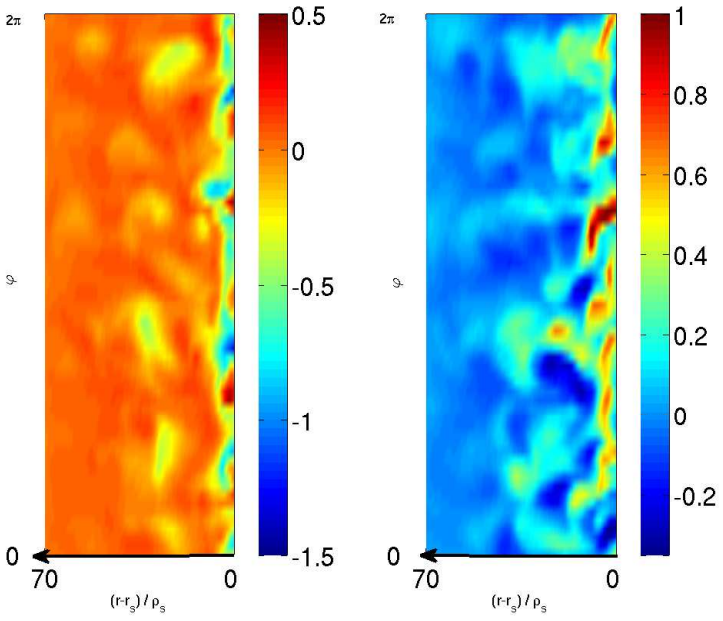

Figure 3.5.4: Snapshot of parallel currents $j_{||} = en(V_{||i} - V_{||e})$ flowing to the top (left panel) and bottom (right panel) sides of the limiter. The coordinate φ denotes the toroidal angle. Results are obtained from the GBS simulations.

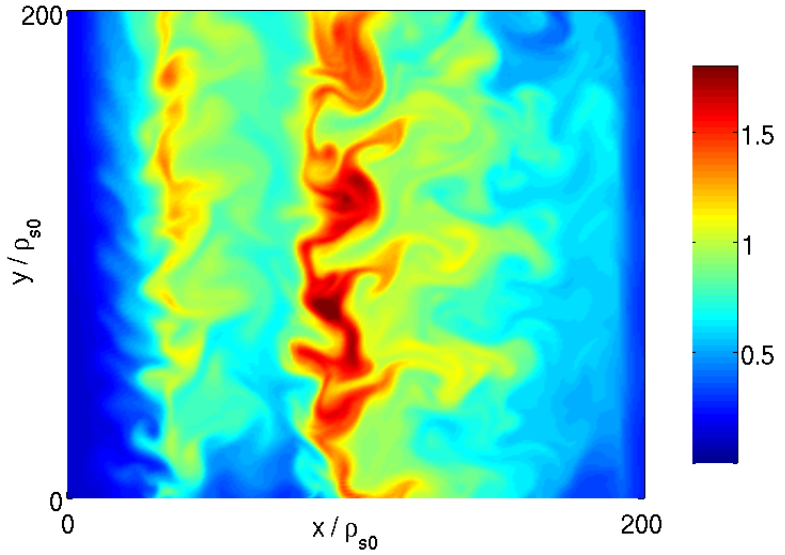

(a)

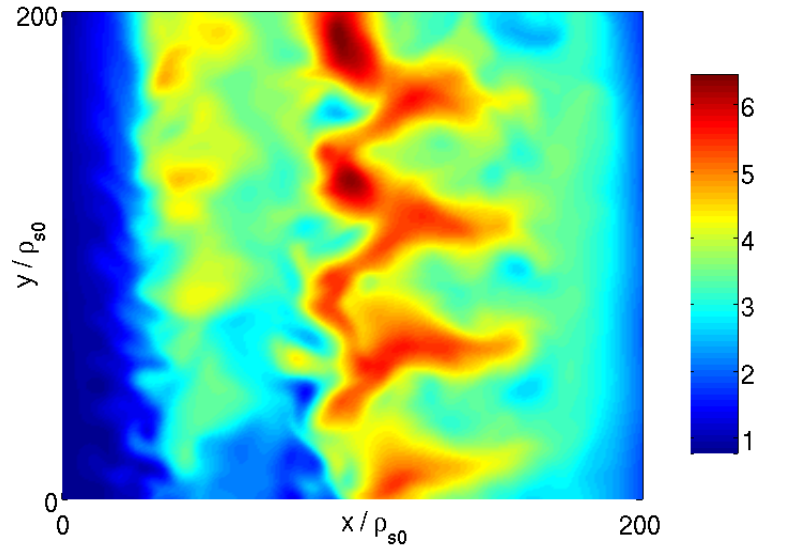

(b)

Figure 3.6.1: Snapshots in a poloidal cross-section of the torus, for (a) the plasma density, and (b) the electrostatic potential. Results are obtained from GBS simulations in SMT conditions, with $N = 4$. Boundary conditions at the MP entrance are implemented at the bottom and at the top of the domain.

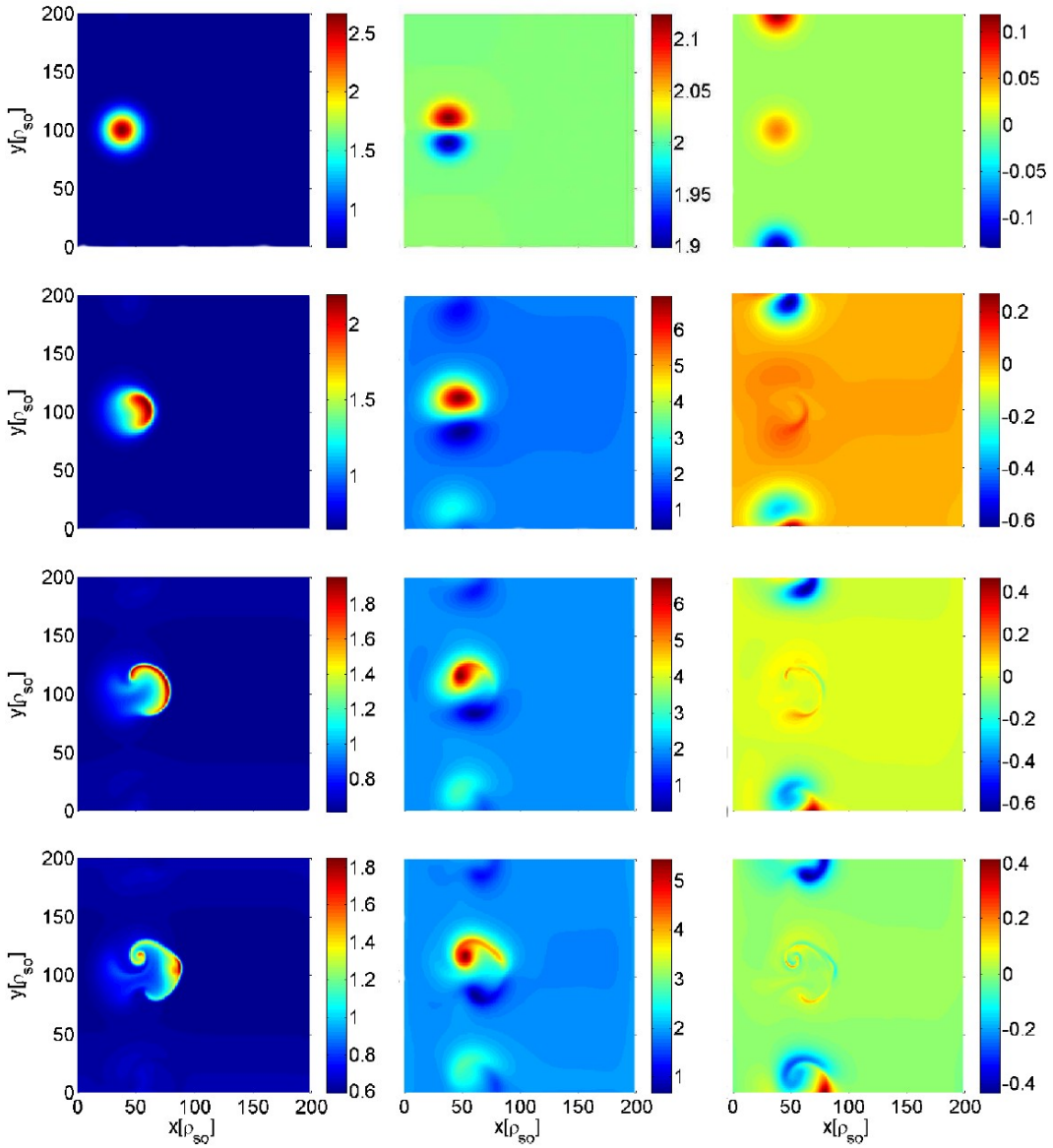

Figure 3.6.2: An example of a three-dimensional seeded blob simulation. The blob density (left column), the blob potential (middle column) and the blob parallel current (right column) are shown at four different simulation times, from $t = 0$ (first row) to $t = 0.72$ (last row). Here $N = 2$.

Chapter 4

Electrostatic potential in open field lines

4.1 Introduction

The origin of a high-confinement regime, where turbulence is suppressed and the formation of a plasma pedestal is observed, is still not fully understood and is the subject of intense theoretical and experimental research. There is nonetheless an increasing experimental evidence for the role of the SOL in regulating the low-to-high (L-H) confinement mode power threshold as well as the toroidal rotation profiles of the entire plasma volume [126, 127].

An essential quantity for the understanding of mean flows and pedestal formation during the L-H transition in a magnetically confined plasma is the self-generated radial electric field. Typically, the relation $e\phi \sim 3T_e$ is invoked for the SOL [16], thus leading to an estimate of the radial electric field as

$$E_r \sim -3\partial_r T_e/e \ . \tag{4.1.1}$$

This relation is based on the assumption that ϕ in the SOL is governed by its value at the sheath, the region where the plasma interacts with the wall. More precisely, if one uses Bohm's law for the sheath parallel current [16],

$$j_{||} = e n_{se} c_s \left[1 - \exp\left(\Lambda - e\phi/T_e\right)\right] \ , \tag{4.1.2}$$

then an ambipolar outflow in the parallel direction imposes $e\phi = \Lambda T_e$ at the sheath edge. Here n_{se} is the plasma density at the sheath edge, c_s is the plasma sound speed and $\Lambda = \log\left[\sqrt{m_i/(2\pi m_e)}\right] \approx 3$ for hydrogen plasmas. Unclear remain, however, the generality and correctness of this result. As we show later, in fact, the parallel dynamics far from the walls can also determine the value of ϕ, e.g. through the

electron adiabaticity condition. As a matter of fact, the question of which mechanism sets the value of the plasma potential in the SOL of magnetic confinement devices is a very general issue, as it arises in all open field line magnetized plasma configurations, including linear devices and simple magnetized toroidal devices.

In this chapter we address this question by means of an analytical model that describes the electrostatic potential in an open field line configuration. We provide a general analytical relation between the equilibrium electrostatic potential and the equilibrium electron temperature and plasma density,

$$\bar{\phi} = \bar{\phi}(\bar{T}_e, \bar{n}) \ , \tag{4.1.3}$$

which includes the combined effect of both the sheath and the main SOL plasma dynamics (overbar denotes time-averaged values). The analytical results suggest that, depending on the density and temperature drops established between the two regions, one mechanism can dominate over the other. This implies that the radial electric field in the SOL may be determined by different mechanisms depending on the particular regime of operation, i.e. the sheath-limited regime as opposed to the detached regime. In order to confirm our analytical predictions, we perform numerical simulations of SOL turbulence using the GBS code [34], with the set of boundary conditions described in Chapter 2.

4.2 Analytical model

Within a drift-reduced fluid model [24], the momentum equation for the electrons in the parallel direction leads to a generalized Ohm's law,

$$m_e n \frac{dV_{\parallel e}}{dt} = en\nabla_\parallel \phi - \nabla_\parallel p_e - 0.71 n \nabla_\parallel T_e + en\nu_\parallel j_\parallel \tag{4.2.1}$$

where $V_{\parallel e}$ is the electron parallel velocity, $d/dt = \partial_t + V_{\parallel e}\nabla_\parallel + \mathbf{V}_E \cdot \nabla_\perp$ is the Lagrangian derivative, $\mathbf{V}_E$ is the $\mathbf{E} \times \mathbf{B}$ velocity, $p_e = nT_e$ is the electron scalar pressure, $j_\parallel = en(V_{\parallel i} - V_{\parallel e})$ is the parallel current and $\nu_\parallel$ is the plasma resistivity. The absence of the electron diamagnetic drift in the Lagrangian derivative is due to the so-called diamagnetic cancellation, which arises from the lowest order term in the pressure tensor. A detailed derivation of Eq. (4.2.1) is given in Sec. 3.3. Higher order terms in the pressure tensor, which correspond to the effect of finite electron viscosity, are smaller than the other terms by a factor $\lambda_e/L_\parallel \ll 1$ and thus are neglected here.

While the electron inertia and the resistivity terms in Eq. (4.2.1) can play an important role in the plasma dynamics (e.g., they can make drift waves unstable by

breaking the electron adiabaticity), the equilibrium profiles do not depend significantly upon those. In fact, the ratio of the inertia term to the parallel electric field term is of the order of the mass ratio $m_e/m_i \ll 1$. Similarly, the resistive term is negligible as long as the electron mean free path is not too small, namely if

$$\sqrt{m_e/m_i} \ll \lambda_e/L_\parallel \ll 1 \quad . \tag{4.2.2}$$

Time-averaging Eq. (4.2.1) and neglecting inertia and resistivity, we are led to an equation balancing the parallel electric field force with the parallel pressure and thermal forces,

$$e\nabla_\parallel \bar{\phi} - \frac{\bar{T}_e}{\bar{n}}\nabla_\parallel \bar{n} - 1.71\nabla_\parallel \bar{T}_e \simeq 0 \tag{4.2.3}$$

where we have assumed that $\overline{(T_e/n)\nabla_\parallel n} \simeq (\bar{T}_e/\bar{n})\nabla_\parallel \bar{n}$. While Eq. (4.2.3) is valid along each magnetic field line in the SOL, it breaks down at the magnetic presheath entrance, where the drift-reduced approximation is violated. Integrating Eq. (4.2.3) along the parallel direction z, from $z = -L_\parallel/2$ to z (where $L_\parallel$ is the parallel connection length, and $z = 0$ is defined half way between the two ends of a field line), we can write

$$e\bar{\phi}(z) = e\phi^- + 1.71\left[\bar{T}_e(z) - T_e^-\right] + \int_{-L_\parallel/2}^{z} \frac{\bar{T}_e}{\bar{n}}\frac{\partial \bar{n}}{\partial z'}dz' \tag{4.2.4}$$

where we denote $\phi^\pm = \bar{\phi}(\pm L_\parallel/2)$ the electrostatic potential at the magnetic presheath entrance at both ends of a field line. Analogously, $\bar{\phi}(z)$ can be obtained by integrating Eq. (4.2.3) from $z = +L_\parallel/2$ to z, i.e.

$$e\bar{\phi}(z) = e\phi^+ + 1.71\left[\bar{T}_e(z) - T_e^+\right] + \int_{+L_\parallel/2}^{z} \frac{\bar{T}_e}{\bar{n}}\frac{\partial \bar{n}}{\partial z'}dz' \quad . \tag{4.2.5}$$

We can estimate $\bar{\phi}(z)$ as the average of the values given by Eqs. (4.2.4) and (4.2.5),

$$e\bar{\phi}(z) = \frac{1}{2}(e\phi^+ + e\phi^-) + 1.71\left[\bar{T}_e(z) - \frac{1}{2}(T_e^+ + T_e^-)\right] + \frac{1}{2}\left[I^+(z) + I^-(z)\right] \tag{4.2.6}$$

where we have defined

$$I^\pm(z) = \int_{\pm L_\parallel/2}^{z} \frac{\bar{T}_e}{\bar{n}}\frac{\partial \bar{n}}{\partial z'}dz' \quad . \tag{4.2.7}$$

In order to progress analytically, we write

$$I^{\pm}(z) = \sigma_0 \int_{\pm L_\parallel/2}^{z} \frac{\partial \bar{n}}{\partial z'} dz' \ , \tag{4.2.8}$$

where

$$\sigma_0 = \frac{\int_{\pm L_\parallel/2}^{z} \sigma(z') \frac{\partial \bar{n}}{\partial z'} dz'}{\int_{\pm L_\parallel/2}^{z} \frac{\partial \bar{n}}{\partial z'} dz'} \tag{4.2.9}$$

and we have introduced the function $\sigma(z) = \bar{T}_e(z)/\bar{n}(z)$. In the case that $\sigma(z)$ does not vary significantly along the field line, the value σ_0 can be estimated, for example, as $\sigma_0 \simeq \langle \sigma \rangle_z$ where $\langle \cdot \rangle_z$ denotes the average along the field line. Equation (4.2.6) thus becomes

$$e\bar{\phi}(z) = \frac{1}{2}(e\phi^+ + e\phi^-) + 1.71 \left[\bar{T}_e(z) - \frac{1}{2}(T_e^+ + T_e^-) \right] + \sigma_0 \left[\bar{n}(z) - \frac{1}{2}(n^+ + n^-) \right] . \tag{4.2.10}$$

We now use the boundary conditions at the magnetic presheath entrance in order to determine the value of $\phi^{\pm}$. We shall assume that the time-average current towards the wall at the magnetic presheath entrance, j_m, is approximately zero, so that quasi-neutrality is ensured in the main plasma. This current is $j_m = j_\parallel \sin\alpha + j_{\perp w} \cos\alpha$, where $j_\parallel = en(V_{\parallel i} - V_{\parallel e})$ is the parallel current at the magnetic presheath entrance, α is the angle between the magnetic field line and the wall, and $j_{\perp w} = en(V_{\perp w,i} - V_{\perp w,e})$ is the component of the perpendicular current at the magnetic presheath entrance that is directed towards the wall. Imposing the condition $j_m = 0$ at the magnetic presheath entrance by using the boundary conditions derived in Chapter 2, Eqs. (2.4.29)-(2.4.34), we find that the electrostatic potential at both ends of the field line must satisfy

$$e\phi^{\pm} \simeq \left(\Lambda \pm \frac{\theta_{T_e}}{2} - \theta_n \right) T_e^{\pm} \ , \tag{4.2.11}$$

where for a generic quantity A we define $\theta_A = \rho_s/(2L_A \tan\alpha)$, ρ_s is the ion sound larmor radius, and L_A is the radial equilibrium scale length of A. Taking typical SOL parameters, e.g. $\rho_s/L_T \simeq 10^{-2}$ and $\alpha = 0.03 \simeq 2°$ [126], we have that $\theta_{T_e} \simeq 0.1$, and similarly for θ_n. We therefore expect that the electrostatic potential at both ends of a magnetic field line will be approximately given by

$$e\phi^{\pm} \simeq \Lambda T_e^{\pm} \ . \tag{4.2.12}$$

We remark that the electrostatic potential is measured with respect to the wall potential, which is assumed to be zero. We can thus write Eq. (4.2.10) as

$$e\bar{\phi}(z) = \frac{1}{2}\Lambda(T_e^+ + T_e^-) + 1.71\left[\bar{T}_e(z) - \frac{1}{2}(T_e^+ + T_e^-)\right] + \sigma_0\left[\bar{n}(z) - \frac{1}{2}(n^+ + n^-)\right]. \tag{4.2.13}$$

Equation (4.2.13) is an analytical relation between the equilibrium electrostatic potential and the equilibrium electron temperature and density in the SOL, $\bar{\phi} = \bar{\phi}(\bar{T}_e, \bar{n})$. The first term on the right hand side of Eq. (4.2.13) represents the effect of the sheath in determining the value of $\bar{\phi}$, while the second and third terms correspond to the effect of the plasma dynamics far from the walls.

We now discuss a few interesting limits of Eq. (4.2.13). First, in the limit of constant density and temperature along the field line, $\bar{T}_e(z) \equiv T_0$ and $\bar{n}(z) \equiv n_0$, Eq. (4.2.13) implies that $\bar{\phi}$ is constant as well, more precisely

$$e\bar{\phi}(z) = \Lambda T_0 \tag{4.2.14}$$

and therefore, in this particular limit, the electrostatic potential is exclusively determined by the sheaths. Eq. (4.2.14) is the widely used relation justifying the estimate of the radial electric field as $E_r = -3\partial_r T_e/e$. However, this is a slightly unrealistic limit, since even in the sheath-limited regime, where the temperature is about constant along the field lines, the density always drops when approaching the wall due to the sink action of the sheaths [16].

Second, another interesting limit of Eq. (4.2.13) is the case $T_e^+ = T_e^- = 0$ and $n^+ = n^- = 0$, namely the case where both the temperature and density drop substantially when approaching the walls. This corresponds to the detached regime, where the plasma strongly recombines and cools down before interacting with the walls [16]. In this particular limit, Eq. (4.2.13) gives

$$e\bar{\phi}(z) = 1.71\bar{T}_e(z) + \sigma_0\bar{n}(z) \tag{4.2.15}$$

and therefore the electrostatic potential is exclusively determined by the value of density and temperature far from the walls.

Third, we may assume arbitrary density and temperature profiles with a constant ratio $\sigma(z) \simeq \sigma_0$. This is a reasonable assumption at least if the particle and heat sources in the SOL have similar locations, a situation that is encountered in low-recycling regimes where most of the plasma in the SOL is refueled by the core.

Under this assumption, Eq. (4.2.13) gives

$$e\bar{\phi}(z) = \frac{1}{2}\Lambda(T_e^+ + T_e^-) + 2.71\left[\bar{T}_e(z) - \frac{1}{2}(T_e^+ + T_e^-)\right] \quad . \tag{4.2.16}$$

Equation (4.2.16) is a simple relation between the equilibrium electrostatic potential and the equilibrium electron temperature in the SOL. As in Eq. (4.2.13), the value of $\bar{\phi}$ is determined by the combined effect of the sheath and the bulk dynamics. Their relative importance depends on the magnitude of the temperature drop established between the bulk and the sheaths. More precisely, we can write Eq. (4.2.16) as

$$e\bar{\phi}(z) = \left[\Lambda f_{sh} + 2.71(1 - f_{sh})\right] T_e(z) \tag{4.2.17}$$

where we have defined

$$f_{sh}(z) = \frac{T_e^+ + T_e^-}{2T_e(z)} \quad . \tag{4.2.18}$$

If the temperature is constant along the field line then $f_{sh} = 1$, whereas $f_{sh} \to 0$ if the temperature drops substantially when approaching the walls. These two limits are roughly representative of the sheath-limited and detached regimes, respectively. In fact, Eq. (4.2.14) is retrieved in the limit $f_{sh} = 1$, while Eq. (4.2.15) is retrieved for $f_{sh} \to 0$ in the case where $\sigma(z) \simeq \sigma_0$.

We would like to remark that, since Λ is very close to 2.71 for hydrogen, Eq. (4.2.17) approximately gives $\bar{\phi}(z) = 3\bar{T}_e(z)$. This means that the widely invoqued relation $E_r \sim -3\partial_r T_e$ should be used carefully. For example, strongly varying temperature profiles along the field line imply that the radial electric field varies accordingly, and thus it must be computed by using the local values of temperature.

4.3 Simulations in SOL conditions

The validity of the analytical prediction for the equilibrium electrostatic potential in the SOL, Eq. (4.2.13), is assessed in the present section by means of global, three-dimensional fluid simulations of SOL turbulence performed with the GBS code. As GBS evolves the plasma dynamics with no separation between equilibrium and fluctuating quantities, it is an adequate tool to assess the validity of the analytical predictions for the equilibrium electrostatic potential derived in the previous section. We remark that, at the moment, GBS simulations do not describe ionization, recombination, or radiative processes. Thus we can only expect to access sheath-limited regimes where convection is the dominant mechanism for particle and heat transport

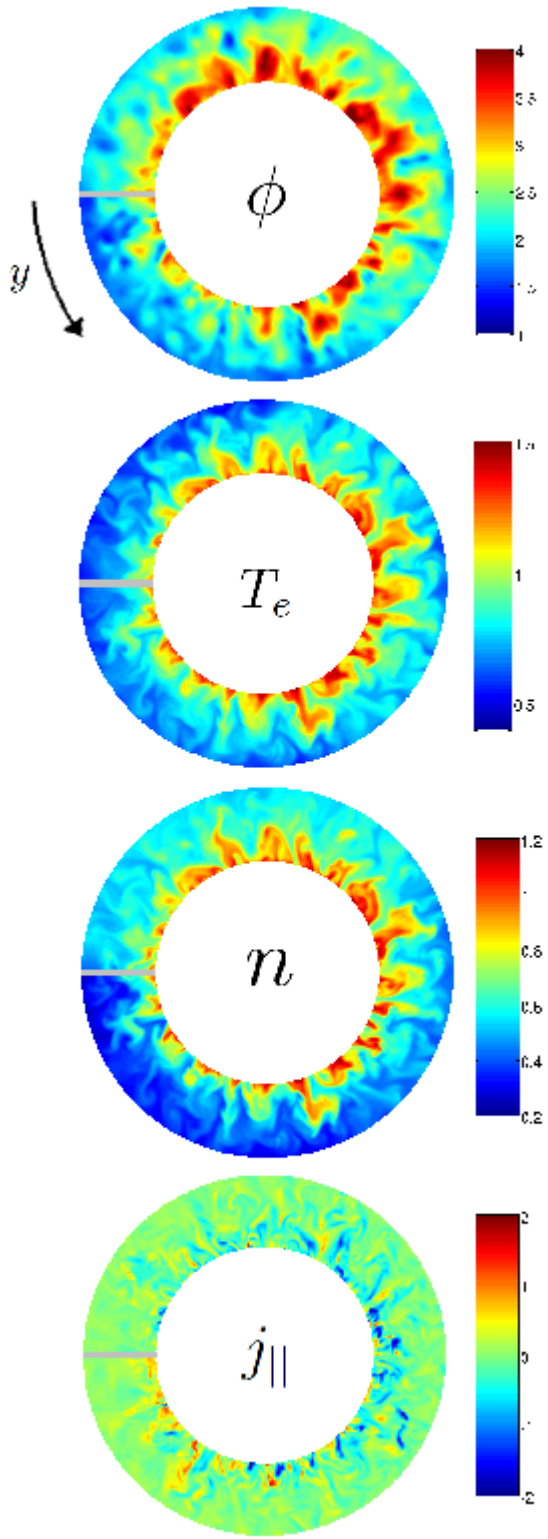

Figure 4.3.1: Snapshots in a poloidal cross-section of the electrostatic potential ϕ, electron temperature T_e, density n, and parallel current $j_{\|}$. Results are obtained from GBS simulations of a limited tokamak SOL. The limiter plate is located at $\theta_l = \pi$. The snaphot covers the radial extension (x_s, L_x).

along the field lines, and parallel gradients are relatively small. Simulations capable of describing high-recycling and detached regimes, where heat conduction becomes important and parallel gradients are larger, are planned and will represent a testbed of the analytical predictions in these regimes.

The system of equations evolved by GBS to study SOL turbulence is given in Chapter 3. We note that while the boundary condition for the electrostatic potential, Eq. (2.4.31), does not impose $\phi = \Lambda T_e$, the latter is expected to fluctuate around this value to ensure that the average current to the wall is essentially zero.

For the simulations presented below, a toroidal limiter is located on the high field side midplane, and we use the same model parameters as in Sec. 3.5. In particular, the resistivity $\nu_\parallel$ is such that the electron mean free path satisfies $\lambda_e/L_\parallel \simeq 1/50 \ll 1$. We notice that even at such high collisionality, a limited SOL is still in the sheath-limited regime as heat conduction cannot build significant parallel gradients of temperature. This is because in the considered limiter configuration the density source is uniformly distributed in the poloidal direction and thus convection plays a crucial role in flattening the parallel temperature gradients. For a detailed proof of this, see Appendix C. In a diverted configuration, however, convection is mainly active near the target where most of the plasma is refueled, and conduction-limited regimes are therefore more easily accessible [16].

Figure 4.3.1 shows typical snaphots of plasma turbulence in a poloidal cross-section for the fields of interest here. For this particular simulation, we have used $\Lambda = 3$ for the sheath boundary conditions, approximately corresponding to the value for hydrogen. Also, the time-averaged Ohm's law is fairly well described by the balance given by Eq. (4.2.3). In fact, Fig. 4.3.2 shows that the first term in Eq. (4.2.3), namely the parallel electric field force, is almost perfectly balanced by the sum of the pressure and thermal forces. Also, the difference between the two can be explained by the finite effect of the resistivity. This is due to the fact that the condition $\sqrt{m_e/m_i} \ll \lambda_e/L_\parallel$ is not exactly satisfied. We can nevertheless conclude that Eq. (4.2.3) is a very reasonable approximation. Finally, the expected value of the plasma potential at both ends of the field lines, $\phi^\pm$, as given by Eq. (4.2.12), is in rather good agreement with the simulation results, as shown in Fig. 4.3.3.

We now assess the validity of the analytical prediction for the equilibrium electrostatic potential, Eq. (4.2.13). Since the system is toroidally symmetric, the equilibrium quantities only depend on x and y and thus the results are shown in a poloidal cross-section. Figure 4.4.1 (left column) shows the time-averaged electrostatic potential as given by the GBS simulation, and compares it with the prediction of Eq. (4.2.13). Also, the widely used expression $\bar{\phi} = \Lambda T_0$, Eq. (4.2.14), is shown for comparison. The prediction of Eq. (4.2.13) agrees rather well with the simulation result, as it is able to capture both the magnitude and the radial and poloidal struc-

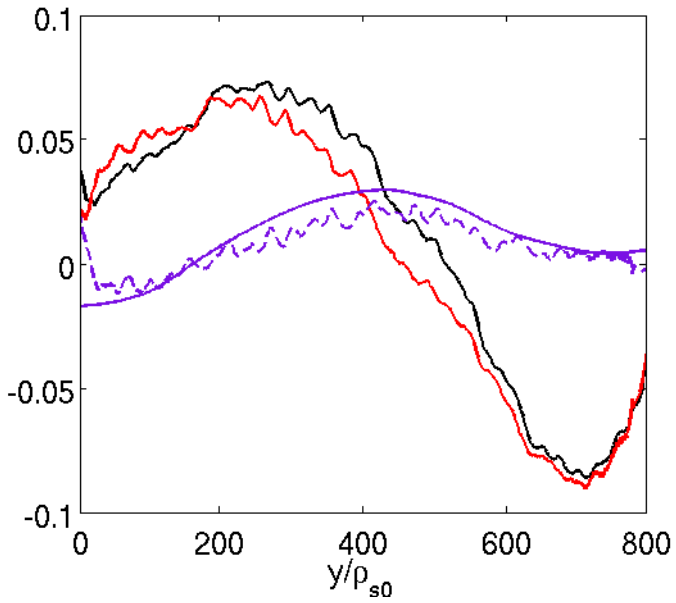

Figure 4.3.2: Balance of the dominant terms in the time-averaged Ohm's law at a given radial location $x = 50\rho_{s0}$, as a function of the poloidal coordinate. The parallel electric field force term $e\nabla_\parallel \bar{\phi}$ (black) is almost balanced by the sum of the terms related to pressure and thermal forces, $\bar{T}_e \nabla_\parallel \bar{n}/\bar{n} + 1.71\nabla_\parallel \bar{T}_e$ (red). The difference of the two is shown in dashed-violet. The resistivity term $\nu_\parallel \bar{j}_\parallel/\bar{n}$ (solid-violet) accounts for this difference.

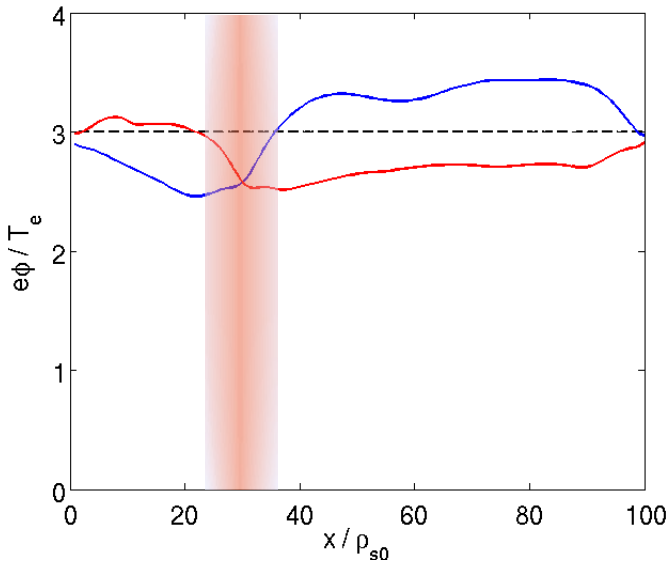

Figure 4.3.3: Radial profile of the time-averaged electrostatic potential normalized to the time-averaged electron temperature, $e\bar{\phi}/\bar{T}_e$, at the top side of the limiter (blue) and at the bottom side of the limiter (red). The dashed-black line shows, as a reference, the value $e\bar{\phi}/\bar{T}_e = \Lambda$. The vertical shaded area indicates the location of the source.

ture of the electrostatic potential. The relation $\bar{\phi} = \Lambda T_0$ does not capture so well the poloidal structure of the potential, but it gives nevertheless the correct order of magnitude. We note that this could be due to the fact that Λ is comparable to 2.71, thus the agreement being a simple coincidence. However, as shown in Fig. 4.4.1 (middle and right columns), simulations with an artificially high value of Λ show that $\bar{\phi} = \Lambda T_0$ is also a reasonable prediction for the order of magnitude of $\bar{\phi}$. In fact, in the sheath-limited simulations presented herein, the parallel gradients are not very large and $f_{sh} \approx 0.8$, thus the effect of the sheath is expected to play a dominant role in setting the value of $\bar{\phi}$ in the SOL.

4.4 Summary and outlook

The electrostatic potential in an open field line plasma configuration, e.g. in the SOL of tokamaks, is set by the combined effect of two different mechanisms. On the one hand, the sheath physics regulates the value of ϕ at the end of the field lines to ensure quasi-neutrality in the main plasma. On the other hand, the electron adiabaticity sets the parallel electric field far from the walls. We have provided a general analytical relation between the equilibrium electrostatic potential and the equilibrium electron temperature and density, $\bar{\phi} = \bar{\phi}(\bar{T}_e, \bar{n})$, which implies that the relative importance of the two mechanisms in setting the value of ϕ depends on the density and temperature drops that are established between the bulk plasma and the sheaths. This suggests that one must be careful when estimating the radial and poloidal electric fields in the SOL of tokamaks, as it may depend on the particular regime of operation: sheath-limited regime, low and high recycling regimes, or detached regime. The validity of Eq. (4.2.13) has been assessed via SOL turbulence simulations in the sheath-limited regime. Future simulations of high-recycling and detached regimes will be a good testbed of our analytical predictions.

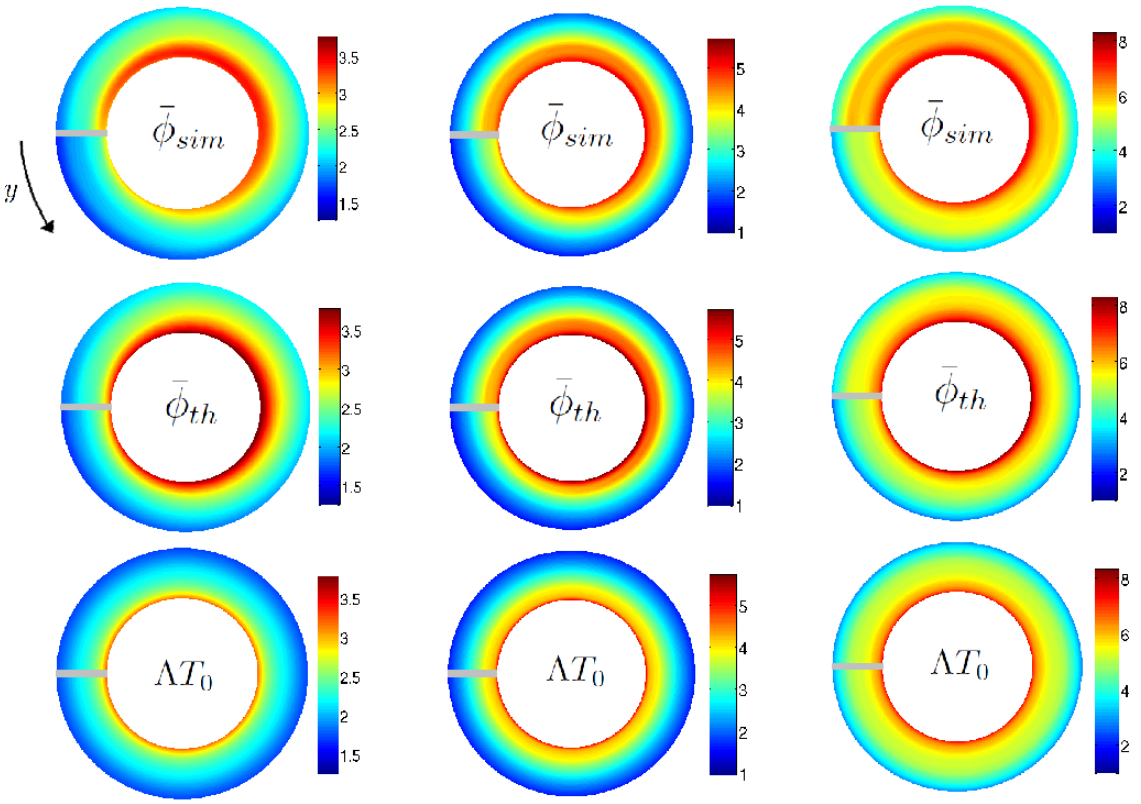

Figure 4.4.1: Equilibrium profiles of the electrostatic potential $\bar{\phi}$ in a poloidal cross-section as given from GBS simulations (top row), from Eq. (4.2.13) (middle row), and from the widely used estimate $\bar{\phi} = \Lambda T_0$ (bottom row) with $T_0 = (T_e^+ + T_e^-)/2$. Here $\Lambda = 3$ (left column), $\Lambda = 6$ (middle column), and $\Lambda = 10$ (right column).

Chapter 5

Intrinsic toroidal rotation in the tokamak SOL

5.1 Introduction

Tokamak plasmas have been observed to spontaneously rotate toroidally even in the absence of momentum injection [128, 129, 130]. As sufficiently large rotation has been shown to stabilize MHD instabilities [131, 132] and reduce turbulent transport [133], understanding the origin and nature of intrinsic toroidal rotation is of special importance for future fusion devices such as ITER where the effective deposition of momentum is expected to be small [134, 135]. While the experimental and theoretical research effort has mostly focused on toroidal rotation inside the LCFS [136, 137, 138, 139, 140, 141, 142, 143, 144, 145, 146, 147], there is strong experimental evidence for the role of the SOL in determining core rotation profiles [126]. Recently it was also found that strong flows in the SOL set the boundary conditions on the confined plasma and can even determine the low-to-high confinement mode power treshold [127]. While some theoretical and numerical studies have focused on SOL rotation driven by classical flows [148, 149], a revealing description of the phenomena that takes into account the fundamental elements of the SOL, such as turbulent momentum transport and plasma sheaths, is still lacking. This is particularly important since, as experimental data reveals [126], explaining parallel flows requires a detailed description of turbulent transport.

In this chapter, the origin and nature of intrinsic toroidal plasma rotation in the SOL of tokamaks is investigated both analytically and through numerical simulations. We start by showing that there is a net volume-averaged toroidal flow in GBS simulations of SOL turbulence despite the fact that no momentum is injected, therefore implying that there are intrinsic toroidal flows established in the SOL. In order to understand the origin of such flows, we provide an analytical description of the generation and transport of intrinsic toroidal plasma rotation in the SOL, based on the plasma momentum balance, the turbulent transport and the sheath

boundary conditions. Results suggest that the equilibrium poloidal $\mathbf{E} \times \mathbf{B}$ flow, the sheath physics, and the presence of poloidal asymmetries in the pressure profile act as sources of parallel flow, while turbulence provides the mechanism for the radial momentum transport. We first derive an equation describing the radial and poloidal dependence of the equilibrium parallel flow by providing, for the first time, a first-principle based estimate of the turbulent momentum transport in the SOL. Second, we present an approximate analytical solution of the equation that describes the toroidal rotation profile in the poloidal plane. Then, the result of global, three-dimensional turbulence simulations of a limited SOL are presented, showing good agreement with our theory. Finally, a first attempt to compare the theoretical predictions with experimental measurements is presented. We show that the analytical solution fairly reproduces experimental trends for the direction and magnitude of toroidal rotation. In particular, results indicate that intrinsic rotation is co-current most of the time, but can be reversed due to pressure asymmetries under certain conditions that are consistent with those observed in tokamaks.

5.2 Intrinsic flows in SOL simulations

In Chapter 3, we have presented results from GBS simulations of SOL turbulence in a limited configuration. According to the drift-reduced Braginskii equations solved by GBS, Eqs. (3.4.4)-(3.4.8), no momentum is injected into the system. However, a careful inspection of the equilibrium parallel ion velocity reveals the existence of a net volume-averaged parallel flow.

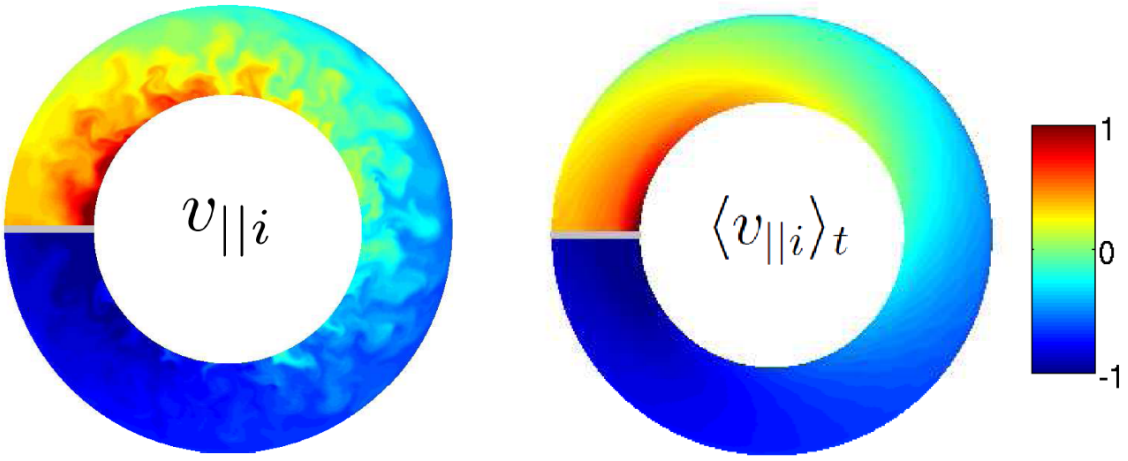

Figure 5.2.1: Snapshot (left) and time-average (right) of the parallel ion velocity in a poloidal cross-section of the tokamak SOL. Results are obtained from GBS simulations. The simulation parameters are given in Sec. 3.5.

Figure 5.2.1 shows a snaphot of $V_{\|i}$ and its time-average $\bar{V}_{\|i}$ in a poloidal cross-section. Since the system is toroidally symmetric, the equilibrium quantities only

depend on the radial and poloidal coordinates and thus we show the equilibrium profiles in a poloidal cross-section. As expected from the magnetic presheath boundary conditions, $V_{\|i}$ is positive on the top side of the limiter, where the magnetic field is directed towards the wall, and negative on the bottom side of the limiter, where the opposite situation applies (Figure 5.2.2). However, the zero of $\bar{V}_{\|i}$ is not half way between the two faces of the limiter, namely at $\theta = 0$. Instead, the SOL region where $\bar{V}_{\|i} < 0$ is larger than the $\bar{V}_{\|i} > 0$ region, and a volume-average of $\bar{V}_{\|i}$ gives a value of approximately $-0.3c_s$. Since the pitch angle α of the magnetic field is very small, $\alpha \ll 1$, $\bar{V}_{\|i}$ represents to a very good approximation the toroidal rotation. Given the direction of the toroidal and poloidal components of the magnetic field, we conclude that the negative, net parallel flow corresponds to a toroidal plasma rotation in the co-current direction, i.e. in the direction of the plasma current I_p (see Fig. 5.2.2).

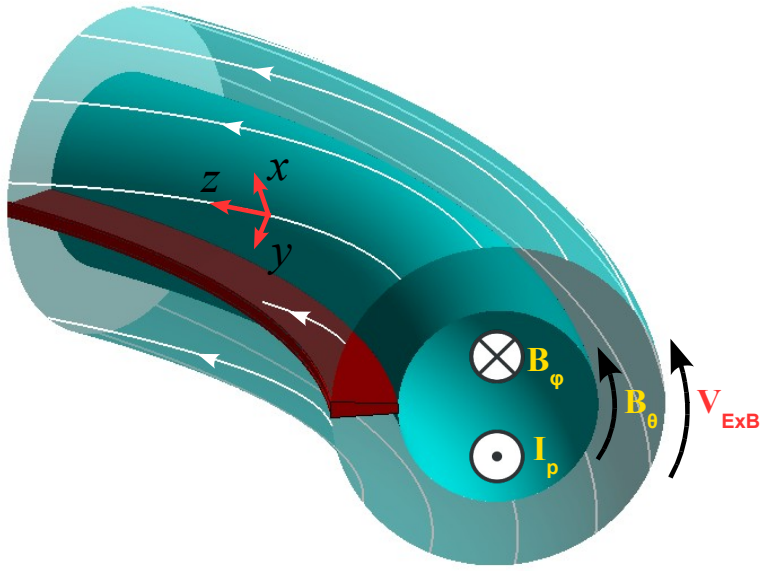

Figure 5.2.2: Sketch of the SOL geometry with its magnetic topology. The directions of the toroidal magnetic field B_φ, the poloidal magnetic field B_θ, and that of the corresponding plasma current I_p are indicated. Also the expected direction of the equilibrium $\mathbf{E} \times \mathbf{B}$ flow is shown.

We now give a qualitative explanation for the origin of this net co-current flow, based on the effect that the sheath has on the parallel ion velocity. Since the radial electric field in the SOL is positive, $E_x > 0$, the poloidal $\mathbf{E} \times \mathbf{B}$ flow is directed from the bottom side of the limiter to its top side (Fig. 5.2.2). As already discussed in Chapter 2, Sec. 2.4, the poloidal $\mathbf{E} \times \mathbf{B}$ flow is recirculated at the magnetic presheath entrance in the parallel direction, in such a way that the ion flow perpendicular to the wall does not depend on the value of the $\mathbf{E} \times \mathbf{B}$ flow. More precisely, the boundary condition for the parallel ion velocity, Eq. (2.4.29), is approximately given by

$$V_{\|i} \simeq c_s \left[\pm 1 - 2\frac{e\phi}{T_e}\theta_\phi \right] \sim c_s \left[\pm 1 - \frac{\Lambda}{\alpha}\frac{\rho_s}{L_\phi} \right] \quad , \tag{5.2.1}$$

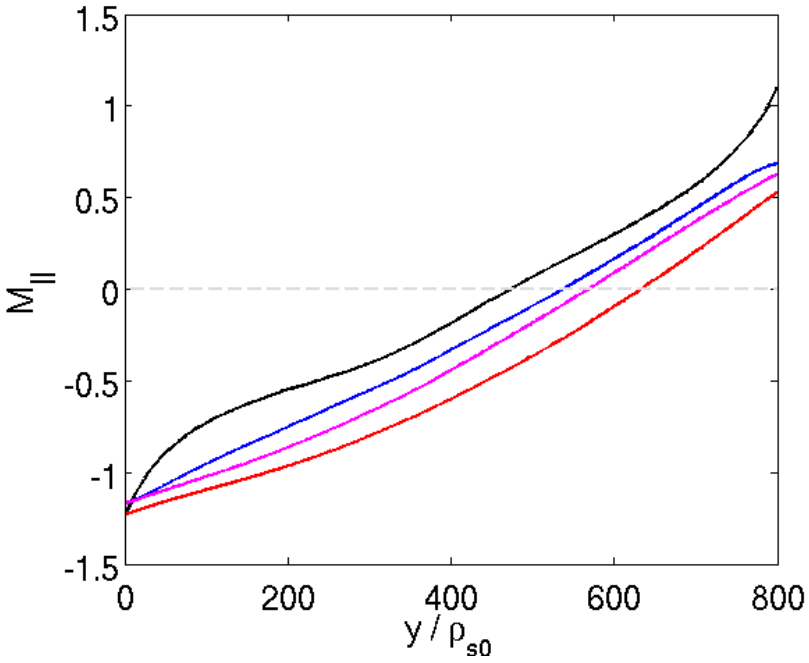

Figure 5.2.3: Poloidal profiles of the equilibrium parallel Mach number, $M_{||} = \bar{V}_{||i}/\bar{c}_s$, at different radial locations: at the source position $x_s = 30\rho_{s0}$ (black), and at $x = 50\rho_{s0}$ (blue), $x = 70\rho_{s0}$ (magenta), and $x = 90\rho_{s0}$ (red). Results are obtained from GBS simulations. The simulation parameters are given in Sec. 3.5.

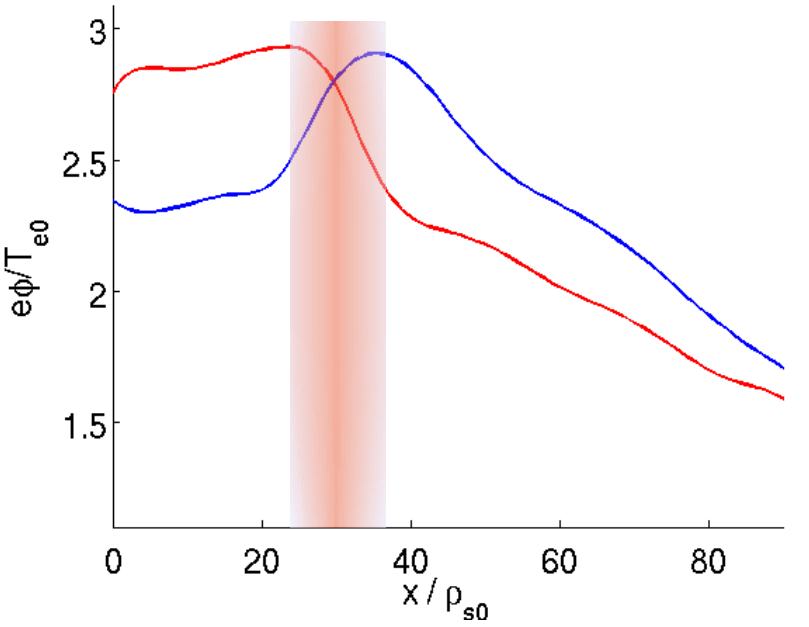

Figure 5.2.4: Radial profile of the time-averaged electrostatic potential in code units, $e\bar{\phi}/T_{e0}$, at the top side of the limiter (blue) and at the bottom side of the limiter (red). The vertical shaded area indicates the location of the source.

where the terms θ_n and θ_{T_e} have been neglected, as they lead to smaller corrections than θ_ϕ, and we have assumed $e\phi \sim \Lambda T_e$ at the magnetic presheath entrance. The deviation from the sound speed in Eq. (5.2.1) is of order one, $\Lambda\rho_s/(\alpha L_\phi) \approx 0.5$, since $\Lambda = 3$, $\alpha = 3.6°$ and $L_\phi \approx 100\rho_s$. Namely, the parallel flows at the bottom and top sides of the limiter are expected to be supersonic and subsonic, respectively. This is confirmed by Fig. 5.2.3, which shows the poloidal profiles of the equilibrium parallel Mach number, $M_\parallel = \bar{V}_{\parallel i}/\bar{c}_s$, at different radial locations. We observe that the profiles are fairly linear and thus almost entirely determined by the boundary conditions. This implies the presence of a negative, net parallel flow as given by the deviation from the sound speed at the boundaries. We remark that there is an asymmetry in the deviation of $\bar{V}_{\parallel i}$ from $\bar{c}_s$, if one compares the two sides of the limiter. This is due to the different radial profiles of $\bar{\phi}$ established at the top and bottom sides of the limiter, as shown in Fig. 5.2.4.

In general, the simple picture of the sheath boundary condition shifting the poloidal profile of $\bar{V}_{\parallel i}$ cannot be used to describe intrinsic flows in the SOL. Figure 5.2.5 shows the results of a simulation carried out with the limiter at the bottom of the tokamak, i.e. with $\theta_l = -\pi/2$. For this configuration, the volume-average of $\bar{V}_{\parallel i}$ gives a value of approximately $-0.05c_s$, hence the net flow is almost zero. This is despite the fact that the parallel flows at the left and right sides of the limiter are, as before, respectively subsonic and supersonic, with deviations from the sound speed comparable to the previous case. The reason is that the poloidal profiles of $M_\parallel$ are no longer linear, as shown in Fig. 5.2.6. This means that there must be another mechanism, competing with the effect of the sheath and determining the rotation profile, such that the resulting net flow is close to zero.

Altogether these results motivated the analytical study of SOL intrinsic flows in a more general framework that includes, in particular, the description of turbulent momentum transport. This study is presented in the reminder of the present chapter.

5.3 Theory of intrinsic rotation in the SOL

In this section, we provide an analytical description of the generation and transport of intrinsic toroidal plasma rotation in the SOL, based on the conservation of plasma momentum, the turbulent transport, and the sheath boundary conditions. We derive an equation describing the radial and poloidal dependence of the equilibrium parallel flow by providing, for the first time, a first-principle based estimate of the turbulent momentum transport. Electrostatic low-frequency turbulence at small wave number, $\omega \ll \omega_{ci}$, $k_\perp\rho_s < 1$, and $k_{||}L_{||} \sim 1$, mainly driven by interchange-like modes such as resistive ballooning modes [150], is believed to dominate the cross-field transport of particles and heat in the SOL. Such modes are also responsible for the turbulent momentum transport that arises from the presence of sheared parallel

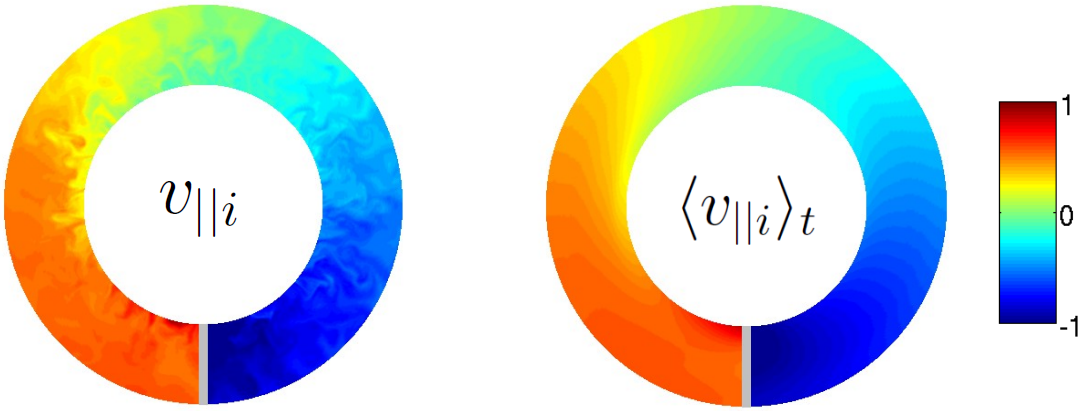

Figure 5.2.5: Snapshot (left) and time-average (right) of the parallel ion velocity in a poloidal cross-section of the tokamak SOL. Results are obtained from GBS simulations. The simulation parameters are the same as in Fig. 5.2.1 but with $\theta_l = -\pi/2$.

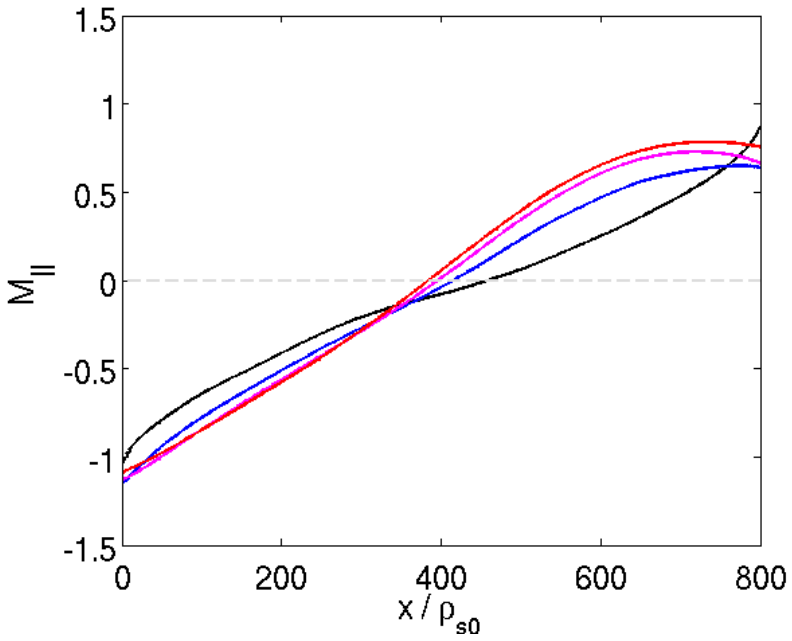

Figure 5.2.6: Poloidal profiles of the equilibrium parallel Mach number, $M_{||} = \bar{V}_{||i}/\bar{c}_s$, at different radial locations: at the source position $x_s = 30\rho_{s0}$ (black), and at $x = 50\rho_{s0}$ (blue), $x = 70\rho_{s0}$ (magenta), and $x = 90\rho_{s0}$ (red). Results are obtained from GBS simulations. The simulation parameters are the same as in Fig. 5.2.1 but with $\theta_l = -\pi/2$, namely with the limiter located on the bottom of the vessel.

flows, namely when $\partial_x M_{||} \neq 0$.

Also, we would like to remark that, for the sake of generality, the model presented herein does not assume cold ions. We include the effect of finite ion temperature without accounting for finite Larmor radius effects.

5.3.1 2D equation for the equilibrium toroidal flow

Let us describe the SOL of a tokamak of major radius R by using a right-handed system of coordinates (y, x, φ), where φ is the toroidal coordinate (counterclockwise direction when looking from the top) and (x, y) define the plane perpendicular to the magnetic field $\mathbf{B}$. The coordinate x is a flux coordinate and extends over the full SOL width, with $x = 0$ at the separatrix. The coordinate y is perpendicular to x and $\mathbf{B}$ and follows the open flux surfaces, with $y = 0$ half way from the two limiter sides or divertor plates, going from $y = -L_y/2$ to $y = L_y/2$ (Figure 5.3.1). In a circular plasma with infinite aspect ratio, x and y correspond to the radial and poloidal coordinates, respectively. The equilibrium magnetic field can be written as $\mathbf{B} = |B_\varphi|\,(\sigma_\varphi \hat{\mathbf{e}}_\varphi + \alpha\sigma_\theta \hat{\mathbf{e}}_\theta)$, where $\alpha = |B_\theta/B_\varphi|$ is the pitch angle and $\sigma_{\varphi,\theta} = \pm 1$ gives the orientation of the magnetic field in the toroidal and poloidal directions. For simplicity, we consider the large aspect ratio limit, therefore the plane (x, y) coincides with the poloidal plane. We also assume that the SOL width is much smaller than the tokamak minor radius.

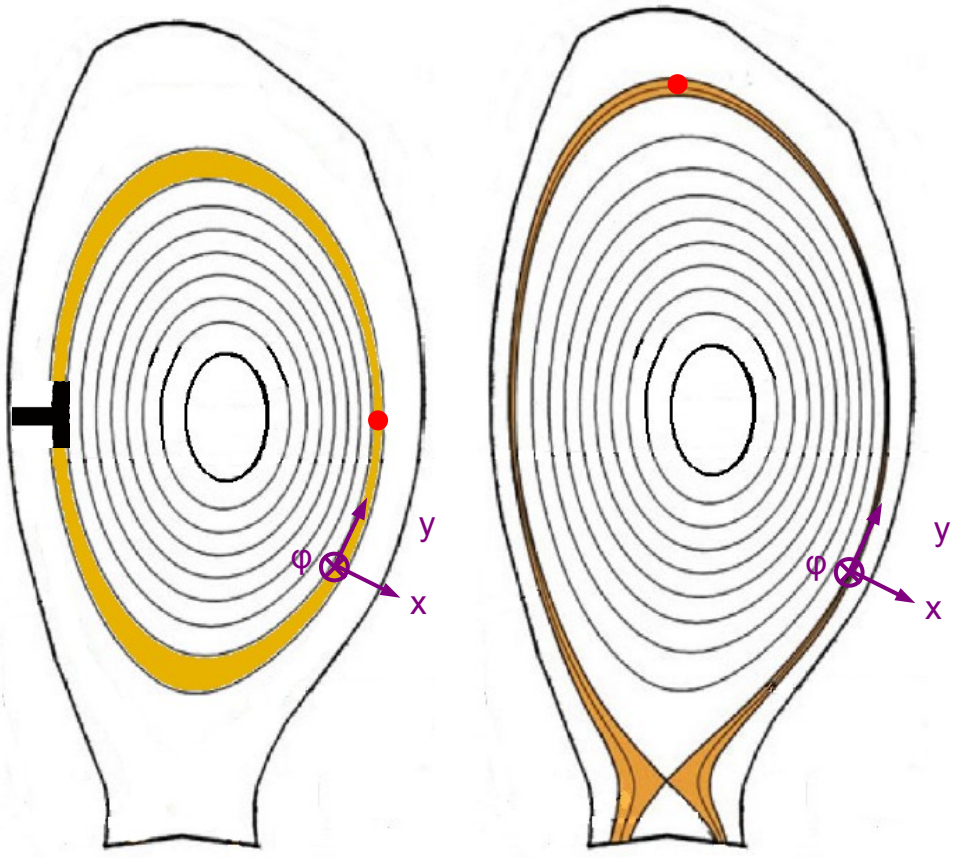

Figure 5.3.1: Coordinate system (y, x, φ) in limited (left) and diverted (right) configurations. The coordinate y follows the open flux surfaces. The red dot indicates the location $y = 0$ half way between the two limiter sides or divertor plates.

Within a drift-reduced fluid model, the evolution of the parallel ion velocity can be obtained by summing the ion and electron parallel momentum equations and neglecting electron inertia,

$$\frac{\partial V_{||i}}{\partial t} + V_{||i}\nabla_{||}V_{||i} + (\mathbf{V}_E \cdot \boldsymbol{\nabla}_\perp)V_{||i} + \frac{1}{m_i n}\nabla_{||}p = 0 \tag{5.3.1}$$

where $p = p_e + p_i$ is the total scalar plasma pressure and $\mathbf{V}_E$ is the $\mathbf{E}\times\mathbf{B}$ velocity. Equation (5.3.1) represents the conservation of plasma parallel momentum and has been derived in Chapter 3 in the limit of cold ions (see Eq. (3.3.35)). A detailed derivation of Eq. (5.3.1) can be found, e.g., in Ref. [24]. The absence of the ion diamagnetic drift in the convection of parallel momentum is due to the so-called diamagnetic cancellation which arises from the lowest order term in the pressure tensor. Also, we have neglected terms of order $\rho_i/L_\perp \ll 1$, $(k_\perp\rho_s)^2 \ll 1$, and $\tau_i \ll L_{||}/c_s$. Here $c_s = \sqrt{(T_e+T_i)/m_i}$ and τ_i is the characteristic time for momentum exchange under ion-ion collisions. Since the pitch angle is typically small, $\alpha \ll 1$, $V_{||i}$ represents to a very good approximation the toroidal rotation.

We now deduce from Eq. (5.3.1) an equation for the equilibrium parallel flow $\bar{V}_{||i}$ in the SOL. We will denote fluctuations with a tilde, and equilibrium with an overbar, e.g. $V_{||i} = \bar{V}_{||i} + \tilde{V}_{||i}$. Time-averaging Eq. (5.3.1) leads to

$$\bar{V}_{||i}\nabla_{||}\bar{V}_{||i} + \boldsymbol{\nabla}_\perp \cdot \overline{\boldsymbol{\Gamma}} + \frac{1}{m_i\bar{n}}\nabla_{||}\bar{p} = 0 \tag{5.3.2}$$

where the cross-field momentum transport term has been written as a divergence of a flux, i.e. $(\mathbf{V}_E \cdot \boldsymbol{\nabla}_\perp)V_{||i} = \boldsymbol{\nabla}_\perp \cdot \boldsymbol{\Gamma}$, where

$$\Gamma_x = \frac{\sigma_\varphi}{|B_\varphi|}\frac{\partial\phi}{\partial y}v_{||i} \tag{5.3.3}$$

and

$$\Gamma_y = -\frac{\sigma_\varphi}{|B_\varphi|}\frac{\partial\phi}{\partial x}v_{||i} \tag{5.3.4}$$

correspond to, respectively, the radial and poloidal fluxes of parallel ion velocity. In Eq. (5.3.2) we have assumed that $\overline{\tilde{V}_{||i}\nabla_{||}\tilde{V}_{||i}} \ll \bar{V}_{||i}\nabla_{||}\bar{V}_{||i}$ and similarly for the pressure term. This is justified because the ratio of the fluctuating and equilibrium terms is at most (if fluctations correlate perfectly) of the order of $k_{||}L_{||}(\tilde{V}_{||i}/c_s)^2$, which is small in typical SOL conditions where $k_{||}L_{||} \sim 1$ and $\tilde{V}_{||i}/c_s \sim 0.1-0.5$ [151]. Assuming toroidal axisymmetry, equilibrium quantities only depend on x and y, thus we can replace $\nabla_{||}$ with $\alpha\sigma_\theta\partial_y$ and, therefore,

$$\alpha\sigma_\theta\bar{V}_{||i}\frac{\partial\bar{V}_{||i}}{\partial y} + \boldsymbol{\nabla}_\perp \cdot \overline{\boldsymbol{\Gamma}} + \frac{\alpha\sigma_\theta}{m_i\bar{n}}\frac{\partial\bar{p}}{\partial y} = 0\ . \tag{5.3.5}$$

The time-average of the radial momentum flux is the sum of a turbulent and an equilibrium term,

$$\overline{\Gamma}_x = \Gamma_x^T + \Gamma_x^E = \frac{\sigma_\varphi}{|B_\varphi|}\overline{\tilde{V}_{||i}\frac{\partial\tilde{\phi}}{\partial y}} + \frac{\sigma_\varphi}{|B_\varphi|}\bar{V}_{||i}\frac{\partial\bar{\phi}}{\partial y} \quad , \tag{5.3.6}$$

and an analogous expression is valid for $\overline{\Gamma}_y$. We first evaluate Γ_x^T, by starting with the estimate of the fluctuations of the parallel ion velocity. Linearizing Eq. (5.3.1) around the equilibrium, and keeping the leading order terms, we have

$$\gamma\tilde{V}_{||i} \sim \frac{\sigma_\varphi}{|B_\varphi|}\frac{\partial\bar{V}_{||i}}{\partial x}\frac{\partial\tilde{\phi}}{\partial y} \tag{5.3.7}$$

where γ is the linear growth rate of the dominant mode. From Eq. (5.3.7) it follows $\Gamma_x^T \sim \overline{(\partial_y\tilde{\phi})^2}$; we are thus led to estimate the amplitude of the poloidal electric field fluctuations. Linearizing the pressure continuity equation, and keeping the dominant terms, we have

$$\gamma\tilde{p} \sim \frac{\sigma_\varphi}{|B_\varphi|}\frac{\partial\tilde{\phi}}{\partial y}\frac{\partial\bar{p}}{\partial x} \ . \tag{5.3.8}$$

It is possible to relate the pressure fluctuations $\tilde{p}$ with its equilibrium value $\bar{p}$ by assuming that the mode growth saturates when the fluctuations are able to remove the instability drive, which is provided by the pressure gradient, i.e. when $\partial_x\tilde{p} \sim \partial_x\bar{p}$. Numerical simulations show that this saturation mechanism can be used to accurately describe the properties of SOL turbulence [110]. Equation (5.3.8) can thus be written as

$$\frac{\sigma_\varphi}{|B_\varphi|}\frac{\partial\tilde{\phi}}{\partial y} \sim \frac{\gamma}{k_x} \tag{5.3.9}$$

where k_x gives the radial extension of the saturated turbulent eddies. This can be estimated using non-local linear theory as $k_x = \sqrt{k_y/L_p}$ [101]. Combining Eqs. (5.3.7) and (5.3.9) we get an expression for the turbulent part of the time-averaged radial momentum flux,

$$\Gamma_x^T = -\frac{\gamma}{k_y}L_p\frac{\partial\bar{V}_{||i}}{\partial x} \ . \tag{5.3.10}$$

At this point we need to give an estimate of the ratio γ/k_y, which should be computed by using the values of γ and k_y of the modes that play the dominant role in the transport. As transport in the SOL is typically dominated by resistive ballooning modes [150, 114], one can use the corresponding ballooning growth rate

$\gamma_b = c_s\sqrt{2/RL_p}$ and wavenumber $k_b = \sqrt{\omega_{ci}B/\gamma_b q^2R^2en\nu_\parallel}$ [123]. However, it is also possible to use the more general relation (see Appendix D for a derivation)

$$L_p \sim \frac{qR}{c_s}\left(\frac{\gamma}{k_y}\right)_{max} , \tag{5.3.11}$$

to express the ratio γ/k_y as a function of L_p. This relation results from a pressure balance between parallel streaming and perpendicular turbulent transport, and has been shown to predict with high accuracy the pressure scale length L_p in global simulations of SOL turbulence [114]. Also, Eq. (5.3.11) has been used to express L_p as a function of the SOL operational parameters, showing good agreement with experimental data from a number of tokamaks [116]. By using Eq. (5.3.11) we can finally write the turbulent part of the time-averaged radial momentum flux, valid for all SOL turbulent regimes, as

$$\Gamma_x^T = -D_{turb}\frac{\partial \bar{V}_{||i}}{\partial x} , \tag{5.3.12}$$

where

$$D_{turb} = \frac{L_p^2 c_s}{qR} \tag{5.3.13}$$

has units of a diffusion coefficient and results from the net momentum transport arising from saturated turbulence. An estimate of the order of magnitude of D_{turb} for typical SOL parameters gives $D_{turb} \sim 1$ m^{2}s^{-1}. Notice that Eq. (5.3.12) is an expression that only involves equilibrium quantities, and that D_{turb} can be written as a function of the tokamak operational parameters. From Eq. (5.3.12) we can also evaluate the relative importance of the equilibrium and turbulent parts of the radial momentum transport. A rough estimate gives $\Gamma_x^E/\Gamma_x^T \sim \rho_s/L_p$, thus the radial momentum transport is mainly turbulent and we shall neglect the equilibrium contribution.

We now focus our attention on the time-average of the poloidal momentum turbulent flux. From Eq. (5.3.7) we have that $\Gamma_y^T \sim \overline{\partial_y\tilde{\phi}\partial_x\tilde{\phi}}$ which is expected to average to approximately zero. In fact, if the potential perturbation has the form $\tilde{\phi} = \tilde{\phi}_0(x)\exp\left[i(k_y y - \omega t)\right]$ where $\tilde{\phi}_0(x)$ describes the radial envelope of the mode, then $\overline{\partial_y\tilde{\phi}\partial_x\tilde{\phi}} = 0$. It follows that $\overline{\Gamma}_y \simeq \Gamma_y^E$ and Eq. (5.3.5) can finally be written as

$$-\frac{\partial}{\partial x}\left(D_{turb}\frac{\partial \bar{V}_{||i}}{\partial x}\right) - \frac{\sigma_\varphi}{|B_\varphi|}\frac{\partial\bar{\phi}}{\partial x}\frac{\partial \bar{V}_{||i}}{\partial y} + \alpha\sigma_\theta\bar{V}_{||i}\frac{\partial \bar{V}_{||i}}{\partial y} + \frac{\alpha\sigma_\theta}{m_i\bar{n}}\frac{\partial\bar{p}}{\partial y} = 0 \quad . \tag{5.3.14}$$

When taking the divergence of the flux, we have neglected the curvature term that arises from the variation of the magnetic field, as $R/L_\perp \gg 1$ in the SOL, and $\bar{V}_{||i}\partial^2_{xy}\bar{\phi}$

has been neglected with respect to $\partial_y \bar{V}_{||i} \partial_x \bar{\phi}$.

Equation (5.3.14) is a differential equation for the equilibrium parallel ion flow $\bar{V}_{||i}(x,y)$, which describes the balance between radial diffusion due to the time-averaged turbulent transport (first term), poloidal convection (second term), parallel convection (third term) and momentum generation by the pressure force (fourth term). Equation (5.3.14) can in principle be solved once $\bar{\phi}(x,y)$ and $\bar{p}(x,y)$ are known. We remark that the radial dependence of D_{turb} leads to a term that acts as an effective radial convection with velocity $v_{turb} = D_{turb}/2L_T > 0$, thus directed radially outwards. Here $L_T^{-1} = |\partial_x(T_e + T_i)/(T_e + T_i)|^{-1}$ corresponds to the radial scale length of the temperature profile.

5.3.2 1D equation for the equilibrium toroidal flow

The solution of Eq. (5.3.14) requires boundary conditions for $\bar{V}_{||i}$ in the radial direction, at the separatrix and at the vessel wall, and in the poloidal direction, at the limiter or divertor plates. The latter are given by the magnetic presheath entrance condition, see Eq. (2.4.29),

$$V_{||i}^{\pm} = \pm \sigma_\theta c_s^{\pm} + \frac{\sigma_\theta \sigma_\varphi}{\alpha |B_\varphi|} \frac{\partial \phi}{\partial x}\bigg|^{\pm} \tag{5.3.15}$$

at $y = \pm L_y/2$ respectively (the θ_n and θ_T corrections to Eq. (5.3.15) are neglected here for simplicity). We note that, as already discussed in Sec. 5.2, the $\mathbf{E} \times \mathbf{B}$ drift correction in Eq. (5.3.15) introduces an asymmetry in the ion parallel flow between the two limiter sides or divertor plates, thus providing a mechanism for net toroidal flow generation.

We now make some further assumptions on the equilibrium profiles in order to progress analytically and find a solution $\bar{V}_{||i}(x,y)$ that satisfies Eq. (5.3.14) with boundary conditions given by Eq. (5.3.15). Let us assume that the equilibrium profiles can be Taylor expanded in the y direction, so that

$$\bar{V}_{||i}(x,y) = u_0(x) + u_1(x) y + u_2(x) y^2. \tag{5.3.16}$$

and similarly for $\bar{\phi}$, $\bar{n}$ and $\bar{T}_e$. This choice is justified by the following argument. In the limit of no turbulence, the ion continuity equation, $\nabla_\parallel (n V_{||i}) + \boldsymbol{\nabla}_\perp (n \mathbf{V}_{\perp i}) = 0$, implies that the poloidal profile of $\bar{V}_{||i}$ follows the Pfirsch-Schluter ion current [16, 152], $\bar{V}_{||i}^{PS} \sim 2 q V_E \cos\theta$. However, the contribution of turbulence in the continuity equation is larger by a factor

$$\frac{\text{Turbulence}}{\text{Pfirsch-Schluter}} \sim \frac{D_{turb}\, \bar{n}/L_n^2}{\cos\theta\, \bar{n} V_E/R} \sim \frac{1}{q \cos\theta} \frac{c_s}{V_E} \sim \frac{1}{q\cos\theta} \frac{L_\perp}{\rho_s} \gg 1\,. \tag{5.3.17}$$

Therefore if turbulence in the SOL does not have a strong poloidal dependence, as has been revealed by numerical simulations of ballooning turbulence [113], the continuity equation gives $\nabla_\parallel(nV_{\parallel i}) \sim const$ and thus a poloidal profile of $\bar{V}_{\parallel i}$ close to linear, as taken into account in Eq. (5.3.16). Imposing the sheath boundary conditions, Eq. (5.3.15), we find the following constraints for the Taylor coefficients:

$$u_1(x) = \left(\bar{V}^+_{\parallel i} - \bar{V}^-_{\parallel i}\right)/L_y \tag{5.3.18}$$

$$u_2(x) = 4\left(u_{sh} - u_0(x)\right)/L_y^2 \tag{5.3.19}$$

where

$$u_{sh}(x) = \left(\bar{V}^+_{\parallel i} + \bar{V}^-_{\parallel i}\right)/2 \tag{5.3.20}$$

represents the asymmetry in the poloidal profile of $\bar{V}_{\parallel i}$ that is introduced by the sheath boundary conditions. The only unconstrained Taylor coefficient is then $u_0(x)$. An equation for $u_0(x)$ can be obtained by inserting Eq. (5.3.16) into Eq. (5.3.14), which leads to

$$-\lambda^2\frac{\partial^2 u_0}{\partial x^2} + \frac{\lambda^2}{2L_T}\frac{\partial u_0}{\partial x} = u_0^\infty - u_0 \quad , \tag{5.3.21}$$

where

$$u_0^\infty = \frac{\sigma_\theta\sigma_\varphi}{\alpha|B_\varphi|}\frac{\partial\phi_0}{\partial x} - \frac{\sigma_\theta p_1}{m_i n_0|u_1|} \tag{5.3.22}$$

and

$$\lambda = \sqrt{D_{turb}/\alpha|u_1|} \quad . \tag{5.3.23}$$

Here we have used the fact that the sign of $u_1(x)$ is at the leading order given by the sign of the poloidal magnetic field, i.e. $u_1 = \sigma_\theta|u_1|$, as implied by Eq. (5.3.15). We are thus left with a one-dimensional differential equation for $u_0(x)$, Eq. (5.3.21), which represents the momentum balance at the zeroth order in y.

5.3.3 Approximate analytical solution

Equation (5.3.21) can be solved analytically assuming that both u_0^∞ and λ remain about constant along x. Under these assumptions, the solution of Eq. (5.3.21) that is regular at $x \to \infty$ is

$$u_0(x) = (u_0^s - u_0^\infty)e^{-x/l} + u_0^\infty \tag{5.3.24}$$

where we impose $u_0^s = u_0(0)$ at the separatrix, and

$$l = \frac{\lambda^2}{4L_T} + \sqrt{\lambda^2 + \left(\frac{\lambda^2}{4L_T}\right)^2}. \tag{5.3.25}$$

For typical SOL parameters, $\lambda \sim L_T$ and therefore $l \sim L_T$. Equations (5.3.18), (5.3.19), and (5.3.24), provide the expression of u_0, u_1, and u_2 in Eq. (5.3.16), and thus of the function $\bar{V}_{||i}(x,y)$, once u_0^s, u_0^∞, and u_{sh} are known.

An estimate of u_{sh} can be obtained by writing $T_e \equiv T$ and $T_i = \tau T$, and assuming a potential of the order of the sheath potential barrier $e\phi_0 \approx \Lambda T_0$. This gives

$$u_{sh} \sim -\sigma_\theta \sigma_\varphi \frac{\Lambda}{(1+\tau)\alpha} \frac{\rho_{s0}}{L_T} c_{s0} \quad , \tag{5.3.26}$$

where $c_{s0} = \sqrt{T_0(1+\tau)/m_i}$ and $T_0 \sim e^{-x/L_T}$ is the lowest order coefficient in the Taylor expansion of T, akin to that in Eq. (5.3.16).

An estimate of u_0^∞ can be obtained as follows. The pressure poloidal asymmetry term in Eq. (5.3.22) is $\sigma_\theta p_1/(m_i n_0 |u_1|) = \sigma_\theta c_{s0}(\delta n + \delta T)/2$, where $\delta n = (n_1/n_0)L_y$ and similarly for δT. We recall that p_1 is the first order coefficient in the Taylor expansion of the pressure profile, and similarly for n and T. Assuming for example that $n_1 \sim (n^+ - n^-)/L_y$, we can estimate δn as the normalized density difference between the two divertor legs or limiter sides, namely $\delta n = (n^+ - n^-)/n_0$, and similarly for δT. This gives

$$u_0^\infty \sim u_{sh} - \frac{\sigma_\theta}{2}(\delta n + \delta T) c_{s0} \quad . \tag{5.3.27}$$

On the other hand, the value of u_0^s cannot be justified solely from SOL physics; a consistent choice should arise from the matching of the solution of Eq. (5.3.14) with the toroidal rotation profile in the closed-flux surface region. We remark that an equivalent situation is encountered when studying rotation in the closed flux surface region [153,154]. In the following, we explicit the solution of Eq. (5.3.14) and discuss a number of implications that are independent of the choice of u_0^s.

In order to easily interpret the toroidal plasma rotation resulting from Eq. (5.3.14), we consider the function

$$M = -\sigma_\theta \sigma_\varphi \frac{\bar{V}_{||i}}{c_{s0}} \quad , \tag{5.3.28}$$

which is the parallel Mach number projected in the toroidal direction along the plasma current I_p, such that $M > 0$ always means co-current toroidal rotation. The approximate solution of Eq. (5.3.14) gives

$$\begin{aligned} M(x,y) = {} & M_s e^{-x/l} + (M_{sh} + M_a)\left(1 - e^{-x/l}\right) \\ & - 2\sigma_\theta \sigma_\varphi \frac{y}{L_y} \\ & + 4\left[(M_{sh} + M_a - M_s)\, e^{-x/l} - M_a\right] \frac{y^2}{L_y^2} \end{aligned} \tag{5.3.29}$$

where $M_s = M(0,0) = -\sigma_\theta \sigma_\varphi u_0^s / c_{s0}$ is the separatrix condition half way between the two limiter sides or divertor legs, $M_{sh} = \Lambda \rho_{s0}/(\alpha(1+\tau)L_T) \sim e^{-x/2L_T}$ represents the effect of the sheath on plasma rotation, and $M_a = \sigma_\varphi(\delta n + \delta T)/2$ is due to the pressure poloidal asymmetry. We remark that the sheath physics determine the value of M_{sh} by setting both the ion flow $\bar{V}_{||i}$ at the boundaries and the radial electric field $\partial_x \phi$ in the main plasma.

Equation (5.3.29) is an analytical expression for the toroidal Mach number in the poloidal plane. We would like to notice that since we did not solve the ion continuity equation, our prediction requires the knowledge of the density and temperature at the end of the field lines, i.e. δn and δT. However, these are typically measured in tokamaks [127] and hence it is possible to compare the prediction of Eq. (5.3.29) with experimental measurements. But first, let us make a comparison with the GBS simulation results, in order to assess the validity of the theoretical model derived herein.

5.4 Comparison with SOL turbulence simulations

In this section, we compare some of the main assumptions and theoretical predictions derived in Sec. 5.3 with the results of GBS simulations carried out with the limiter at four different positions, namely on the high field side ($\theta_l = \pi$), on the low field side ($\theta_l = 0$), on the top ($\theta_l = \pi/2$) and on the bottom ($\theta_l = -\pi/2$).

We start by considering the time-averaged radial and poloidal momentum fluxes, $\bar{\Gamma}_x$ and $\bar{\Gamma}_y$, as defined in Eq. (5.3.6). In Sec. 5.3 we assume that the radial flux is mainly due to turbulence while the poloidal flux is mainly due to equilibrium convection, namely $\bar{\Gamma}_x \simeq \Gamma_x^T$ and $\bar{\Gamma}_y \simeq \Gamma_x^E$.
Figure 5.4.1 shows the profile of $\bar{\Gamma}_x$ in the unfolded poloidal plane, together with its components Γ_x^T and Γ_x^E, for the case $\theta_l = \pi$ (limiter on the high field side). The largest contribution to $\bar{\Gamma}_x$ clearly comes from Γ_x^T, except for the region close to the limiter plates, where the presheath electric field, which is in the poloidal direction, produces an $\mathbf{E} \times \mathbf{B}$ flow in the radial direction. We can nevertheless conclude that the assumption $\bar{\Gamma}_x \simeq \Gamma_x^T$ is reasonable in most of the domain.
Figure 5.4.2 shows the profile of $\bar{\Gamma}_y$ in the unfolded poloidal plane, together with its components Γ_y^T and Γ_y^E, for the same simulation. The turbulent component is negligible and hence the assumption $\bar{\Gamma}_y \simeq \Gamma_y^E$ is very good. Figures 5.4.3 and 5.4.4 show that the same conclusions apply to the case $\theta_l = -\pi/2$ (limiter on the bottom).

We now focus on the estimate of the turbulent momentum flux, Γ_x^T, which we assumed to result from the net transport arising from saturated turbulence, Eq. (5.3.12). Figure 5.4.5 shows the theoretical prediction for Γ_x^T as given by Eq.(5.3.12) and compares it to the value obtained from GBS simulation results with $\theta_l = \pi$. The

agreement is rather good, and the same conclusion applies to the case $\theta_l = -\pi/2$, as shown in Fig. 5.4.6.

Finally, we consider the equilibrium Mach number $M(x, y)$ as defined in Eq. (5.3.28). Figures 5.4.7, 5.4.8, 5.4.9 and 5.4.10, show the corresponding profile of $M(x, y)$ and its analytical prediction given by Eq. (5.3.29), for the four limiter positions. The agreement is generally rather good, as the prediction captures both the magnitude and the radial and poloidal structure of the Mach number. For comparison, the profile of $M(x, y)$ as given by Eq. (5.3.29) in the limit of no turbulence, i.e. taking $D_{turb} \to 0$, is also shown. This emphasizes the importance of the turbulent momentum transport in the description of the equilibrium rotation profiles. In particular, the volume-averaged Mach number, $\langle M \rangle_{x,y}$, is only well reproduced when using Eq. (5.3.29) with the appropriate value of D_{turb}, as shown in Table 5.1.

	$\langle M_{sim} \rangle_{x,y}$	$\langle M_{th} \rangle_{x,y}$	$\langle M_{th,noturb} \rangle_{x,y}$
$\theta_l = 0$	0.12	0.08	0.02
$\theta_l = \pi$	0.30	0.32	0.53
$\theta_l = \pi/2$	0.26	0.36	0.65
$\theta_l = -\pi/2$	0.05	0.05	-0.06

Table 5.1: Volume-averaged Mach number, $\langle M \rangle_{x,y}$, for different limiter positions and as given by the simulation results (left column), from Eq. (5.3.29) (middle column), and from Eq. (5.3.29) in the limit $D_{turb} \to 0$.

We conclude this section by discussing the main possible sources of discrepancy between the simulated Mach number and its theoretical prediction given by Eq. (5.3.29). First, the equilibrium component of the radial momentum flux, Eq. (5.3.6), has been neglected. However, as shown in Fig. 5.4.3, its contribution may become important in the vicinity of the limiter. Second, the Taylor expansion of the equilibrium ion parallel velocity, Eq. (5.3.16), is not always very accurate, especially when the poloidal asymmetries are strong. Considering higher order terms in the expansion may require to solve the continuity equation and to take into account the poloidal dependence of the turbulence drive, e.g. considering that $D_{turb} = D_{turb}(\theta)$. Third, Eq. (5.3.21) has been solved analytically by assuming that its right hand side is about constant, although it has a radial dependence. Finally, the term related to the effect of the sheath, Eq. (5.3.21), has been computed by assuming that the radial electric field has no poloidal dependence. However, as discussed in Chapter 4, this is in general not true. In fact, strong poloidal asymmetries yield significantly different radial electric fields at the two sides of the limiter.

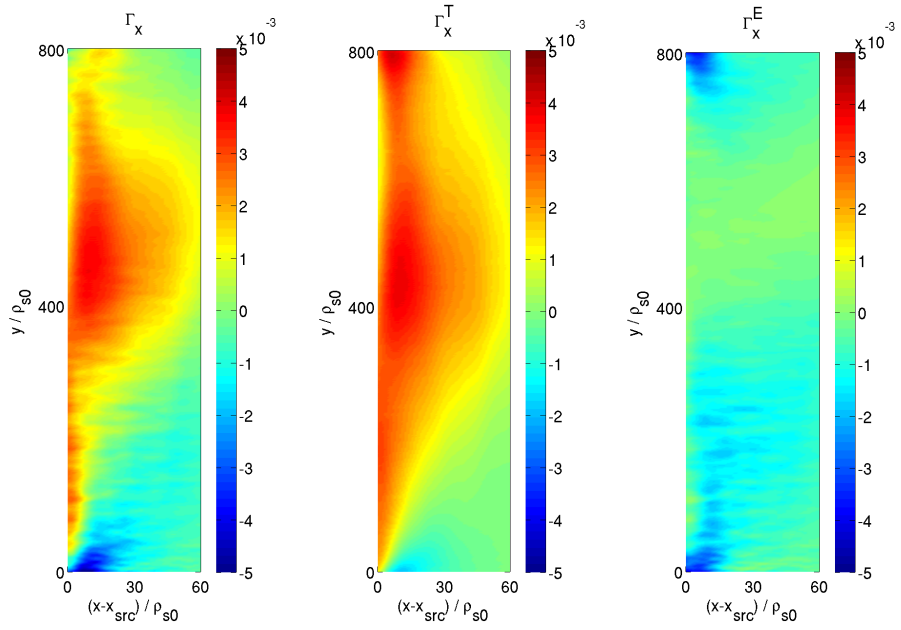

(a) (b) (c)

Figure 5.4.1: Time-averaged radial momentum flux in the unfolded poloidal plane, computed from GBS simulation results with $\theta_l = \pi$. (a) $\bar{\Gamma}_x$ as defined in Eq. (5.3.6), (b) its turbulent component Γ_x^T, and (c) its equilibrium component Γ_x^E.

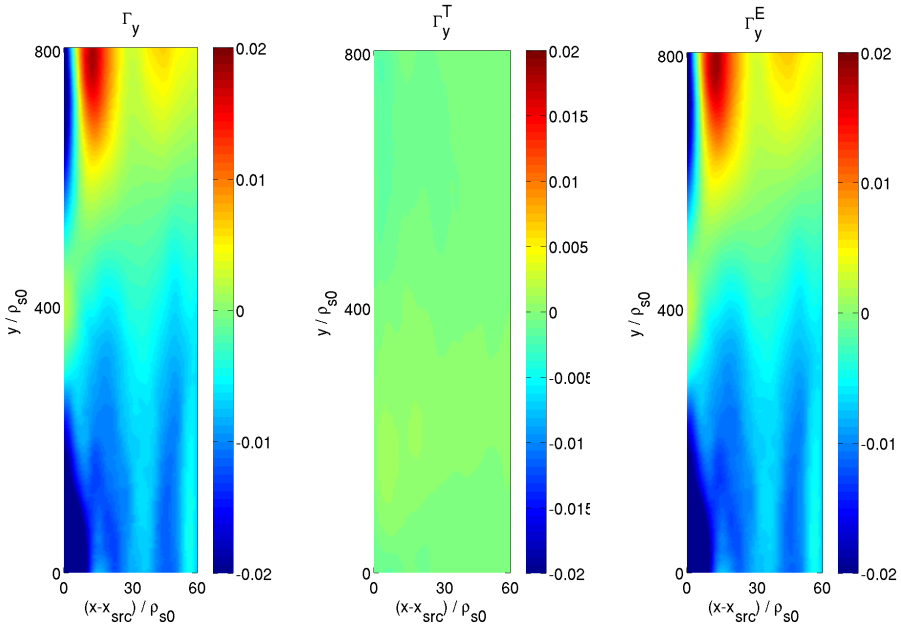

(a) (b) (c)

Figure 5.4.2: Time-averaged poloidal momentum flux in the unfolded poloidal plane, computed from GBS simulation results with $\theta_l = \pi$. (a) $\bar{\Gamma}_y$ as defined in Eq. (5.3.6), (b) its turbulent component Γ_y^T, and (c) its equilibrium component Γ_y^E.

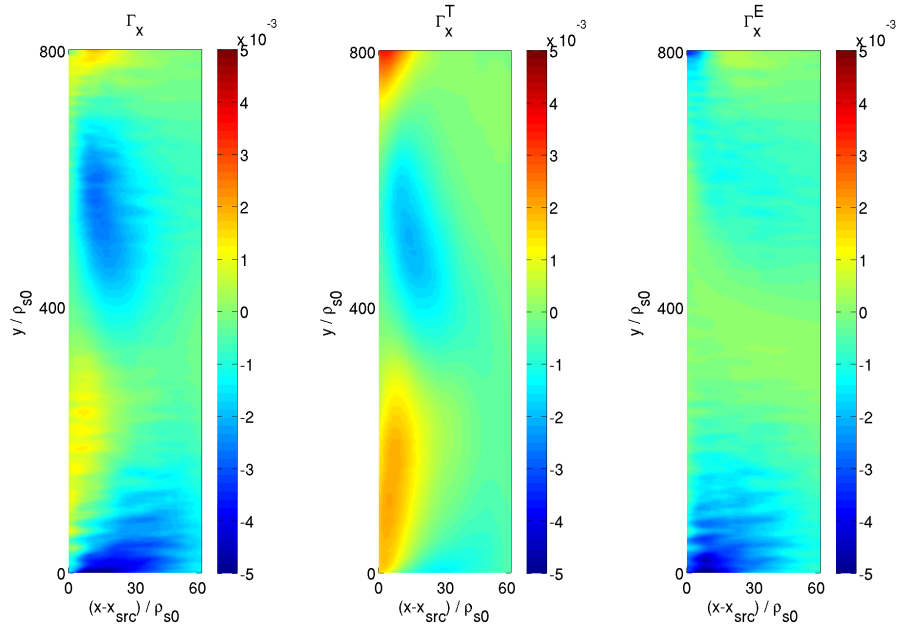

(a) (b) (c)

Figure 5.4.3: Time-averaged radial momentum flux in the unfolded poloidal plane, computed from GBS simulation results with $\theta_l = -\pi/2$. (a) $\bar{\Gamma}_x$ as defined in Eq. (5.3.6), (b) its turbulent component Γ_x^T, and (c) its equilibrium component Γ_x^E.

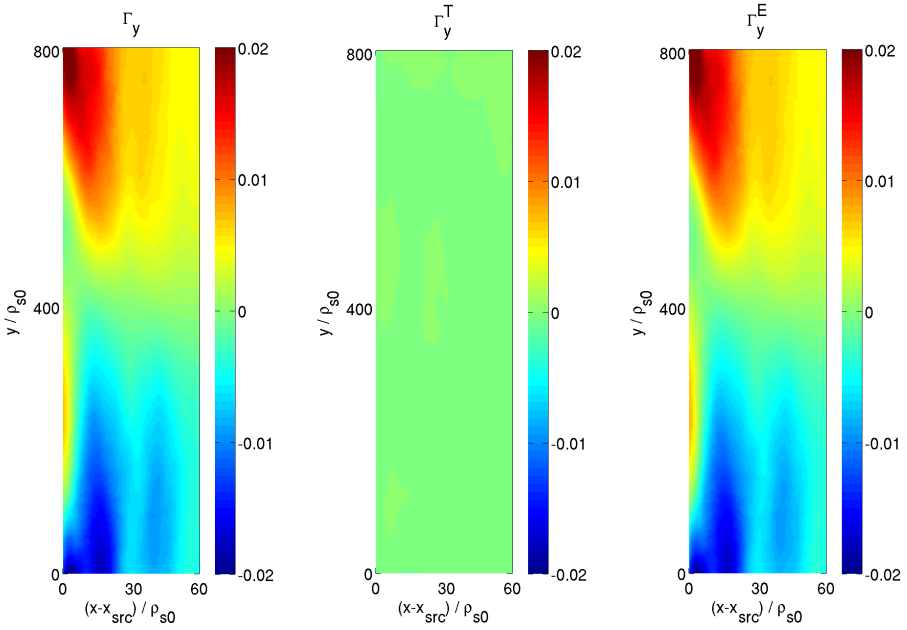

(a) (b) (c)

Figure 5.4.4: Time-averaged poloidal momentum flux in the unfolded poloidal plane, computed from GBS simulation results with $\theta_l = -\pi/2$. (a) $\bar{\Gamma}_y$ as defined in Eq. (5.3.6), (b) its turbulent component Γ_y^T, and (c) its equilibrium component Γ_y^E.

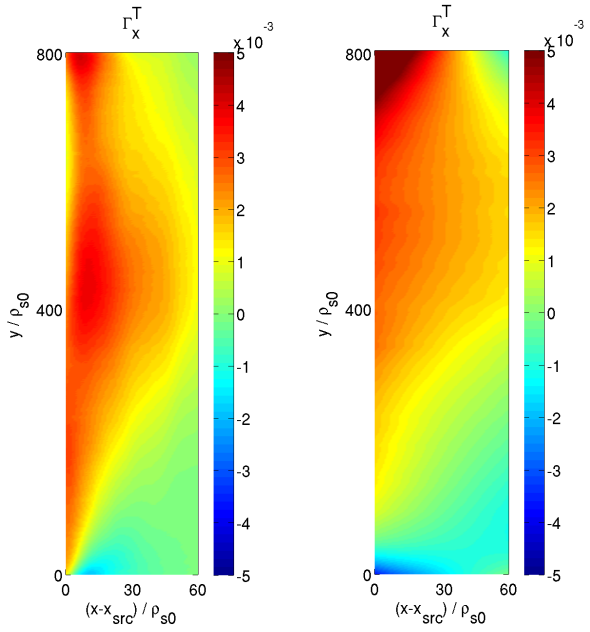

(a) (b)

Figure 5.4.5: Time-average of the turbulent radial momentum flux Γ_x^T in the unfolded poloidal plane, computed from (a) GBS simulation results with $\theta_l = \pi$, and (b) the theoretical prediction as given by Eq.(5.3.12).

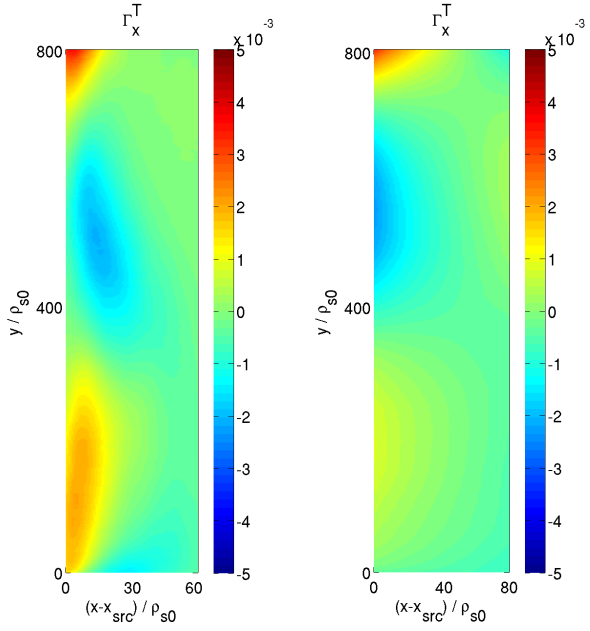

(a) (b)

Figure 5.4.6: Time-average of the turbulent radial momentum flux Γ_x^T in the unfolded poloidal plane, computed from (a) GBS simulation results with $\theta_l = -\pi/2$, and (b) the theoretical prediction as given by Eq.(5.3.12).

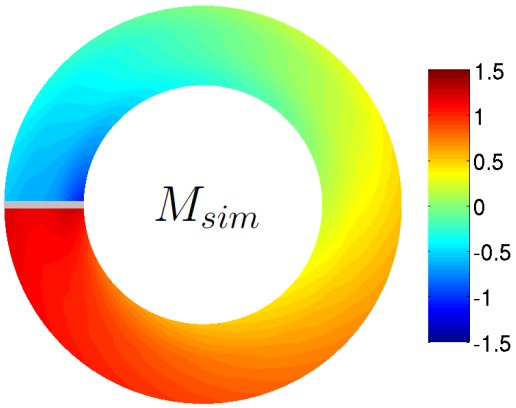

(a)

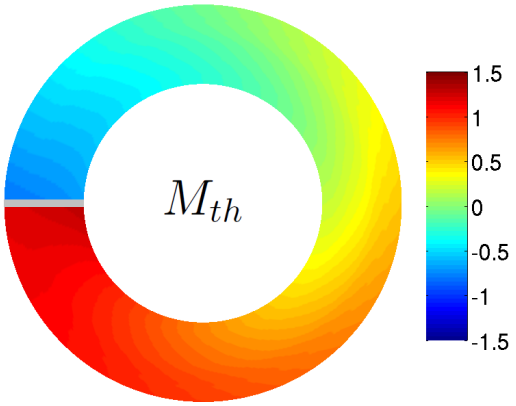

(b)

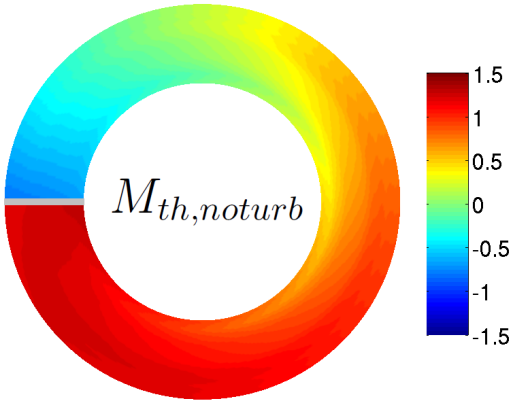

(c)

Figure 5.4.7: Poloidal profile of the time-averaged Mach number $M(x, y)$. (a) From GBS simulations with $\theta_l = \pi$. (b) As given by the prediction of Eq. (5.3.29). (c) As given by Eq. (5.3.29) in the limit of $D_{turb} \to 0$.

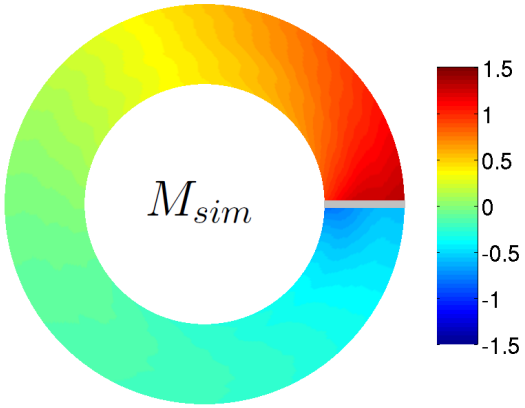

(a)

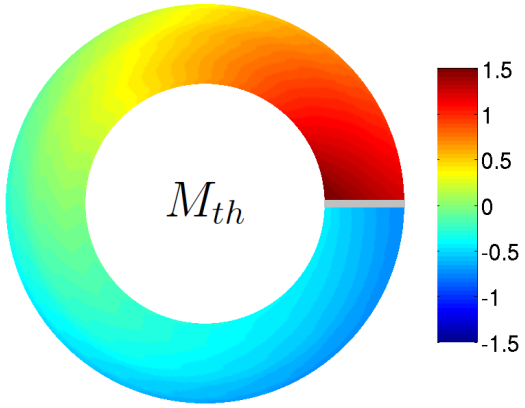

(b)

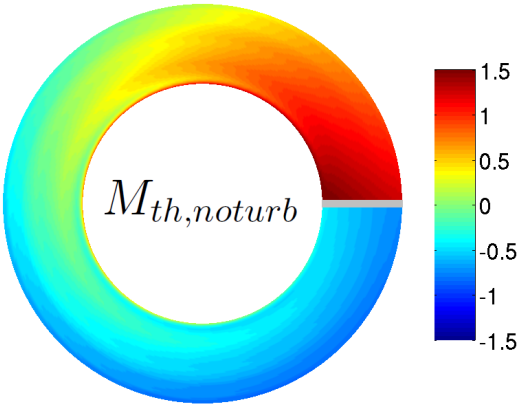

(c)

Figure 5.4.8: Poloidal profile of the time-averaged Mach number $M(x, y)$. (a) From GBS simulations with $\theta_l = 0$. (b) As given by the prediction of Eq. (5.3.29). (c) As given by Eq. (5.3.29) in the limit of $D_{turb} \to 0$.

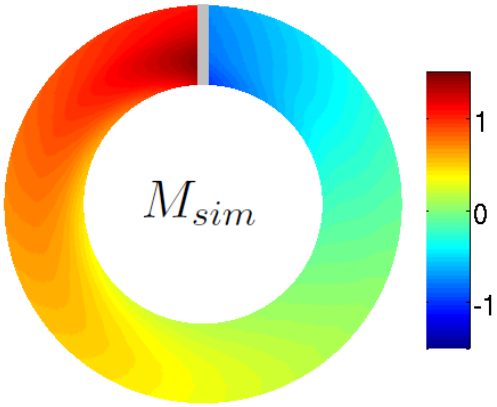

(a)

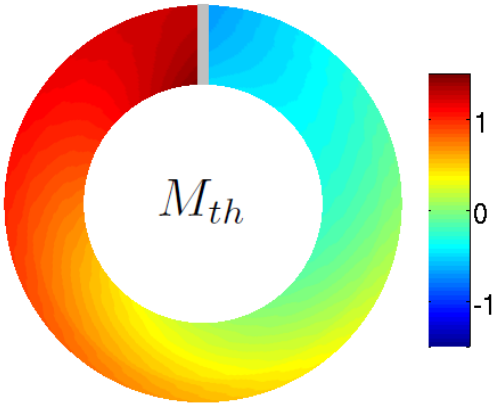

(b)

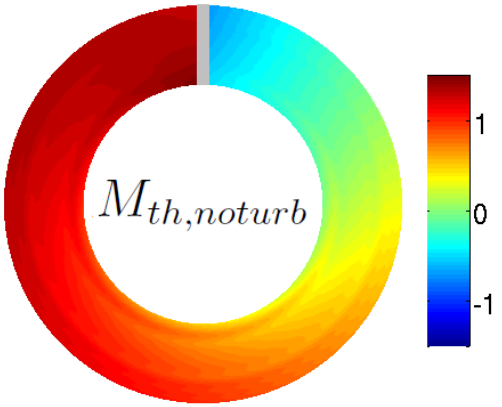

(c)

Figure 5.4.9: Poloidal profile of the time-averaged Mach number $M(x, y)$. (a) From GBS simulations with $\theta_l = \pi/2$. (b) As given by the prediction of Eq. (5.3.29). (c) As given by Eq. (5.3.29) in the limit of $D_{turb} \to 0$.

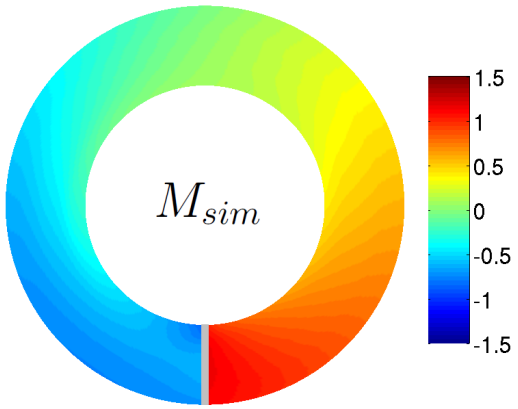

(a)

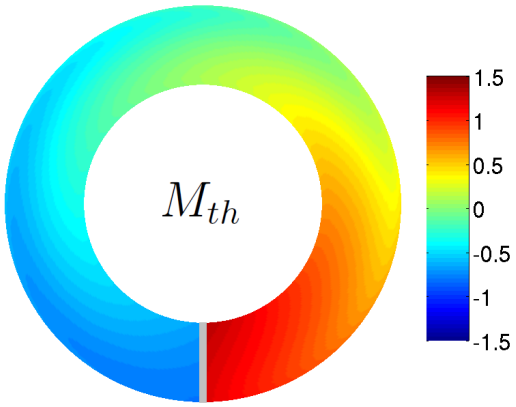

(b)

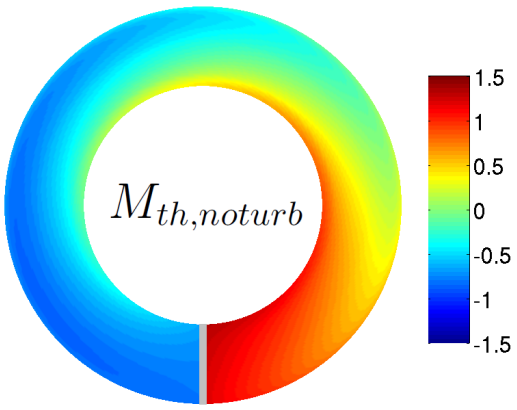

(c)

Figure 5.4.10: Poloidal profile of the time-averaged Mach number $M(x, y)$. (a) From GBS simulations with $\theta_l = -\pi/2$. (b) As given by the prediction of Eq. (5.3.29). (c) As given by Eq. (5.3.29) in the limit of $D_{turb} \to 0$.

5.5 Comparison with experimental trends

In this section, we show that the estimate of the toroidal Mach number profile given by Eq. (5.3.29) can explain the observed experimental trends for the toroidal rotation in the SOL of tokamaks.

First of all, the direction of the toroidal rotation is typically measured to be in the co-current direction, even when the toroidal magnetic field [155] or the total magnetic field [127] is reversed. This is captured by the term $M_{sh} > 0$ in Eq. (5.3.29) which always contributes to co-current flow regardless of the sign of $\mathbf{B}$. Moreover, we can estimate the magnitude of the toroidal rotation, which is typically measured to be $M \lesssim 1$. Taking typical SOL parameters, e.g. $\Lambda = 3$, $\alpha = 0.03 \simeq 2°$ and $\rho_s/L_T = 10^{-2}$ [126], we get $M_{sh} \simeq 0.5$.

It has been observed, nevertheless, that the magnitude and direction of toroidal rotation are not always exactly the same when reversing the magnetic field: rotation can become stronger or weaker in the co-current direction [155, 127], and under certain conditions it can even become counter-current [150]. We now show that this can be explained by the term $M_a \sim \sigma_\varphi \delta n$ in Eq. (5.3.29), which represents the effect of a pressure poloidal asymmetry. Far from the two divertor legs, $y/L_y \ll 1$, M_a gives a co-current contribution if $\sigma_\varphi \delta n > 0$ and a counter-current contribution if $\sigma_\varphi \delta n < 0$. The effect of this term is illustrated in Fig. 5.5.1 where the function $M(x, 0)$ is shown for different values of $\sigma_\varphi \delta n$, and for two different values of M_s, showing that the choice of the latter does not affect the trends explored here. This effect explains the differences in the net toroidal flow observed between SOL simulations with different limiter positions. As Table 5.2 shows, in fact, the net co-current toroidal flow is stronger when $\delta n > 0$ and weaker when $\delta n < 0$ ($\sigma_\varphi = 1$ in all cases). The mechanism responsible for the sign of δn is, as a matter of fact, the ballooning character of turbulent transport, which leads to a larger plasma pressure around the low field side, where the turbulence drive is the largest, with a peak that may be shifted poloidally by an equilibrium $\mathbf{E} \times \mathbf{B}$ flow, as sketched in Fig. 5.5.2. Thus the sign of δn depends on the position of the limiter with respect to the poloidal location of the pressure peak.

	$\langle M_{sim} \rangle_{x,y}$	δn
$\theta_l = 0$	0.12	< 0
$\theta_l = \pi$	0.30	> 0
$\theta_l = \pi/2$	0.26	> 0
$\theta_l = -\pi/2$	0.05	< 0

Table 5.2: Time and volume-averaged Mach number, $\langle M \rangle_{x,y}$, for different limiter positions and the corresponding sign of δn. For all cases $\sigma_\varphi = 1$.

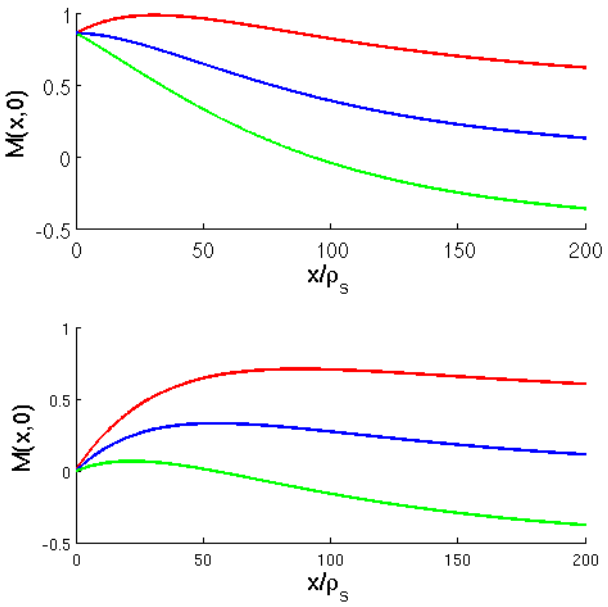

Figure 5.5.1: Profile of $M(x,0)$ for $\sigma_\varphi \delta n = 0.25$ (red), $\sigma_\varphi \delta n = 0$ (blue), and $\sigma_\varphi \delta n = -0.25$ (green). Top is for $M_s = M_{sh}(0)$ and bottom is for $M_s = 0$. Here $\alpha = 2°$ and $l = L_T = 50\rho_s$.

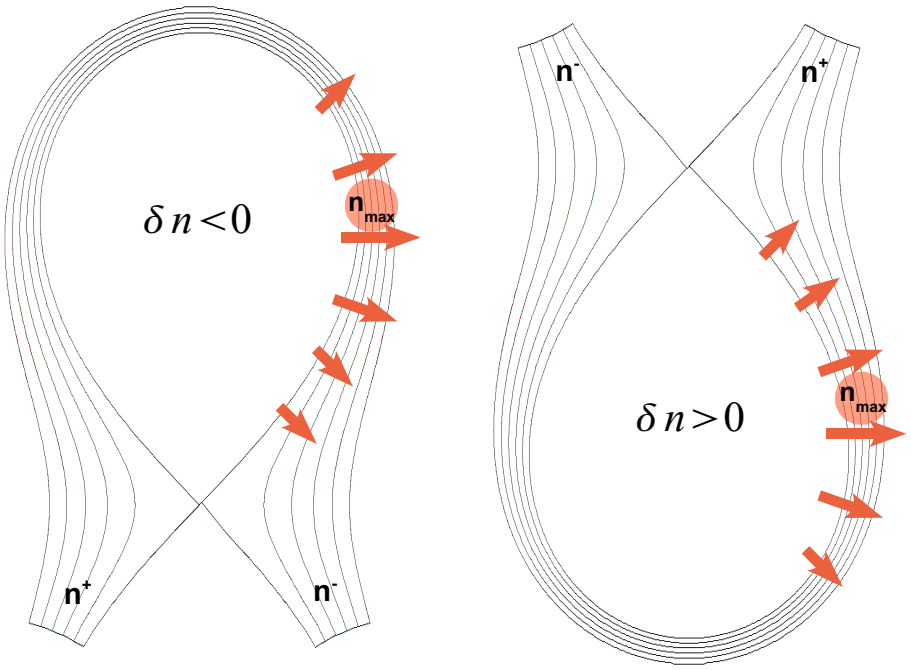

Figure 5.5.2: The effect of the ballooned transport on the poloidal pressure asymmetry. The maximum of the density is always around the LFS. Depending on the limiter or divertor position, this gives $\delta n \sim (n^+ - n^-) < 0$ (left) or $\delta n \sim (n^+ - n^-) > 0$ (right).

In a tokamak, if the plasma is diverted with a single null, one thus expects $\delta n < 0$ for a lower X-point and $\delta n > 0$ for an upper X-point, two configurations that have been explored in Alcator C-Mod [150]. As summarized in Fig. 5.5.3, in this tokamak it was concluded that favourable co-current situations in the SOL are those with *normal B, lower single null* ($\sigma_\varphi < 0$, $\delta n < 0$) and *reversed B, upper single null* ($\sigma_\varphi > 0$, $\delta n > 0$). Similarly, favourable counter-current situations are those with *normal B, upper single null* ($\sigma_\varphi < 0$, $\delta n > 0$) and *reversed B, lower single null* ($\sigma_\varphi > 0$, $\delta n < 0$). Therefore these observations are all consistent with the contribution of the term M_a. Similarly, this model may be used to explain the trends observed in the SOL of other tokamaks, e.g. the TCV tokamak [155] or the Tore Supra tokamak [156].

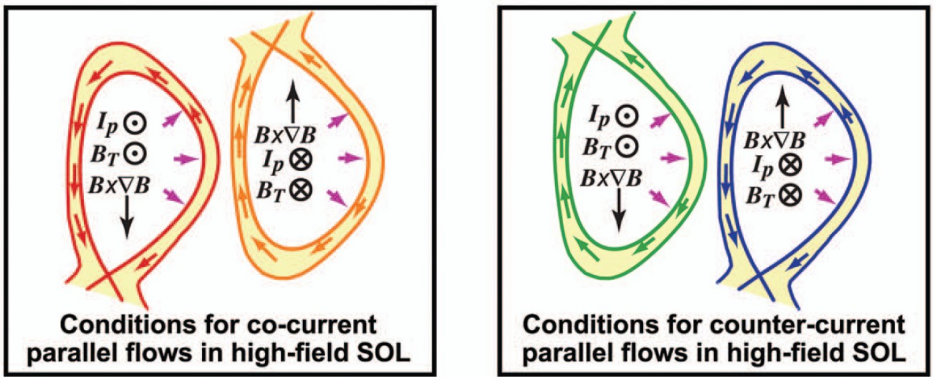

Figure 5.5.3: Cartoon drawings of X-point topologies, field directions, and poloidal projections of the parallel flows measured in the high field side SOL. From [127], with permission from the author.

5.6 Summary and outlook

In this Chapter, we have presented a first-principle based analytical theory to describe the generation and transport of toroidal plasma rotation in the SOL. The presence of the sheath, equilibrium poloidal $\mathbf{E} \times \mathbf{B}$ flows and pressure poloidal asymmetries can explain the origin of intrinsic rotation, which is radially transported by turbulence. The sheath physics leads to a co-current toroidal rotation, while the effect of the poloidal pressure asymmetry can explain the flow reversals observed in tokamaks. Such flow reversals may occur when either the magnetic field or the limiter/divertor position are reversed, and this is explained by the ballooning character of the turbulence. Our theoretical predictions agree rather well with three-dimensional simulations of SOL turbulence.

The main limitation of our model is that ionization and recombination processes, which may affect the poloidal profile of $\bar{V}_{||i}$, are not taken into account. This may

restrict the validity of the presented results to low-recycling regimes. Also, the theory derived herein ceases to be valid in regimes where turbulence is significantly suppressed and Pfirsch-Schluter ion flows play an important role, in particular in modulating the poloidal profile of the parallel ion velocity.

Finally, we would like to notice that the rotation theory presented here is also applicable to other open field line configurations, e.g. in simple magnetized toroidal devices such as TORPEX [21], where significant net toroidal flows have been observed [157]. Thanks to the two-dimensional Mach probe measurements performed in different magnetic configurations, TORPEX is a very good testbed in which to validate the theoretical predictions for the two-dimensional profile of the toroidal Mach number.

Chapter 6

Effects of the limiter position on the SOL equilibrium profiles

6.1 Introduction

The plasma start-up in ITER will be in a limited configuration [158], using either the inner or outer vessel wall as limiting surface (Figure 6.1.1). Since this part of the tokamak vessel is not designed to handle large particle and heat fluxes, the start-up scenario must be carefully tailored to minimize its power load. In the last years, dedicated experiments have been conducted in a number of tokamaks in order to characterize the fluctuations and equilibrium profiles in the SOL of limited plasmas [159, 160, 161, 162, 163, 164]. Substantially large asymmetries have been observed between the different explored configurations, e.g. for inner wall limited (IWL) versus outer wall limited (OWL) [163]. A common conclusion is that poloidally asymmetric parallel flows are both a cause and a symptom of these differences [165]. Along with these experimental studies, numerical models have been used to get insights on the underlying physical mechanisms that lead to such asymmetries [166, 167, 168]. The common conclusion is that the inclusion of anomalous, ballooning-like cross-field transport is required in order to reproduce the general qualitative behaviour observed in the experiments. However, such models included the anomalous transport in an *ad hoc* manner, namely via transport coefficient asymmetries or arbitrary unphysical forces [160].

In this chapter, we present the results of global, three-dimensional simulations of SOL turbulence carried out with the GBS code, which self-consistently contain, in particular, the physics of ballooning modes. Four different limiter positions are considered: high field side (HFS), low field side (LFS), top and bottom. We focus on the effect of the limiter position on the SOL width, the electrostatic potential and the toroidal rotation. For each case we give a qualitative explanation for the differences observed in the simulation results, by invoking the ballooning character of the turbulent transport and the effect that the limiter has on it.

We would like to notice that the SOL configuration considered herein is oversimplified with respect to the experiments (circular magnetic flux surfaces, no magnetic shear, cold ions, electrostatic, infinite aspect ratio, etc.). Therefore we do not target a quantitative comparison with experimental measurements. Yet, for the first time we provide global, flux-driven, full-n, three-dimensional simulations of plasma turbulence in different limited SOL configurations, with first-principle turbulent transport and self-consistent sheath boundary conditions.

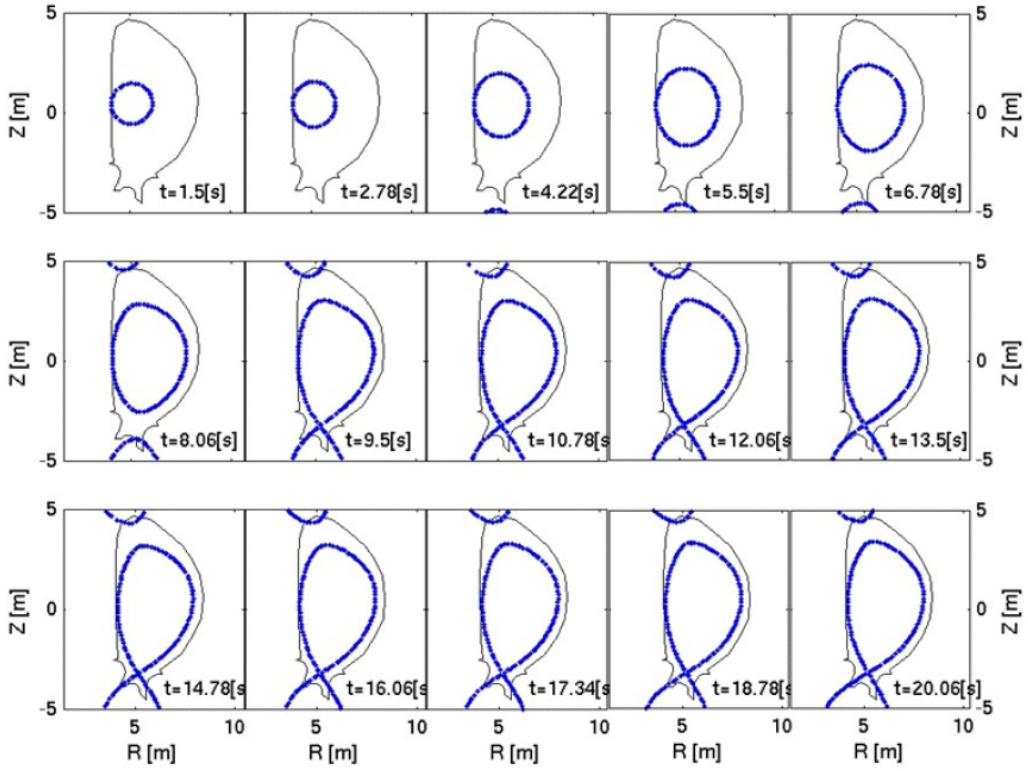

Figure 6.1.1: Simulated evolution of the plasma boundary in ITER, from the plasma initiation to the X-point formation. With permission from [158].

6.2 Effect on the scrape-off layer width

The peak heat load onto the plasma facing components of tokamak devices depends on the SOL width [169,164], which results from a balance between plasma injection from the core region, turbulent transport, and losses to the divertor or limiter plates [116]. Typically, the operational definition for the SOL width is the scale length λ_q of the radial profile of the parallel heat flux, $q_\parallel$, at the location of the limiter or divertor. Here we define the SOL width as the radial scale length of the plasma

pressure,

$$L_p = \left(\frac{1}{\bar{p}} \frac{\partial \bar{p}}{\partial x} \right)^{-1} , \tag{6.2.1}$$

which is computed from the simulation results by fitting, at each poloidal location, the equilibrium pressure profile with a radially decaying exponential function. We note that this simple fitting procedure has been recently questioned as some experimental measurements show two different scale lengths in the near and far SOL [164]. Our simulations do not show evidence of such phenomena. An example of a pressure radial profile resulting from a GBS simulation, together with its exponential fit, are shown in Fig. 6.2.1.

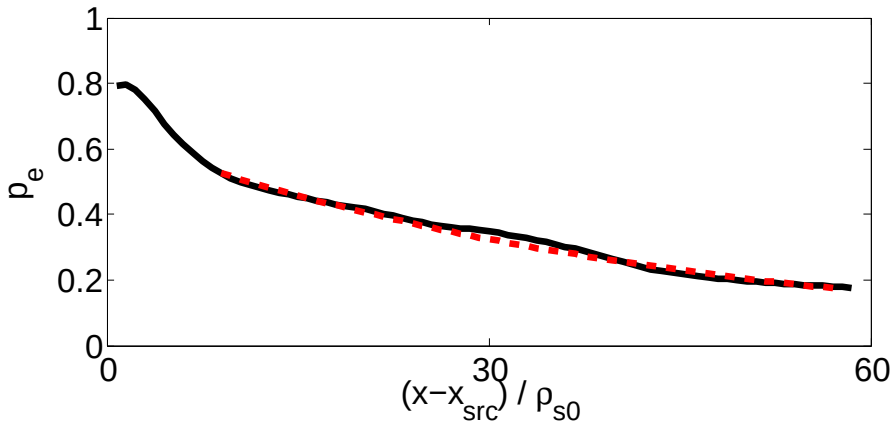

Figure 6.2.1: Example of equilibrium pressure profile on the low field side mid-plane ($\theta = 0$), for a simulation with the limiter on the high field side mid-plane ($\theta_l = \pi$). The source radial extension is approximately $10\rho_{s0}$. In the source-free region, a reasonable fit of the radial profile can be obtained with an exponential function (dashed red line), leading to $L_p \simeq 45\rho_{s0}$.

Figure 6.2.2 shows the equilibrium pressure profiles in a poloidal cross-section, for the four limiter configurations. The corresponding value of $L_p(\theta)$ is shown in Fig. 6.2.3. Clearly the value of L_p has a poloidal dependence, $L_p = L_p(\theta)$, which depends on the limiter configuration. We remark that the effect of the flux expansion is not present in these simulations, thus the poloidal dependence of L_p is only due to the poloidal asymmetries in the plasma turbulence and flows.

First of all, we observe that the value of L_p in the HFS-limited case (red curve in Fig. 6.2.3) is larger than in the LFS-limited case (blue curve in Fig. 6.2.3), as observed experimentally [163]. However there is less than a factor of 2 difference, while factors of 3 and higher have been obtained experimentally [161, 164]. Second,

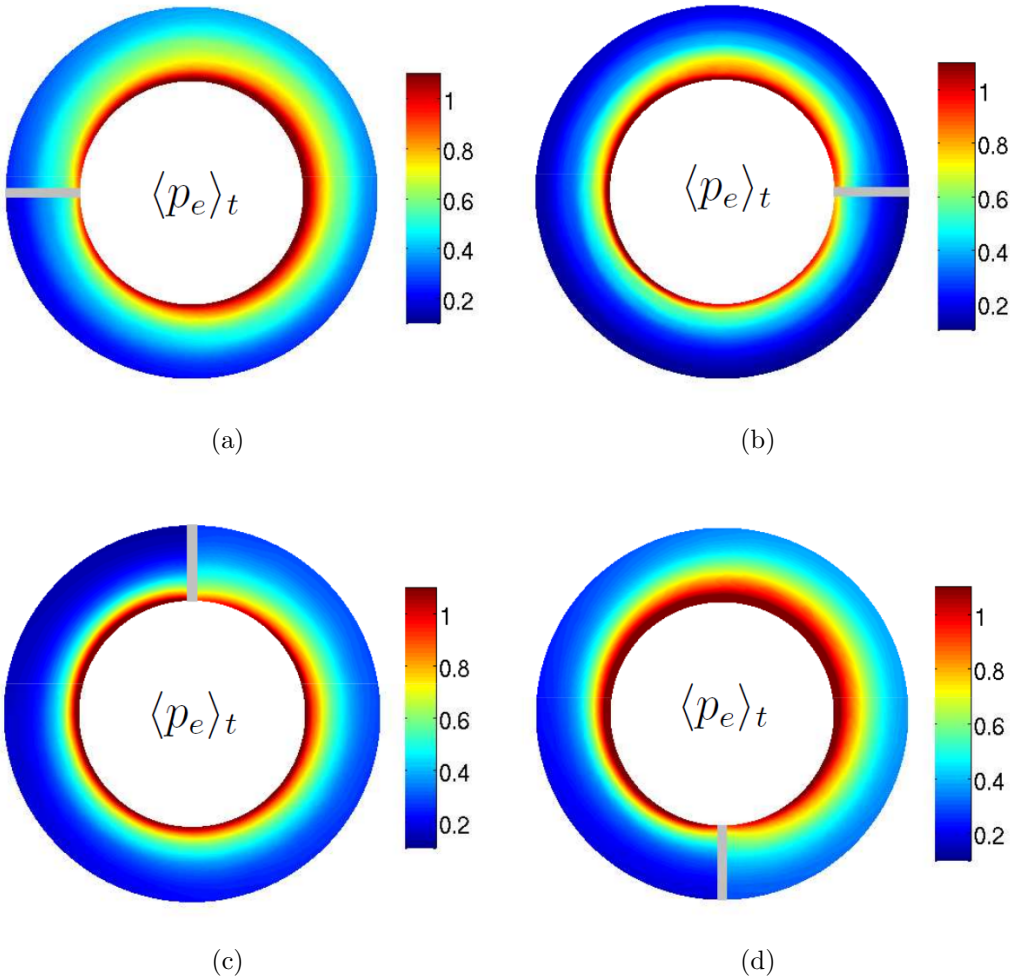

Figure 6.2.2: Equilibrium pressure profiles in a poloidal cross-section, with the limiter (a) on the HFS equatorial mid-plane, (b) on the LFS equatorial mid-plane, (c) on the top of the vessel, and (d) on the bottom of the vessel.

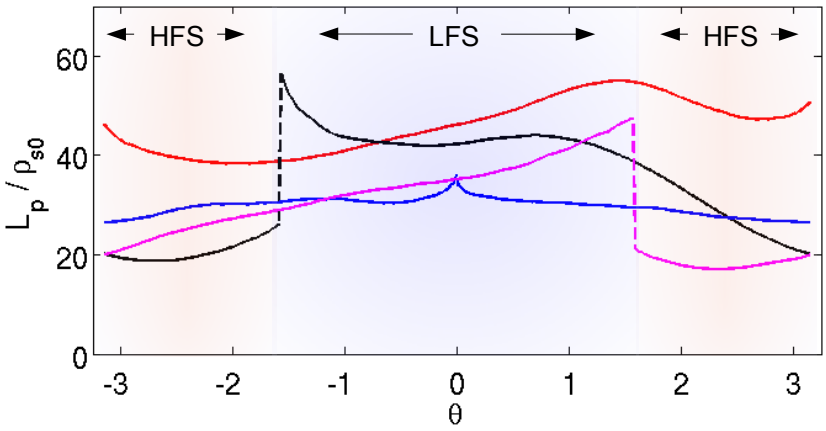

Figure 6.2.3: SOL width L_p as a function of the poloidal angle, for a limiter on the HFS (red), on the LFS (blue), on the top (magenta), and on the bottom (black).

in the four configurations considered, the values of L_p tend to be larger on the LFS than on the HFS, consistent with the ballooning character of the turbulent transport.

We note that $L_p(\theta)$ is not only modulated by a ballooned transport localized around $\theta = 0$. As a matter of fact the function $L_p(\theta)$ depends on the limiter configuration. Figure 6.2.4 shows the time-averaged turbulent radial flux of plasma pressure, $\Gamma_p = \overline{\tilde{p}\partial_y\tilde{\phi}}$, in a poloidal cross-section and for the four limiter positions. In the HFS-limited, top-limited, and bottom-limited configurations, the transport is clearly ballooned on the LFS. However, in the LFS-limited configuration, the transport is almost poloidally symmetric, consistent with the week dependence of L_p on the poloidal angle, as shown in Fig. 6.2.3.

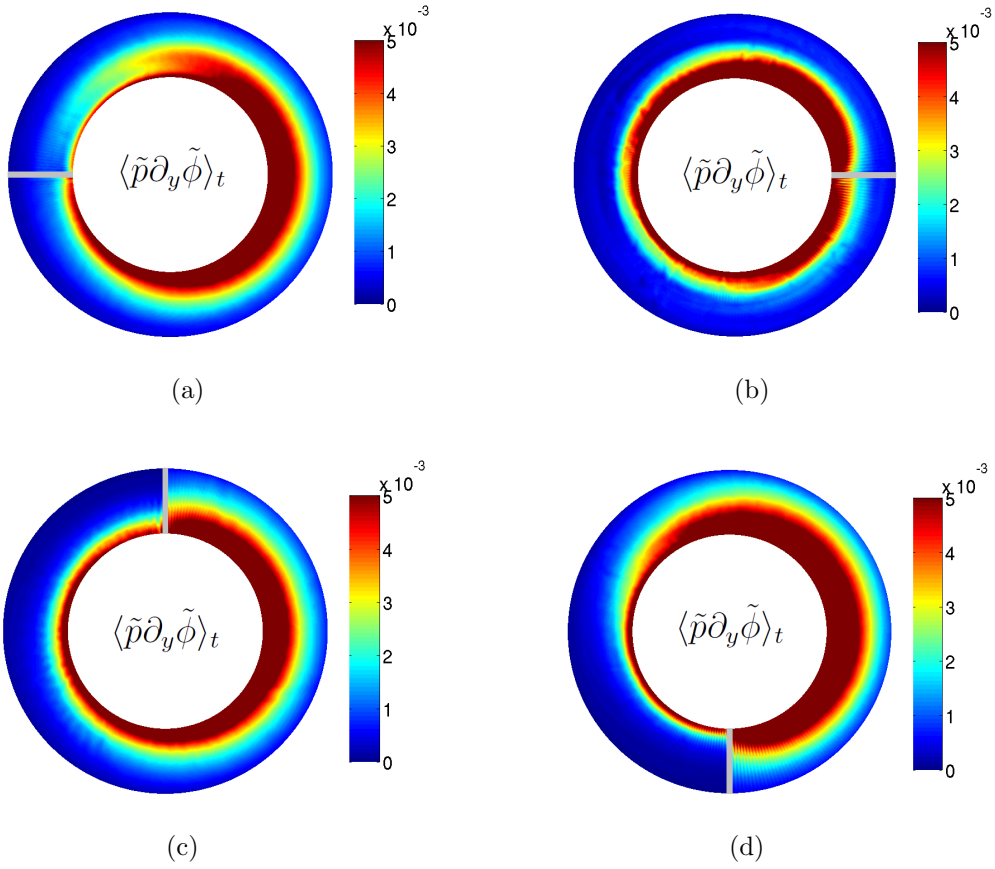

Figure 6.2.4: Time-averaged turbulent radial flux of plasma pressure, $\overline{\tilde{p}\partial_y\tilde{\phi}}$, in a poloidal cross-section and with the limiter (a) on the HFS mid-plane, (b) on the LFS mid-plane, (c) on the top, and (d) on the bottom.

These observations suggest that ballooning modes may become less efficient when the limiter is at the location of their maximum drive, thus steepening the pressure profiles, and that the tranport may become drift-wave dominated, thus yielding more symmetric poloidal profiles. To confirm this hypothesis, we proceed as follows.

As discussed in Chapter 5, the value of L_p satisfies Eq. (5.3.11), namely

$$L_p \sim \frac{qR}{c_s}\left(\frac{\gamma}{k_y}\right)_{max} . \tag{6.2.2}$$

The linear growth rate γ of the unstable mode present in the system that maximizes the ratio γ/k_y is evaluated by using a linear code described in Ref. [123]. Since the linear code requires L_p as an input value, the resulting value of $(\gamma/k_y)_{max}$ depends on L_p. We can then find numerically the value of L_p that is consistent with Eq. (6.2.2). This procedure, described in detail in Ref. [114], provides an estimate for the value of the pressure scale length L_p expected in nonlinear simulations. Table 6.1 shows the result of this procedure, which has been carried out for both HFS-limited and LFS-limited configurations. A reduction from $L_p \approx 40\rho_{s0}$ to $L_p \approx 30\rho_{s0}$ is expected when going from the HFS-limited configuration to the LFS-limited configuration, which is in good agreement with the nonlinear simulations results shown in Fig. 6.2.3. Moreover, Table 6.1 also shows the results obtained by following the same procedure but with the ballooning drive turned off (i.e., the curvature term in the vorticity equation, Eq. (3.4.5), is zeroed out). From the fact that turning off the ballooning drive only affects the value of L_p in the HFS-limited case, we can deduce that transport in the HFS-limited configuration is dominated by ballooning modes, while in the LFS-limited configuration transport is dominated by drift-waves.

Limiter position	L_p $[\rho_{s0}]$ predicted	L_p $[\rho_{s0}]$ from GBS
HFS	40.2	44.2
HFS (no interchange drive)	27.5	-
LFS	29.9	29.4
LFS (no interchange drive)	28.0	-

Table 6.1: Values of the poloidally averaged pressure scale length L_p predicted by the gradient removal theory (middle column) and obtained from nonlinear simulations (right column), for the HFS-limited and LFS-limited cases. The prediction of L_p in the case of no interchange drive is also shown.

6.3 Effect on the electrostatic potential

The equilibrium profile of the electrostatic potential in a poloidal cross-section is shown in Fig. 6.3.1 for the four different limiter configurations. Strong poloidal asymmetries are clearly visible in each configuration, which means that the radial electric field varies significantly in the poloidal direction. As shown in Chapter 4, the equilibrium electrostatic potential can be related to the equilibrium density and temperature by means of the analytical relation given by Eq.(4.2.13), as shown in Fig. 6.3.2 for the four limiter configurations.

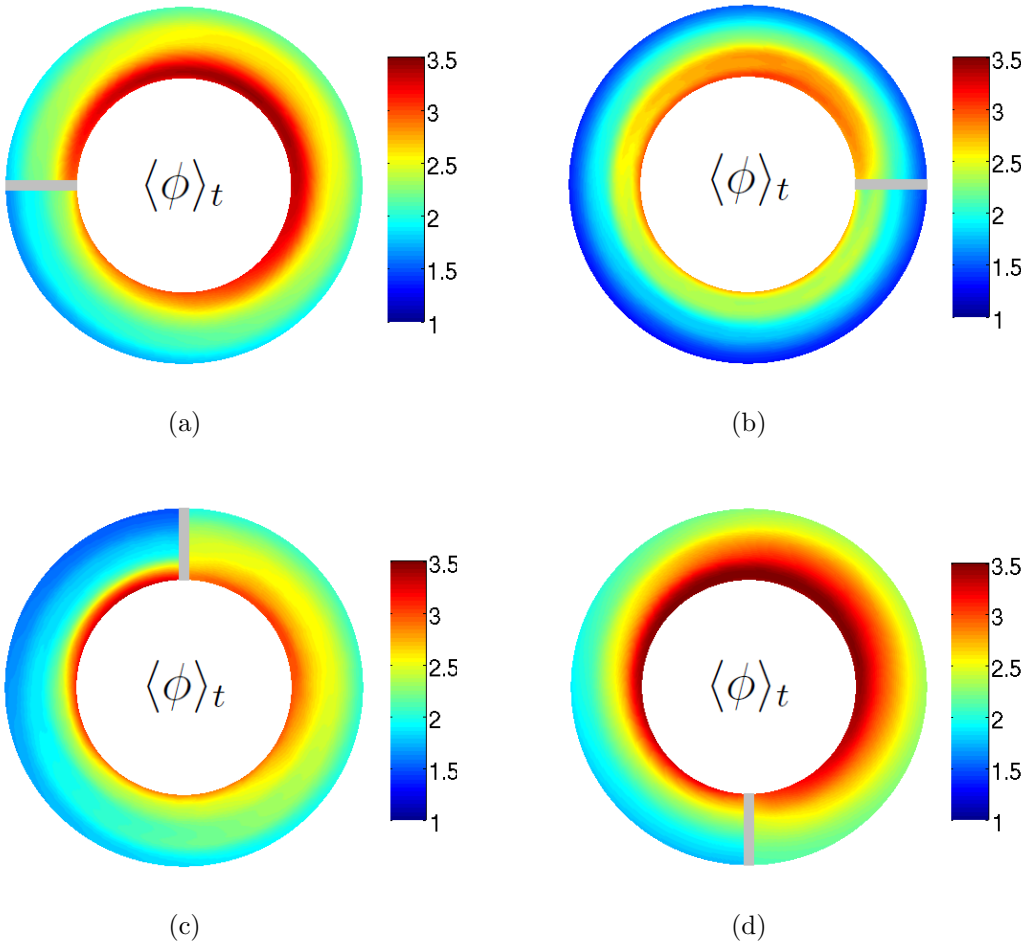

Figure 6.3.1: Equilibrium electrostatic potential profiles in a poloidal cross-section, with the limiter (a) on the HFS mid-plane, (b) on the LFS mid-plane, (c) on the top, and (d) on the bottom. Results are obtained from GBS simulations.

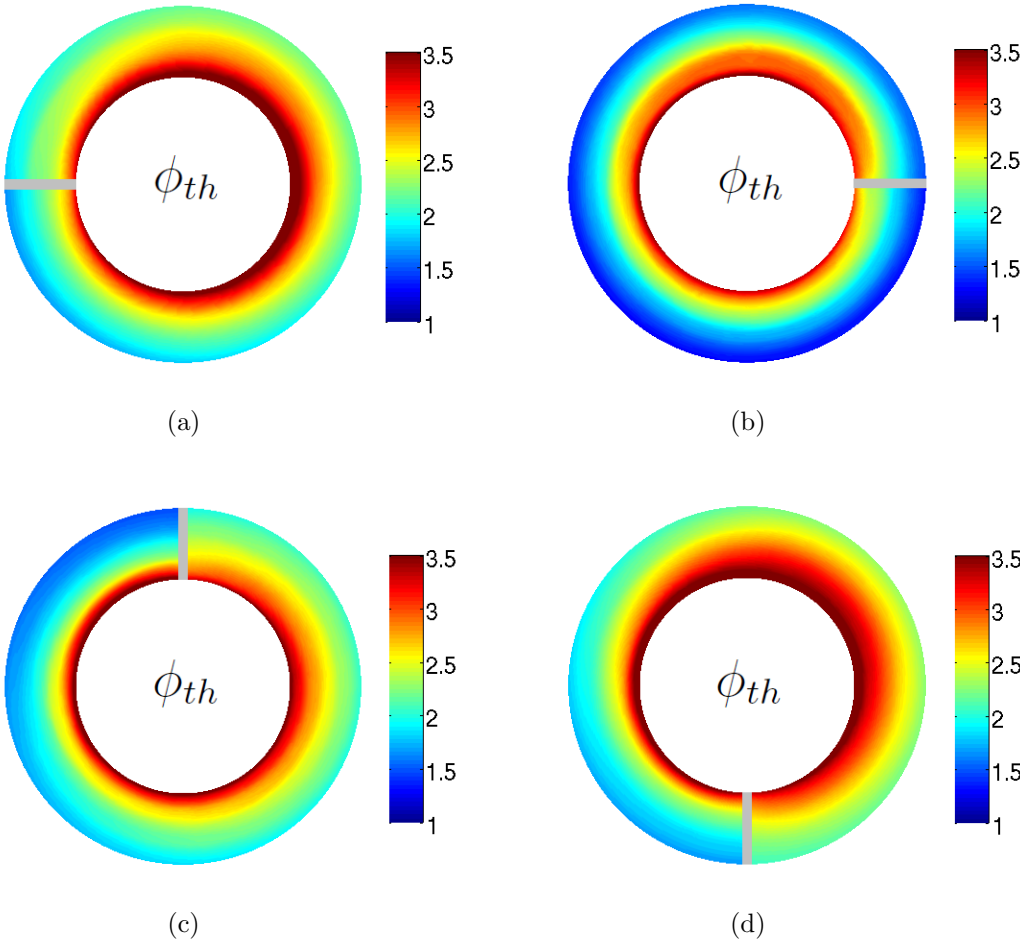

Figure 6.3.2: Equilibrium electrostatic potential profiles in a poloidal cross-section, with the limiter (a) on the HFS mid-plane, (b) on the LFS mid-plane, (c) on the top, and (d) on the bottom. Results are obtained from Eq. (4.2.13).

6.4 Effect on intrinsic rotation

In Chapter 5, we have investigated the generation and transport of intrinsic parallel flows both analytically and through the use of numerical simulations. Fig. 6.4.1 summarizes the effect of the limiter position on the equilibrium profile of the Mach number in a poloidal cross-section. These profiles can be fairly well reproduced analytically by means of Eq. (5.3.29). The more favourable co-current configurations are those with a limiter on the HFS and on the top. However, according to Eq. (5.3.29) this situation reverses if the direction of the toroidal magnetic field is reversed. Including the possibility of changing the direction of the magnetic field in GBS would allow to test this prediction.

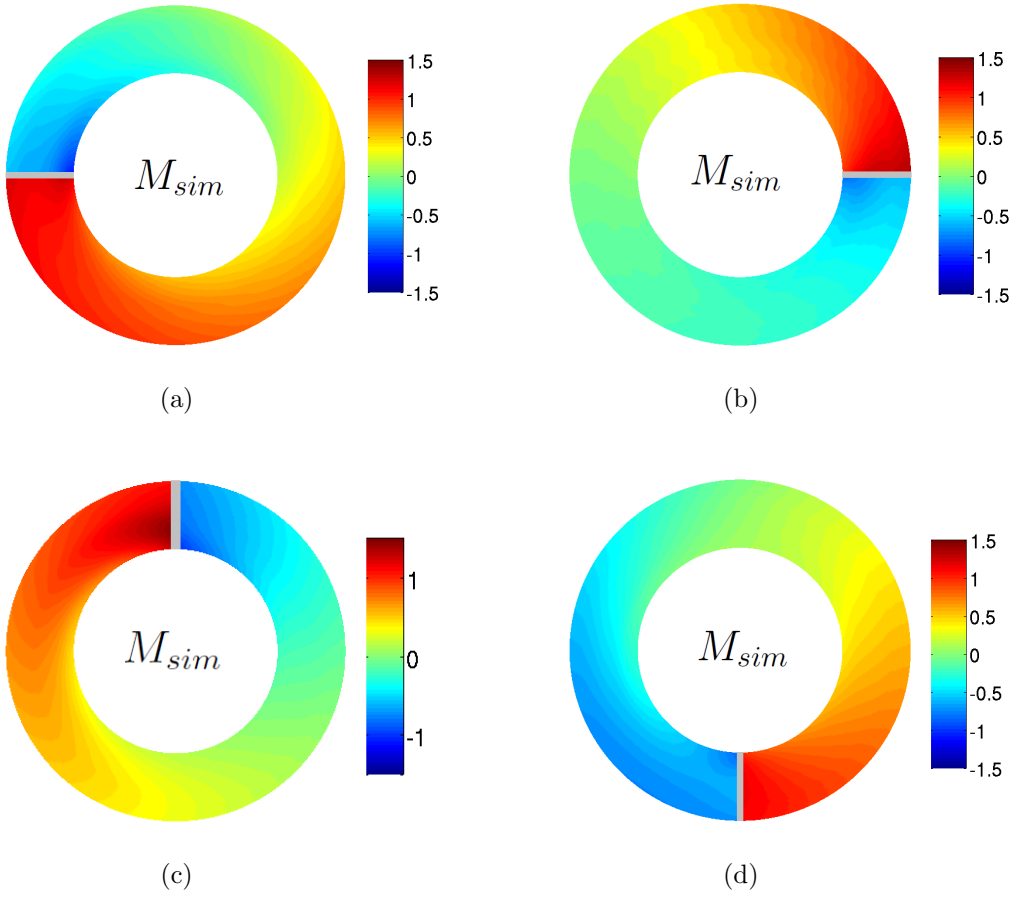

Figure 6.4.1: Equilibrium Mach number profiles ($M > 0$ means co-current) in a poloidal cross-section, with the limiter (a) on the HFS mid-plane, (b) on the LFS mid-plane, (c) on the top, and (d) on the bottom.

6.5 Summary and outlook

In this chapter, the effect of the limiter position on the SOL equilibrium profiles has been investigated via GBS simulations of four different limiter configurations: a limiter on the high field side, low field side, top and bottom.

The width of the SOL varies significantly with the limiter position and has a clear poloidal dependence which is explained qualitatively by the ballooning character of the turbulent transport. Consistent with experimental measurements in a number of tokamaks, the SOL width is reduced when going from a LFS-limited configuration to a HFS-limited configuration, although the reduction is not as large as observed experimentally. In GBS simulations, this reduction is explained by a change in the turbulence regime. Transport in the HFS-limited configuration is dominated by ballooning modes, while in the LFS-limited configuration transport is dominated by drift-waves.

The limiter position also modifies substantially the equilibrium electrostatic potential and the intrinsic rotation profiles. The analytical models developed in Chapters 4 and 5 are able to capture these dependences.

In the future, it would be interesting to study how the flux expansion affects the poloidal variation of the SOL width for the different limiter configurations. This should be possible with the recent GBS developments [115].

Chapter 7

Conclusions

A number of questions related to plasma sheaths and their effect on magnetized plasma turbulence and flows have been addressed throughout the present thesis. As sheaths are present in all laboratory plasmas, these questions are of general interest in plasma physics, in particular for fusion energy research. Below, the main results of this thesis are summarized and possible future studies are proposed.

The ODISEE code has been developed as a numerical tool to gain insights on the physics of the plasma-wall transition and to guide the derivation of analytical models describing this region. Simulations of an unmagnetized plasma in contact with a conducting wall revealed the existence of subsonic sheaths in the presence of electron currents. An analytical model based on a kinetic description of the plasma predicts this behavior and generalizes the Bohm criterion.
The effect of wall biasing on the plasma potential has been investigated in a simple framework. An analytical model describing the dynamics of a plasma bound between two biased walls predicts an abrupt transition of the plasma potential when the ratio of ion to electron wall currents exceeds a certain threshold. The predicted behaviour of the plasma potential is retrieved in ODISEE simulations and has been qualitatively well reproduced in a dedicated experiment carried out in the TORPEX device. This study opens the way to the development of a device capable of measuring T_i in edge plasma conditions.
Leveraging the acquired experience on the unmagnetized sheath, a simple mathematical framework is developed from which one can derive a complete set of boundary conditions at the entrance of the magnetic presheath, where the ion drift approximation breaks down. ODISEE simulations of the magnetized plasma-wall transition support the analytical results. This set of boundary conditions can supply the sheath physics to fluid codes that are based on the drift-reduced approximation. Future studies should look at the generalization of the magnetic presheath boundary conditions to the case of finite ion temperature.

Starting from the Braginskii equations, which describe the dynamics of a strongly collisional, strongly magnetized plasma, the drift-reduced Braginskii equations are

derived in the cold ion limit, for the description of low frequency plasma turbulence in open field lines. Then, the GBS code is presented, which is based on the drift-reduced Braginskii equations. The implementation of the model equations and that of the magnetic presheath boundary conditions are described. Examples of GBS simulations in both SOL and SMT conditions are shown. Results indicate compatibility of the boundary conditions with three-dimensional global fluid turbulence simulations. Simulations of plasma turbulence with a proper treatment of the plasma-wall transition, now possible with the GBS code, have allowed a detailed study of the turbulent regimes present in the SOL, a comparison with experimental results from a number of tokamaks, simulation of turbulence in the SMT configuration, as well as a dedicated study of blob dynamics, which has been carried out via three-dimensional simulations of seeded blobs. In the remaining of the thesis, the role of the sheath in determining the electrostatic potential, the equilibrium flows, as well as the SOL width has been thoroughly investigated.

The electrostatic potential in an open field line plasma configuration, e.g. in the SOL of tokamaks, is set by the combined effect of two different mechanisms. On the one hand, the sheath physics regulates the value of ϕ at the end of the field lines to ensure quasi-neutrality in the main plasma. On the other hand, the electron adiabaticity sets the parallel electric field far from the walls. A general analytical relation between the equilibrium electrostatic potential and the equilibrium electron temperature and density, $\bar{\phi} = \bar{\phi}(\bar{T}_e, \bar{n})$, has been provided, which implies that the relative importance of the two mechanisms in setting the value of ϕ depends on the density and temperature drops that are established between the bulk plasma and the sheaths. This suggests that one must be careful when estimating the radial and poloidal electric fields in the SOL of tokamaks, as the mechanism setting ϕ depends on the particular regime of operation: sheath-limited regime, low and high recycling regimes, or detached regime. The validity of the analytical predictions has been assessed via SOL turbulence simulations in the sheath-limited regime. Future simulations of high-recycling and detached regimes will be a good testbed of our analytical predictions.

Intrinsic toroidal flows are observed in GBS simulations of SOL turbulence. In order to unravel the mechanisms leading to such flows, a first-principle based analytical theory has been developed to describe the generation and transport of toroidal plasma rotation in the SOL. The presence of the sheath, equilibrium poloidal $\mathbf{E} \times \mathbf{B}$ flows and pressure poloidal asymmetries can explain the origin of intrinsic rotation, which is radially transported by turbulence. The sheath physics leads to a co-current toroidal rotation, while the effect of the poloidal pressure asymmetry can explain the flow reversals observed in tokamaks. Such flow reversals may occur when either the magnetic field or the limiter/divertor position are reversed, and this is explained by the ballooning character of the turbulence. Our theoretical predictions agree rather well with three-dimensional simulations of SOL turbulence.

The main limitation of our model is that ionization and recombination processes, which may affect the poloidal profile of $\bar{V}_{||i}$, are not taken into account. This may restrict the validity of the presented results to low-recycling regimes. Also, the theory derived herein ceases to be valid in regimes where turbulence is significantly suppressed and Pfirsch-Schluter ion flows play an important role, in particular in modulating the poloidal profile of the parallel ion velocity.
The rotation theory presented in this thesis is also applicable to other open field line configurations, e.g. in simple magnetized toroidal devices such as TORPEX, where significant net toroidal flows have been observed. Thanks to the two-dimensional Mach probe measurements performed in different magnetic configurations, TORPEX is a very good testbed in which to validate the theoretical predictions for the two-dimensional profile of the toroidal Mach number.

The effect of the limiter position on the SOL equilibrium profiles has been investigated via GBS simulations of four different limiter configurations: a limiter on the high field side, low field side, top and bottom. The width of the SOL varies significantly with the limiter position and has a clear poloidal dependence which is explained qualitatively by the ballooning character of the turbulent transport. Consistent with experimental measurements in a number of tokamaks, the SOL width is reduced when going from a LFS-limited configuration to a HFS-limited configuration, although the reduction is not as large as observed experimentally. In GBS simulations, this reduction is explained by a change in the turbulence regime. Transport in the HFS-limited configuration is dominated by ballooning modes, while in the LFS-limited configuration transport is dominated by drift-waves.
Finally, the limiter position also modifies substantially the equilibrium electrostatic potential and the intrinsic rotation profiles. The analytical models developed in this thesis are able to capture these dependences.

Appendix A

Phase velocity of ion-acoustic waves at the sheath entrance

Let us consider the general dispersion relation of electrostatic waves in a one-dimensional, cold ion plasma,

$$\omega_{pe}^2 \int_L \frac{\frac{df_e}{dv}}{v-\omega/k} dv + \omega_{pi}^2 \int_L \frac{\frac{df_i}{dv}}{v-\omega/k} dv = k^2 \tag{A.0.1}$$

which is obtained from the linearized Vlasov-Poisson model. The distribution functions are defined such that

$$\int_{-\infty}^{+\infty} f_{e,i}(v) dv = 1 \quad . \tag{A.0.2}$$

For ion-acoustic waves in a cold ion plasma, we assume quasineutrality, namely $n_e \simeq n_i$ and thus $k^2\lambda_D^2 \ll 1$. This allows us to neglect the term on the right hand side of Eq. (A.0.4). Also, we assume

$$v_{thi} \ll \omega/k \ll v_{the} \quad , \tag{A.0.3}$$

and therefore we can simplify the Landau integrals by Taylor expanding the denominators and using vk/ω as an ordering parameter. This leads to

$$\omega_{pe}^2 \int_L \frac{\frac{df_e}{dv}}{v} dv - \omega_{pi}^2 \frac{k^2}{\omega^2} \int_L \frac{df_i}{dv} v dv = 0 \tag{A.0.4}$$

Considering an electron distribution function given by a truncated Maxwellian, Eq. (2.3.2), we have

$$\frac{df_e}{dv} = \begin{cases} -\frac{v}{v_{the}^2} f_e(v) & v < v_{cut}(\eta) \\ -\delta(v - v_{cut}) f_e(v) & v = v_{cut}(\eta) \\ 0 & v > v_{cut}(\eta) \end{cases} \tag{A.0.5}$$

which is inserted in Eq. (A.0.4). One finally finds the expression for the phase velocity

$$v_{sound} = \frac{\omega}{k} = c_{sb}\sqrt{\frac{1}{1+\kappa}} \ . \tag{A.0.6}$$

Equation (A.0.6) corresponds to Eq. (2.3.8). Since $\kappa \to \infty$ for $\eta \to 0$, the sound speed at the sheath entrance goes to zero in this limit.

Appendix B

Magnetic presheath entrance with non-isothermal electrons

Here we present the derivation of the MP entrance condition when the assumption of isothermal electrons is relaxed. For the sake of simplicity, we consider the case of no gradients in the x direction. Therefore, according to the IDA one has $v_{yi} = 0$ and thus $v_{si} = v_{||i} \sin\alpha$. Considering non-isothermal electrons requires the use of a heat equation, such as Eq. (3.4.8), which in steady-state conditions and neglecting curvature and diffusion, can be written as

$$nv_{\|e} \sin\alpha \frac{\partial T_e}{\partial s} + \frac{2T_e}{3}\Big[1.71n \sin\alpha \frac{\partial v_{\|e}}{\partial s} - 0.71n \sin\alpha \frac{\partial v_{\|i}}{\partial s} - 0.71(v_{\|i} - v_{\|e}) \sin\alpha \frac{\partial n}{\partial s}\Big] = S_T \ . \tag{B.0.1}$$

For non-isothermal electrons, the parallel electron momentum equation, Eq. (2.4.8), gives

$$\mu \sin\alpha T_e \frac{\partial n}{\partial s} + 1.71\mu n \sin\alpha \frac{\partial T_e}{\partial s} - \mu n \sin\alpha \frac{\partial \phi}{\partial s} = S_{||me} \tag{B.0.2}$$

where we have included the contribution of the thermal force, $0.71\mu n \sin\alpha \partial_s T_e$, in GBS Ohm's law, Eq. (3.4.6).

We now assume that the parallel electron velocity can be expressed as $v_{||e} = v_{||e}(\phi, T_e)$ in the proximity of the MP entrance. It follows that

$$\frac{\partial v_{||e}}{\partial s} = c_\phi \frac{\partial \phi}{\partial s} + c_{T_e} \frac{\partial T_e}{\partial s} \tag{B.0.3}$$

where $c_\phi = \partial_\phi v_{||e}$ and $c_{T_e} = \partial_{T_e} v_{||e}$ are assumed to be known functions. Equation (B.0.1) can then be written as a linear combination of $\partial_s n$, $\partial_s v_{||i}$, $\partial_s \phi$, and

$\partial_s T_e$. Equations (2.4.5), (2.4.7), (B.0.2) and (B.0.1) describe the plasma dynamics in the CP and they can be written as a matrix system, $\mathbf{M}\overrightarrow{X} = \overrightarrow{S}$, where $\overrightarrow{X} = (\partial_s n, \partial_s v_{||i}, \partial_s \phi, \partial_s T_e)$ and $\overrightarrow{S} = (S_{pi}, S_{||i}, S_{||e}, S_T)$, with

$$\mathbf{M} = \begin{pmatrix} v_{si} & n\sin\alpha & 0 & 0 \\ 0 & nv_{si} & n\sin\alpha & 0 \\ \mu\sin\alpha T_e & 0 & -\mu n\sin\alpha & 1.71\mu n\sin\alpha \\ \frac{2}{3}0.71T_e(v_{||e}-v_{||i})\sin\alpha & -\frac{2}{3}0.71nT_e\sin\alpha & \frac{2}{3}1.71c_\phi nT_e\sin\alpha & (nv_{||e}+\frac{2}{3}1.71c_{T_e}nT_e)\sin\alpha \end{pmatrix}. \tag{B.0.4}$$

We note that, discarding the last row and column of the matrix $\mathbf{M}$, related to temperature fluctuations, one retrieves the matrix obtained in Eq. (2.4.12). The condition defining the MP entrance is obtained by imposing $\det(\mathbf{M}) = 0$, that is

$$v_{||i} = c_s\sqrt{\frac{1+\frac{2}{3}1.71(\hat{c}_{T_e}-0.71)}{1+\frac{2}{3}1.71(\hat{c}_{T_e}+1.71\hat{c}_\phi)}}\,, \tag{B.0.5}$$

where $\hat{c}_\phi = c_\phi T_e/v_{||e}$, $\hat{c}_{T_e} = c_{T_e}T_e/v_{||e}$, and we have used the relation $v_{si} = v_{||i}\sin\alpha$. Analytical progress can be achieved by using Eq. (2.4.26), $v_{||e} = \sqrt{T_e}\exp(\Lambda - \phi/T_e)$, which gives $\hat{c}_\phi = -1$ and $\hat{c}_{T_e} = 0.5 + \phi/T_e \simeq 0.5 + \Lambda$. Equation (B.0.5) thus gives $v_{||i} \approx 1.17c_s$ for $\Lambda = 3$. Finally, one can get an expression for the temperature gradient,

$$\partial_s T_e = \left[\frac{1+0.71(1-T_e/v_{||i}^2)}{\frac{3}{2}+1.71(0.5+\Lambda)}\right]\partial_s\phi \approx 0.15\;\partial_s\phi \tag{B.0.6}$$

which is an order of magnitude smaller than the gradient of the potential, therefore justifying the assumption ($\partial_s T_e = 0$) made in Sec. 2.4.

Appendix C

Parallel heat transport in limited plasmas

Let us consider the one-dimensional (along the field line), steady-state, particle and energy balance equations in a limited SOL,

$$\frac{d}{dz}\Gamma = S_n \tag{C.0.1}$$

$$\frac{d}{dz}q_{conv} + \frac{d}{dz}q_{cond} = S_Q \tag{C.0.2}$$

where S_n is the volumetric density source (in $\mathrm{s}^{-1}\mathrm{m}^{-3}$), S_Q is the volumetric heat source (in Wm^{-3}), Γ is the particle flux (in $\mathrm{s}^{-1}\mathrm{m}^{-2}$), q_{conv} is the total heat flux due to convection (in Wm^{-2}) and q_{cond} is the total heat flux due to conduction (in Wm^{-2}). Since the electron parallel heat conductivity is much larger than the ion parallel heat conductivity, q_{cond} is essentially given by the electron contribution.

We now make the following assumptions: the system is symmetric with respect to $z = 0$, which defines the position half way between the two targets, which are located at $z = \pm L$. The heat and particle sources are uniform along z, namely $S_Q = const$ and $S_n = const$. The flow is ambipolar, i.e. $v_i = v_e = v$. Finally, the expressions for q_{conv} and q_{cond} are given by

$$q_{conv} = ec_0 nvT_e \tag{C.0.3}$$

$$q_{cond} = -\chi_0 T_e^{5/2}\frac{dT_e}{dz} \tag{C.0.4}$$

where T_e is the electron temperature (in eV), e is the electron charge (in Coulombs), z is expressed in meters, $\chi_0 \approx 2000$ is the part of the electron heat diffusivity χ_e that does not depend on the temperature [16], and $c_0 \approx 2.5 - 5.5$ is a constant that depends on the ion temperature and the ion flow strength [16]. We remark that the only free parameters are the source strenghts S_n and S_Q.

We now solve Eqs. (C.0.1) and (C.0.2) in order to find an expression for the temperature profile, $T_e(z)$, and its dependence on the source parameters. By integrating Eq. (C.0.1) from $z = 0$ to z, we find

$$\Gamma = nv = S_n z \ , \tag{C.0.5}$$

where we have used the fact that $v(0) = 0$ by symmetry. Then, by integrating Eq. (C.0.2) from $z = 0$ to z, and using Eq. (C.0.5), we find

$$ec_0 S_n z T_e - \chi_0 T_e^{5/2} \frac{dT_e}{dz} = S_Q z \tag{C.0.6}$$

where we have imposed $T_e'(0) = 0$ because of symmetry. Equation (C.0.6) can be written as

$$z dz = -\frac{1}{a} \frac{T_e^{5/2} dT_e}{1 - bT_e} \ , \tag{C.0.7}$$

where $a = S_Q/\chi_0$ measures the strength of the heat source, and $b = ec_0(S_n/S_Q)$ measures the relative strength of the particle and heat sources. Equation (C.0.7) can be integrated from z to $z = L$ to give

$$\frac{1}{2}(L^2 - z^2) = -\frac{1}{a}\left(F[T_e(L)] - F[T_e(z)]\right) \ , \tag{C.0.8}$$

where

$$F[T] = -\frac{2}{15b^{7/2}}\left(\sqrt{bT}(3b^2T^2 + 5bT + 15) - 15\tanh^{-1}(\sqrt{bT})\right) \ . \tag{C.0.9}$$

We notice that in the limit of negligible particle source, $b \to 0$, which corresponds to neglecting q_{conv} in Eq. (C.0.6), we have

$$\lim_{b\to 0} F[T] = \frac{2}{7} T^{7/2} \tag{C.0.10}$$

retrieving the $T_e(z)$ profile obtained in Ref. [16] for a conduction-limited regime. The general solution for $T_e(z)$ as given by Eq. (C.0.8) can be found numerically, imposing the value of the target temperature, $T_e(L)$, as a boundary condition. An expression for $T_e(L)$ can be found by noting that all the heat injected into the system must be carried out at the target. At this location, the heat flux is essentially given by $e\gamma n(L)c_s(L)T_e(L)$, where $\gamma \approx 5 - 7$ is the sheath heat transmission coefficient [16]. Therefore we have that

$$S_Q L = e\gamma n(L)c_s(L)T_e(L) = \gamma S_n L T_e(L) \ , \tag{C.0.11}$$

where we have used Eq. (C.0.5) to express the particle flux. Equation (C.0.11) reduces to

$$T_e(L) = \frac{1}{e\gamma}\frac{S_Q}{S_n} = \frac{c_0}{\gamma}\frac{1}{b} \ , \tag{C.0.12}$$

and thus the value of $T_e(L)$ is uniquely determined by the parameter b. We can finally solve numerically Eq. (C.0.8) and find the profile $T_e(z)$ for a given set of parameters (a, b). In all cases, the maximum of $T_e(z)$ occurs at $z = 0$ and its

minimum at $z = \pm L$. Figure 1 shows the ratio $T_e(0)/T_e(L)$ as a function of the two independent parameters a and b. We remark that this ratio is always close to one, regardless of the values of a and b. This can be understood as follows: in the limit of large b, the particle source is large and so is the particle flow, thus the convection of heat is important and the profiles of temperature are flattened. On the other hand, if the particle source becomes negligible ($b \to 0$), convection of heat is reduced but the target temperature $T_e(L)$ increases according to Eq. (C.0.11) in order to ensure that all the injected heat can be dissipated at the sheath. Therefore in this case the profiles are also flattened. We notice that these results are valid under the assumption of uniform particle and heat sources, which is reasonable for limited tokamak plasmas. If the particle source becomes localized near the target (as assumed in Ref. [16]), which is common in diverted tokamak plasmas, then the result for $T_e(0)/T_e(L)$ is quite different (essentially because Eq. (C.0.11) is modified), allowing large temperature gradients to build up and thus the establishment of the conduciton-limited regime.

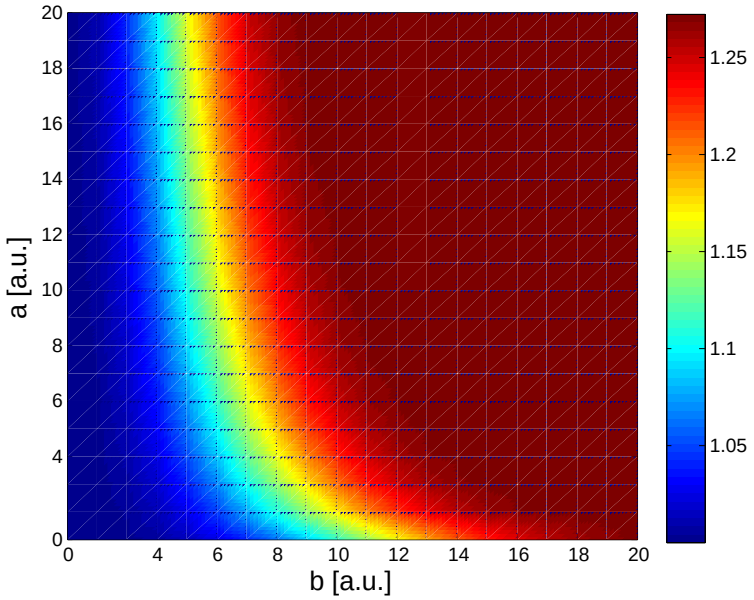

Figure 1: $T_e(0)/T_e(L)$ as a function of the two independent parameters a and b. Results obtained from the solution of Eq. (C.0.8), with $\gamma = 7$.

Appendix D

Scaling of the equilibrium pressure scale length

Within the drift-reduced fluid model, a pressure continuity equation can be obtained by combining the density and temperature equations, Eqs. (3.3.38) and (3.3.42). Assuming that the dominant terms are the parallel convection and the radial turbulent transport, we are left with an approximate pressure balance

$$\frac{\partial p}{\partial t} + \frac{\partial \Gamma_p}{\partial x} + \nabla_\parallel (p V_{\parallel e}) = 0 \quad , \tag{D.0.1}$$

where $\Gamma_p = \tilde{p}\partial_y \tilde{\phi}/B$ is the turbulent radial flux of plasma pressure. Writing

$$\langle \partial_x \Gamma_p \rangle_t \sim \bar{\Gamma}_p / L_p \tag{D.0.2}$$

and

$$\langle \nabla_\parallel \left(p V_{\parallel e} \right) \rangle_t \sim \bar{p} c_s / qR \quad , \tag{D.0.3}$$

the time-average of Eq. (D.0.1) leads to

$$L_p \sim \frac{qR}{c_s} \frac{\bar{\Gamma}_p}{\bar{p}}. \tag{D.0.4}$$

An estimate of $\bar{\Gamma}_p = \langle \tilde{p}\partial_y \tilde{\phi} \rangle_t / B$ can be obtained as follows. Linearizing Eq. (D.0.1) and keeping the dominant terms, one has

$$\gamma \tilde{p} \sim \frac{1}{B} \frac{\partial \tilde{\phi}}{\partial y} \frac{\partial \bar{p}}{\partial x} \ , \tag{D.0.5}$$

thus relating the electric field fluctuations with the pressure fluctuations. Therefore we have $\bar{\Gamma}_p \sim (\gamma L_p / \bar{p}) \langle \tilde{p}^2 \rangle_t$. Finally, we can relate $\tilde{p}$ with $\bar{p}$ by using the *gradient*

removal hypothesis, namely by assuming that the mode growth saturates when the fluctuations are able to remove the instability drive, which is provided by the pressure gradient, i.e. when

$$\frac{\partial \tilde{p}}{\partial x} \sim \frac{\partial \bar{p}}{\partial x} \quad . \tag{D.0.6}$$

This condition can be written as $k_x \tilde{p} \sim \bar{p}/L_p$, where k_x gives the radial extension of the saturated turbulent eddies. This can be estimated using non-local linear theory as $k_x = \sqrt{k_y/L_p}$ [101]. We can therefore write

$$\langle \tilde{p}^2 \rangle_t \sim \frac{\bar{p}^2}{k_y L_p} \quad . \tag{D.0.7}$$

Hence we are left with an expression for the radial pressure flux, $\bar{\Gamma}_p$, as a function of equilibrium quantities,

$$\bar{\Gamma}_p \sim \bar{p} \left(\frac{\gamma}{k_y} \right)_{max} \quad , \tag{D.0.8}$$

where the linear growth rate γ and the wavenumber k_y must be chosen in order to maximize the ratio of γ/k_y, thus maximizing the transport. Finally, we can replace this expression into Eq. (D.0.4), leading to

$$L_p \sim \frac{qR}{c_s} \left(\frac{\gamma}{k_y} \right)_{max} . \tag{D.0.9}$$

Bibliography

[1] C. Suplee, *The Plasma Universe*. Cambridge University Press, 2009.

[2] F. F. Chen, *Introduction to plasma physics and controlled fusion*. Plenum Press, 1984.

[3] A. Meadows, *Stellar Evolution*. Pergamon Press, 1967.

[4] M. Chesaux, *A Grid Reactor with Low Ion Bombardment Energy for Large Area PECVD of Thin Film Silicon Solar Cells*. Phd thesis, EPFL, 2013.

[5] D. M. Goebel and I. Katz, *Fundamentals of Electric Propulsion: Ion and Hall Thrusters*. JPL Space Science & Technology Series, 2012.

[6] E. Ahedo, "Plasmas for space propulsion," *Plasma Physics and Controlled Fusion*, vol. 53, p. 124037, Dec. 2011.

[7] D. Meade, "50 years of fusion research," *Nuclear Fusion*, vol. 50, p. 014004, Jan. 2010.

[8] J. Li, J. Zhang, and X. Duan, "Magnetic fusion development for global warming suppression," *Nuclear Fusion*, vol. 50, p. 014005, Jan. 2010.

[9] J. D. Lawson, "Some Criteria for a Power Producing Thermonuclear Reactor," *Proceedings of the Physical Society. Section B*, vol. 70, pp. 6–10, Jan. 1957.

[10] J. Jacquinot, "Fifty years in fusion and the way forward," *Nuclear Fusion*, vol. 50, p. 014001, Jan. 2010.

[11] M. Shimada, D. Campbell, V. Mukhovatov, M. Fujiwara, N. Kirneva, K. Lackner, M. Nagami, V. Pustovitov, N. Uckan, J. Wesley, N. Asakura, A. E. Costley, A. Donné, E. Doyle, A. Fasoli, C. Gormezano, Y. Gribov, O. Gruber, T. Hender, W. Houlberg, S. Ide, Y. Kamada, A. Leonard, B. Lipschultz, A. Loarte, K. Miyamoto, T. Osborne, A. Polevoi, and A. Sips, "Chapter 1: Overview and summary," *Nuclear Fusion*, vol. 47, pp. S1–S17, June 2007.

[12] J. Wesson, *Tokamaks*. Oxford University Press, 2011.

[13] L. Spitzer, *Physics of fully ionized gases*. Interscience Publication, New York, 1962.

[14] F. Wagner and U. Stroth, "Transport in toroidal devices-the experimentalist's view," *Plasma Physics and Controlled Fusion*, vol. 35, pp. 1321–1371, Oct. 1993.

[15] W. Horton, "Drift waves and transport," *Reviews of Modern Physics*, vol. 71, pp. 735–778, Apr. 1999.

[16] P. C. Stangeby, *The Plasma Boundary of Magnetic Fusion Devices*. Institute of Physics, Berkshire, 2000.

[17] B. Lipschultz, X. Bonnin, G. Counsell, A. Kallenbach, A. Kukushkin, K. Krieger, A. Leonard, A. Loarte, R. Neu, R. A. Pitts, T. Rognlien, J. Roth, C. Skinner, J. Terry, E. Tsitrone, D. Whyte, S. Zweben, N. Asakura, D. Coster, R. Doerner, R. Dux, G. Federici, M. Fenstermacher, W. Fundamenski, P. Ghendrih, A. Herrmann, J. Hu, S. Krasheninnikov, G. Kirnev, A. Kreter, V. Kurnaev, B. LaBombard, S. Lisgo, T. Nakano, N. Ohno, H. Pacher, J. Paley, Y. Pan, G. Pautasso, V. Philipps, V. Rohde, D. Rudakov, P. Stangeby, S. Takamura, T. Tanabe, Y. Yang, and S. Zhu, "Plasma–surface interaction, scrape-off layer and divertor physics: implications for ITER," *Nuclear Fusion*, vol. 47, pp. 1189–1205, Sept. 2007.

[18] A. Loarte, B. Lipschultz, A. Kukushkin, G. Matthews, P. Stangeby, N. Asakura, G. Counsell, G. Federici, A. Kallenbach, K. Krieger, A. Mahdavi, V. Philipps, D. Reiter, J. Roth, J. Strachan, D. Whyte, R. Doerner, T. Eich, W. Fundamenski, A. Herrmann, M. Fenstermacher, P. Ghendrih, M. Groth, A. Kirschner, S. Konoshima, B. LaBombard, P. Lang, A. Leonard, P. Monier-Garbet, R. Neu, H. Pacher, B. Pegourie, R. A. Pitts, S. Takamura, J. Terry, E. Tsitrone, t. I. S.-o. L. Group, and Diver, "Chapter 4: Power and particle control," *Nuclear Fusion*, vol. 47, pp. S203–S263, June 2007.

[19] W. Gekelman, H. Pfister, Z. Lucky, J. Bamber, D. Leneman, and J. Maggs, "Design, construction, and properties of the large plasma research device—The LAPD at UCLA," *Review of Scientific Instruments*, vol. 62, no. 12, p. 2875, 1991.

[20] A. G. Lynn, M. Gilmore, C. Watts, J. Herrea, R. Kelly, S. Will, S. Xie, L. Yan, and Y. Zhang, "The HelCat dual-source plasma device.," *The Review of scientific instruments*, vol. 80, p. 103501, Oct. 2009.

[21] A. Fasoli, A. Burckel, L. Federspiel, I. Furno, K. Gustafson, D. Iraji, B. Labit, J. Loizu, G. Plyushchev, P. Ricci, C. Theiler, A. Diallo, S. H. Mueller, M. Podestà, and F. Poli, "Electrostatic instabilities, turbulence and fast ion interactions in the TORPEX device," *Plasma Physics and Controlled Fusion*, vol. 52, p. 124020, Dec. 2010.

[22] K. W. Gentle and H. He, "Texas Helimak Texas Helimak device," vol. 284, 2008.

[23] S. Braginskii, "Transport processes in a plasma," *Reviews of Plasma Physics*, vol. 1, pp. 205–311, 1965.

[24] A. Zeiler, J. F. Drake, and B. Rogers, "Nonlinear reduced Braginskii equations with ion thermal dynamics in toroidal plasma," *Physics of Plasmas*, vol. 4, no. June, p. 2134, 1997.

[25] W. Dorland and G. W. Hammett, "Gyrofluid turbulence models with kinetic effects," *Physics of Fluids B*, vol. 5, p. 812, 1993.

[26] A. B. Mikhailovskii and V. S. Tsypin, "Transport Equations of Plasma in a Curvilinear Magnetic Field," *Beiträge aus der Plasmaphysik*, vol. 24, no. 4, pp. 335–354, 1984.

[27] B. D. Scott, "Free-energy conservation in local gyrofluid models," *Physics of Plasmas*, vol. 12, no. 10, p. 102307, 2005.

[28] O. Garcia, V. Naulin, A. Nielsen, and J. Rasmussen, "Computations of Intermittent Transport in Scrape-Off Layer Plasmas," *Physical Review Letters*, vol. 92, p. 165003, Apr. 2004.

[29] V. Naulin, T. Windisch, and O. Grulke, "Three-dimensional global fluid simulations of cylindrical magnetized plasmas," *Physics of Plasmas*, vol. 15, no. 1, p. 012307, 2008.

[30] T. T. Ribeiro and B. Scott, "Gyrofluid turbulence studies of the effect of the poloidal position of an axisymmetric Debye sheath," *Plasma Physics and Controlled Fusion*, vol. 50, p. 055007, May 2008.

[31] D. A. Russell, J. R. Myra, and D. A. D'Ippolito, "Saturation mechanisms for edge turbulence," *Physics of Plasmas*, vol. 16, no. 12, p. 122304, 2009.

[32] B. Dudson, M. Umansky, X. Xu, P. Snyder, and H. Wilson, "BOUT++: A framework for parallel plasma fluid simulations," *Computer Physics Communications*, vol. 180, pp. 1467–1480, Sept. 2009.

[33] P. Tamain, P. Ghendrih, E. Tsitrone, V. Grandgirard, X. Garbet, Y. Sarazin, E. Serre, G. Ciraolo, and G. Chiavassa, "TOKAM-3D: A 3D fluid code for transport and turbulence in the edge plasma of Tokamaks," *Journal of Computational Physics*, vol. 229, pp. 361–378, Jan. 2010.

[34] P. Ricci, F. D. Halpern, S. Jolliet, J. Loizu, a. Mosetto, a. Fasoli, I. Furno, and C. Theiler, "Simulation of plasma turbulence in scrape-off layer conditions: the GBS code, simulation results and code validation," *Plasma Physics and Controlled Fusion*, vol. 54, p. 124047, Dec. 2012.

[35] I. Hutchinson, *Principles of plasma diagnostics*. Cambridge University Press, Cambridge, 2002.

[36] I. H. Hutchinson, "Oblique ion collection in the drift approximation: How magnetized Mach probes really work," *Physics of Plasmas*, vol. 15, no. 12, p. 123503, 2008.

[37] I. Langmuir, "The Interaction of Electron and Positive Ion Space Charges in Cathode Sheaths," *Physical Review*, vol. 33, pp. 954–989, June 1929.

[38] K. U. Riemann, "The Bohm criterion and sheath formation," *Journal of Physics D: Applied Physics*, vol. 24, pp. 493–518, Apr. 1991.

[39] J. E. Allen, "The plasma–sheath boundary: its history and Langmuir's definition of the sheath edge," *Plasma Sources Science and Technology*, vol. 18, p. 014004, Feb. 2009.

[40] D. Bohm, *The Characteristics of Electrical Discharges in Magnetic Fields*. A. Guthrie and R.K. Wakerling, McGraw-Hill, New York, 1949.

[41] K.-U. Riemann, "Plasma-sheath transition in the kinetic Tonks-Langmuir model," *Physics of Plasmas*, vol. 13, no. 6, p. 063508, 2006.

[42] D. Lee, L. Oksuz, and N. Hershkowitz, "Exact Solution for the Generalized Bohm Criterion in a Two-Ion-Species Plasma," *Physical Review Letters*, vol. 99, p. 155004, Oct. 2007.

[43] N. Jelic, K.-U. Riemann, T. Gyergyek, S. Kuhn, M. Stanojevic, and J. Duhovnik, "Fluid and kinetic parameters near the plasma-sheath boundary for finite Debye lengths," *Physics of Plasmas*, vol. 14, no. 10, p. 103506, 2007.

[44] I. Hutchinson, "Ion Collection by Oblique Surfaces of an Object in a Transversely Flowing Strongly Magnetized Plasma," *Physical Review Letters*, vol. 101, p. 035004, July 2008.

[45] D. Sydorenko, I. Kaganovich, Y. Raitses, and A. Smolyakov, "Breakdown of a Space Charge Limited Regime of a Sheath in a Weakly Collisional Plasma Bounded by Walls with Secondary Electron Emission," *Physical Review Letters*, vol. 103, p. 145004, Oct. 2009.

[46] S. Baalrud, C. Hegna, and J. Callen, "Instability-Enhanced Collisional Friction Can Determine the Bohm Criterion in Multiple-Ion-Species Plasmas," *Physical Review Letters*, vol. 103, p. 205002, Nov. 2009.

[47] N. Hershkowitz, "Sheaths: More complicated than you think," *Physics of Plasmas*, vol. 12, no. 5, p. 055502, 2005.

[48] L. Oksuz and N. Hershkowitz, "Plasma, presheath, collisional sheath and collisionless sheath potential profiles in weakly ionized, weakly collisional plasma," *Plasma Sources Science and Technology*, vol. 14, pp. 201–208, Feb. 2005.

[49] T. Lunt, G. Fussmann, and O. Waldmann, "Experimental Investigation of the Plasma-Wall Transition," *Physical Review Letters*, vol. 100, p. 175004, May 2008.

[50] R. J. Procassini, C. K. Birdsall, and E. C. Morse, "A fully kinetic, self-consistent particle simulation model of the collisionless plasma-sheath region," *Physics of Fluids B*, vol. 2, p. 3191, 1990.

[51] R. J. Procassini and C. K. Birdsall, "Particle simulation plasma model of transport in a bounded, Coulomb collisional plasma," *Physics of Fluids B*, no. 3, p. 1876, 1991.

[52] J. Loizu, P. Ricci, and C. Theiler, "Existence of subsonic plasma sheaths," *Physical Review E*, vol. 83, p. 016406, Jan. 2011.

[53] J. Loizu, J. Dominski, P. Ricci, and C. Theiler, "Potential of a plasma bound between two biased walls," *Physics of Plasmas*, vol. 19, no. 8, p. 083507, 2012.

[54] T. Hayes and M. Gilmore, "Dynamics of Turbulence Suppression in a Helicon Plasma," in *54th Annual Meeting of the APS Division of Plasma Physics, Providence, USA*, 2012.

[55] J. Loizu, P. Ricci, F. D. Halpern, and S. Jolliet, "Boundary conditions for plasma fluid models at the magnetic presheath entrance," *Physics of Plasmas*, vol. 19, no. 12, p. 122307, 2012.

[56] G. Lapenta, J. U. Brackbill, and P. Ricci, "Kinetic approach to microscopic-macroscopic coupling in space and laboratory plasmas," *Physics of Plasmas*, vol. 13, no. 5, p. 055904, 2006.

[57] C. K. Birdsall and A. B. Langdon, *Plasma Physics via computer simulations*. Taylor & Francis Group, New York, 2005.

[58] D. Potter, *Computational physics*. Wiley, New York, 1973.

[59] T. Takizuka and H. Abe, "A binary collision model for plasma simulation with a particle code," *Journal of Computational Physics*, vol. 25, pp. 205–219, Nov. 1977.

[60] CSCS, "http://www.cscs.ch/."

[61] E. Zawaideh, N. S. Kim, and F. Najmabadi, "Structure of the plasma sheath in collisional to weakly collisional plasmas," *Physics of Fluids B: Plasma Physics*, vol. 2, no. 3, p. 647, 1990.

[62] K.-U. Riemann, "The influence of collisions on the plasma sheath transition," vol. 4, no. 11, 1997.

[63] Q. Gao and X. Chen, "Subsonic ion flow at the presheath entrance in tokamak divertors," *Physics of Plasmas*, vol. 10, no. 5, p. 1389, 2003.

[64] G. Kawamura and A. Fukuyama, "Kinetic modeling of a sheath layer in a magnetized collisionless plasma," *Physics of Plasmas*, vol. 14, no. 8, p. 083502, 2007.

[65] S. W. Rayment and N. D. Twiddy, "Electron Energy Distributions in the Low-Pressure Mercury-Vapour Discharge: The Langmuir Paradox," *Proceedings of the Royal Society A: Mathematical, Physical and Engineering Sciences*, vol. 304, pp. 87–98, Apr. 1968.

[66] A. Maresca, K. Orlov, and U. Kortshagen, "Experimental study of diffusive cooling of electrons in a pulsed inductively coupled plasma," *Physical Review E*, vol. 65, p. 056405, May 2002.

[67] S. D. Baalrud, N. Hershkowitz, and B. Longmier, "Global nonambipolar flow: Plasma confinement where all electrons are lost to one boundary and all positive ions to another boundary," *Physics of Plasmas*, vol. 14, no. 4, p. 042109, 2007.

[68] T. Rognlien and M. Shimada, "ExB drift, current, and kinetic effects on divertor plasma profiles during ELMs," *Journal of Nuclear Materials*, vol. 313-316, pp. 1000–1004, Mar. 2003.

[69] M. E. Fenstermacher, A. W. Leonard, P. B. Snyder, J. A. Boedo, N. H. Brooks, R. J. Colchin, D. S. Gray, R. J. Groebner, M. Groth, E. Hollmann, C. J. Lasnier, T. H. Osborne, T. W. Petrie, D. L. Rudakov, H. Takahashi, J. G. Watkins, L. Zeng, and the DIII-D Team, "ELM particle and energy transport in the SOL and divertor of DIII-D," *Plasma Physics and Controlled Fusion*, vol. 45, pp. 1597–1626, Sept. 2003.

[70] S. Barral, K. Makowski, Z. Peradzynnski, N. Gascon, and M. Dudeck, "Wall material effects in stationary plasma thrusters. II. Near-wall and in-wall conductivity," *Physics of Plasmas*, vol. 10, no. 10, p. 4137, 2003.

[71] C. B. Dwivedi, P. K. Karmakar, and S. C. Tripathy, "A Gravito electrostatic Sheath Model for Surface Origin of Subsonic Solar Wind Plasma," *The Astrophysical Journal*, vol. 663, pp. 1340–1353, July 2007.

[72] K. M. Frederick-Frost and K. A. Lynch, "Experimental studies of low density and temperature ion and electron sheaths," *Physics of Plasmas*, vol. 14, no. 12, p. 123503, 2007.

[73] T. A. Carter and J. E. Maggs, "Modifications of turbulence and turbulent transport associated with a bias-induced confinement transition in the Large Plasma Device," *Physics of Plasmas*, vol. 16, no. 1, p. 012304, 2009.

[74] D. L. Toufen, Z. O. Guimaraes-Filho, I. L. Caldas, F. A. Marcus, and K. W. Gentle, "Turbulence driven particle transport in Texas Helimak," *Physics of Plasmas*, vol. 19, no. 1, p. 012307, 2012.

[75] B. Li, B. N. Rogers, P. Ricci, K. W. Gentle, and A. Bhattacharjee, "Turbulence and bias-induced flows in simple magnetized toroidal plasmas," *Physical Review E*, vol. 83, p. 056406, May 2011.

[76] A. Douglass, V. Land, K. Qiao, L. Matthews, and T. Hyde, "Determination of the levitation limits of dust particles within the sheath in complex plasma experiments," *Physics of Plasmas*, vol. 19, no. 1, p. 013707, 2012.

[77] D. D. Ryutov, P. Helander, and R. H. Cohen, "On the possibility of inducing strong plasma convection in the divertor of MAST," *Plasma Physics and Controlled Fusion*, vol. 43, pp. 1399–1423, Oct. 2001.

[78] S. J. Zweben, R. J. Maqueda, A. L. Roquemore, C. E. Bush, R. Kaita, R. J. Marsala, Y. Raitses, R. H. Cohen, and D. D. Ryutov, "Local scrape-off layer control using biased electrodes in NSTX," *Plasma Physics and Controlled Fusion*, vol. 51, p. 105012, Oct. 2009.

[79] C. Theiler, I. Furno, J. Loizu, and a. Fasoli, "Convective Cells and Blob Control in a Simple Magnetized Plasma," *Physical Review Letters*, vol. 108, p. 065005, Feb. 2012.

[80] S. Kuhn, "The Physics of Bounded Plasma Systems (BPS's): Simulation and Interpretation," *Contributions to Plasma Physics*, vol. 34, no. 4, pp. 495–538, 1994.

[81] G. G. Comisar, "Nonlinear Stability of a Collisionless Electron Sheath," *Journal of Applied Physics*, vol. 38, no. 2, p. 905, 1967.

[82] V. Chabloz, *Experimental investigation of the electric potential of a plasma bound between two biased walls.* Master thesis, Ecole Polytechnique Federale de Lausanne, 2013.

[83] T. T. Ribeiro and B. Scott, "Tokamak turbulence computations on closed and open magnetic flux surfaces," *Plasma Physics and Controlled Fusion*, vol. 47, pp. 1657–1679, Oct. 2005.

[84] R. Chodura, "Plasma–wall transition in an oblique magnetic field," *Physics of Fluids*, vol. 25, no. 9, p. 1628, 1982.

[85] K.-U. Riemann, "Theory of the collisional presheath in an oblique magnetic field," *Physics of Plasmas*, vol. 1, no. 3, p. 552, 1994.

[86] T. M. G. Zimmermann, M. Coppins, and J. E. Allen, "Fluid model of the boundary of a one-dimensional plasma under the influence of an oblique magnetic field for a wide range of collisionality," *Physics of Plasmas*, vol. 15, no. 7, p. 072301, 2008.

[87] E. Ahedo and D. Carralero, "Model of a source-driven plasma interacting with a wall in an oblique magnetic field," *Physics of Plasmas*, vol. 16, no. 4, p. 043506, 2009.

[88] J. Kovacic, T. Gyergyek, and M. Cercek, "Pre-sheath formation in an oblique magnetic field: fluid model and PIC simulation," *The European Physical Journal D*, vol. 54, pp. 383–389, Mar. 2009.

[89] N. S. Krasheninnikova, X. Tang, and V. S. Roytershteyn, "Scaling of the plasma sheath in a magnetic field parallel to the wall," *Physics of Plasmas*, vol. 17, no. 5, p. 057103, 2010.

[90] R. H. Cohen and D. D. Ryutov, "Plasma sheath in a tilted magnetic field: Closing of the diamagnetic currents; effect on plasma convection," *Physics of Plasmas*, vol. 2, no. 6, p. 2011, 1995.

[91] P. C. Stangeby, "The Bohm–Chodura plasma sheath criterion," *Physics of Plasmas*, vol. 2, no. 3, p. 702, 1995.

[92] P. C. Stangeby and A. V. Chankin, "The ion velocity (Bohm–Chodura) boundary condition at the entrance to the magnetic presheath in the presence of diamagnetic and E×B drifts in the scrape-off layer," *Physics of Plasmas*, vol. 2, no. 3, p. 707, 1995.

[93] I. H. Hutchinson, "The magnetic presheath boundary condition with E×B drifts," *Physics of Plasmas*, vol. 3, no. 1, p. 6, 1996.

[94] D. Tskhakaya and S. Kuhn, "Effect of ExB drift on the plasma flow at the magnetic presheath entrance," *Contributions to Plasma Physics*, vol. 42, p. 302, 2002.

[95] M. Stanojevic, J. Duhovnik, N. Jelić, A. Kendl, and S. Kuhn, "Fluid model of the magnetic presheath in a turbulent plasma," *Plasma Physics and Controlled Fusion*, vol. 47, pp. 685–712, May 2005.

[96] S. Devaux and G. Manfredi, "Vlasov simulations of plasma-wall interactions in a magnetized and weakly collisional plasma," *Physics of Plasmas*, vol. 13, no. 8, p. 083504, 2006.

[97] R. H. Cohen and D. D. Ryutov, "Spreading particle trajectories near a perfectly reflecting surface in a tilted magnetic field," *Physics of Plasmas*, vol. 2, no. 11, p. 4118, 1995.

[98] R. H. Cohen and D. D. Ryutov, "Particle trajectories in a sheath in a strongly tilted magnetic field," *Physics of Plasmas*, vol. 5, no. 3, p. 808, 1998.

[99] P. Helander and D. J. Sigmar, *Collisional Transport in Magnetized Plasmas*. Cambridge University Press, 2002.

[100] P. Ricci, B. N. Rogers, and S. Brunner, "High- and Low-Confinement Modes in Simple Magnetized Toroidal Plasmas," *Physical Review Letters*, vol. 100, p. 225002, June 2008.

[101] P. Ricci and B. N. Rogers, "Transport scaling in interchange-driven toroidal plasmas," *Physics of Plasmas*, vol. 16, no. 6, p. 062303, 2009.

[102] P. Ricci, C. Theiler, A. Fasoli, I. Furno, B. Labit, S. H. Muller, M. Podesta, and F. M. Poli, "Langmuir probe-based observables for plasma-turbulence code validation and application to the TORPEX basic plasma physics experiment," *Physics of Plasmas*, vol. 16, no. 5, p. 055703, 2009.

[103] P. Ricci and B. N. Rogers, "Three-dimensional fluid simulations of a simple magnetized toroidal plasma," *Physics of Plasmas*, vol. 16, no. 9, p. 092307, 2009.

[104] B. Li, B. N. Rogers, P. Ricci, and K. W. Gentle, "Plasma transport and turbulence in the Helimak: Simulation and experiment," *Physics of Plasmas*, vol. 16, no. 8, p. 082510, 2009.

[105] P. Ricci and B. N. Rogers, "Turbulence Phase Space in Simple Magnetized Toroidal Plasmas," *Physical Review Letters*, vol. 104, p. 145001, Apr. 2010.

[106] B. N. Rogers and P. Ricci, "Low-Frequency Turbulence in a Linear Magnetized Plasma," *Physical Review Letters*, vol. 104, p. 225002, June 2010.

[107] P. Ricci, C. Theiler, A. Fasoli, I. Furno, K. Gustafson, D. Iraji, and J. Loizu, "Methodology for turbulence code validation: Quantification of simulation-experiment agreement and application to the TORPEX experiment," *Physics of Plasmas*, vol. 18, no. 3, p. 032109, 2011.

[108] I. Furno, C. Theiler, D. Lançon, a. Fasoli, D. Iraji, P. Ricci, M. Spolaore, and N. Vianello, "Blob current structures in TORPEX plasmas: experimental measurements and numerical simulations," *Plasma Physics and Controlled Fusion*, vol. 53, p. 124016, Dec. 2011.

[109] V. Naulin and A. H. Nielsen, "Accuracy of Spectral and Finite Difference Schemes in 2D Advection Problems," *SIAM Journal on Scientific Computing*, vol. 25, pp. 104–126, Jan. 2003.

[110] P. Ricci and B. N. Rogers, "Plasma turbulence in the scrape-off layer of tokamak devices," *Physics of Plasmas*, vol. 20, no. 1, p. 010702, 2013.

[111] H. R. Wilson, S. C. Cowley, A. Kirk, and P. B. Snyder, "Magneto-hydrodynamic stability of the H-mode transport barrier as a model for edge localized modes: an overview," *Plasma Physics and Controlled Fusion*, vol. 48, pp. A71–A84, May 2006.

[112] J. T. Omotani and B. D. Dudson, "Non-local approach to kinetic effects on parallel transport in fluid models of the scrape-off layer," *Plasma Physics and Controlled Fusion*, vol. 55, p. 055009, May 2013.

[113] F. D. Halpern, S. Jolliet, J. Loizu, A. Mosetto, and P. Ricci, "Ideal ballooning modes in the tokamak scrape-off layer," *Physics of Plasmas*, vol. 20, no. 5, p. 052306, 2013.

[114] A. Mosetto, F. D. Halpern, S. Jolliet, J. Loizu, and P. Ricci, "Turbulent regimes in the tokamak scrape-off layer," *Physics of Plasmas*, vol. 20, no. 9, p. 092308, 2013.

[115] S. Jolliet, F. D. Halpern, J. Loizu, A. Mosetto, and P. Ricci, "Aspect ratio effects on turbulence in Scrape-Off Layer limited plasmas," *Physics of Plasmas, to be submitted*, 2013.

[116] F. D. Halpern, P. Ricci, B. Labit, I. Furno, S. Jolliet, J. Loizu, A. Mosetto, G. Arnoux, J. P. Gunn, J. Horacek, M. Kocan, B. LaBombard, C. Silva, and J.-E. contributors, "Scaling of the SOL width in circular, limited tokamak plasmas," *Nuclear Fusion, in press*, 2013.

[117] J. Loizu, P. Ricci, F. D. Halpern, S. Jolliet, and A. Mosetto, "On the electrostatic potential in the scrape-off layer of magnetic confinement devices," *Plasma Physics and Controlled Fusion, in press*, 2013.

[118] J. Loizu, P. Ricci, F. D. Halpern, S. Jolliet, and A. Mosetto, "Intrinsic toroidal plasma rotation in the scrape-off layer of tokamaks," *Nuclear Fusion, to be submitted*, 2013.

[119] J. Loizu, P. Ricci, F. D. Halpern, S. Jolliet, and A. Mosetto, "Effects of the limiter position on the scrape-off layer width, radial electric field and intrinsic flows," *Nuclear Fusion, to be submitted*, 2013.

[120] A. Cardellini, *Three-dimensional simulations of plasma blob dynamics in a simple magnetized torus*. Master thesis, Politecnico di Torino, 2013.

[121] G. Q. Yu, S. I. Krasheninnikov, and P. N. Guzdar, "Two-dimensional modelling of blob dynamics in tokamak edge plasmas," *Physics of Plasmas*, vol. 13, no. 4, p. 042508, 2006.

[122] A. Arakawa, "Computational design for long-term numerical integration of the equations of fluid motion: Two-dimensional incompressible flow. Part I," *Journal of Computational Physics*, vol. 1, pp. 119–143, Aug. 1966.

[123] A. Mosetto, F. D. Halpern, S. Jolliet, and P. Ricci, "Low-frequency linear-mode regimes in the tokamak scrape-off layer," *Physics of Plasmas*, vol. 19, no. 11, p. 112103, 2012.

[124] R. A. Pitts, S. Alberti, P. Blanchard, J. Horacek, H. Reimerdes, and P. Stangeby, "ELM driven divertor target currents on TCV," *Nuclear Fusion*, vol. 43, pp. 1145–1166, Oct. 2003.

[125] D. A. D'Ippolito, J. R. Myra, and S. J. Zweben, "Convective transport by intermittent blob-filaments: Comparison of theory and experiment," *Physics of Plasmas*, vol. 18, no. 6, p. 060501, 2011.

[126] B. LaBombard, J. Rice, A. E. Hubbard, J. Hughes, M. Greenwald, J. Irby, Y. Lin, B. Lipschultz, E. Marmar, C. Pitcher, N. Smick, S. Wolfe, S. Wukitch, and the Alcator Group, "Transport-driven Scrape-Off-Layer flows and the boundary conditions imposed at the magnetic separatrix in a tokamak plasma," *Nuclear Fusion*, vol. 44, pp. 1047–1066, Oct. 2004.

[127] B. LaBombard, J. W. Hughes, N. Smick, A. Graf, K. Marr, R. McDermott, M. Reinke, M. Greenwald, B. Lipschultz, J. L. Terry, D. G. Whyte, and S. J. Zweben, "Critical gradients and plasma flows in the edge plasma of Alcator C-Mod," *Physics of Plasmas*, vol. 15, no. 5, p. 056106, 2008.

[128] L.-G. Eriksson, E. Righi, and K.-D. Zastrow, "Toroidal rotation in ICRF-heated H-modes on JET," *Plasma Physics and Controlled Fusion*, vol. 39, pp. 27–42, Jan. 1997.

[129] I. H. Hutchinson, J. Rice, R. Granetz, and J. Snipes, "Self-acceleration of a tokamak plasma during ohmic H mode," *Physical review letters*, vol. 84, pp. 3330–3, Apr. 2000.

[130] A. Bortolon, B. Duval, A. Pochelon, and A. Scarabosio, "Observation of Spontaneous Toroidal Rotation Inversion in Ohmically Heated Tokamak Plasmas," *Physical Review Letters*, vol. 97, p. 235003, Dec. 2006.

[131] A. Bondeson and D. Ward, "Stabilization of external modes in tokamaks by resistive walls and plasma rotation," *Physical Review Letters*, vol. 72, pp. 2709–2712, Apr. 1994.

[132] E. Strait, T. Taylor, A. Turnbull, J. Ferron, L. Lao, B. Rice, O. Sauter, S. Thompson, and D. Wróblewski, "Wall Stabilization of High Beta Tokamak Discharges in DIII-D," *Physical Review Letters*, vol. 74, pp. 2483–2486, Mar. 1995.

[133] P. Mantica, D. Strintzi, T. Tala, C. Giroud, T. Johnson, H. Leggate, E. Lerche, T. Loarer, A. Peeters, A. Salmi, S. Sharapov, D. Van Eester, P. de Vries, L. Zabeo, and K.-D. Zastrow, "Experimental Study of the Ion Critical-Gradient Length and Stiffness Level and the Impact of Rotation in the JET Tokamak," *Physical Review Letters*, vol. 102, p. 175002, Apr. 2009.

[134] A. Eriksson, H. Nordman, P. Strand, J. Weiland, T. Tala, E. Asp, G. Corrigan, C. Giroud, M. de Greef, I. Jenkins, H. C. M. Knoops, P. Mantica, K. M. Rantamäki, P. C. de Vries, and K.-D. Zastrow, "Predictive simulations of toroidal momentum transport at JET," *Plasma Physics and Controlled Fusion*, vol. 49, pp. 1931–1943, Nov. 2007.

[135] F. D. Halpern, A. H. Kritz, G. Bateman, A. Y. Pankin, R. V. Budny, and D. C. McCune, "Predictive simulations of ITER including neutral beam driven toroidal rotation," *Physics of Plasmas*, vol. 15, no. 6, p. 062505, 2008.

[136] A. Scarabosio, A. Bortolon, B. P. Duval, A. Karpushov, and A. Pochelon, "Toroidal plasma rotation in the TCV tokamak," *Plasma Physics and Controlled Fusion*, vol. 48, pp. 663–683, May 2006.

[137] J. S. de Grassie, "Tokamak rotation sources, transport and sinks," *Plasma Physics and Controlled Fusion*, vol. 51, p. 124047, Dec. 2009.

[138] B. P. Duval, A. Bortolon, A. Karpushov, R. A. Pitts, A. Pochelon, and A. Scarabosio, "Bulk plasma rotation in the TCV tokamak in the absence of external momentum input," *Plasma Physics and Controlled Fusion*, vol. 49, pp. B195–B209, Dec. 2007.

[139] S. H. Muller, J. A. Boedo, K. H. Burrell, J. S. de Grassie, R. A. Moyer, D. L. Rudakov, and W. M. Solomon, "Experimental Investigation of the Role of Fluid Turbulent Stresses and Edge Plasma Flows for Intrinsic Rotation Generation in DIII-D H-Mode Plasmas," *Physical Review Letters*, vol. 106, p. 115001, Mar. 2011.

[140] Y. Camenen, A. Peeters, C. Angioni, F. Casson, W. Hornsby, A. Snodin, and D. Strintzi, "Transport of Parallel Momentum Induced by Current-Symmetry Breaking in Toroidal Plasmas," *Physical Review Letters*, vol. 102, p. 125001, Mar. 2009.

[141] W. X. Wang, T. S. Hahm, S. Ethier, L. E. Zakharov, and P. H. Diamond, "Trapped Electron Mode Turbulence Driven Intrinsic Rotation in Tokamak Plasmas," *Physical Review Letters*, vol. 106, p. 085001, Feb. 2011.

[142] A. G. Peeters, C. Angioni, A. Bortolon, Y. Camenen, F. Casson, B. Duval, L. Fiederspiel, W. A. Hornsby, Y. Idomura, T. Hein, N. Kluy, P. Mantica, F. Parra, A. P. Snodin, G. Szepesi, D. Strintzi, T. Tala, G. Tardini, P. de Vries, and J. Weiland, "Overview of toroidal momentum transport," *Nuclear Fusion*, vol. 51, p. 094027, Sept. 2011.

[143] J. W. Connor and H. R. Wilson, "A review of theories of the L-H transition," *Plasma Physics and Controlled Fusion*, vol. 42, pp. R1–R74, Jan. 2000.

[144] O. D. Gurcan, P. H. Diamond, C. J. McDevitt, and T. S. Hahm, "A simple model of intrinsic rotation in high confinement regime tokamak plasmas," *Physics of Plasmas*, vol. 17, no. 3, p. 032509, 2010.

[145] F. I. Parra, M. F. F. Nave, A. A. Schekochihin, C. Giroud, J. S. de Grassie, J. H. F. Severo, P. de Vries, and K.-D. Zastrow, "Scaling of Spontaneous Rotation with Temperature and Plasma Current in Tokamaks," *Physical Review Letters*, vol. 108, p. 095001, Feb. 2012.

[146] T. Stoltzfus-Dueck, "Transport-Driven Toroidal Rotation in the Tokamak Edge," *Physical Review Letters*, vol. 108, p. 065002, Feb. 2012.

[147] N. Fedorczak, P. Diamond, G. Tynan, and P. Manz, "Shear-induced Reynolds stress at the edge of L-mode tokamak plasmas," *Nuclear Fusion*, vol. 52, p. 103013, Oct. 2012.

[148] A. Chankin and W. Kerner, "Edge toroidal momentum and its effect on the scrape-off layer," *Nuclear Fusion*, vol. 36, pp. 563–569, May 1996.

[149] V. Rozhansky, S. Voskoboynikov, E. Kaveeva, D. Coster, and R. Schneider, "Simulation of tokamak edge plasma including self-consistent electric fields," *Nuclear Fusion*, vol. 41, pp. 387–401, Apr. 2001.

[150] B. LaBombard, J. Hughes, D. Mossessian, M. Greenwald, B. Lipschultz, J. Terry, and the Alcator C-Mod Team, "Evidence for electromagnetic fluid drift turbulence controlling the edge plasma state in the Alcator C-Mod tokamak," *Nuclear Fusion*, vol. 45, pp. 1658–1675, Dec. 2005.

[151] C. Hidalgo, B. Gonçalves, C. Silva, M. Pedrosa, K. Erents, M. Hron, and G. Matthews, "Experimental Investigation of Dynamical Coupling between Turbulent Transport and Parallel Flows in the JET Plasma-Boundary Region," *Physical Review Letters*, vol. 91, p. 065001, Aug. 2003.

[152] A. Aydemir, "Shear Flows at the Tokamak Edge and Their Role in Core Rotation and the L-H Transition," *Physical Review Letters*, vol. 98, p. 225002, June 2007.

[153] P. Diamond, C. McDevitt, O. Gürcan, T. Hahm, W. X. Wang, E. Yoon, I. Holod, Z. Lin, V. Naulin, and R. Singh, "Physics of non-diffusive turbulent transport of momentum and the origins of spontaneous rotation in tokamaks," *Nuclear Fusion*, vol. 49, p. 045002, Apr. 2009.

[154] V. A. Rozhansky and I. Y. Senichenkov, "1D equation for toroidal momentum transport in a tokamak," *Plasma Physics and Controlled Fusion*, vol. 52, p. 065003, June 2010.

[155] R. A. Pitts, J. Horacek, W. Fundamenski, O. Garcia, A. Nielsen, M. Wischmeier, V. Naulin, and J. Juul Rasmussen, "Parallel SOL flow on TCV," *Journal of Nuclear Materials*, vol. 363-365, pp. 505–510, June 2007.

[156] N. Fedorczak, *Etude Expérimentale du Transport Turbulent au Bord d'un Plasma de Tokamak*. Phd thesis, Université de Provence, 2010.

[157] B. Labit, C. Theiler, A. Fasoli, I. Furno, and P. Ricci, "Blob-induced toroidal momentum transport in simple magnetized plasmas," *Physics of Plasmas*, vol. 18, no. 3, p. 032308, 2011.

[158] K. Besseghir, *Free-Boundary Simulations of ITER Advanced Scenarios*. Phd thesis, EPFL, 2013.

[159] J. Hugill, "Interpretation of asymmetries in tokamak scrape-off layers in terms of poloidal variation of anomalous transport and diamagnetic effects," *Journal of Nuclear Materials*, vol. 196-198, pp. 918–922, Dec. 1992.

[160] J. Gunn, C. Boucher, M. Dionne, I. Duran, V. Fuchs, T. Loarer, I. Nanobashvili, R. Pánek, J.-Y. Pascal, F. Saint-Laurent, J. Stöckel, T. Van Rompuy, R. Zagórski, J. Adámek, J. Bucalossi, R. Dejarnac, P. Devynck, P. Hertout, M. Hron, G. Lebrun, P. Moreau, F. Rimini, A. Sarkissian, and G. Van Oost, "Evidence for a poloidally localized enhancement of radial transport in the scrape-off layer of the Tore Supra tokamak," *Journal of Nuclear Materials*, vol. 363-365, pp. 484–490, June 2007.

[161] M. Kocan and J. P. Gunn, "Comparison of scrape-off layer profiles in outboard- versus inboard-limited plasmas in Tore Supra," *Plasma Physics and Controlled Fusion*, vol. 52, p. 045010, Apr. 2010.

[162] D. Rudakov, J. A. Boedo, R. A. Pitts, G. Jackson, C. Lasnier, A. Leonard, R. A. Moyer, P. Stangeby, G. Tynan, and J. Watkins, "SOL width in limited versus diverted discharges in DIII-D," *Journal of Nuclear Materials*, vol. 415, pp. S387–S390, Aug. 2011.

[163] C. Silva, G. Arnoux, S. Devaux, D. Frigione, M. Groth, J. Horacek, P. Lomas, S. Marsen, G. Matthews, and R. A. Pitts, "Comparison of scrape-off layer

transport in inner and outer wall limited JET plasmas," *Journal of Nuclear Materials*, vol. 438, pp. S189–S193, July 2013.

[164] G. Arnoux, T. Farley, C. Silva, S. Devaux, M. Firdaouss, D. Frigione, R. Goldston, J. Gunn, J. Horacek, S. Jachmich, P. Lomas, S. Marsen, G. Matthews, R. A. Pitts, M. Stamp, and P. Stangeby, "Scrape-off layer properties of ITER-like limiter start-up plasmas in JET," *Nuclear Fusion*, vol. 53, p. 073016, July 2013.

[165] N. Asakura, "Understanding the SOL flow in L-mode plasma on divertor tokamaks, and its influence on the plasma transport," *Journal of Nuclear Materials*, vol. 363-365, pp. 41–51, June 2007.

[166] A. Y. Pigarov, S. I. Krasheninnikov, T. D. Rognlien, M. J. Schaffer, and W. P. West, "Tokamak edge plasma simulation including anomalous cross-field convective transport," *Physics of Plasmas*, vol. 9, no. 4, p. 1287, 2002.

[167] G. Kirnev, G. Corrigan, D. Coster, S. Erents, W. Fundamenski, G. Matthews, and R. A. Pitts, "EDGE2D code simulations of SOL flows and in–out divertor asymmetries in JET," *Journal of Nuclear Materials*, vol. 337-339, pp. 271–275, Mar. 2005.

[168] R. Zagórski, J. P. Gunn, and I. Nanobashvili, "Numerical investigations of edge plasma flows in the Tore Supra tokamak," *Plasma Physics and Controlled Fusion*, vol. 49, pp. S97–S108, July 2007.

[169] M. A. Makowski, D. Elder, T. K. Gray, B. LaBombard, C. J. Lasnier, A. W. Leonard, R. Maingi, T. H. Osborne, P. C. Stangeby, J. L. Terry, and J. Watkins, "Analysis of a multi-machine database on divertor heat fluxes," *Physics of Plasmas*, vol. 19, no. 5, p. 056122, 2012.

Acknowledgements

First of all, I would like to thank my advisor Paolo Ricci. You were like a mentor to me. Thanks for making me enjoy science as I never had before. Also thanks for your constant availability, which was always accompanied by optimism and good humor. The almost daily discussions we had were a real pleasure. I will never forget these four years and I hope we can work once again in the future.

I would like to thank Prof. Hutchinson, Prof. Wilson, and Prof. Fasoli, who carefully read my thesis and gave me a hard time by challenging my knowledge of physics during my thesis defense.

I would also like to thank all the people from the TORPEX group, who adopted me and fed my curiosity as much as one could dream of. In particular, I would like to thank Ambrogio Fasoli and Ivo Furno. You made me understand how important is the connection between experiments and theory, and I learned a lot from the hundreds of TORPEX meetings we had.

I am also really thankful to Christian Theiler. You are one of the most intelligent persons I have ever met. We shared a marvelous collection of curiosity-driven discussions and a great deal of fun, and I am sure this is not over.

A special thanks to Alexandre Bovet, Fabio Avino, and Kyle Gustafson, with whom I could never stop smiling. You have the beautiful virtue of looking at the bright side of life.

I am also very thankful to the people of the Edge Theory group. Annamaria, Federico, and Sébastien, none of this would have been possible without your precious help and your constant motivation. Interacting with you was always very pleasant.

I would also like to thank Karim Besseghir. We shared more than an office, indeed. I really appreciated your kindness, your rationale, and your absurd look at the futile questions of everyday life. You are also one of the persons that has challenged the most my understanding of the world. Thanks a lot for stimulating my curiosity.

Thanks to all the PhD students at CRPP, Francesco, Teo, Thibaut, David Lescure, David Pfefferlé, Julien, Jonathan, Falk, Josef, and all the others. I learned a lot from each of you, not only about physics but also about the meaning of life.

Thanks to all my friends in Lausanne and Switzerland, Paula, Diego, Eden, Carmen, Lucia, Benoit, Teresa, Kate, Karin, Antoine, Bernhard, and all the others. I have many great memories with each of you.

A special thanks to my dear soul-friends from Barcelona, Edu, Pau, Adria Argemi, Adria Llairo, Tito, and Julieta. You are part of my life and you will always be.

I would like to thank all my family, in particular my parents and brothers, to which I owe most of what I am today. And thanks for the love of cooking.

Finally, and most importantly, I would like to thank Susana. You are the best that ever happened to me. My everyday enthusiasm is born in your smile, in your tears, in your imagination, in your dreams, and in the passion you show when you appreciate the tiny little pleasures of life.

Joaquim Loizu Cisquella
Date of birth: 25/11/1986
Email: joaquim.loizu@a3.epfl.ch

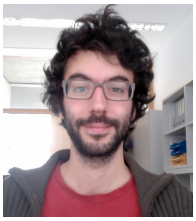

EDUCATION

- **PhD candidate at the Swiss Federal Institute of Technology Lausanne (EPFL)** since 09/2009
  - PhD defense 10/2013
  - PhD in plasma physics: "The role of the sheath in magnetized plasma turbulence and flows" at the Centre de Recherches en Physique des Plasmas (CRPP).
  - Work description: Development of a PIC code for studying plasma-wall interactions; analytical theory to derive boundary conditions for drift-fluid models and implementation in a global fluid code; study of the effect of the sheath on scrape-off-layer physics.
  - Supervisor: Prof. Paolo Ricci
- **Diploma in physics, Swiss Federal Institute of Technology Lausanne (EPFL)** 10/2004 – 03/2009
  - Exchange year in London, UK, at Imperial College London 10/2006 – 06/2007
  - Diploma thesis: "Biophysics of light sensitive neurons: Quantum bump in Drosophila" at the Center for Bio-Inspired Technology, Imperial College London
- **Baccalaureat** (French university entrance qualification), Lycée Français de Barcelone 07/2004

TEACHING EXPERIENCE AND REFEREEING ACTIVITIES

- Teaching assistant for different Bachelor and Master courses: General Physics with Prof. Ansermet, General Physics with Prof. Baldereschi, Numerical Physics with Prof. Villard, Plasma Physics II with Prof. Ricci, General Physics with Prof. Ricci during MSc & PhD
- **Prize for exceptional assistantship work at EPFL** during PhD
- Supervision of two student projects on sheath simulations during PhD
- Co-supervision of one Master thesis on experimental sheath physics in the TORPEX device during PhD
- Refereeing papers for different Journals: Physics of Plasmas, Contributions to Plasma Physics, European Physical Journal D, Journal of Plasma Physics during PhD

LANGUAGE KNOWLEDGE

Spanish	mother tongue
French	mother tongue
Catalan	mother tongue
English	fluent

CONFERENCE CONTRIBUTIONS AND INVITED TALKS (1ST AUTHOR)

- **"The role of the sheath in magnetized plasma fluid turbulence",** invited talk presented at the 40th EPS conference in plasma physics, 2013, Espoo, Finland
- **"Intrinsic toroidal plasma rotation in the Scrape-Off-Layer",** poster presented at the US-EU Joint Transport Task Force conference, 2013, Santa Rosa, California
- **"Tokamak SOL fluid simulations with self-consistent boundary conditions at the magnetic presheath edge",** poster presented at the 54th APS conference on plasma physics, 2012, Providence, Rhode Island

- **"Review and perspectives of electrostatic turbulence and transport studies in the basic plasma physics device TORPEX",** poster presented at the 54th APS conference on plasma physics, 2012, Providence, Rhode Island
- **"The validation project on the TORPEX basic plasma physics device",** talk presented at the US-EU Joint Transport Task Force conference, 2011, San Diego, California
- **"Boundary conditions for plasma fluid models at the magnetic presheath entrance",** poster presented at the US-EU Joint Transport Task Force conference, 2011, San Diego, California
- **"Sheath boundary conditions for plasma fluid models",** poster presented at the Varenna Fusion Theory conference, 2010, Varenna, Italy

PUBLICATIONS

- **First Author**
  - J. Loizu, Paolo Ricci, S. Jolliet, F.D. Halpern and A. Mosetto, "Intrinsic toroidal plasma rotation in the scrape off-layer of tokamaks", submitted to **Nucl. Fusion** (2013)
  - J. Loizu, Paolo Ricci, S. Jolliet, F.D. Halpern and A. Mosetto, "Effects of the limiter position on the scrape-off layer width, radial electric field, and intrinsic flows", submitted to **Nucl. Fusion** (2013)
  - J. Loizu, Paolo Ricci, S. Jolliet, F.D. Halpern and A. Mosetto, "On the electrostatic potential in the Scrape Off-Layer of magnetic confinement devices", in press, **Plasma Phys. Control. Fusion** (2013)
  - J. Loizu, P. Ricci, F. D. Halpern and S. Jolliet, "Boundary conditions for plasma fluid models at the magnetic presheath entrance", **Phys. Plasmas** 19, 122307 (2012)
  - J. Loizu, J. Dominski, P. Ricci and C. Theiler, "Potential of a plasma bound between two biased walls", **Phys. Plasmas** 19, 083507 (2012)
  - J. Loizu, Paolo Ricci and C. Theiler, "Existence of subsonic plasma sheaths", **Phys. Rev. E** 83, 016406 (2011)
- **Co-author**
  - F. D. Halpern, A. Cardellini, P. Ricci, S. Jolliet, J. Loizu and A. Mosetto, "Three-dimensional similations of blob dynamics in a simple magnetized torus", to be submitted, **Phys. Plasmas** (2013)
  - I. Furno, C. Theiler, V. Chabloz, A. Fasoli and J. Loizu, "Pre-sheath density drop induced by ion-neutral friction along plasma blobs and implications for blob velocities", submitted to **Phys. Plasmas** (2013)
  - S. Jolliet, F. D. Halpern, J. Loizu, A. Mosetto and P. Ricci, "Aspect ratio effects on plasma turbulence in scrape-off layer limited plasmas", submitted to **Phys. Plasmas** (2013)
  - F. D. Halpern, P. Ricci, B. Labit, I. Furno, S. Jolliet, J. Loizu, *et al.*, "Theory-based scaling of the SOL width in circular limited tokamak plasmas", **Nucl. Fusion** 53, 122001 (2013)
  - A. Mosetto, F. D. Halpern, S. Jolliet, J. Loizu and P. Ricci, "Turbulence regimes in the tokamak scrape-off layer", **Phys. Plasmas** 20, 092308 (2013)
  - A. Fasoli, F. Avino, A. Bovet, I. Furno, K. Gustafson, S. Jolliet, J. Loizu *et al.*, "Basic investigations of electrostatic turbulence and its interaction with plasma and suprathermal ions in a simple magnetized toroidal plasma", **Nucl. Fusion** 53, 063013 (2013)
  - F. D. Halpern, S. Jolliet, J. Loizu, A. Mosetto and P. Ricci, "Ideal ballooning modes in the tokamak scrape-off layer", **Phys. Plasmas** 20, 052306 (2013)
  - P. Ricci, F. D. Halpern, S. Jolliet, J. Loizu, A. Mosetto, A. Fasoli, I. Furno and C. Theiler, "Simulation of plasma turbulence in scrape-off layer conditions: the GBS code, simulation results and code validation", **Plasma Phys. Control. Fusion** 54, 124047 (2012)
  - C. Theiler, J. Loizu *et al.*, "Properties of convective cells generated in magnetized toroidal plasmas", **Phys. Plasmas** 19, 082304 (2012)
  - C. G. Theiler, I. Furno, J. Loizu and A. Fasoli, "Convective cells and blob control in a simple magnetized plasma", **Phys. Rev. Lett.** 108, 065005 (2012)

- P. Ricci, C. Theiler, A. Fasoli *et al.*, "Methodology for turbulence code validation: Quantification of simulation-experiment agreement and application to the TORPEX experiment", **Phys. Plasmas** 18, 032109 (2011)
- A. Fasoli, A. Burckel, L. Federspiel *et al.*, "Electrostatic instabilities, turbulence and fast ion interactions in the TORPEX device", **Plasma Phys. Control. Fusion** 52, 124020 (2010)
- K. Nikolic, J. Loizu *et al.*, "A stochastic model of the single photon response in *Drosophila* photoreceptors", **Integrative Biology** 2, 354-370 (2010)
- K. Nikolic and J. Loizu, "Noise reduction in analogue computation of *Drosophila* photoreceptors", **J. Comput. Electr.** 7, 458-461 (2008)